

GEORGIA DOT RESEARCH PROJECT 17-29

FINAL REPORT

**DEVELOPMENT OF POSSIBLE SOLUTIONS TO
ELIMINATE OR REDUCE DECK CRACKING ON
SKEWED BRIDGES BUILT BY USING THE
ACCELERATED BRIDGE CONSTRUCTION METHOD**



**OFFICE OF PERFORMANCE-BASED
MANAGEMENT AND RESEARCH
600 WEST PEACHTREE ST. NW
ATLANTA, GA 30308-3607**

1. Report No.: FHWA-GA-19-1729	2. Government Accession No.:	3. Recipient's Catalog No.:	
4. Title and Subtitle: Development of Possible Solutions to Eliminate or Reduce Deck Cracking on Skewed Bridges Built by Using the Accelerated Bridge Construction Method		5. Report Date: December 2019	
		6. Performing Organization Code:	
7. Author(s): Mi G. Chorzepa, Ph.D., P.E. Chnar Solae Stephan Durham, Ph.D., P.E. S. Sonny Kim, Ph.D., P.E.		8. Performing Organization Report No.:	
9. Performing Organization Name and Address: University of Georgia College of Engineering Driftmier Engineering Center, Athens, GA 30602 Phone: (706) 357-0038 Email: chorzepa@uga.edu		10. Work Unit No.:	
		11. Contract or Grant No.: PI# 0012795	
12. Sponsoring Agency Name and Address: Georgia Department of Transportation Office of Performance-Based Management and Research 15 Kennedy Drive Forest Park, GA 30297-2534		13. Type of Report and Period Covered: Final; December 2017 – December 2019	
		14. Sponsoring Agency Code:	
15. Supplementary Notes: Prepared in cooperation with the U.S. Department of Transportation, Federal Highway Administration.			
16. Abstract: The Georgia Department of Transportation (GDOT) employed Accelerated Bridge Construction (ABC) technology to reduce construction impacts and delays when replacing the State Route 299 bridge at I-24 in Dade County, Georgia, over a single weekend in May 2017. Self-Propelled Modular Transporters (SPMTs) were used for the bridge replacement. A few months after the replacement, GDOT observed a large number of visible cracks on the bridge deck. This study investigates possible causes of deck cracking observed on the SR299 bridge at I-24 in Dade County, Georgia. The research team has documented the distress observed in the SR299 bridge by creating a crack map, studying the material compositions, and conducting a finite element analysis. Design and construction details associated with thermal restraints are studied. In addition, displacements and forces imposed on the cast-in-place concrete bridge deck are studied. The main goal of this research is to establish a decision matrix for determining possible causes of cracking in the skewed bridge decks used for ABC, leading to the development of solutions to eliminate or reduce such cracking and recommendations for preventive measures. It is concluded from this study that skewed decks are more susceptible to cracking than straight decks due to asymmetric expansion and contraction. When skewed deck geometries exist in a semi-integral abutment bridge, the skewed corners on the abutment sides are vulnerable to developing cracks, regardless of the bearing details at expansion joint locations. Therefore, when designing a skewed bridge, a semi-integral abutment design should be avoided, if possible. If such design is necessary in conjunction with ABC technologies, bearings require greater consideration in order to minimize cracks resulting from temperature changes. Asymmetric thermal movements should be expected when an asymmetric deck geometry exists; thus, bearings and steel reinforcement in the deck must be designed accordingly.			
17. Keywords: Skewed Bridge, Integral Bridge, Bearing, Accelerated Bridge Construction, ABC, SPMT, Thermal, Finite Element Analysis, Cracking		18. Distribution Statement:	
19. Security Classification (of this report): Unclassified	20. Security Classification (of this page): Unclassified	21. No. of Pages: 208	22. Price: N/A

GDOT Research Project No. 17-29

DEVELOPMENT OF POSSIBLE SOLUTIONS TO ELIMINATE OR REDUCE
DECK CRACKING ON SKEWED BRIDGES BUILT BY USING THE
ACCELERATED BRIDGE CONSTRUCTION METHOD

Final Report

By

Mi G. Chorzepa, Ph.D., P.E.
Associate Professor of Civil Engineering

Chnar Solae
Graduate Student

Stephan Durham, Ph.D., P.E.
Professor of Civil Engineering

S. Sonny Kim, Ph.D., P.E.
Associate Professor of Civil Engineering

University of Georgia
College of Engineering

Contract with

Georgia Department of Transportation

In cooperation with

U.S. Department of Transportation
Federal Highway Administration

December 2019

The contents of this report reflect the views of the authors, who are responsible for the facts and accuracy of the data presented herein. The contents do not necessarily reflect the official views of the Georgia Department of Transportation or the Federal Highway Administration. This report does not constitute a standard, specification, or regulation.

TABLE OF CONTENTS

	Page
TABLE OF CONTENTS	iv
LIST OF TABLES	viii
LIST OF FIGURES	ix
EXECUTIVE SUMMARY	xiv
ACKNOWLEDGEMENT.....	xvi
1 INTRODUCTION	1
1.1 Background	1
1.2 Georgia Department of Transportation’s Bridge Replacement Using Accelerated Bridge Construction	2
1.3 Problem Statement	4
1.4 Objectives	7
1.5 Research Methodology and Procedure	8
1.6 Summary of Sections	10
2 LITERATURE REVIEW.....	11
2.1 Introduction.....	11
2.2 Accelerated Bridge Construction.....	11
2.2.1 Introduction to Accelerated Bridge Construction	11
2.2.2 Structural Placement Methods (SPM).....	12
2.2.3 Challenges and Barriers.....	14
2.2.4 Best Practices	16
2.3 Integral Abutment Design.....	18
2.4 Curved and Skewed Bridges.....	19
2.4.1 Curved Bridges.....	19
2.4.2 Skewed Bridges.....	20
2.5 Bridge Deck Cracking.....	23
2.5.1 Structural Design.....	24
2.5.2 Material Design	26
2.5.3 Construction	27
2.6 Practices to Alleviate Deck Cracking	27
2.6.1 Controlling Cracks on Bridge Decks.....	28
2.6.1.1 Structural design recommendations	28

2.6.1.2	Material properties recommendations	28
2.6.1.3	Construction method recommendations	29
2.6.2	State Departments of Transportation Approaches to Control Cracking.....	30
2.7	Finite Element Analysis of Concrete Cracking	31
2.8	Summary of Literature Review.....	32
3	FIELD INVESTIGATIONS.....	33
3.1	Introduction.....	33
3.2	First Bridge Site Visit	33
3.2.1	Procedure.....	33
3.2.2	Summary of Findings	33
3.3	Infrared and High-Definition Bridge Deck Scan	35
3.3.1	Introduction	35
3.3.2	Summary of Findings	35
3.4	Petrographic Evaluation of Concrete Deck.....	36
3.4.1	Introduction	36
3.4.2	Summary of Findings	38
3.5	Second Bridge Site Visit.....	38
3.5.1	Introduction	38
3.5.2	Procedure.....	39
3.5.3	Summary of Findings	43
3.5.3.1	Traffic data	43
3.5.3.2	Cracking conditions.....	45
3.6	Summary of Site Investigations	56
4	ANALYTICAL INVESTIGATIONS	57
4.1	Introduction.....	57
4.2	SR299 Bridge Geometry.....	57
4.2.1	Deck Geometry Details	58
4.2.2	Reinforcement Details	62
4.2.3	Girders Details.....	63
4.2.4	Diaphragms, Endwalls, and Edge Beams Details	66
4.3	Material Properties.....	68
4.3.1	Deck Material Properties.....	68
4.3.2	Reinforcement Material Properties	68
4.3.3	Girders Material Properties	69

4.3.4 Prestressing Strands Material Properties	69
4.3.5 Diaphragms, Endwalls, and Edge Beams Material Properties	70
4.4 Boundary Conditions	70
4.4.1 Structural Boundary Conditions	71
4.4.1.1 Structural boundary condition at Bent 1 and Bent 3	73
4.4.1.2 Structural boundary condition at Intermediate Bent 2	75
4.4.2 Summary	81
4.5 Element Types	82
4.6 Bridge Deck Geometries.....	83
4.6.1 Straight Bridge Deck	84
4.6.2 Inclined Bridge Deck.....	85
4.6.3 Skewed and Curved Bridge Deck	86
4.6.4 Highly Skewed Bridge Deck	86
4.7 Thermal Loading.....	87
4.7.1 Twelve Thermal Analysis Cases	91
4.8 Structural Loading	93
4.8.1 Live load Case A	94
4.8.2 Live load Case B	95
4.9 Vertical Displacement Loading	95
4.10 Validation and Verification	98
4.10.1 Validation of the Procedure.....	98
4.10.2 Verification of the Bridge Model	98
4.10.2.1 Verification of mesh size and convergence.....	98
4.10.2.2 Total weight vs. reaction	101
5 RESULTS FROM ANALYTICAL INVESTIGATIONS.....	102
5.1 Summary of Results	102
5.2 Results from Thermal Analysis	102
5.3 Results from Coupled Thermal-Structural Analyses	104
5.3.1 Straight Bridge Deck	104
5.3.1.1 Case 1: Straight-FR	104
5.3.1.2 Case 2: Straight-LVR	107
5.3.1.3 Case 3: Straight-VR.....	111
5.3.2 Inclined Bridge Deck.....	114
5.3.2.1 Case 4: Inclined-FR.....	114

5.3.2.2 Case 5: Inclined-LVR.....	117
5.3.2.3 Case 6: Inclined-VR	120
5.3.3 Skewed and Curved Bridge Deck	123
5.3.3.1 Case 7: Skewed & Curved-FR	123
5.3.3.2 Case 8: Skewed & Curved-LVR	126
5.3.3.3 Case 9: Skewed & Curved-VR.....	129
5.3.4 Highly Skewed Bridge Deck Geometry	131
5.3.4.1 Case 10: Highly Skewed-FR	132
5.3.4.2 Case 11: Highly Skewed-LVR.....	135
5.3.4.3 Case 12: Highly Skewed-VR	137
5.4 Results from Live Load Analysis	141
5.5 Results from Induced-Displacement Load Analysis.....	142
6 ANALYSIS AND SYNTHESIS OF THE RESULTS	144
6.1 Effect of Boundary Conditions for Varying Deck Geometries	144
6.1.1 Straight Deck.....	152
6.1.2 Inclined Deck	152
6.1.3 Skewed and Curved Deck	153
6.1.4 Discussion	154
6.2 Effect of Skew Angle.....	155
6.3 Effect of Coefficient of Thermal Expansion.....	161
6.4 Effect of Reinforcing Steel Pattern in the Deck.....	163
6.5 Effect of Live Loads and Induced Vertical Displacements	165
6.6 Synthesis of Results and Potential Causes of Cracks	165
7 CONCLUSIONS.....	171
8 RECOMMENDATIONS AND FUTURE WORK.....	173
REFERENCES.....	175
APPENDIX A	A-1
APPENDIX B	B-1

LIST OF TABLES

Table No.	Page
Table 1 – Decision matrix for screening out factors relevant to cracking.	8
Table 2 – Best practices in implementing ABC methods (Culmo, 2017).	17
Table 3 – Best practices for precast deck panel connections in ABC (Culmo, 2017).	18
Table 4 – Length and condition of repaired and unrepaired cracks in SR299 bridge.	36
Table 5 – Dimensions of Spans 1 and 2 (SR299 bridge).	59
Table 6 – Deck curvature details (SR299 bridge).	59
Table 7 – Deck reinforcement details (SR299 bridge).	62
Table 8 – Dimensions of diaphragms, endwalls, and edge beams.	66
Table 9 – Material properties of SR299 bridge deck concrete.	68
Table 10 – Material properties of bridge deck reinforcement.	69
Table 11 – Material properties of girders.	69
Table 12 – Material properties of prestressing strands.	70
Table 13 – Material properties of diaphragms, endwalls, and edge beams.	70
Table 14 – Bridge deck geometry cases.	84
Table 15 – Temperature differentials within a concrete superstructure (Imbsen et al., 1985).	89
Table 16 – Temperatures applied in SR299 bridge deck analysis.	90
Table 17 – Twelve analysis cases reflecting thermal boundary conditions and deck geometries.	92
Table 18 – Induced vertical displacement magnitudes at bearing locations.	97
Table 19 – Mesh sensitivity of the Span 1 model.	100
Table 20 – Decision matrix for screening out factors relevant to cracking.	170

LIST OF FIGURES

Figure No.	Page
Figure 1 – Location of SR299 bridge (Google, 2019).....	2
Figure 2 – SR299 bridge superstructure plan (GDOT-DRW, 2016).	4
Figure 3 – Section view of the SR299 bridge superstructure (GDOT-DRW, 2016).....	4
Figure 4 – SR299 bridge site photo (Side View).....	5
Figure 5 – Typical deck corner cracks in Span 1.....	6
Figure 6 – Typical cracks in the acute corner of Span 1.....	6
Figure 7 – Typical longitudinal cracks at the expansion joint.	6
Figure 8 – SPM construction procedure (GarverUSA, 2013).....	14
Figure 9 – Fully integral vs. semi-integral bridges.	19
Figure 10 – Illustration of a skew angle in a skewed bridge.	21
Figure 11 – Force flow of skewed edges (Rajagopalan, 2006).....	21
Figure 12 – Recommended reinforcement pattern for skewed decks (Anusreebai & Krishnachandran, 2016).	23
Figure 13 – Longitudinal cracks at the expansion joint on SR299 bridge (eastbound lane of Spans 1 and 2).	34
Figure 14 – Typical diagonal corner cracks on SR299 bridge (eastbound lane of Span 2).	34
Figure 15 – Additional cracks along SR299 bridge (westbound lane shoulder of Span 1).	34
Figure 16 – Core locations and cross sections on SR299 bridge.....	37
Figure 17 – FHWA vehicle classification (FHWA, 2019).	40
Figure 18 – I-24 total traffic volume versus Class 9 trucks in December 2017.	40
Figure 19 – I-24 Class 9 truck traffic in December 2017.	41
Figure 20 – Exiting and merging loops of I-24.....	42
Figure 21 – Traffic volume for eastbound loops of I-24.	42
Figure 22 – Traffic volume for westbound loops of I-24.	42
Figure 23 – I-24 Class 9 trucks traffic volume for half of December 2018.....	43
Figure 24 – Traffic volume and vehicle classes on the SR299 bridge.....	44
Figure 25 – Total traffic and Class 9 truck traffic counts on the SR299 bridge.....	44
Figure 26 – Back to back Class 9 trucks crossing SR299 bridge.	45
Figure 27 – Oversize load Class 9 truck crossing SR299 bridge.....	45
Figure 28 – New and old cracks on both spans of SR299 bridge.....	46
Figure 29 – Crack through the expansion joint.....	46
Figure 30 – Untreated diagonal cracks without epoxy coatings.	47
Figure 31 – Untreated longitudinal cracks without epoxy coatings.	47
Figure 32 – Crack width measurement (0.016 in. or 0.41 mm).....	48
Figure 33 – Crack width measurement (0.020 in. or 0.51 mm).....	48
Figure 34 – Crack width measurement (0.025 in. or 0.64 mm).....	48
Figure 35 – Crack width measurement (0.030 in. or 0.76 mm).....	49
Figure 36 – Crack width measurement (0.040 in. or 1.02 mm).....	49
Figure 37 – Old photo showing cracks at eastbound corner of Span 2.....	50
Figure 38 – New photo showing cracks at eastbound corner of Span 2.	50

Figure 39 – Old photo showing cracks in eastbound lane at Span 2 end.....	51
Figure 40 – New photo showing cracks in eastbound lane at Span 2 end.	51
Figure 41 – Old photo showing cracks thru expansion joint between Spans 1 and 2.....	52
Figure 42 – New photo showing cracks thru expansion joint between Spans 1 and 2.	52
Figure 43 – Old photo showing cracks at the obtuse corner of eastbound Span 1.	53
Figure 44 – New photo showing cracks at the obtuse corner of eastbound Span 1.....	53
Figure 45 – Old photo showing cracks at the acute corner of westbound Span 1.	54
Figure 46 – New photo showing cracks at the acute corner of westbound Span 1.....	54
Figure 47 – Old photo showing cracks from westbound lane of Span 2.	55
Figure 48 – New photo showing cracks from westbound lane of Span 2.....	55
Figure 49 – SR299 bridge.	58
Figure 50 – Deck curvature (SR299 bridge).....	59
Figure 51 – Bridge deck curvature layout in DIANA.....	60
Figure 52 – Bridge circular curve with skewed bridge spans.	60
Figure 53 – Spans 1 and 2 showing skew angles (SR299 bridge).....	60
Figure 54 – Vertical curve data (SR299 bridge) (GDOT-DRW, 2016).	61
Figure 55 – Isometric view in DIANA.	61
Figure 56 – Mild steel reinforcement layout in DIANA.....	63
Figure 57 – Plan view showing Span 1 PSC girders (GDOT-DRW, 2016).	64
Figure 58 – Plan view showing Span 2 PSC girders (GDOT-DRW, 2016).	64
Figure 59 – Section view of a PSC girder (SR299 bridge).....	65
Figure 60 – Isometric view of PSC girders of Span 1 in DIANA.	65
Figure 61 – Top view showing PSC girders of Spans 1 and 2 in DIANA.	66
Figure 62 – Isometric view showing prestressed strands in Span 1 girders.	66
Figure 63 – Modeled diaphragms (SR299 bridge) in DIANA.	67
Figure 64 – Bridge model showing structural components of the SR299 bridge.....	67
Figure 65 – SR299 bridge span support conditions (GDOT-DRW, 2016).....	72
Figure 66 – Endwall support condition at Bents 1 and 3.....	74
Figure 67 – Typical sole plate details at End Bents 1 and 3 (GDOT-DRW, 2016).....	74
Figure 68 – Typical bearing support at Bents 1 and 3.	75
Figure 69 – Expansion joint at Intermediate Bent 2.	76
Figure 70 – Design of sole plate at Intermediate Bent 2 (GDOT-DRW, 2016).	76
Figure 71 – Bearing details at Intermediate Bent 2.	78
Figure 72 – Structural boundary condition for FR.....	79
Figure 73 – Structural boundary condition for LVR.	80
Figure 74 – Structural boundary condition for VR.....	81
Figure 75 – CHX60 solid brick element (DIANA, Version 10.2).....	83
Figure 76 – BQ4HT boundary element (DIANA, Version 10.2).	83
Figure 77 – Plan view of straight bridge deck.	84
Figure 78 – Isometric view of inclined bridge deck.	85
Figure 79 – Front view of inclined bridge deck.....	85
Figure 80 – Rear view of inclined bridge deck.....	85
Figure 81 – Plan view of curved and skewed deck (Span 1 of the SR299 bridge).....	86
Figure 82 – Plan view of highly skewed deck (Span 2 of the SR299 bridge).	87
Figure 83 – Maximum solar radiation zones for the United States (Imbsen et al., 1985). ..	89

Figure 84 – Temperature gradient within a concrete superstructure (Imbsen et al., 1985).	89
Figure 85 – Four bridge deck geometries considered in this study (plan view).	92
Figure 86 – Applied live load on SR299 bridge (FHWA, 2000).	93
Figure 87 – Type 3-S2 truck load distribution.	94
Figure 88 – Truck distribution for maximum bending moment on Span 2.	94
Figure 89 – Truck distribution for maximum shear force on Span 2.	95
Figure 90 – SPMT location for moving Span 2 (GDOT, 2016).	96
Figure 91 – Bearing locations for moving Span 2 in DIANA.	97
Figure 92 – Top view of deck mesh elements.	99
Figure 93 – Isometric view of mesh girder elements.	99
Figure 94 – Isometric view of endwall, diaphragms, and edge beam elements.	99
Figure 95 – Strain value vs. element size.	101
Figure 96 – Temperature rise of SR299 bridge superstructure.	103
Figure 97 – Temperature distribution in the bridge superstructure.	103
Figure 98 – Temperature distribution through superstructure (Span 1).	104
Figure 99 – Temperature distribution through deck depth at mid-span location.	104
Figure 100 – Total displacement in Straight-FR.	105
Figure 101 – Longitudinal displacement in Straight-FR.	106
Figure 102 – Transverse displacement in Straight-FR.	106
Figure 103 – Top view showing cracked elements in Straight-FR.	106
Figure 104 – Bottom view showing cracked elements in Straight-FR.	107
Figure 105 – Top view showing crack widths in Straight-FR.	107
Figure 106 – Top view showing crack orientations in Straight-FR.	107
Figure 107 – Total displacement in Straight-LVR.	108
Figure 108 – Longitudinal displacement in Straight-LVR.	109
Figure 109 – Transverse displacement in Straight-LVR.	109
Figure 110 – Top view showing cracked elements in Straight-LVR.	109
Figure 111 – Bottom view showing cracked elements in Straight-LVR.	110
Figure 112 – Top view showing crack widths in Straight-LVR.	110
Figure 113 – Top view showing crack orientations in Straight-LVR.	110
Figure 114 – Total displacement in Straight-VR.	111
Figure 115 – Longitudinal displacement in Straight-VR.	112
Figure 116 – Transverse displacement in Straight-VR.	112
Figure 117 – Top view showing cracked elements in Straight-VR.	112
Figure 118 – Bottom view showing cracked elements in Straight-VR.	113
Figure 119 – Top view showing crack widths in Straight-VR.	113
Figure 120 – Top view showing crack orientations in Straight-VR.	113
Figure 121 – Total displacement in Inclined-FR.	114
Figure 122 – Longitudinal displacement in Inclined-FR.	115
Figure 123 – Transverse displacement in Inclined-FR.	115
Figure 124 – Top view showing cracked elements in Inclined-FR.	115
Figure 125 – Bottom view showing cracked elements in Inclined-FR.	116
Figure 126 – Top view showing crack widths in Inclined-FR.	116
Figure 127 – Top view showing crack orientations in Inclined-FR.	116
Figure 128 – Total displacement in Inclined-LVR.	117

Figure 129 – Longitudinal displacement in Inclined-LVR.....	118
Figure 130 – Transverse displacement in Inclined-LVR.....	118
Figure 131 – Top view showing cracked elements in Inclined-LVR.....	118
Figure 132 – Bottom view showing cracked elements in Inclined-LVR.....	119
Figure 133 – Top view showing crack widths in Inclined-LVR.	119
Figure 134 – Top view showing crack orientations in Inclined-LVR.	119
Figure 135 – Total displacement in Inclined-VR.	120
Figure 136 – Longitudinal displacement in Inclined-VR.	121
Figure 137 – Transverse displacement in Inclined-VR.	121
Figure 138 – Top view showing cracked elements in Inclined-VR.....	121
Figure 139 – Bottom view showing cracked elements in Inclined-VR.	122
Figure 140 – Top view showing crack widths in Inclined-VR.....	122
Figure 141 – Top view showing crack orientations in Inclined-VR.....	122
Figure 142 – Total displacement in Skewed & Curved-FR.....	124
Figure 143 – Longitudinal displacement in Skewed & Curved-FR.	124
Figure 144 – Transverse displacement in Skewed & Curved-FR.....	124
Figure 145 – Top view showing cracked elements in Skewed & Curved-FR.....	125
Figure 146 – Bottom view showing cracked elements in Skewed & Curved-FR.	125
Figure 147 – Top view showing crack widths in Skewed & Curved-FR.	125
Figure 148 – Top view showing crack orientations in Skewed & Curved-FR.....	126
Figure 149 – Total displacement in Skewed & Curved-LVR.....	126
Figure 150 – Longitudinal displacement in Skewed & Curved-LVR.	127
Figure 151 – Transverse displacement in Skewed & Curved-LVR.	127
Figure 152 – Top view showing cracked elements in Skewed & Curved-LVR.....	127
Figure 153 – Bottom view showing cracked elements in Skewed & Curved-LVR.	128
Figure 154 – Top view showing crack widths in Skewed & Curved-LVR.....	128
Figure 155 – Top view showing crack orientations in Skewed & Curved-LVR.....	128
Figure 156 – Total displacement in Skewed & Curved-VR.	129
Figure 157 – Longitudinal displacement in Skewed & Curved-VR.....	129
Figure 158 – Transverse displacement in Skewed & Curved-VR.....	130
Figure 159 – Top view showing cracked elements in Skewed & Curved-VR.	130
Figure 160 – Bottom view showing cracked elements in Skewed & Curved-VR.....	130
Figure 161 – Top view showing crack widths in Skewed & Curved-VR.	131
Figure 162 – Top view showing crack orientations in Skewed & Curved-VR.	131
Figure 163 – Total displacement in Highly Skewed-FR.	132
Figure 164 – Longitudinal displacement in Highly Skewed-FR.	133
Figure 165 – Transverse displacement in Highly Skewed-FR.	133
Figure 166 – Top view showing cracked elements in Highly Skewed-FR.....	133
Figure 167 – Bottom view showing cracked elements in Highly Skewed-FR.	134
Figure 168 – Top view showing crack widths Highly Skewed-FR.	134
Figure 169 – Top view showing crack orientations in Highly Skewed-FR.....	134
Figure 170 – Total displacement in Highly Skewed-LVR.	135
Figure 171 – Longitudinal displacement in Highly Skewed-LVR.	135
Figure 172 – Transverse displacement in Highly Skewed-LVR.	136
Figure 173 – Top view showing cracked elements in Highly Skewed-LVR.	136
Figure 174 – Bottom view showing cracked elements in Highly Skewed-LVR.....	136

Figure 175 – Top view showing crack widths in Highly Skewed-LVR.....	137
Figure 176 – Top view showing crack orientations in Highly Skewed-LVR.....	137
Figure 177 – Total displacement in Highly Skewed-VR.....	138
Figure 178 – Longitudinal displacement in Highly Skewed-VR.....	138
Figure 179 – Transverse displacement in Highly Skewed-VR.....	139
Figure 180 – Top view showing cracked elements in Highly Skewed-VR.....	139
Figure 181 – Bottom view showing cracked elements in Highly Skewed-VR.	139
Figure 182 – Top view showing crack widths in Highly Skewed-VR.	140
Figure 183 – Top view showing crack orientations in Highly Skewed-VR.	140
Figure 184 – Total displacement contour for Live Load Case A.	141
Figure 185 – Total displacement contour for Live Load Case B.....	141
Figure 186 – Stress intensity for Live Load Case A.....	142
Figure 187 – Stress intensity for Live Load Case B.	142
Figure 188 – Total displacement contour for Displacement Case V4.....	143
Figure 189 – Tensile stress intensity plot for Displacement Case V4.....	143
Figure 190 – Effect of restraints on displacements (Straight Deck).	145
Figure 191 – Effect of restraints on displacements (Inclined Deck).	146
Figure 192 – Effect of restraints on displacements (Skewed & Curved Deck).	147
Figure 193 – Effect of restraints and deck geometries on crack width.....	148
Figure 194 – Effect of deck geometries on displacements (movements fully restrained).	149
Figure 195 – Effect of deck geometries on displacements (longitudinal and vertical movements restrained).	150
Figure 196 – Effect of deck geometries on displacements (vertical movements restrained).	151
Figure 197 – Predicted cracks in Spans 1 and 2.	155
Figure 198 – Comparison of longitudinal displacements between Spans 1 and 2.....	156
Figure 199 – Comparison of transverse displacements between Spans 1 and 2.....	157
Figure 200 – Comparison of total displacements between Spans 1 and 2.....	158
Figure 201 – Comparison of crack widths between Spans 1 and 2.	159
Figure 202 – Sensitivity of Crack width for reduced CTE.....	161
Figure 203 – Crack plots showing the effect of reduced CTE.....	162
Figure 204 – Two different reinforcing steel patterns.	163
Figure 205 – Crack width plots showing the effect of reinforcement pattern.	164
Figure 206 – Observed and computed cracks on SR299 bridge deck (Span 1).....	166
Figure 207 – Observed and computed cracks on SR299 bridge deck (Span 2).....	167

EXECUTIVE SUMMARY

This study investigates possible causes of deck cracking observed on the SR299 bridge at I-24 in Dade County, Georgia. This bridge was completed in May 2017 utilizing accelerated bridge construction (ABC) technology. A few months after construction, the Georgia Department of Transportation (GDOT) observed a large number of visible cracks on the bridge deck.

This research study aims to document the distress observed in the SR299 bridge by creating a crack map, studying the material compositions, and conducting a finite element analysis. Design and construction details associated with thermal restraints are studied. In addition, displacements and forces imposed on the cast-in-place concrete bridge deck are studied. The main goal of this research is to establish a decision matrix for determining possible causes of cracking in the skewed bridge decks used for ABC, leading to the development of solutions to eliminate or reduce such cracking and recommendations for preventive measures.

It is concluded from this study that skewed decks are more susceptible to cracking than straight decks due to asymmetric expansion and contraction. When skewed deck geometries exist in a semi-integral abutment bridge, the skewed corners on the abutment sides are vulnerable to developing cracks, regardless of the bearing details at expansion joint locations. Therefore, when designing a skewed bridge, a semi-integral abutment design should be avoided, if possible. If such design is necessary in conjunction with ABC technologies, bearings require greater consideration in order to minimize cracks caused by temperature changes. Asymmetric thermal movements should be expected when an

asymmetric deck geometry exists. Therefore, bearings and steel reinforcement in the deck must be designed accordingly.

In case of the SR299 bridge, it was susceptible to deck cracking due to the skewed deck geometries at the integrated bridge ends. These two factors (skewed and semi-integral) were inevitable design features to enable a bridge replacement by ABC. Additionally, inspection report indicates that sole plate details may not be adequate to accommodate thermal movements from temperature variations. However, the design details show adequate sole plate details with slots of sufficient size. This sole plate discrepancy may have exacerbated thermal cracking, particularly in the acute corners at the expansion joint location. In summary, there are multiple factors that may have caused the distress on the deck.

Best practices for working with skewed decks include using a bridge deck thickness greater than 6.50 in. (165 mm), designing reinforcement patterns for skewed deck geometries and environmental conditions, lowering cement content, and using a smaller size of aggregate to prevent shrinkage. In terms of reinforcement orientation and details, there appears to be no strong consensus on how to mitigate cracking in skewed decks. A best practice guide for a wide range of skewed deck geometries is strongly recommended.

ACKNOWLEDGEMENT

The University of Georgia greatly appreciates the financial support provided by the Georgia Department of Transportation (GDOT) for this work. This report includes major findings of the research study completed by Chnar Solae in partial fulfillment of her MS degree requirements. The authors would like to thank the personnel at GDOT who assisted with this study. A special thanks to Dr. Peter Wu (Office of Materials), Darryl VanMeter, Andrew Hoenig, Natale Marini (Office of Innovative Delivery), and Mr. David Jared P.E. (Performance-based Management and Research) for their research support and the provision of pertinent information. Special thanks also to Mr. Binh Bui, the project manager, who advised the research team in successfully performing the study and coordinated project meetings with GDOT's Office of Materials and Office of Innovative Delivery.

1 INTRODUCTION

1.1 Background

Bridges come in various design forms and shapes. In many instances, topographical conditions prohibit bridges from having straight or rectangular shapes and layouts, resulting in skewed bridges. For example, topographical obstacles may result in horizontally curved bridge decks. These bridges are mainly constructed in complex interchanges with complicated geometries and limited right of way. Similarly, skewed bridges are necessary when roadways are not perpendicular to the bridge centerline at bridge support locations. These skewed bridges have skewed deck edges, and the degree of skewness affects the live load distribution at skewed deck ends, as well as bridge deck behavior, such as thermal expansion and contraction.

There are more than 14,863 bridges used by travelers every day in the state of Georgia (FHWA, 2017), part of which requires replacement. Accelerated Bridge Construction (ABC) technologies are one of the most recent construction methods adopted by state Departments of Transportation (DOTs) in the U.S. and are known to reduce construction-related closures and traffic delays for travelers and commuters. For instance, the Structural Placement Method (SPM) is often used (see Section 2.2.2). This method implies the construction of bridge components off- or adjacent to the site and involves removing the existing bridge as well as transporting bridge components to the site for accelerated installation.

In Georgia, bridge decks are mainly constructed from concrete materials, also reinforced concrete members are designed for cracked sections. Cracks occur for numerous reasons, such as shrinkage, thermal expansion, and sulfate attack; however, when

significant cracking (i.e., involving cracks with widths greater than 0.0625 in. (1.6 mm)) develops on a bridge deck, durability is compromised. Such cracks, if not properly sealed, can increase the risk of deterioration or corrosion.

1.2 Georgia Department of Transportation's Bridge Replacement Using Accelerated Bridge Construction

The Georgia Department of Transportation (GDOT) employed an innovative, accelerated method to replace the existing two-lane State Route 299 bridge at I-24, located in Dade County, Georgia, north of the City of Trenton. The location of the bridge is shown in Figure 1 (Google, 2019). This project—completed over a 56-hour time span from May 12 to May 14, 2017—was expected to improve bridge safety and utilize a technique designed to shorten bridge construction time and thus minimize the impact of construction on the traveling public (GDOT BuildSmart, 2017).



Figure 1 – Location of SR299 bridge (Google, 2019).

The new bridge, hereafter referred to as the ‘SR299 bridge’, includes two 12-ft (3.66 m) travel lanes and two 8-ft (2.44 m) shoulders. It consists of two skewed reinforced

concrete deck slabs, Spans 1 and 2, for which GDOT employed SPMT to move. Span 1 measures 103.83 ft (31.65 m) in length, and Span 2 measures 97.75 ft (29.79 m) in length. The deck is simply supported and horizontally curved with a radius of 818.50 ft (249.28 m) and skew angles of 16.15°, 23.42°, and 30.26°. These angles define the angle between centerline of the bridge supports (i.e., End Bent 1, Intermediate Bent 2, and End Bent 3) and a line perpendicular to the centerline of the bridge (i.e., centerline of Spans 1 and 2).

The bridge has a side slope of 7% down to its left, with a vertical slope of 0.12° for Span 1 and 0.61° for Span 2. The deck is made of normal cast-in-place concrete, which is reinforced in two ways with two layers of steel reinforcement. While the longitudinal reinforcement is placed parallel to the girders, the transverse reinforcement is placed radially along the bridge deck curvature.

Seven American Association of State Highway and Transportation Officials (AASHTO) Type III prestressed girders support each span. The girders are connected at mid-span by diaphragms. Moreover, the deck is integrated with endwalls at abutment ends. An integral bridge, like this one, contains no expansion joint on the abutment side and thus experiences increased movement on the other side of the integrated abutment. Edge beams are provided at the ends of each span on the expansion joint side. The plan for the SR299 bridge is presented in Figure 2 (GDOT-DRW, 2016) and shows the two spans, girders, diaphragms, endwalls, and edge beams. Figure 3 shows a cross section view through the bridge deck (GDOT-DRW, 2016). The bridge superstructure was constructed on temporary supports adjacent to the in-service bridge and slid into its final position by two SPMTs.

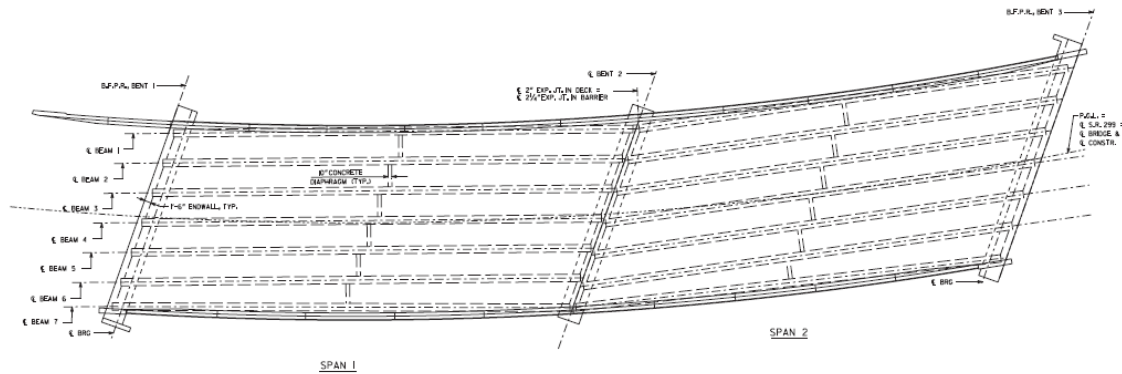


Figure 2 – SR299 bridge superstructure plan (GDOT-DRW, 2016).

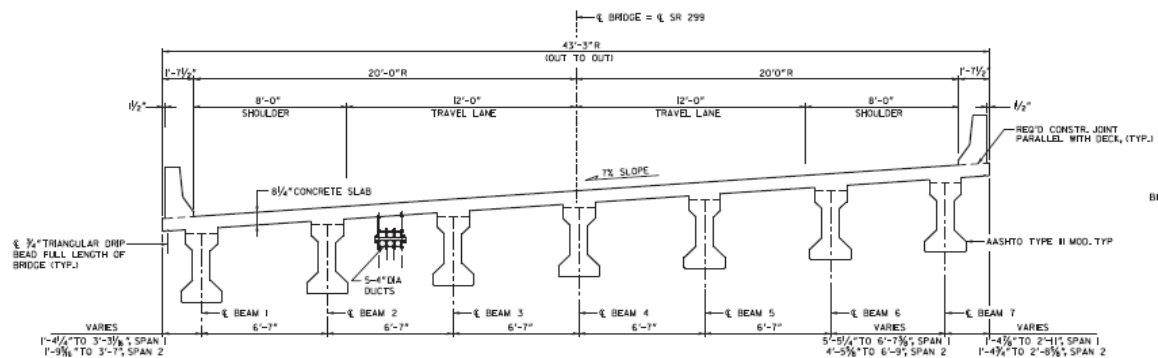


Figure 3 – Section view of the SR299 bridge superstructure (GDOT-DRW, 2016).

1.3 Problem Statement

ABC often involves an innovative construction method that aids in the reduction of construction time and traffic disruption. New technologies that alleviate detours and traffic delays have become important among state DOTs, and GDOT has successfully delivered an ABC project. This project involved replacing a skewed and curved bridge. However, large number of cracks were discovered on the bridge deck in late August 2017. Cores extracted from the deck indicate that the cracks run full-depth. To the best of the research team's knowledge, an epoxy injection was provided to seal the cracks, though the cores that were taken after the injection indicate that the epoxy material did not fully fill the

cracks. This bridge was last inspected on August 16, 2017, and the deck was in good (State 1) condition. Since the first inspection, however, cracks have become noticeably visible on the bridge deck. The orientation of these cracks varies. Longitudinal cracks running parallel to the precast beams (or bridge span direction) are observed along the expansion joint where the two edge beams join the two spans. In addition, diagonal cracks appear at the acute corners of the two-deck slabs. Figure 4 shows a site photo of the SR299 bridge. Figures 5 through 7 show cracks that were found on the SR299 bridge deck.

Deck cracking is one of the most common problems in bridge decks, particularly in skewed bridge decks. Despite this challenge, few studies investigate the causes of bridge deck cracking and identify potential solutions. More specifically, cracking distress resulting from the use of ABC technologies has not been fully investigated since these technologies are still in their infancy. This study identifies potential solutions for reducing deck cracking in skewed bridges and hypothesizes that ABC technologies introduce other design and construction factors that may affect bridge construction outcomes.



Figure 4 – SR299 bridge site photo (Side View).



Figure 5 – Typical deck corner cracks in Span 1.



Figure 6 – Typical cracks in the acute corner of Span 1.



Figure 7 – Typical longitudinal cracks at the expansion joint.

1.4 Objectives

Ultimately, this study aims to reduce the extent of cracks developed in cast-in-place reinforced concrete bridge decks and prevent cracking altogether. This overall goal is consistent with GDOT's commitment to bridge safety and supports GDOT's use of a state-of-the-art technique designed to shorten construction times. Accordingly, the primary objective involves evaluating three facets—structural design, material design, and construction practices—of the ABC project in question and identifying the root cause of cracking in the bridge deck.

The specific objectives of this special research study are to:

- 1) Document the distress on the SR299 bridge deck;
- 2) Build a decision matrix (similar to Table 1) to determine possible factors causing the deck cracks; and,
- 3) Provide recommendations on how to alleviate or prevent future distress.

Table 1 – Decision matrix for screening out factors relevant to cracking.

Category	Factors Causing the Distress	Major	Moderate	Minor
Structural Design	Thermal restraint			
	Reinforcement layout			
	Deck thickness			
	Skew angle			
	Deflection during placement			
Material Design	Paste volume			
	Aggregate type			
	Shrinkage/creep			
	Water-to-cement ratio			
	Heat of Hydration			
	Supplementary materials			
Construction	Placement method			
	Curing method			
	Weather/ Time of casting			
	Elevation corrections (jacking/shimming)			

1.5 Research Methodology and Procedure

To meet the study’s objectives, the project is divided into five tasks:

Task 1 - Review design/construction documents & other available resources.

The research team has reviewed the deck construction procedure, including any corrective actions (e.g., shimming) taken during construction, and completed a literature review. The findings of this task mainly appear in Section 4.

Task 2 - Conduct site investigations to create a crack map.

The research team has documented the distress (or crack) patterns and crack widths by creating a crack map. Sections 3.2 and 3.5 present the findings from two site visits.

Task 3 - Conduct a petrographic examination.

A petrographic examination has been completed to better understand the material composition and cracks. Section 3.4 discusses these findings.

Task 4 - Conduct a nonlinear analysis.

Task 4.1 - Conduct a thermal analysis.

A finite element analysis (FEA) model has been constructed for thermal analysis. As-built conditions of the SR299 bridge are reflected in this model, and a corresponding coupled thermal-structural analysis has been completed. The procedures and results are presented in Sections 4 and 5, respectively. In addition, a sensitivity analysis is conducted to study the effect of deck geometries and boundary conditions.

Task 4.2 - Conduct service load and induced displacement analyses.

In Sections 5 and 6, an in-service live load analysis is conducted. Finally, the maximum allowed elevation correction/adjustment is analyzed.

Task 5 - Synthesize results.

Section 5 presents the FEA analysis results, and Section 6 provides analysis and synthesis of these results.

1.6 Summary of Sections

This report consists of eight sections. Section 1 provides general background information for the study and states the objectives. Section 2 summarizes the literature on ABC, integral abutment bridges, deck cracking, and FEA. Section 3 mainly presents findings from two site visits. Section 4 presents a plan for analytical investigations and describes the bridge model geometry, materials, boundary conditions, and loading conditions used for analysis. In Section 5, the results from the analytical investigations are presented. Section 6 provides an analysis of the results. Finally, Section 7 summarizes the findings, and Section 8 provides recommendations.

2 LITERATURE REVIEW

2.1 Introduction

In the U. S., there are about 615,000 bridges in service; of these, more than 54,560 bridges require active/immediate maintenance (FHWA, 2017). Currently, many bridges require rehabilitation or replacement, conditions that necessitate detours, construction of temporary bridges, or employment of innovative construction technologies to reduce the impact on commuters. This section reviews the literature on ABC technologies and investigates the effects of curvature and skewness in bridge decks on the extent of cracking. A summary of factors affecting bridge deck cracking, crack types, and practices to alleviate cracking is presented. Finally, this section includes the results of previous numerical investigations.

2.2 Accelerated Bridge Construction

2.2.1 Introduction to Accelerated Bridge Construction

ABC, a fairly new method of bridge construction, employs innovative construction materials, design, fabrication, and construction techniques. ABC often implies constructing bridge components off-site and transporting them to the bridge site for installation. The Federal Highway Administration (FHWA) defines ABC as “bridge construction that uses innovative planning, design, materials, and construction methods in a safe and cost-effective manner to reduce the onsite construction time that occurs when building new bridges or replacing and rehabilitating existing bridges.” (FHWA, 2011). The ABC structural solutions include Prefabricated Bridge Elements and Systems (PBES), Structural Placement Methods (SPM), and Ultra-High Performance Concrete (UHPC) connections for PBES. The PBES involves constructing structural components off-site and transporting

them to the bridge site for installation, while the SPM involves the construction of the new bridge on a temporary support frame parallel to the bridge's permanent location before the new bridge is moved transversely to its final location by cables or hydraulic systems (FHWA, 2011). Altogether, the ABC process involves a weekend or short-term closure.

ABC has existed in the United States for more than 20 years. Recently, the desire to reduce construction impact on travelers has motivated more states to consider ABC (FHWA, 2011). These technologies are known to reduce the total project delivery time and improve material quality and durability, and work-zone safety for traveling public and contractor personnel. Moreover, ABC saves onsite construction time, which in turn reduces costs, traffic congestion, and project delivery time delays due to weather restrictions (Alashari, 2016). Finally, ABC minimizes environmental effects, impacts to existing roadway alignment, and utility relocations (FHWA, 2011). Despite all the benefits documented in the literature, ABC might not be the right solution for all projects. Each project's use of ABC needs to be evaluated (FHWA, 2011) as ABC can increase the cost of a project or pose undesirable challenges during and after bridge construction (Alashari, 2016). Alashari (2016) provides a flowchart for decision-making and a table listing important considerations for ABC projects.

2.2.2 Structural Placement Methods (SPM)

The SPM technique is one of the most common ABC technologies. SPM shortens the time and reduces the cost required to replace an old/existing bridge. This method allows the old bridge to remain open to traffic while either the new superstructure is constructed on temporary support or the substructure is repaired or built (FHWA, 2014). With SPM, roadway closures last from 48 to 72 hours (FHWA, 2018). Slide-In Bridge Construction

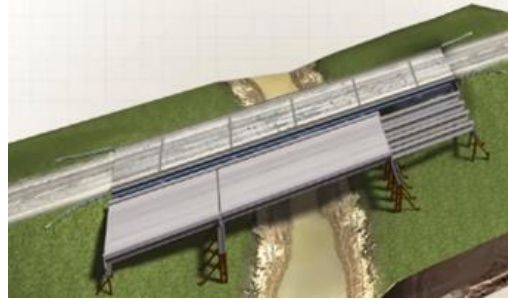
(SIBC) and Self-Propelled Modular Transporters (SPMTs) are two methods of SPM that are applied by many state transportation agencies to improve the safety, quality, and durability of their projects, as well as to reduce construction and user delay costs and minimize environmental impacts (FHWA, 2014).

A SPM project generally proceeds in two phases. Phase I, shown in Figure 8 (a) and (b) (GarverUSA, 2013), involves the construction of a superstructure on temporary supports parallel to or near an existing bridge. While the superstructure is under construction, the new substructure is built or rehabilitated under the old bridge. Phase II, shown in Figure 8 (c) and (d) (GarverUSA, 2013), involves closing the bridge and removing the old bridge. Subsequently, the new bridge is transported to its permanent location using SIBC or SPMT, as shown in Figure 8 (e) (GarverUSA, 2013). Finally, the bearing connections, approach slabs, and pavements are completed (Alashari, 2016; FHWA, 2014).

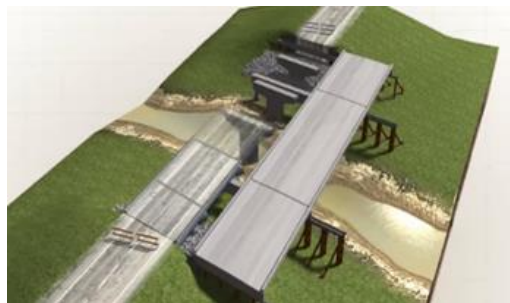
During the SIBC moving process, the superstructure is either pushed or pulled across rails, rollers, or pads using hydraulic rams, jacks, bulldozers, or winches. However, SPMT is of multi-axle platforms that use the state-of-the-art computer-controlled system to lift, carry, and set large heavy loads of bridge superstructures (FHWA, 2018). These two processes require sufficient right-of-way and appropriate, smooth terrain adjacent to the old bridge. The weight of the bridge structure is a crucial factor that needs to be considered while sliding-in or setting a new superstructure. Additionally, if rollers are used in the moving process of SIBC, a significant point load might be created if any obstructions exist in the roller channels (FHWA, 2014).



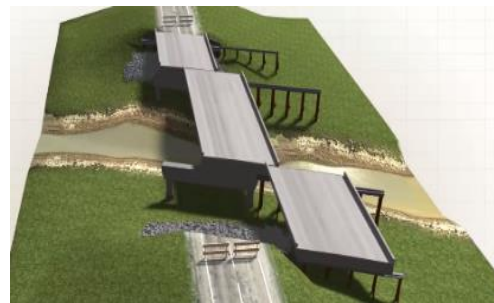
(a) Phase I of SPM construction: constructing substructure and placing temporary supports.



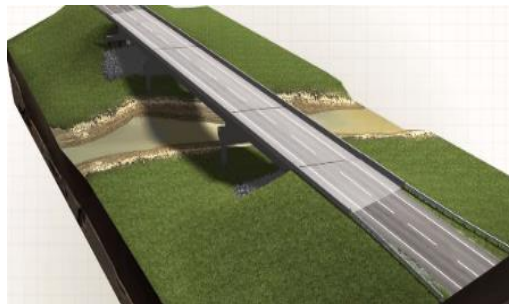
(b) Phase I of SPM construction: constructing superstructure on temporary supports.



(c) Phase II of SPM construction: demolishing/removing the old bridge.



(d) Phase II of SPM construction: sliding in the newly constructed bridge.



(e) Finishing the newly constructed bridge.

Figure 8 – SPM construction procedure (GarverUSA, 2013).

2.2.3 Challenges and Barriers

Despite the positive attributes of ABC discussed in Sections 2.2.1 and 2.2.2, state transportation agencies have concerns about implementing innovative ABC technologies. Projects involving ABC often increase the total cost of construction because ABC requires

skilled laborers and specialized equipment, such as a SPMT, to enable a state-of-the-art computer-controlled bridge move (FHWA, 2018). If bridge owners do not have adequate financial support for ABC, experienced workers, or demanding and necessary access to the surrounding highway area within a short period of time, conventional construction methods are preferable over ABC methods (Alashari, 2016). Research from states that have utilized ABC technologies highlight additional concerns regarding costs, environmental effects, construction problems, cracking, and safety. The following list reviews issues with ABC as reported by different states:

- California indicated the limitation of ABC with respect to seismic events, long-term durability, and the cost of construction (Ofili, 2015).
- Missouri revealed a significant increase in the cost of its ABC projects compared to its conventional bridge construction projects (Ofili, 2015).
- Minnesota identified problems associated with precast connections and is working on developing design criteria for SPM (Ofili, 2015).
- Washington did not realize positive outcomes from its experience with ABC projects beyond improved project safety (Ofili, 2015). Also, Washington DOT found increased cracking at the edge of deck panels in ABC projects compared to deck panels in bridges constructed with conventional methods (Pantelides & Weber, 2011). According to Pantelides & Weber (2011), cracking in bridge decks constructed using the SPM method is attributed to lifting and placing bridge elements. SPM generally involves vertical adjustments of members, though these adjustments are often minor (FHWA, 2011). Other challenges associated with

moving technologies include equipment failure, uneven movement, and fatality (FHWA, 2014).

- Oregon found a discrepancy between design and as-built substructure locations. Hence, to deliver the project on time, material selections had to be adjusted during construction (Goodall, 2019).
- Utah observed transverse and corner cracking in its bridges built using the SPMT method (Culmo, 2017). Transverse deck cracking was attributed to drying shrinkage during the concrete curing process, and the diagonal cracks were attributed to thermal cracking.

2.2.4 Best Practices

ABC projects are becoming more prevalent as state DOTs gain experience and learn the best solutions to overcome challenges. Utah DOT (2017) has successfully implemented ABC methods in many of its recent bridge projects and has documented best practices based on their work. According to the Utah DOT, ABC methods provide a service life span of 75 years (Culmo, 2017). The Oregon DOT (2019) has implemented ABC in many of its recently constructed bridges, as well, and has, in turn, recommended that as-built drawings and details be documented when an ABC project is completed, as each bridge design might be unique and subject to changes based on site conditions. In addition, the Oregon DOT (2019) made the following recommendations: 1) structural components and materials of the existing bridge should be examined for reuse, 2) the construction area should be reviewed and cleared before an ABC project starts, 3) the construction schedule and specifications should be reviewed to account for delays due to site conditions, and 4) the

use of cast-in-place concrete decks in ABC bridges should be considered first (Goodall, 2019).

Table 2 summarizes the main ABC challenges and recommendations identified by the Utah DOT (Culmo, 2017). Table 3 presents the best practices for joint connections used in building deck panels (Culmo, 2017).

Table 2 – Best practices in implementing ABC methods (Culmo, 2017).

ABC Method	Problems	Recommendations
SPMT	<ul style="list-style-type: none"> - Transverse deck cracking (Shrinkage) - Diagonal cracking on corner bays (Thermal) - Cracking due to negative lifting moments 	<ul style="list-style-type: none"> - Limit cantilever (<0.15 span length) - Control deck stresses - Design longitudinal reinforcement - Support at lift points during casting - Use lightweight concrete to reduce deck and girder stresses
SIBC	<ul style="list-style-type: none"> - No problems 	<ul style="list-style-type: none"> - Consider as first choice for bridge move over low volume roads - Can move large bridges - Move approach slab with the superstructure
Precast abutments	<ul style="list-style-type: none"> - Alignment problems 	<ul style="list-style-type: none"> - Consider appropriate tolerance
Precast integral abutments	<ul style="list-style-type: none"> - Minor leakage problem through joints 	<ul style="list-style-type: none"> - Consider using vertical panels - Use vertical joints in abutment stems and wall stems
Precast piers	<ul style="list-style-type: none"> - No problems 	<ul style="list-style-type: none"> - None

Table 3 – Best practices for precast deck panel connections in ABC (Culmo, 2017).

Connections in Full Depth Deck Panels	Life-Span (year)	Problems	Recommendations
Welded tie connections	15	<ul style="list-style-type: none">- Cannot transfer significant bending moment- Leads to cracking	<ul style="list-style-type: none">- Not recommended
Post-tensioned connections	75	<ul style="list-style-type: none">- No problems	<ul style="list-style-type: none">- Recommended- Prevent leakage at joints- Excellent performance
Dowel bars in pockets	25	<ul style="list-style-type: none">- Connection problems in negative moments	<ul style="list-style-type: none">- Not recommended in negative moment areas
UHPC and RC connections	75	<ul style="list-style-type: none">- No problems	<ul style="list-style-type: none">- Recommended
Shear connectors	75	<ul style="list-style-type: none">- Minor shrinkage gaps	<ul style="list-style-type: none">- Recommended

2.3 Integral Abutment Design

Fully integral abutments eliminate the need for expansion joints at the ends of a bridge. This design is referred to as “fully integral” because the endwall (or end diaphragm), which is a part of the superstructure, is directly connected with the substructure (abutments), or vice versa. Therefore, there are no bearings or expansion joints at the bridge ends (NYDOT, 2007), as shown in Figure 9 (a). On the other hand, with a semi-integral abutment, bridge girders rest on bearings while the endwall of the superstructure is directly connected to or resting on the bridge substructure (see Figure 9 (b)). In the latter design, “the superstructure, endwall, and approach slab move together into and away from the backfill during thermal expansion and contraction” (NYDOT, 2007).

(a) Fully integral abutment bridge
(NYDOT, 2007)

(b) Semi-integral abutment bridge (GDOT-
DRW, 2016)

Figure 9 – Fully integral vs. semi-integral bridges.

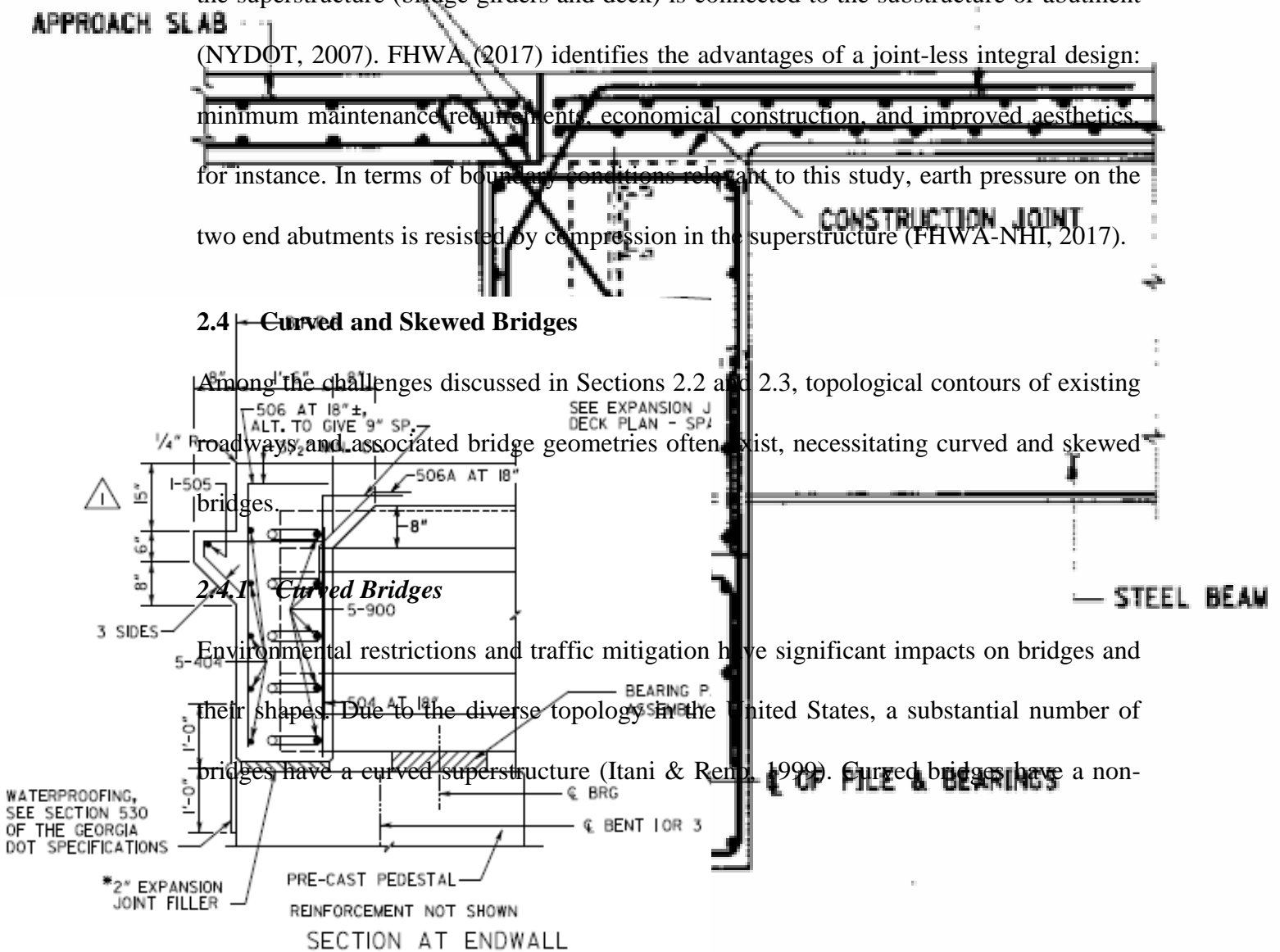
The SR299 bridge is a semi-integral abutment bridge. In integral abutment bridges, the superstructure (bridge girders and deck) is connected to the substructure or abutment (NYDOT, 2007). FHWA (2017) identifies the advantages of a joint-less integral design: minimum maintenance requirements, economical construction, and improved aesthetics, for instance. In terms of boundary conditions relevant to this study, earth pressure on the two end abutments is resisted by compression in the superstructure (FHWA-NHI, 2017).

2.4 Curved and Skewed Bridges

Among the challenges discussed in Sections 2.2 and 2.3, topological contours of existing roadways and associated bridge geometries often exist, necessitating curved and skewed bridges.

2.4.1 Curved Bridges

Environmental restrictions and traffic mitigation have significant impacts on bridges and their shapes. Due to the diverse topology in the United States, a substantial number of bridges have a curved superstructure (Itani & Remp, 1999). Curved bridges have a non-



uniform mass and stiffness distribution, which yields torsional shear stresses and flexural stresses in structural components. The angle of curvature, span length, and geometry of girders affect the magnitude of these internal forces (Itani & Reno, 1999).

More specifically, horizontally curved bridges result in a considerable torsional moment in the girders, especially when the angle of curvature ranges between 30° and 40° . Variable bending moment distributions among the girders also affect curved bridges, with the outer girders receiving a significantly larger bending moment than the inner girders. Prior research has reported that deflection of a horizontally curved bridge increases by 80% for a bridge curvature of 30° compared to that of a straight bridge (Albajet, 1999; DeSantiago, Mohammadi, & Albajet, 2005).

2.4.2 Skewed Bridges

Skewed bridges have a straight path and are generally orthogonal to traffic flows, though site restrictions prevent their longitudinal axes from being perpendicular to the major axes of their supporting systems (see Figure 10). The skew angle is defined by most state DOTs as the angle between the centerline of the bridge support (e.g., abutment) and a line perpendicular to the centerline of the bridge. GDOT defines the skew angle with respect to the centerline of the bridge support and the centerline of the bridge deck (GDOT, 2019). For example, GDOT specifies a 75° skew angle for what other DOTs call a 25° skew angle. For skew angles 85° or greater, GDOT requires that transverse rebar be placed parallel to the bent. For skew angles 75° or less, GDOT requires that transverse bars be placed perpendicular to the centerline of the bridge and skewed corner bars be added (GDOT, 2019). For the remainder of this report, the skew angle convention adopted by the majority of state DOTs will be used.

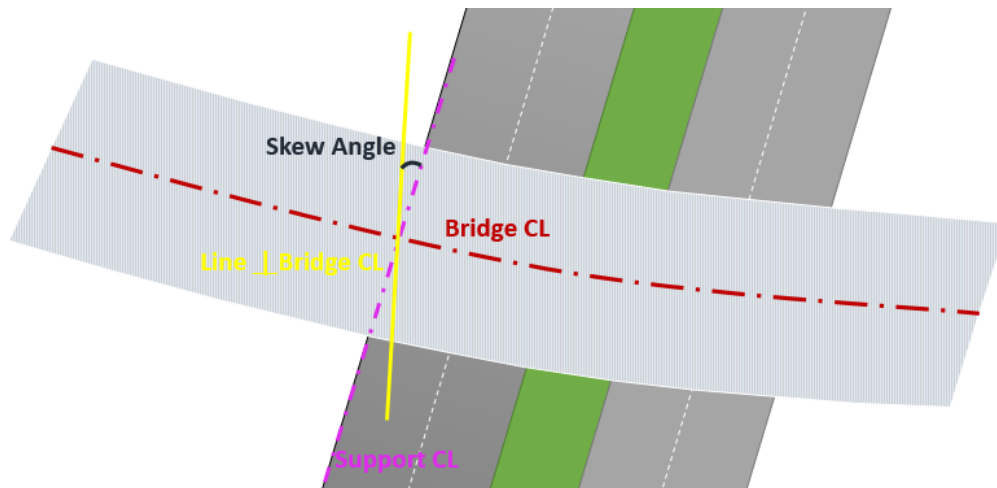


Figure 10 – Illustration of a skew angle in a skewed bridge.

Skewed edges create additional internal structural forces. These forces change the behavior of the bridge deck and complicate bridge design and analysis (Rajagopalan, 2006). Deck behavior mainly depends on the skew angle, span length, and girder spacing (Marx, Khachaturian, & Gamble, 1991). The forces from the free/unsupported edges travel toward the centerline of the bridge and take the shortest path to the supported edges. Thus, in skewed bridges, maximum deflection generally occurs at skewed corners. The force flow of skewed bridges is shown in Figure 11 (Rajagopalan, 2006).

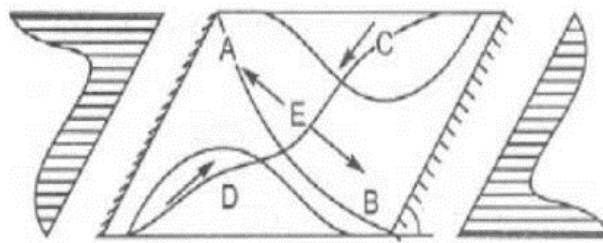


Figure 11 – Force flow of skewed edges (Rajagopalan, 2006).

Sindhu, Ashwin, Dattatreya, and S. V. (2013) performed a FEA on the behavior of skewed bridges under a static load. The results of this analysis show that the deflection and longitudinal bending moment of skewed bridges decrease with an increase in skew angle

(Sindhu et al., 2013). As well, the torsional moment doubles with an increase in skew angle up to 45° and decreases for angles larger than 45° (Sindhu et al., 2013). The support reactions at corners with an obtuse angle increase by 50% for skew angles between 15° and 45° , and by 80% for skew angles up to 60° (Sindhu et al., 2013). For skew angles greater than 20° , skewed bridges also affect the magnitude of shear and bending moment (Sindhu et al., 2013). To overcome these problems, several state DOTs, including GDOT, prescribe requirements for skewed bridge structures. For example, an increased number of rebars in the acute corners and various reinforcement orientations are specified based on skew angles (Zhuang, Fu, Ji, & Chen, 2011).

Reinforcement layouts for a straight bridge are parallel to the edges of the bridge in each direction. For skewed bridges, on the other hand, such layout is not always practical. Anusreebai and Krishnachandran (2016) performed a study to understand the behavior of skewed slabs for various reinforcement patterns, and their results, presented in Figure 12, show that a skewed slab has the highest load-carrying capacity when the reinforcement pattern in the longitudinal direction is parallel to the free edge and in the transverse direction is perpendicular to the free edge. This reinforcement pattern results in minimum deflection in comparison to other reinforcement patterns (Anusreebai & Krishnachandran, 2016).

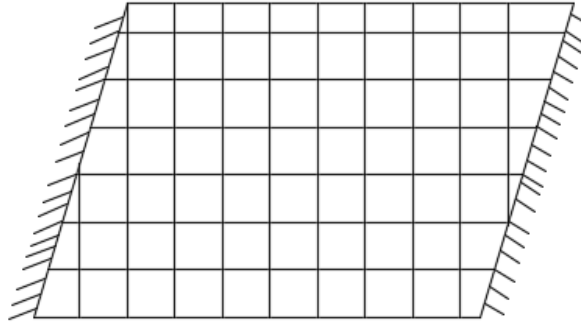


Figure 12 – Recommended reinforcement pattern for skewed decks (Anusreebai & Krishnachandran, 2016).

Menassa, Mabsout, Tarhini, and Frederick (2007) investigated the AASHTO Standard Specifications and the Load and Resistance Factor Design (LRFD) Specifications (2004) for skewed bridge designs and compared them to the results of a FEA (Menassa et al., 2007). Based on this comparison, for skew angles less than 20° , the longitudinal bending moment has results consistent with the AASHTO specifications, but when skew angles exceed 20° , the AASHTO specifications overestimate the maximum bending moment by 20%, 50%, and 100% for skew angles of 30° , 40° , and 50° , respectively. Thus, skewed bridges with a skew angle of 20° or less can be designed as straight bridges, and FEA should be used for skewed bridges with a skew angle greater than 20° . The design of skewed bridges using FEA is also recommended by other state DOTs (CDOT, 2018).

Curved and skewed bridge deck geometries pose unique challenges, and when these two attributes coexist, the causes of distress in bridge decks can be confounding. Curved and skewed bridges require a detailed analysis (Itani & Reno, 1999).

2.5 Bridge Deck Cracking

Bridge deck cracking is a widespread problem among state DOTs in the United States (FHWA, 2011). Several studies have been conducted to study deck cracking and its effect

on long-term durability. Despite reoccurring problems and a negative connotation, few reports provide solutions to eliminate or mitigate cracking. A larger number of bridges have recently developed cracking early in their ages immediately after being open to service (Wan, 2010). Deck cracking has become so common that most state DOTs often take it for granted until a major problem occurs.

Commonly, cracks are an early sign of concrete distress whether minor or major. Cracks occur when the internal principal tensile stress in a concrete member exceeds the concrete tensile strength due to service load, restraint force, or a combination of both (Hopper et al., 2015; Leonhardt, 1988). The crack formation can cause corrosion of reinforcing steel by allowing the penetration of sulfates, chlorides, and moisture. Cracking is undesirable because it undermines bridge appearance, increases maintenance and repair costs, and decreases bridge riding quality and smoothness (Wan, 2010; Hopper et al., 2015). In this section, three main factors affecting deck cracking are studied: structural design, material design, and construction.

2.5.1 Structural Design

Structural design variables, such as thermal restraint, reinforcement layout, deck thickness, and degree of deck curvature and skew, can affect the extent of cracking in concrete bridge decks. Cracks in concrete occur when a restrained mass of concrete experiences volume changes (IOWADOT, 2014). Thermal expansion and contraction caused by the heat of hydration in fresh concrete can cause early age cracking (Hopper et al., 2015). Drying shrinkage and thermal shrinkage, in the process of concrete hydration, can yield large strains and stresses and ultimately result in cracking (Purvis, Babaei, Udani, Qanbari, & Williams, 1995; Fu, Feng, Dimaria, & Zhuang, 2007; Zhuang et al., 2011).

Strains and stresses caused by structural loading are relatively small— not enough to initiate concrete deck cracking. Whereas, strains and stresses caused by thermal loading can be significantly higher than those induced by structural loads (Fu, Zhuang, & Feng, 2011; Hopper et al., 2015). However, structural loading is likely to widen cracks already initiated by other loads (ElSafty & Abdel-Mohti, 2013).

Further, reinforcement rebar size, spacing, and orientation affect the degree of cracking. Accordingly, reinforcement should be designed to meet the required strength for design (Leonhardt, 1988). For example, larger rebar sizes can have a negative effect on deck cracking (Schmitt & Darwin, 1995). In turn, minimizing rebar spacing and maximizing rebar size induce more cracking in bridge decks (French, Eppers, Le, & Hajjar, 1999). At the same time, maximizing rebar spacing alone can cause an increase in crack width (Frosch, Blackman, & Radabaugh, 2003).

Deck thickness is another factor that influences cracking. Thicker decks can reduce drying shrinkage as they can retain more moisture, while thin decks can induce more cracking by increasing drying shrinkage (Krauss & Rogalla, 1996; French et al., 1999).

The skewed geometry of bridge decks results in increased stress and cracking in the deck (Fu et al., 2007). The crack pattern in skewed angle areas is generally parallel to the supported edges (Anusreebai & Krishnachandran, 2016). Skewed deck corners are susceptible to cracking, as well, though few studies have been published on corner cracking. Zhuang et al. (2011) found that the maximum principal stresses in skewed decks appear near deck extremities and in areas where a deck slab joins with girders and increase with an increase in skew angle. In Zhuang et al.'s (2011) study, cracks appeared 0.8-1.2 days in the first 3 days of concrete curing, which were perpendicular to the principal stress

directions or deck edges. Truck (or fatigue) loading was determined not to have an effect on concrete cracking beyond making deck cracking more visible (Zhuang et al., 2011).

Interactions among design features can also affect the development of stress and strains that cause cracking. Deng, Phares, Greimann, Shryack, and Hoffman (2015) concluded that the curvature and skew along with integral abutment create thermal stress variation in bridge decks and that these feature interactions should be considered in bridge designs.

2.5.2 *Material Design*

Paste volume, aggregate type, shrinkage, water-to-cement ratio, the heat of hydration, and supplementary materials contribute to the material design of concrete. Concrete material properties and material-related mechanisms usually lead to early age bridge deck cracking (Krauss & Rogalla, 1996). French et al. (1998) concluded that the dominant parameters associated with cracking in bridge decks are cement content, aggregate type and quantity, and air content. The researchers indicated that soft aggregates, such as sandstone, tend to result in increased drying shrinkage, whereas hard aggregates, such as dolomite and limestone, tend to decrease drying shrinkage (French et al., 1999).

Meanwhile, cement induces a differential temperature during concrete hardening from the heat of cement hydration, and rapid hardening can increase cracking potential. That is, the rapid development of concrete strength yields increased internal stresses in concrete at the time of curing. In contrast, concrete mixtures with a lower heat of hydration reduce the risk of cracking (Wan, 2010). Finally, relatively high or low levels of water content in concrete can contribute to cracking, and a high water-to-cement ratio has been found to increase cracking potential (Schmitt & Darwin, 1995).

2.5.3 Construction

Cracking may be caused by construction procedures such as placement method, casting weather and time, curing method, and elevation adjustment in ABC/SPM. Therefore, careful handling of concrete members during bridge construction is crucial to avoid crack initiation. Besides, high ambient temperatures during concrete deck placement can induce thermal stresses and thus are considered one of the main construction-related factors affecting deck cracking (French et al., 1999).

On the other hand, a concrete temperature differential resulting from heating under the sun and cooling at night can restrain concrete bridge decks and lead to early cracking if the concrete is not properly cured (Leonhardt, 1988). Besides, improper curing can cause shrinkage inside concrete within four to six days after concrete placement. In turn, concrete shrinkage can create tensile stress in bridge decks, which leads to cracking. This type of cracking is usually invisible initially and only becomes visible after the bridge opens to traffic (Wan, 2010). Further, during placement of the concrete deck, a temperature differential between the freshly placed concrete and precast girders can cause deck cracking (French et al., 1999).

2.6 Practices to Alleviate Deck Cracking

To prolong the lifespan of bridges, the extent of cracking needs to be controlled and monitored during design, construction, and routine inspections. Thermal cracks are likely to appear at an early age of a bridge's service-life and widen in crack width as the bridge is subjected to various service loads (e.g., traffic and weather cycles). Researchers have suggested various remedies for eliminating and minimizing bridge deck cracking. Some

state DOTs have also provided material and structural design requirements for bridge construction to prevent and reduce instances of deck cracking.

2.6.1 Controlling Cracks on Bridge Decks

Many studies have been conducted to investigate bridge deck cracking and its prevention. Overall, the literature recommends improvement in structural design, material design, and construction procedures.

2.6.1.1 Structural design recommendations

- Deck thickness should be 6.5 in. (165 mm) at a minimum and optimally 8-9 in. (203-229 mm) thick; thin decks should be eliminated (French et al., 1999; Krauss & Rogalla, 1996; ElSafty & Abdel-Mohti, 2013).
- Expansion joints or simply supported spans should be used to minimize longitudinal restraints in bridge decks.
- Increasing girder spacing should be considered to reduce restraints by girders.
- Reducing rebar size or increasing rebar spacing should be considered to reduce transverse cracking (French et al., 1999). Specifically, French et al. (1999) recommend using the U.S. No. 5 rebars at 5.5 in. (140 mm) increments or the U.S. No. 6 rebars at 6.5-7 in. (165-178 mm) increments.

2.6.1.2 Material properties recommendations

- Limit concrete compressive strength to 5000 psi (34.5 MPa) to prevent transverse cracking (ElSafty & Abdel-Mohti, 2013).
- Use cement with a low heat of hydration or a limited amount of cement content (600 lb/cy) or (356 kg/m³) (Wan, 2010; Leonhardt, 1988; French et al., 1999).

- Limit water content and the water-to-cement ratio to a maximum of 0.4 (Wan, 2010; French et al., 1999).
- Increase the air content of cement to a higher percentage (above 6 percent) (Wan, 2010; French et al., 1999) since increasing air content can promote internal expansion during freeze-thaw cycles and thus prevent expansion and shrinkage cracking (Balakumaran, Weyers, & Brown, 2018).
- Maximize coarse and fine aggregate contents and aggregates with low absorption capacity and high modulus of elasticity in concrete mixtures (Krauss & Rogalla, 1996; French et al., 1999); an increase in aggregate content can reduce autogenous and thermal stresses while concrete hydrates (Balakumaran et al., 2018).

2.6.1.3 Construction method recommendations

- Cure freshly poured concrete appropriately to minimize hydration and reduce cracking.
- To prevent the rapid evaporation of water during curing, immediately apply water, covering, or thermal insulation after concrete placement (Leonhardt, 1988).
- Cure for at least seven days and apply a curing compound (Russell, 2017).
- Cast concrete in ambient air temperature between 40 °F (4.44 °C) and 90 °F (32.22 °C) to reduce the heat of hydration (French et al., 1999).
- Avoid concrete placement when variation in daily ambient temperature reaches 50 °F (10 °C).
- In high or low humidity conditions, cast concrete members at night (Russell, 2017).

2.6.2 State Departments of Transportation Approaches to Control Cracking

The Wisconsin DOT performed research on early-age cracking in concrete bridge decks and provided recommendations based on the results. It recommends using curing compounds instantly after bridge placement to prevent plastic shrinkage cracking due to evaporation. Further, limiting cement content to 600 lbs/yd³ (356 kg/m³) is also suggested as a solution to eliminating concrete's high modulus of elasticity at an early age. Moreover, a water-to-cement ratio below 0.4 and air content greater than 6% are considered effective preventive measures against moisture loss. A concrete placement rate of 0.6 span length per hour or faster is also recommended. Finally, a concrete cover of 2.50 in. (63.50 mm) is suggested for top reinforcement to prohibit cracking (Wan, Foley, & Komp, 2010).

Research for the Alabama DOT has recommended the use of fly ash or slag cement to reduce cracking in hot weather conditions (Schindler, Hughes, Barnes, & Byard, 2010). If the bridge deck is placed between May and September, Schindler et al. (2010) recommend the partial replacement of cement with Class F fly ash by 20%, Class C fly ash by 30%, or slag by 30% (Schindler et al., 2010). Best practices for preventing cracking in skewed bridges are mainly related to reinforcement orientations and details. The Colorado DOT (2018) suggests placing transverse reinforcements perpendicular to the main supporting members for skew angles greater than 25° and requires adding additional reinforcement in acute corners of the deck to prevent cracking. Moreover, Caltrans (2015) and the Connecticut DOT (2003) require placing transverse deck reinforcement parallel to the skewed edge (i.e., parallel to the centerline of the abutment) for skews less than 20°; for skews of 20° or greater, they require the transverse reinforcement to be perpendicular to the centerline of the girders. For the Texas DOT (2018), this skew angle is limited to

15°, while the Washington DOT (2008) requires transverse reinforcement to be placed perpendicular to the bridge centerline for any skewed bridge. In addition, increased amounts of reinforcement in both transverse and longitudinal directions are required in the end zones for skew angles greater than 25° (WSDOT, 2008).

In addition to steel reinforcement layouts, the Connecticut DOT (2003) requires that intermediate diaphragms be placed in line with the skew angle for skew angles less than 20°; for skew angles greater than 20°, the diaphragms should be placed normal to the main members and staggered. Further, additional reinforcement parallel to the skew edge is required in acute corners of the deck if the skew angle exceeds 20° (CTDOT, 2003). Overall, state DOTs recommend a variety of approaches for skewed bridges in terms of reinforcement patterns (transverse versus radial), specified skew angles (15°-25°), and additional corner reinforcement such as fan-shaped reinforcement.

2.7 Finite Element Analysis of Concrete Cracking

Previous studies have used FEA to better understand the behavior of structural forms, concrete materials, and concrete cracking (Biggs, Barton, Gomez, Massarelli, & McKeel, 2000; Menassa et al., 2007; CDOT, 2018). Results have been validated with experimental results and thus proven to be accurate (Barsoum, El Safty, & Phillip, 2012). Wan et al. (2010) used FEA to evaluate the effects of truck loading and shrinkage on bridge deck cracking and found that truck loading is not likely to initiate cracking in bridge decks, whereas shrinkage can cause transverse cracking within four to eight days after concrete placement. In addition, the researchers concluded that if cracks do not appear on a bridge deck before the bridge opens to traffic, a combination of shrinkage and truck loading may cause cracking (Wan et al., 2010).

Ma and Kwan (2017) used FEA to study concrete shrinkage cracking and indicated that shrinkage causes cracking due to the restraints that prohibit its deformation. They also developed a finite element method and determined that it correctly predicts the number of cracks, crack patterns, and average crack spacing and locations; as a result, they recommended the use of FEA to anticipate crack patterns and average crack widths (Ma & Kwan, 2017). Schindler et al. (2010) used FEA to investigate cracking in skewed bridge decks and found that FEA can accurately predict stress distribution in bridge decks. For continuous and skewed bridges, the researchers reported that cracks propagate on the top surface of the deck near the intermediate supports, and with an increase in skew angles, the number of cracks increases in the deck, appearing parallel to the skewed edges, due to corresponding increases in tensile stresses (Schindler et al., 2010).

2.8 Summary of Literature Review

This section summarizes previous studies on ABC, skewed and curved bridges, and reviews factors affecting deck cracking. Previous studies identify multiple factors for deck cracking associated with material design, structural design, and construction method and show that deck cracking is rarely attributed to a single factor. In terms of structural design variables, deck thickness, reinforcement patterns, deck shape, and other geometric parameters affect deck cracking. Material design factors affecting deck cracking are related to concrete composition and include cement type, aggregate size, water content, shrinkage, and more. Finally, construction involving SPM may induce cracks due to the dynamic nature of the method. Best practices to minimize cracking include using a bridge deck thickness greater than 6.50 in. (165 mm), designing reinforcement patterns for skewed deck geometries, lowering cement content, and using a smaller size of aggregate.

3 FIELD INVESTIGATIONS

3.1 Introduction

A few months after the SR299 bridge opened to traffic, visible cracks appeared on the bridge deck. To document the distress locations, the research team visited the bridge twice. The first visual investigation was performed on August 25, 2017, approximately three months after the bridge was open to traffic. During this visual observation, crack locations, patterns, and widths were recorded. Following the first site visit, the research team worked with Nexco-West, Inc. to map crack locations (visible and invisible to the human eyes) on the bridge deck. The vendor used an infrared, high-definition visual bridge deck scanning device.

Consequently, a petrographic examination was conducted on four core samples of the bridge deck to determine constituent materials and crack depth. Finally, during the second site visit, the bridge deck was observed again, approximately one year after the first site visit. The second visual observation focused on identifying changes in crack patterns and crack widths.

3.2 First Bridge Site Visit

3.2.1 Procedure

A crack measure gauge and a measuring tape were used to measure crack widths and lengths. Photos showing crack orientations and patterns were taken.

3.2.2 Summary of Findings

A large number of cracks were seen on the bridge deck. Longitudinal cracks were observed across the expansion joint in the middle of the bridge. Figure 13 shows the longitudinal cracks running parallel to the direction of the precast girders.



Figure 13 – Longitudinal cracks at the expansion joint on SR299 bridge (eastbound lane of Spans 1 and 2).



Figure 14 – Typical diagonal corner cracks on SR299 bridge (eastbound lane of Span 2).



Figure 15 – Additional cracks along SR299 bridge (westbound lane shoulder of Span 1).

Diagonal cracks were also found at two corners of the two-deck slabs on the abutment sides, as shown in Figure 14 and Figure 15, respectively. The diagonal and longitudinal cracks were approximately 1/32 in. (0.80 mm) wide. Moreover, transverse cracks were about 1/64 in. (0.40 mm) wide and propagated on the bridge deck. These cracks were mainly found at the acute corners with a skew angle ranging between 16.15° and 30.26°. Cracks were more visible because they were repaired with epoxy injection. Finally, hairline cracks that appear to be shrinkage cracks were observed, although they were found in limited areas with crack widths significantly smaller than those of the diagonal and longitudinal cracks described above.

3.3 Infrared and High-Definition Bridge Deck Scan

3.3.1 Introduction

Deck Top Scanning System (DTSS) is a method for imaging top bridge deck surfaces using a group of instruments to assist in locating, classifying, and quantifying deficiencies in roadway structures. DTSS system instruments are mobile and consist of an infrared thermography (IR) camera, two line-scanning cameras, a GPS unit, and a speedometer. The data collected by these instruments locate surface and subsurface defects in bridge decks or roadways. DTSS was performed on the SR299 bridge in October 2017 by NEXCO-WestUSA, Inc. to locate cracks and create a crack map. The complete report is presented in Appendix A.

3.3.2 Summary of Findings

Bridge scanning results aided in providing information and detailing distress, such as cracking, spalling, patchwork, and delamination. The results indicated “no existence of unsound patch, major spall, nor heavy pattern cracking.” However, scanning data showed

the existence of both repaired and unrepaired cracks. These cracks were distributed in both directions over both spans of the deck. The untreated cracks were classified based on their severity condition states. Based on the DTSS results, summarized in Table 4, cracking on the SR299 bridge in October 2017 involved cracks with insignificant widths (<0.0625 in. (1.60 mm)), as well as many repaired cracks on both eastbound and westbound lanes.

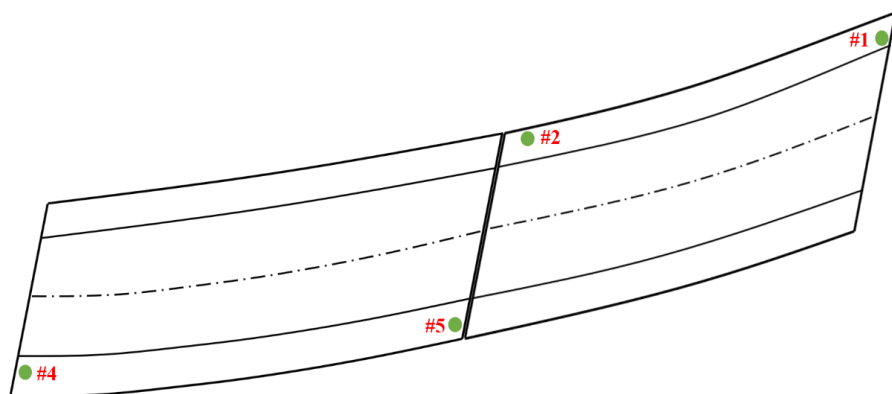
Table 4 – Length and condition of repaired and unrepaired cracks in SR299 bridge.

Direction	Span		Crack length, ft (m)			
			Repaired	Insignificant (<0.0625 in.) (<1.60 mm)	Moderate (0.0625-0.125 in.) (1.60-3.20 mm)	Severe (>0.125 in.) (>3.20 mm)
Eastbound	1	Lane	67.44 (20.56)	21.05 (6.42)	3.27 (1)	-
		Shoulder	54.12 (16.50)	-	-	-
	2	Lane	-	1.89 (0.58)	5.8 (1.77)	-
		Shoulder	-	-	-	-
	Total		121.56 (37.05)	22.94 (6.99)	9.07 (2.77)	-
Westbound	1	Lane	120.85 (36.84)	1.26 (0.38)	-	-
		Shoulder	2.61 (0.80)	-	-	-
	2	Lane	23.74 (7.24)	9.29 (2.83)	-	-
		Shoulder	10.04 (3.06)	-	-	-
	Total		157.24 (47.93)	10.55 (3.22)	-	-

3.4 Petrographic Evaluation of Concrete Deck

3.4.1 Introduction

A petrographic examination studies the properties of materials through microscopic examinations and is generally performed to evaluate the quality of concrete mixture materials and provide information on constituents. It also provides information (e.g., pattern and size) on cracks developed in a concrete sample. A petrographic examination was performed by TEC Services, Inc. on four core samples extracted from the SR299 bridge deck in February 2018. The cores are labeled #1, #2, #4, and #5, and their locations and cross sections are shown in Figure 16.



(a) Core locations

(b) Cross section of core #1



3.4.2 Summary of Findings

Core sample results indicated a moderate porosity and a water absorption ranging from 0.42 to 0.47, which is considered high. However, this absorption ratio is attributed to the presence of cracks in the concrete core samples. The petrographic study also indicated that aggregates were well distributed with coarse aggregates consisting of 94% to 97% crushed limestone and fine aggregates consisting mostly of quartz. The paste was found to be type I/II Portland cement with a fair to moderate hydration. An inconsistent porosity was found due to the presence of cracks in the core specimens. The water-to-cement ratio was expected to be between 0.42 and 0.47.

Cracks including shrinkage cracks were found in all four core samples. These cracks were mostly vertical, and they ran through the entire depth of the concrete cores. The cracks were wider at the top of the cores compared to the bottom. These cracks had sheared the coarse and fine aggregate particles of the concrete, which often indicates the development of significant splitting tensile stress in concrete. Epoxy injected to repair the cracks was found at the surface of the cracks and had penetrated only $\frac{1}{4}$ to $\frac{1}{2}$ in. (6.35 to 12.70 mm) of the crack depth. The research team was informed that the cracks had received another epoxy injection to treat the full depth between the first and second site visits.

3.5 Second Bridge Site Visit

3.5.1 Introduction

The results and findings from Sections 3.2 through 3.4 were thoroughly reviewed before the second site investigation. Cracks generally continue to develop and grow once they appear on a concrete surface. Therefore, the research team visited the bridge a second time to monitor the development of existing cracks as well as the appearance of new cracks, if

any. The second visual inspection focused on studying changes in crack patterns in the previously cracked areas. In addition, a traffic study was conducted to measure the average percentage of truck traffic to understand and verify truck loading on the bridge. During the first site visit, unusually high truck traffic volume was observed. Thus, during the second visit, the service live load on the bridge was studied.

3.5.2 Procedure

To investigate whether cracks formed or exacerbated over about a year period, the research team visually inspected the bridge deck surface at noon on December 12, 2018. This specific date and time were selected because the 2017 traffic data (GDOT TADA, 2018) indicated peak truck traffic volume then, as described below. Based on the nearest traffic count site on I-24, which runs beneath the SR299 bridge, a rough estimate of traffic volume was developed. The research team identified vehicles in this count by class based on the Federal Highway Administration (FHWA) vehicle classification shown in Figure 17 (FHWA, 2019). The most expected truck class on I-24 was the Class 9 vehicle. Figure 18 presents the total daily volume of vehicles and the total volume of Class 9 trucks for the full month of December 2017 on both eastbound and westbound routes of I-24. Figure 19 shows the total daily volume of Class 9 trucks and the volume of Class 9 trucks during the peak hour of the day for December 2017.

The 2017 traffic data provided in Figure 18 and Figure 19 enabled the team to determine which day of the week experienced peak truck traffic. Class 9 trucks peaked mid-week (Tuesdays, Wednesdays, and Thursdays of each week), and Wednesdays saw the highest traffic volume of Class 9 trucks. Finally, the data indicated that most truck

traffic occurred around noon. Therefore, the second Wednesday of mid-December in 2018 expected to be a good day for collecting traffic data on the SR299 bridge.



































Class 1 Motorcycles		Class 7 Four or more axle, single unit	
Class 2 Passenger cars			
			
		Class 8 Four or less axle, single trailer	
			
Class 3 Four tire, single unit		Class 9 5-Axle tractor semitrailer	
			
		Class 10 Six or more axle, single trailer	
Class 4 Buses			
		Class 11 Five or less axle, multi trailer	
		Class 12 Six axle, multi-trailer	
Class 5 Two axle, six tire, single unit			
		Class 13 Seven or more axle, multi-trailer	
			
Class 6 Three axle, single unit			
			
			

Figure 17 – FHWA vehicle classification (FHWA, 2019).

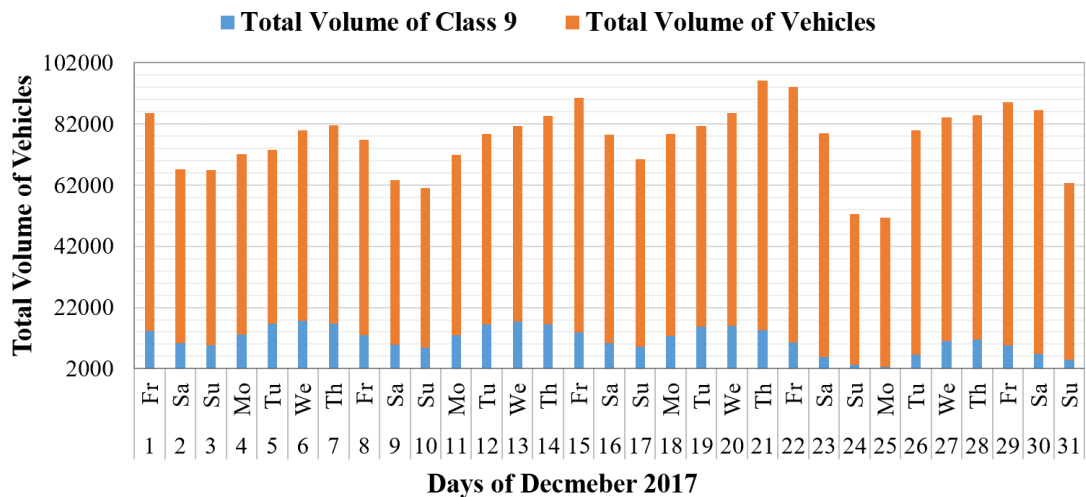


Figure 18 – I-24 total traffic volume versus Class 9 trucks in December 2017.

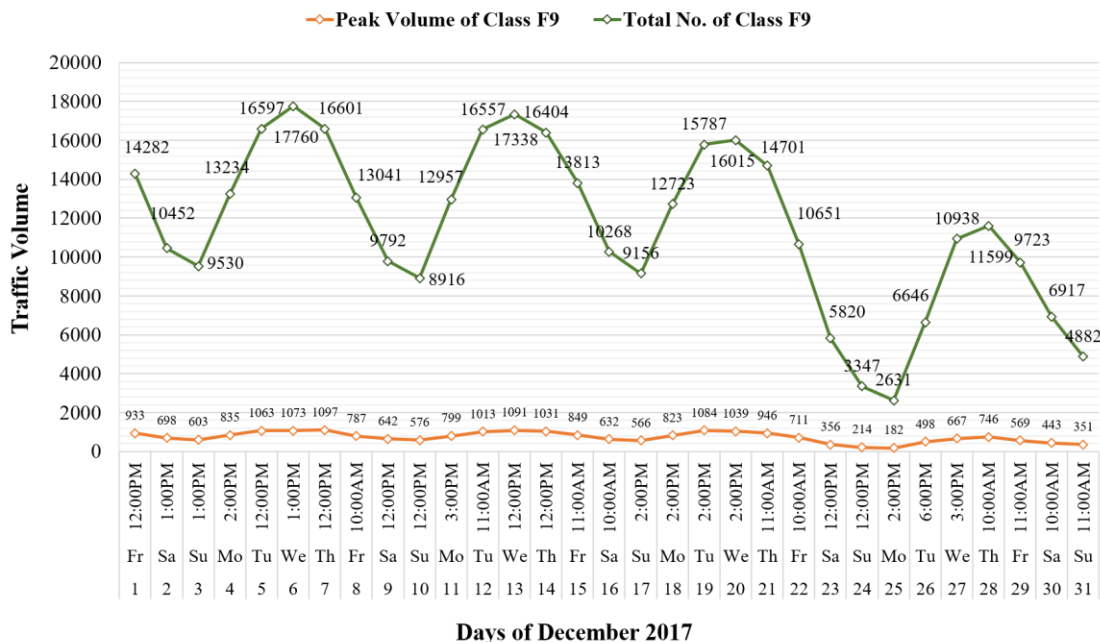


Figure 19 – I-24 Class 9 truck traffic in December 2017.

In addition to the traffic counter on I-24, traffic counts were available for the exiting and merging loops of I-24 onto the SR299 bridge (see Figure 20) for a few hours over three days in 2018. Based on this data, trucks appear to use the bridge mostly due to the presence of gas stations and fast-food restaurants on both sides of the two ramps. One of the largest gas stations, which appears to offer sufficient space for truck parking, is located on the east side of the bridge. This attracts trucks exiting I-24 westbound. The data for westbound loops (loop 1 and 2) and eastbound loops (loop 3 and 4) are shown in Figure 21 and Figure 22, respectively. Together, these figures present the total volume of vehicles exiting and merging onto I-24 in the loops. The date and hour for peak traffic volume were later verified by checking the GDOT's website (GDOT TADA, 2018) for traffic volume until mid-December (GDOT TADA, 2018). Figure 23 shows the total traffic volume of Class 9 trucks along with the corresponding peak volume and hour from December 1 to December 15 of 2018.



Figure 20 – Exiting and merging loops of I-24.

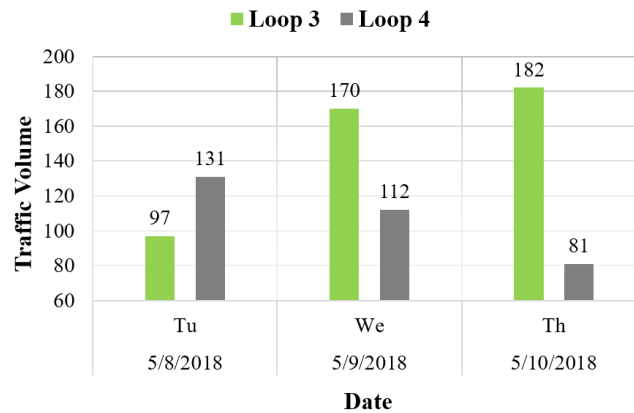


Figure 21 – Traffic volume for eastbound loops of I-24.

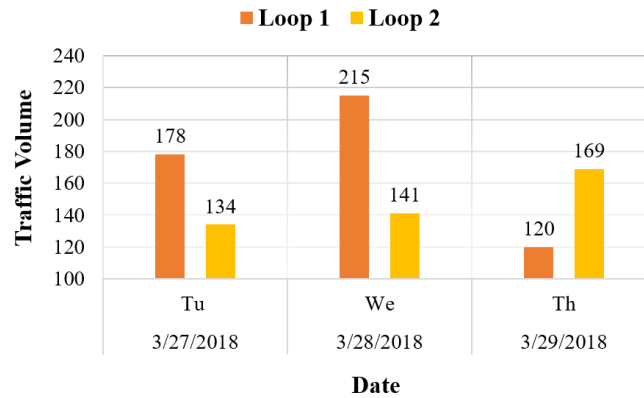


Figure 22 – Traffic volume for westbound loops of I-24.

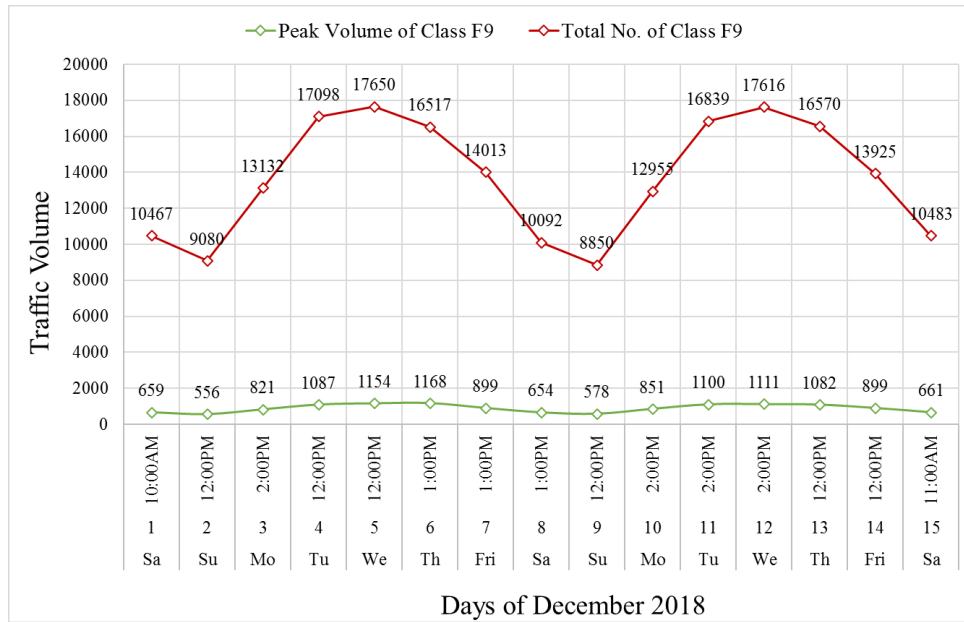


Figure 23 – I-24 Class 9 trucks traffic volume for half of December 2018.

In light of the traffic data discussed above, the research team classified trucks from 11:00 a.m. to 12:00 p.m. and manually counted traffic from 12:00 p.m. to 1:00 p.m. during the second site visit on December 12, 2018. At this time, data were collected for both eastbound and westbound traffic and trucks on the SR299 bridge. These manual counts were verified with a recorded video file. Beyond studying traffic, the research team also discovered and documented additional cracks to compare to crack patterns observed during the first site visit in 2017.

3.5.3 Summary of Findings

3.5.3.1 Traffic data

Figure 24 presents the results from the traffic counts. Numerous Class 2 and Class 3 vehicles were observed on the bridge, and a few Class 6 and Class 8 trucks were seen, as well. However, most (about 20% of the total traffic volume) vehicles were Class 9 trucks. Most trucks, if not all, that exited westbound took the westbound lane toward the gas station

located on the east side of the bridge. Then, the eastbound traffic merged onto I-24. During the one-hour observation window (from 12:00 p.m. to 1:00 p.m.) the eastbound truck volume was 25% higher than the westbound truck volume; yet, a higher total traffic volume was observed on the westbound lane (see Figure 25).

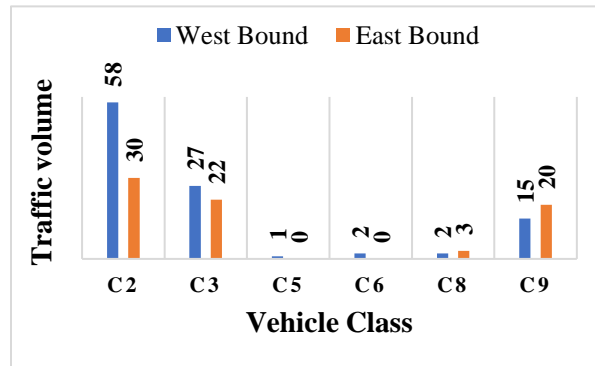


Figure 24 – Traffic volume and vehicle classes on the SR299 bridge.

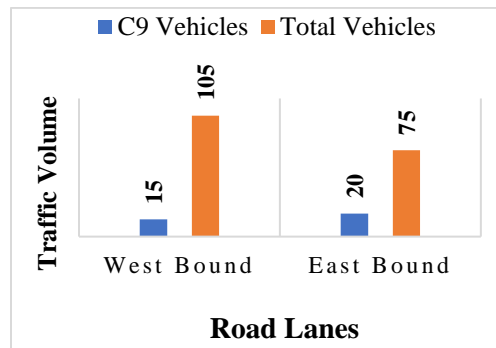


Figure 25 – Total traffic and Class 9 truck traffic counts on the SR299 bridge.

The results from the 2018 traffic count were consistent with the findings from the first site investigation: an unusually high number of Class 9 trucks used the bridge. Figure 26 illustrates a few cases where trucks traveling back-to-back were observed. Trucks traveling in both directions were also observed, along with a few oversized load trucks, shown in Figure 27. In conclusion, such service live (i.e., truck) load patterns might have

caused additional cracks—as the load distribution changes at the skewed deck edges—or contributed to widening the existing cracks.



Figure 26 – Back to back Class 9 trucks crossing SR299 bridge.



Figure 27 – Oversize load Class 9 truck crossing SR299 bridge.

3.5.3.2 Cracking conditions

Due to traffic and dark de-coloration, visibly identifying cracks during the second visit was more challenging. The cracks observed during the first site investigation were identified and mapped based on the site photos. Additionally, newly developed cracks, which were untreated with an epoxy injection, were found on both spans. These cracks were mostly found in the middle length and at the acute corners of both skew deck spans. Figure 28

presents crack patterns present on the bridge deck during the second visit. Specifically, Span 2 had a higher number of cracks at the acute corner on both the expansion side and the abutment side, and cracks ran across the expansion joint between Span 1 and Span 2, as shown in Figure 29. Several untreated cracks are shown in Figure 30 and Figure 31.

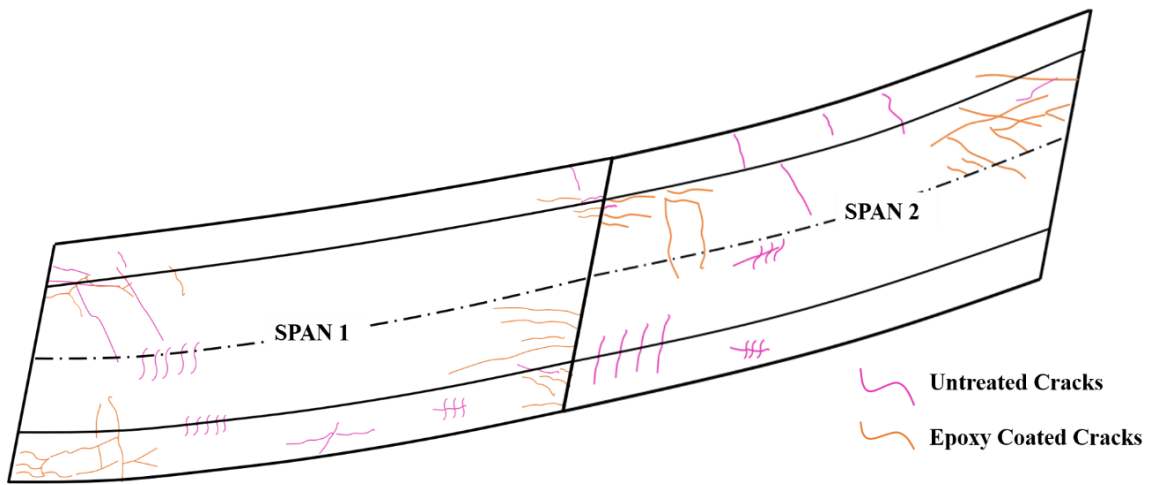


Figure 28 – New and old cracks on both spans of SR299 bridge.



Figure 29 – Crack through the expansion joint.

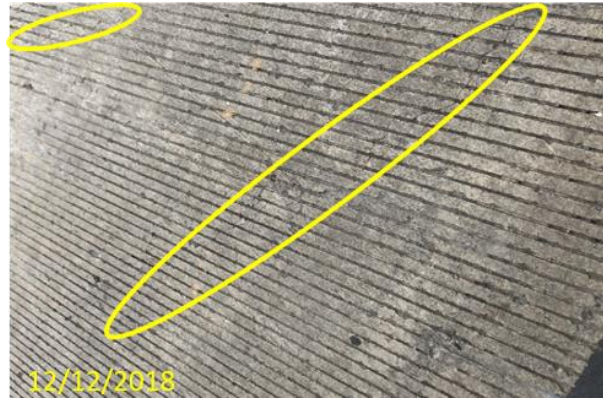


Figure 30 – Untreated diagonal cracks without epoxy coatings.



Figure 31 – Untreated longitudinal cracks without epoxy coatings.

New crack widths ranged between 1/64 in. (0.40 mm) and 1/25 in. (1.02 mm). Cracks in the shoulder areas and at the skewed corners were wider than cracks in other areas. Figure 32 through Figure 36 show crack widths measured with a crack width gauge. In reviewing these photos, it is important to recognize that crack width varies along the length of the crack.



Figure 32 – Crack width measurement (0.016 in. or 0.41 mm).



Figure 33 – Crack width measurement (0.020 in. or 0.51 mm).



Figure 34 – Crack width measurement (0.025 in. or 0.64 mm).



Figure 35 – Crack width measurement (0.030 in. or 0.76 mm).



Figure 36 – Crack width measurement (0.040 in. or 1.02 mm).

To review the condition of cracks documented in the first site visit, select pictures were replicated during the second visit. To facilitate comparison, an effort was made to take photos from a similar angle; at the same time, deck staining (or discoloring) made it hard to distinguish between old and new pictures, new cracks were not clearly visible from distance, and some of the old cracks were no longer visible. Figure 37 through Figure 48 present bridge deck surfaces during the first and second site visits for comparison. Accordingly, the pictures are described as “old” and “new” photos, respectively.



Figure 37 – Old photo showing cracks at eastbound corner of Span 2.



Figure 38 – New photo showing cracks at eastbound corner of Span 2.



Figure 39 – Old photo showing cracks in eastbound lane at Span 2 end.



Figure 40 – New photo showing cracks in eastbound lane at Span 2 end.



Figure 41 – Old photo showing cracks thru expansion joint between Spans 1 and 2.



Figure 42 – New photo showing cracks thru expansion joint between Spans 1 and 2.



Figure 43 – Old photo showing cracks at the obtuse corner of eastbound Span 1.



Figure 44 – New photo showing cracks at the obtuse corner of eastbound Span 1.



Figure 45 – Old photo showing cracks at the acute corner of westbound Span 1.



Figure 46 – New photo showing cracks at the acute corner of westbound Span 1.



Figure 47 – Old photo showing cracks from westbound lane of Span 2.



Figure 48 – New photo showing cracks from westbound lane of Span 2.

As shown in the photos above, new, untreated, and sizable cracks were found on both spans. During the second visit, no cracks were seen on the girders nor at the endwalls.

3.6 Summary of Site Investigations

During the first site investigation of the SR299 bridge, visible and noticeable longitudinal and diagonal cracks were observed on the bridge deck. DTSS results indicated that the bridge deck showed few significant cracks and severe crack patterns, and most of the full-depth cracks were repaired with an epoxy injection. Finally, no major spalls or unsound patches were found.

The petrographic examination indicated a slightly higher water absorption ratio in comparison to the ratio of normal concrete due to the existence of full-depth cracks. Overall, the constituent materials, including aggregate, sand, and cement, were considered normal. Most of the cracks were found to be vertical (in the cores) and full-depth, with widths greater at the top and thinning toward the bottom. In addition, the cracks were partially filled with epoxy resin that did not penetrate full-depth. The cracks also had sheared aggregate particles in the concrete mixture. The quality of some of the horizontal cracks indicated that they might have resulted from shrinkage.

The second site investigation aided in attaining the latest traffic data and crack patterns for the SR299 bridge. The traffic data collected during the visual observation showed a large percentage of Class 9 trucks crossing the bridge. Additionally, newly developed cracks were observed on the top of the bridge deck surface, primarily at the skewed corners. These cracks are visible, sizeable, and unfilled with epoxy resin; crack widths range between 1/64 in. (0.40 mm) and 1/25 in. (1.02 mm).

4 ANALYTICAL INVESTIGATIONS

4.1 Introduction

This section includes the description of a numerical model developed for a nonlinear FEA. The DIANA software (Version 10.2) was used to build a model geometry resembling the SR299 bridge. In an analytical model, the behavior of concrete material is often assumed to be linear; however, concrete behaves nonlinearly. This means that the stress-strain relationship must be nonlinear. That is, the concrete material model should recognize a significant reduction in tensile stress when concrete cracks. The DIANA software offers two nonlinear material models and is known for successfully solving nonlinear finite element equations.

The finite element method is one of the most effective numerical methods used to gain a better understanding of distresses observed in structures, such as cracking in concrete bridge decks. The factors affecting deck cracking generally include bridge geometries, structural, and thermal loading. This section describes a FEA model developed to analytically investigate these factors and their effect on the SR299 bridge.

First, loads and restraints to define the service condition and environment are described in this section. Then in Section 5, the results of the analysis are presented and compared with the information gathered in Section 3. Finally, in Section 6, the decision matrix presented in Section 1.4 is completed based on the results from the FEA.

4.2 SR299 Bridge Geometry

The SR299 bridge (see Figure 49) consists of two spans and was constructed using an ABC technology. Its deck is skewed, inclined, and curved. The bridge deck is supported by the

girders, which in turn are supported by substructure components such as pier caps, bearing plates, and columns.



Figure 49 – SR299 bridge.

In building a FEA model, the model geometry consists of the following superstructure components: deck, deck reinforcements, girders with prestressing strands, diaphragms, edge beams, and endwalls. Meanwhile, substructure elements were not included in the model because the boundary conditions were sufficiently represented by defining restraint conditions at the bearing plate locations and endwalls.

4.2.1 Deck Geometry Details

The details of the two spans are shown in Table 5. Table 6 and Figure 50 present the parameters that define the bridge circular curve with a radius of 818.51 ft (249.48 m). Based on the design and construction drawings (GDOT-DRW, 2016), a deck model is built in DIANA by creating the circular curve on a plane, as illustrated in Figure 51. The curved bridge deck is presented in Figure 52. As evident in Figure 53, the skew angles at the two edges of each span are both 16.15° for Span 1 and 23.42° and 30.26° for Span 2. The skew edge lines were established by determining the beginning and end points of the bridge deck on the curvature and rotating them by the skew angle at each edge.

Table 5 – Dimensions of Spans 1 and 2 (SR299 bridge).

Deck	Lane Width ft-in. (m)	Shoulder Width ft-in. (m)	Total Width ft-in. (m)	Total Length ft-in. (m)	Thickness in. (mm)
Span 1	12-0 (3.66)	8-0 (2.44)	43-3 (13.18)	103-10 (31.65)	8¾ (222.25)
Span 2	12-0 (3.66)	8-0 (2.44)	43-3 (13.18)	97-9 (29.79)	8¾ (222.25)

Table 6 – Deck curvature details (SR299 bridge).

Circular Curvature Details		
PC = 43+73.43	PT = 53+83.67	PI = 49+54.23
$\Delta = 70^\circ 43' 01.1''$	$D = 07^\circ 00' 00''$	$T = 580.79 \text{ ft (177 m)}$
$L = 1010.24 \text{ ft (307.92 m)}$	$L_c = 201.58 \text{ ft (61.44 m)}$	$R = 818.51 \text{ ft (249.48 m)}$
$E = 185.51 \text{ ft (56.54 m)}$	$C = 947.33 \text{ ft (288.75 m)}$	$S. E = 7.00\%$

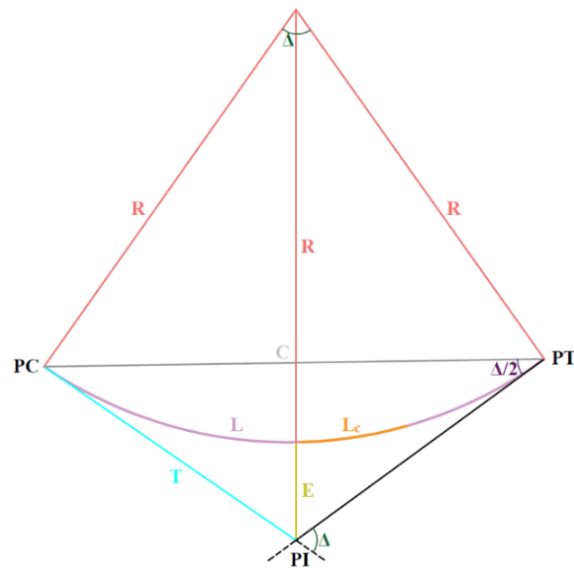


Figure 50 – Deck curvature (SR299 bridge).

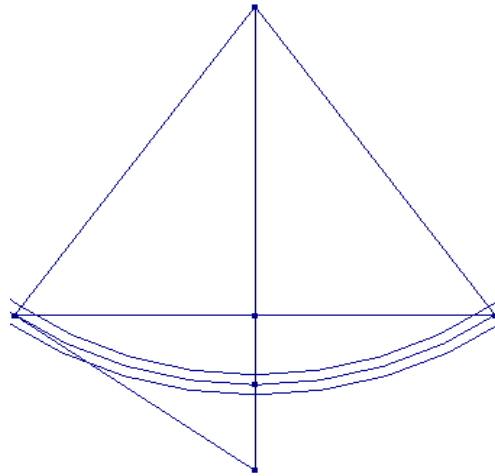


Figure 51 – Bridge deck curvature layout in DIANA.

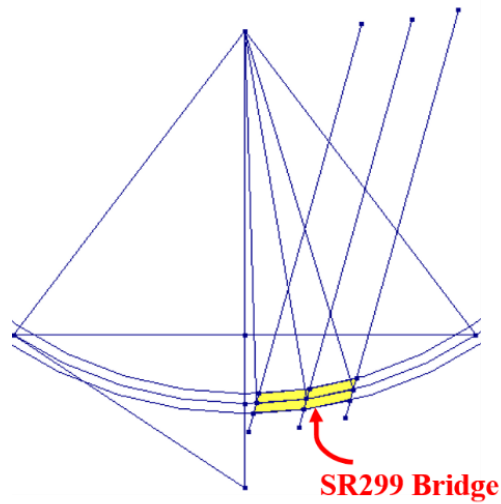


Figure 52 – Bridge circular curve with skewed bridge spans.

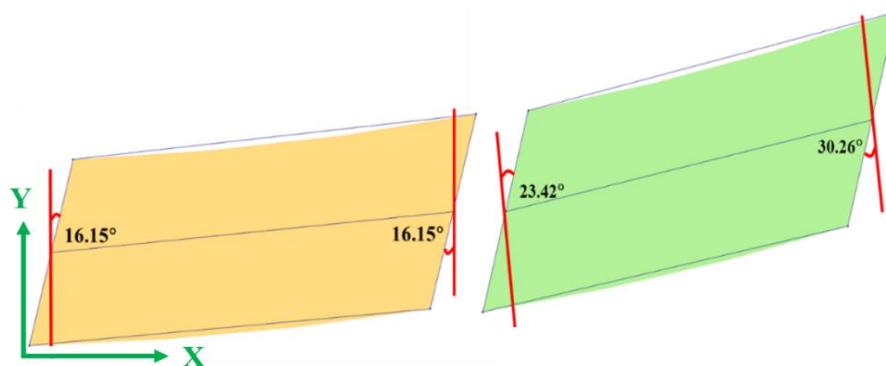


Figure 53 – Spans 1 and 2 showing skew angles (SR299 bridge).

Side slope and vertical elevations of the two spans are deduced from Figure 54 and are incorporated into the FEA model by rotating the spans on their X- and Y-axes. The highest point of the vertical curvature is located approximately at mid-length of Span 1. Figure 55 shows an isometric view of the SR299 bridge deck model in DIANA.

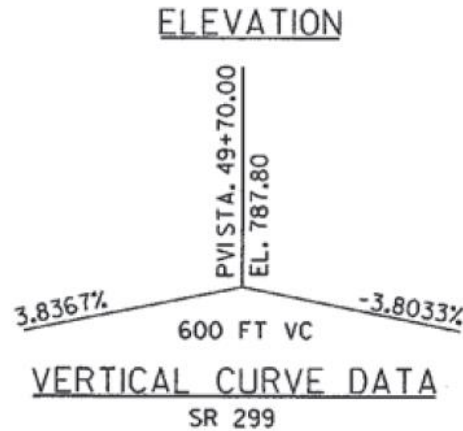


Figure 54 – Vertical curve data (SR299 bridge) (GDOT-DRW, 2016).

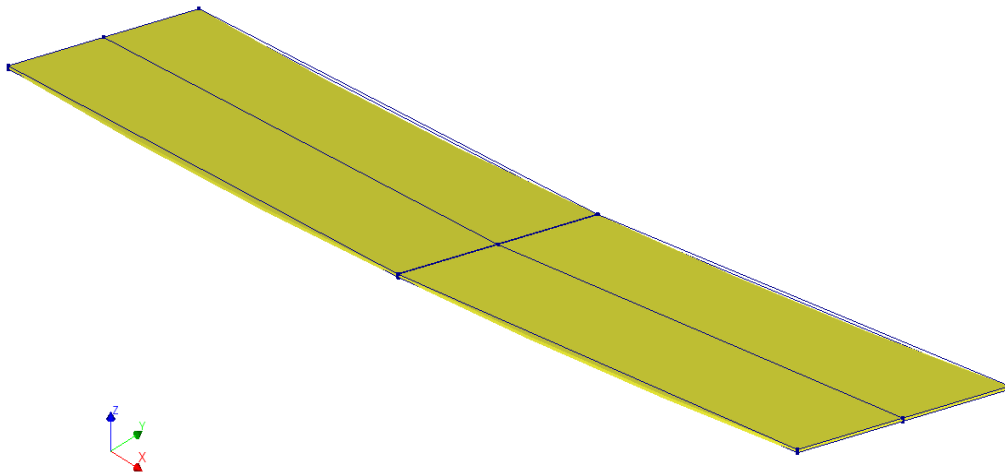


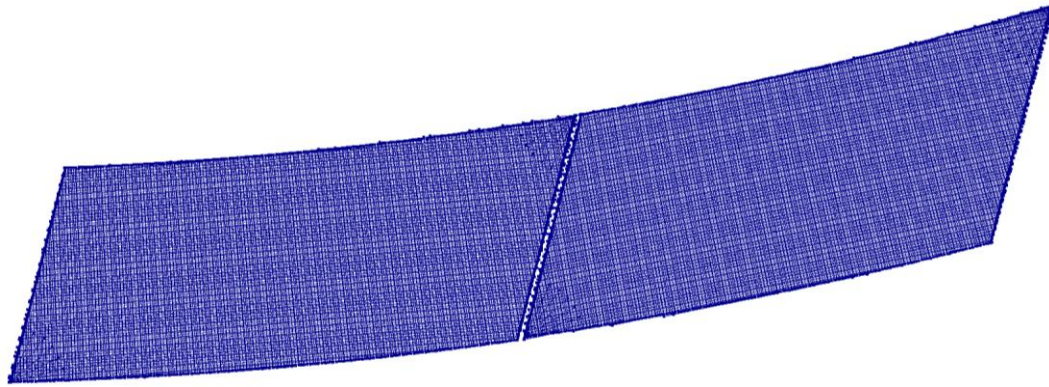
Figure 55 – Isometric view in DIANA.

4.2.2 Reinforcement Details

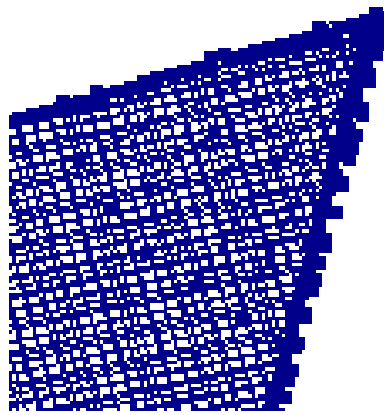
The bridge deck is reinforced with two layers of mild steel reinforcement in both longitudinal and transverse directions. The longitudinal direction reinforcement runs along the direction of the girders (or traffic), whereas the transverse reinforcement is radially placed. In addition, radial fan-shaped rebars are placed at the acute corners of the bridge deck. Reinforcement details are summarized in Table 7, and the designations are based on the GDOT Bridge Detailing Guidelines (2015). The plan view of the deck reinforcement layout is shown in Figure 56.

Table 7 – Deck reinforcement details (SR299 bridge).

Properties		Span 1	Span 2	Notes
Clear cover	Top	2¾ in (70 mm)	2¾ in (70 mm)	
	Bottom	1 in (25 mm)	1 in (25 mm)	
	Left side	4 ⅜ in (111 mm)	4 ⅜ in (111 mm)	Radially
	Right side	3 in (76 mm)	3 in (76 mm)	Radially
Transverse rebars	Top	590@7in (178 mm)	590@7 in (178 mm)	Epoxy coated
	Bottom	501@9in (229 mm)	501@9in (229 mm)	
Longitudinal rebars	Top	35-490 64-690	35-490 64-690	Epoxy coated
	Bottom	68-4	68-4	
Corner rebars	Left skewed corner	5-5	5-5	
	Right skewed corner	5-5	5-5	



(a) Plan view



(b) Typical corner reinforcement

Figure 56 – Mild steel reinforcement layout in DIANA.

4.2.3 Girders Details

Each deck span is supported by seven AASHTO type III modified prestressed concrete (PSC) girders. These girders are parallel to each other except for girder No. 7, as specified in the drawings (GDOT-DRW, 2016). The length of girders 1 through 6 of Span 1 is 103.93 ft (31.68 m), and girder No. 7 is 103.48 ft (31.54 m) long. The length of girders 1 through 6 of Span 2 is 98.61 ft (30.06 m), and girder No. 7 is 97.03 ft (29.58 m) long. The plan views showing the girders of Span 1 and Span 2 appear in Figure 57 and Figure 58, respectively.

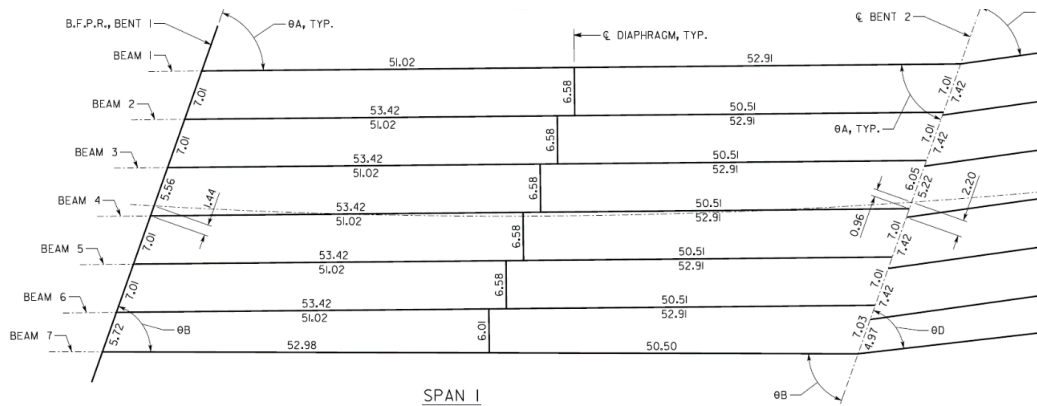


Figure 57 – Plan view showing Span 1 PSC girders (GDOT-DRW, 2016).

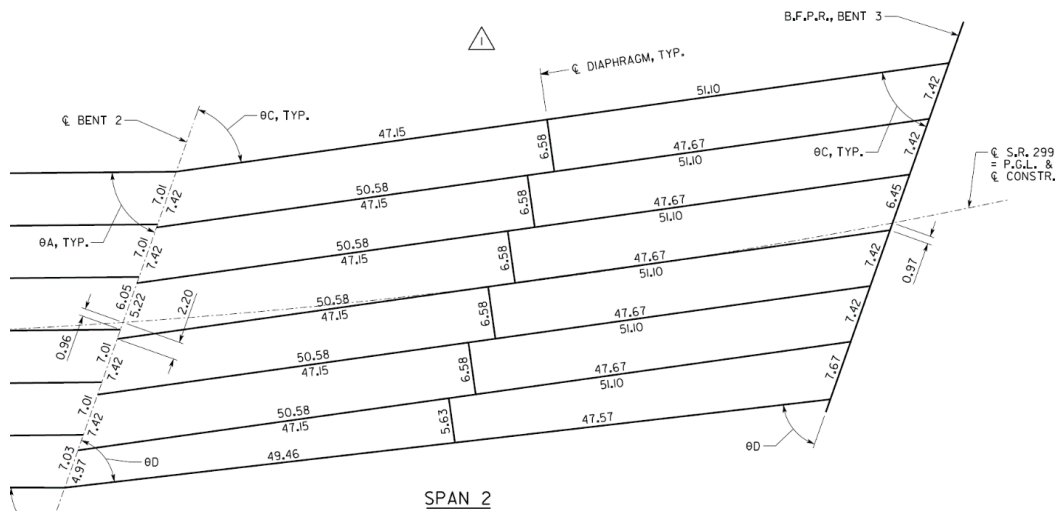


Figure 58 – Plan view showing Span 2 PSC girders (GDOT-DRW, 2016).

Each girder has 44 low-relaxation prestressed strands, each with a diameter of 0.6 in. (15.24 mm). The area of each strand is 0.217 in² (140 mm²). A section view of one of the girders is shown in Figure 59 and includes girder dimensions and the location of the prestressing strands at both mid-span and girder ends.

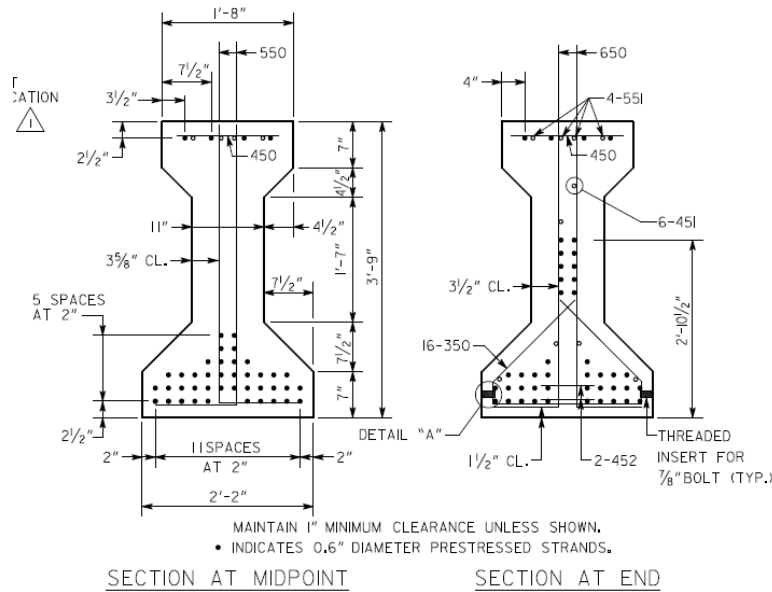


Figure 59 – Section view of a PSC girder (SR299 bridge).

The girder geometry is drawn in the DIANA software by creating a cross section on a plane (YZ-Plane) and extruding the cross section. Then, the prestressing strand profiles are created inside each girder based on the locations and spacing shown on the construction drawings. Figure 60 shows an isometric view of the girders created for Span 1. Figure 61 shows the top view of the PSC girders of Spans 1 and 2. Finally, Figure 62 shows an isometric view of the prestressing strands in the Span 1 girders.

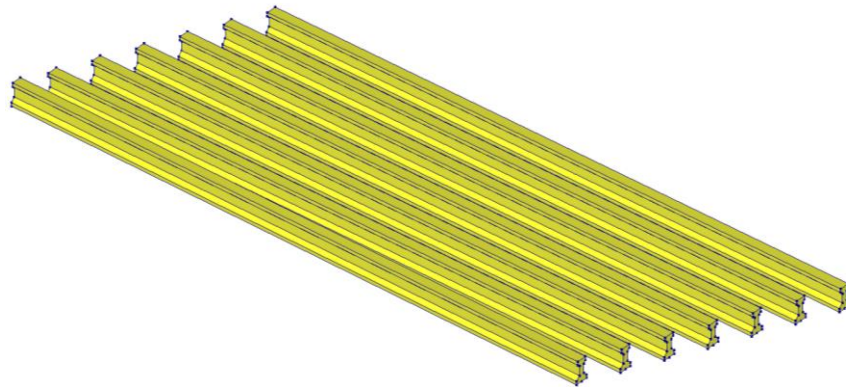


Figure 60 – Isometric view of PSC girders of Span 1 in DIANA.

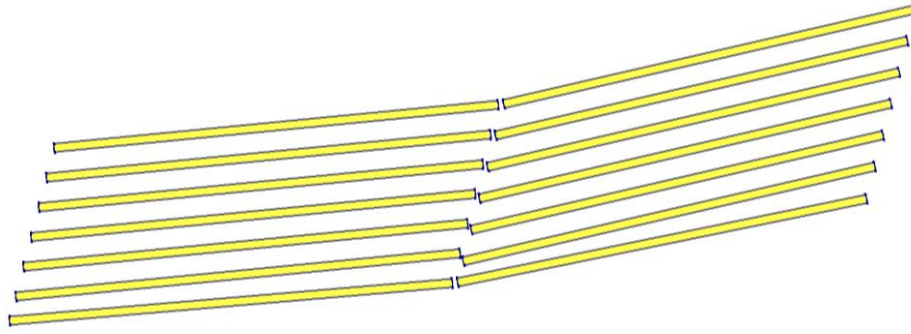


Figure 61 – Top view showing PSC girders of Spans 1 and 2 in DIANA.

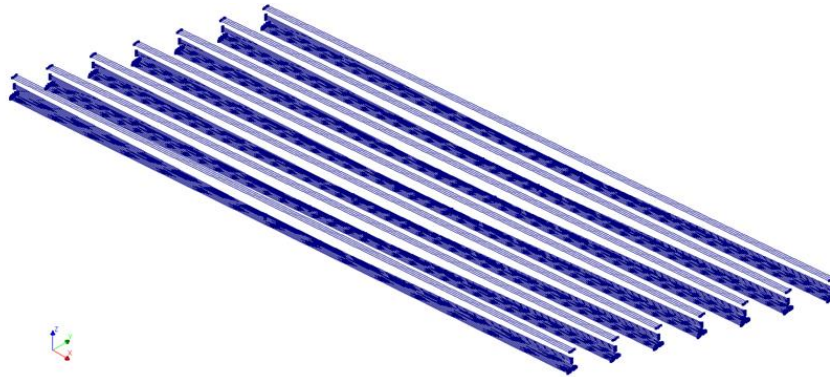


Figure 62 – Isometric view showing prestressed strands in Span 1 girders.

4.2.4 Diaphragms, Endwalls, and Edge Beams Details

Other structural elements are created in the FEA model to represent the boundary conditions accurately. The dimensions of diaphragms, endwalls, and edge beams are presented in Table 8. In general, the diaphragms run perpendicularly between the girders at mid-length and are shown in Figure 63. Depending on location, the widths of the diaphragms differ slightly.

Table 8 – Dimensions of diaphragms, endwalls, and edge beams.

Elements	Length, ft-in. (m)	Width, ft-in. (m)	Height, ft-in. (m)
Diaphragm	0-10 (0.25)	varies	3-0 (0.91)
Endwall	1-6 (0.46)	43-3 (13.18)	3-11 (1.20)
Edge beam	1-0 (0.31)	43-3 (13.18)	2-8 (0.81)

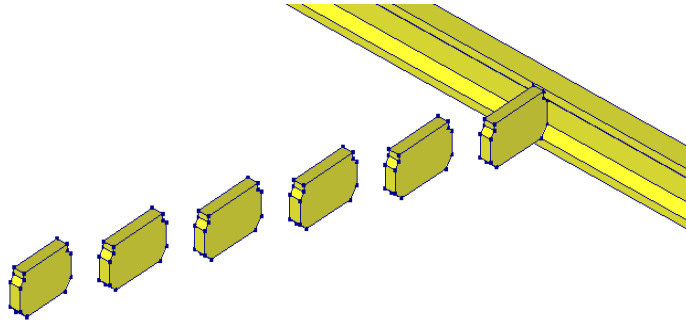


Figure 63 – Modeled diaphragms (SR299 bridge) in DIANA.

Figure 64 shows the endwalls created at the two ends of the bridge deck. They are connected with the deck and girders and rest on the precast pedestal (i.e., abutment stem). Additionally, an edge beam is generated at the mid-span of the deck.

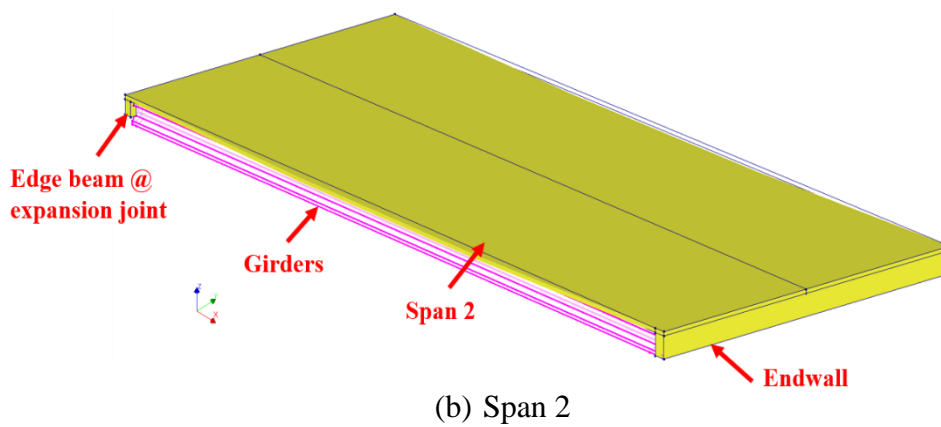
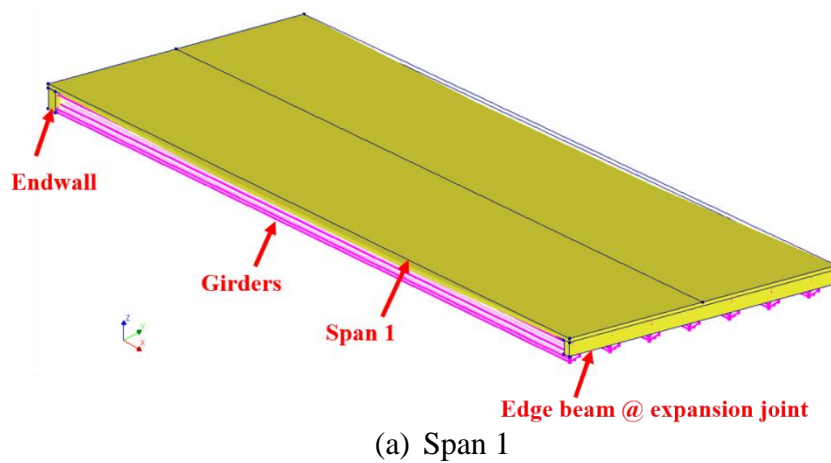


Figure 64 – Bridge model showing structural components of the SR299 bridge.

4.3 Material Properties

A nonlinear material model is assigned to the deck concrete. Based on preliminary runs, the girders, prestress strands, endwalls, diaphragms, edge beams, and steel reinforcement remain linear and thus are assigned linear elastic material properties. This assignment was reasonable as other bridge components are expected to behave linearly. Material properties such as the modulus of elasticity, Poisson's ratio, and mass density are assigned based on the information provided by the construction drawings.

4.3.1 Deck Material Properties

The properties of the deck concrete material model are summarized in Table 9. The compressive strength is used to determine the tensile cracking strain and identify elements that are considered cracked. The reduced coefficient of thermal expansion resulting from limestone aggregate is accounted for in the concrete material model available in DIANA.

Table 9 – Material properties of SR299 bridge deck concrete.

Deck	
Deck concrete	Class D
Compressive strength, f_c	4000 psi (28 MPa)
Modulus of elasticity, E	3.6×10^6 psi (25 GPa)
Density	145 lb/ft ³ (2300 kg/m ³)
Coefficient of thermal expansion (CTE) *	5.5×10^{-6} in/in/°F (1.0×10^{-5} cm/cm/°C)

* DIANA model reduces CTE by approximately 8-10% to account for limestone aggregate.

4.3.2 Reinforcement Material Properties

The properties of the deck reinforcement steel are summarized in Table 10.

Table 10 – Material properties of bridge deck reinforcement.

Reinforcement	
Reinforcement material	Steel
Grade	60
Yield strength, f_y	60,000 psi (415 MPa)
Coefficient of thermal expansion	7.2×10^{-6} in/in/ °F (1.3×10^{-5} cm/cm/ °C)

4.3.3 Girders Material Properties

The properties of the girders are summarized in Table 11.

Table 11 – Material properties of girders.

Girders	
Girder concrete	Class AAA
Compressive strength, f'_c	8000 psi (55 MPa)
Tensile strength, f_t	573 psi (4 MPa)
Modulus of elasticity, E	5.10×10^6 psi (35 GPa)
Density	145 lb/ft ³ (2300 kg/m ³)
Coefficient of thermal expansion	5.5×10^{-6} in/in/ °F (1.0×10^{-5} cm/cm/ °C)

4.3.4 Prestressing Strands Material Properties

Table 12 gives the material properties of the prestressing strands used for analysis. More specifically, the effect of the prestressing strands in the girders is represented by the following information available on the drawings:

- 44 - 0.6 in. (15.24 mm) diameter low relaxation strands; $A = 0.217 \text{ in}^2$ (140 mm²)
- Pretension strands to 43,943 lbs (196 kN) each
- Pretension released when concrete $f'_c = 6,500$ psi (45 MPa)
- Top and bottom jacking force = 1,933,492 lbs (8600 kN)
- Top and bottom net prestressing force of the strands after all losses = 1,487,242 lbs (6616 kN)

- Prestress load after all losses per area of each strand = 155,764.77 psi (1074 MPa)

Table 12 – Material properties of prestressing strands.

Prestress Strands	
Prestress strand material	ASTM A416
Grade	270
Tensile strength	270,000 psi (1862 MPa)
Coefficient of thermal expansion	7.2×10^{-6} in/in/ °F (1.3×10^{-5} cm/cm/ °C)

4.3.5 Diaphragms, Endwalls, and Edge Beams Material Properties

The material properties of the diaphragms, endwalls, and edge beams are summarized in Table 13.

Table 13 – Material properties of diaphragms, endwalls, and edge beams.

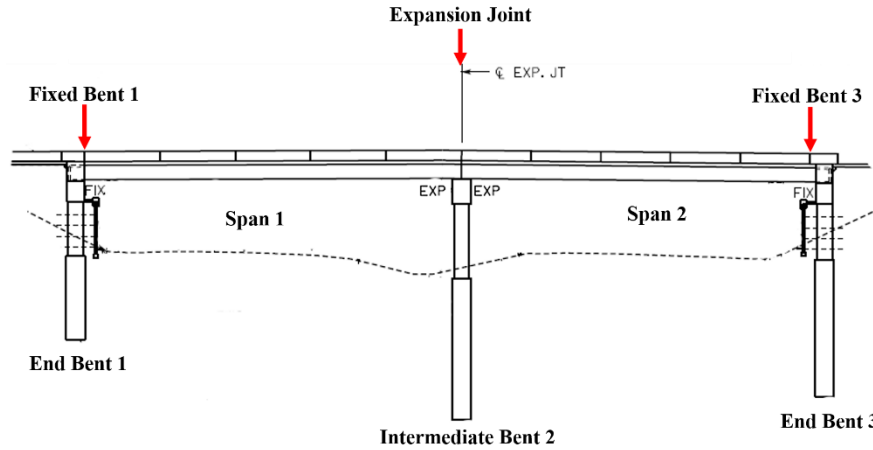
Diaphragms, Endwalls, Edge Beams	
Superstructure concrete	Class D
Compressive strength, f'_c	4000 psi (28 MPa)
Modulus of elasticity, E	3.6×10^6 psi (25 GPa)
Density	145 lb/ft ³ (2300 kg/m ³)
Coefficient of thermal expansion	5.5×10^{-6} in/in/ °F (1.0×10^{-5} cm/cm/ °C)

4.4 Boundary Conditions

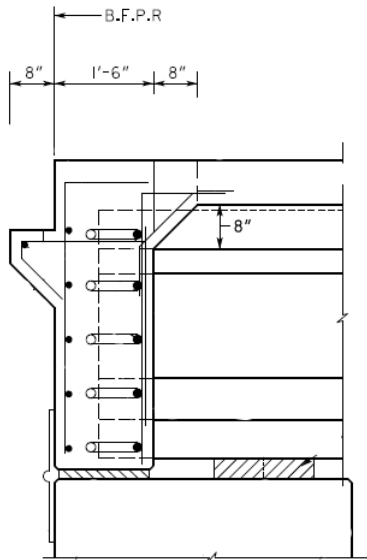
During the analysis, structural and thermal boundary conditions are imposed on the SR299 bridge model. The structural boundary conditions include the bridge's substructural elements (e.g., pier caps, columns, drilled shaft, and Mechanically Stabilized Earth (MSE) walls) which define the state of supports for the bridge superstructure. The thermal boundary conditions involve the environmental conditions affecting the thermal behavior of the bridge model.

4.4.1 Structural Boundary Conditions

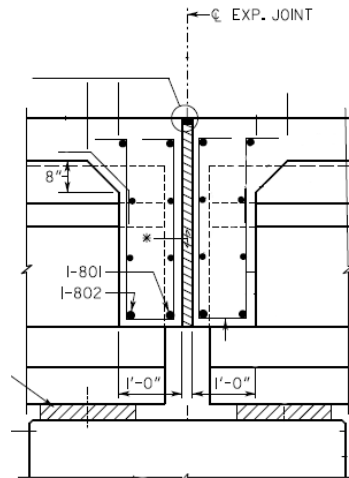
Structural boundary conditions define the physical support conditions of the SR299 bridge model. The structural boundary condition details of the SR299 bridge is shown in Figure 65 (GDOT-DRW, 2016). The substructure is composed of three bents (End Bent 1, Intermediate Bent 2, and End Bent 3) supporting the bridge's two spans. Pier caps, columns, and drilled shafts exist at each bent. The soil at End Bents 1 and 3 is further supported by abutments. The bridge deck end at Bents 1 and 3 is fixed (GDOT-DRW, 2016); however, at Intermediate Bent 2, expansion joint is provided to allow movement (see Figure 65 (a)). Figure 65 (b) shows the elevation view of the deck details at End Bents 1 and 3 where construction joints are provided. Figure 65 (c) shows elevation view of expansion joint details at Intermediate Bent 2. Figure 65 (d) shows plan view of End Bents 1 and 3 at the location of the construction joint. Figure 65 (e) shows the plan view of Intermediate Bent 2 joint between Span 1 and Span 2.



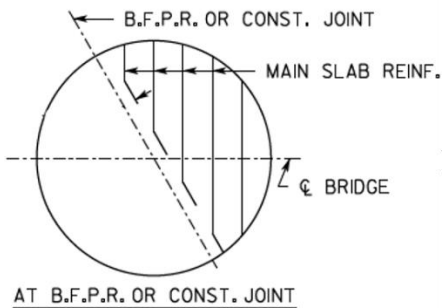
(a) Elevation view of fixed Bents 1 and 3, and expansion joint at Bent 2.



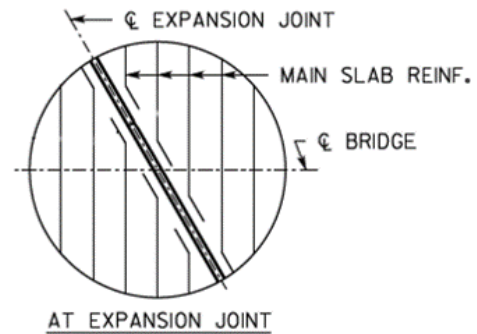
(b) Elevation view at Bent 1 & 3.



(c) Elevation view at Bent 2.



(d) Plan view of End Bent 1 & 3.



(e) Plan view of Intermediate Bent 2.

Figure 65 – SR299 bridge span support conditions (GDOT-DRW, 2016).

Furthermore, at End Bents 1 and 3, the bridge deck is integrated with endwalls and vertically supported by the substructure. Endwalls and wingwalls retain soil fill to provide additional longitudinal and transverse restraints at the bridge extremities. At Intermediate Bent 2, edge beams are integrated with the deck, and the bridge superstructure is further supported at the base of the girders by bearings that include shim plates, sole plates, and bearing pads. The girders are connected to the sole plates by anchor bolts with a 1 in. (25.40 mm) diameter. In the finite element model, reflecting the sole plate connection is important to adequately represent the superstructure support condition, and by doing so, the substructure elements do not need to be included in the model. Thus, in the FEA model, the girders are supported at bearing plate locations at Bents 1, 2, and 3. The support conditions for girders at Bents 1 and 3 are similar but are different at the Intermediate Bent 2, as described below.

4.4.1.1 Structural boundary condition at Bent 1 and Bent 3

The endwalls and bridge deck at Bents 1 and 3 are supported longitudinally and transversely by abutments and vertically by bent caps. Thus, in the finite element model, the horizontal faces of the endwalls and bridge deck are restrained in the global X-direction (referred to as longitudinal direction). The lateral faces are restrained in the global Y-direction (referred to as transverse direction), and the bottom faces of the endwalls are restrained vertically in the global Z-direction. The restraining conditions of the bridge deck and endwalls at End Bents 1 and 3 are shown in Figure 66.

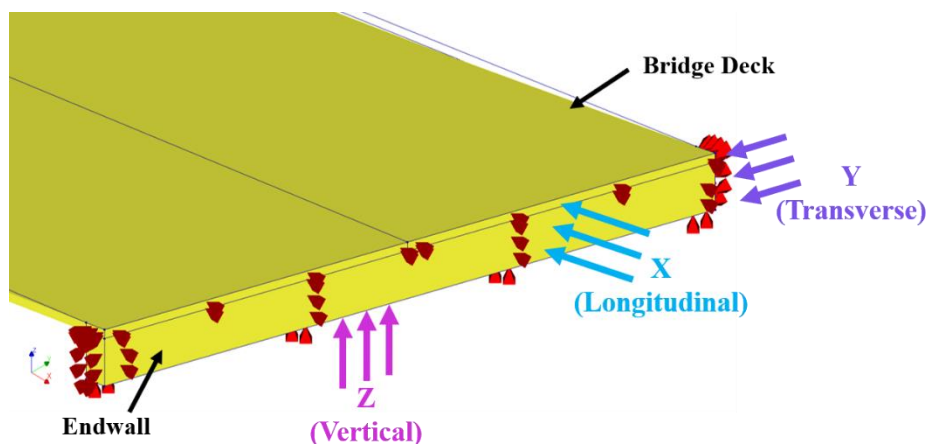


Figure 66 – Endwall support condition at Bents 1 and 3.

The design details of the sole plates at the girder ends at Bents 1 and 3 are identical (see Figure 67). These sole plates define the supporting conditions of the bridge girders at the two end bents and are designed to prevent the bridge superstructure from moving in longitudinal, transverse, and vertical directions at End Bents 1 and 3. In the finite element model, the girder bases at the bearing locations are thus restrained from XYZ-direction movements at Bents 1 and 3 (see Figure 68) to best reflect the integral design described in Section 2.3.

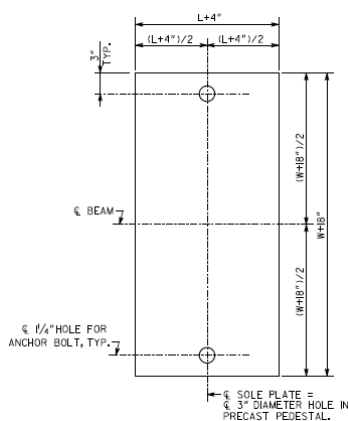


Figure 67 – Typical sole plate details at End Bents 1 and 3 (GDOT-DRW, 2016).

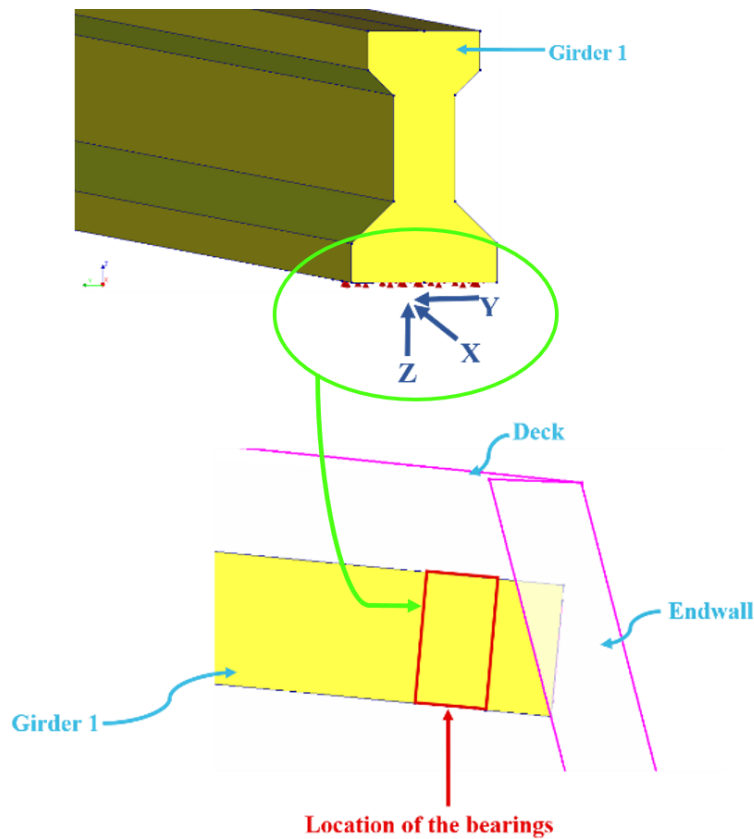


Figure 68 – Typical bearing support at Bents 1 and 3.

4.4.1.2 Structural boundary condition at Intermediate Bent 2

The girders in the two spans are resting on a substructure system at Intermediate Bent 2. At the joint between the two spans, an expansion joint is provided, which appears in Figure 69. The expansion joint at Intermediate Bent 2 allows each span to expand and move about 1.25 in. (31.75 mm) longitudinally in the global X-direction. As a result, the deck edges are allowed to expand freely in the longitudinal direction. In the FEA model, the deck edges of the two spans are not restrained at Intermediate Bent 2.

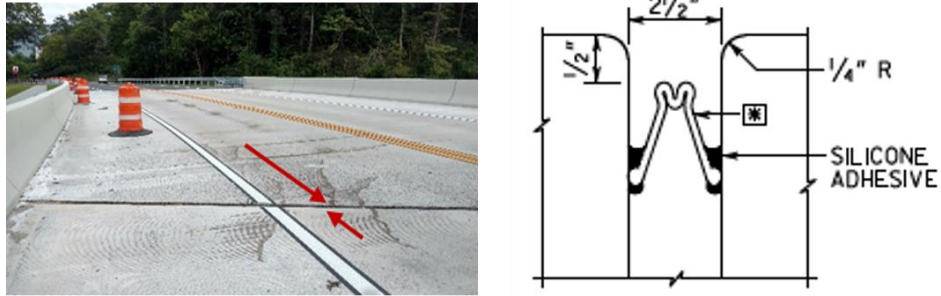


Figure 69 – Expansion joint at Intermediate Bent 2.

Additionally, the girders at Intermediate Bent 2 rest on bearings consisting of shim plates, sole plates, and bearing pads. The sole plates connect the girders to the substructure elements. They are designed to allow the girders of each span to move about 0.75 in. (19.05 mm) longitudinally and 0.0625 in. (1.59 mm) transversely. This movement allows the bridge deck to contract and expand due to thermal loading without inducing high tensile stress in the deck concrete. Design details for the sole plate at Intermediate Bent 2 are shown in Figure 70.

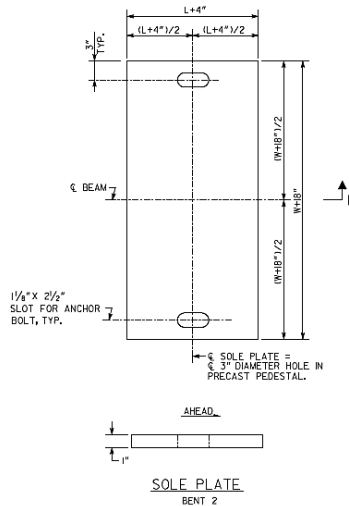
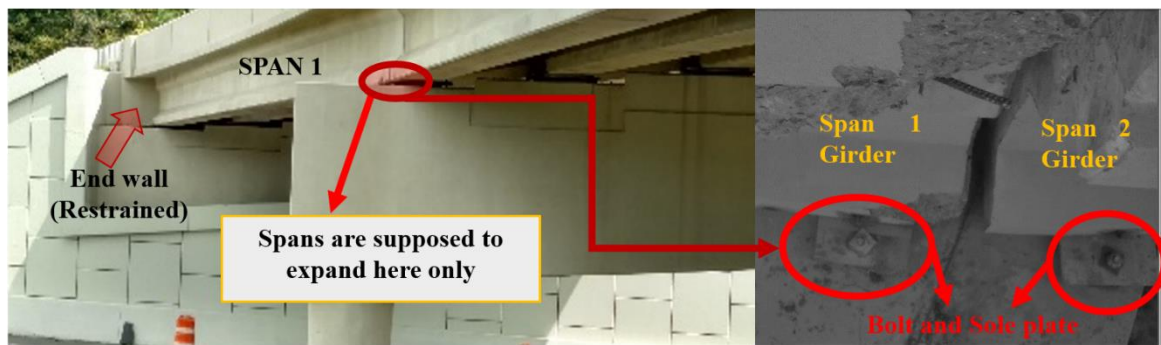


Figure 70 – Design of sole plate at Intermediate Bent 2 (GDOT-DRW, 2016).

According to bridge inspection photos (GDOT BIR, 2017) taken after the bridge was placed in its final location, however, the sole plates at Intermediate Bent 2 are different from those designed in the bridge drawings. Instead, the same sole plates used for Bents 1 and 3 are used at Intermediate Bent 2. Figure 71 (a) shows an illustration of the boundary condition at Intermediate Bent 2. Figure 71 (b) shows the bearing conditions during the first bridge inspection performed by GDOT (GDOT BIR, 2017). Figure 71 (c) shows bearing conditions during the first site investigation performed by the study team. Figure 71 (d) shows bearing conditions enlarged from the photo shown in Figure 71 (c). In the FEA, a comparison is made between using as-built versus as-designed sole plates to study the effect of the sole plates on restraining the bridge deck from thermal contraction and expansion (see Section 5.3.3). The following subsections describe three boundary conditions considered in this study.



(a) Sole plates at Bent 2 shown in the inspection report (GDOT BIR, 2017).



(b) Bearing conditions during the first bridge inspection by GDOT (GDOT BIR, 2017).



(c) Bearing conditions during the first site investigation (by this study team).



(d) Bearing conditions enlarged from the photo shown in (c).

Figure 71 – Bearing details at Intermediate Bent 2.

4.4.1.2.1 Fully restrained (FR) at Intermediate Bent 2

In this case, the support condition of the bridge is represented by the sole plates at Intermediate Bent 2 (i.e., as-built condition). Accordingly, the girders are restrained in XYZ-directions, which prohibits the superstructure movement in longitudinal, transverse, and vertical directions. The support condition of FR is shown in Figure 72.

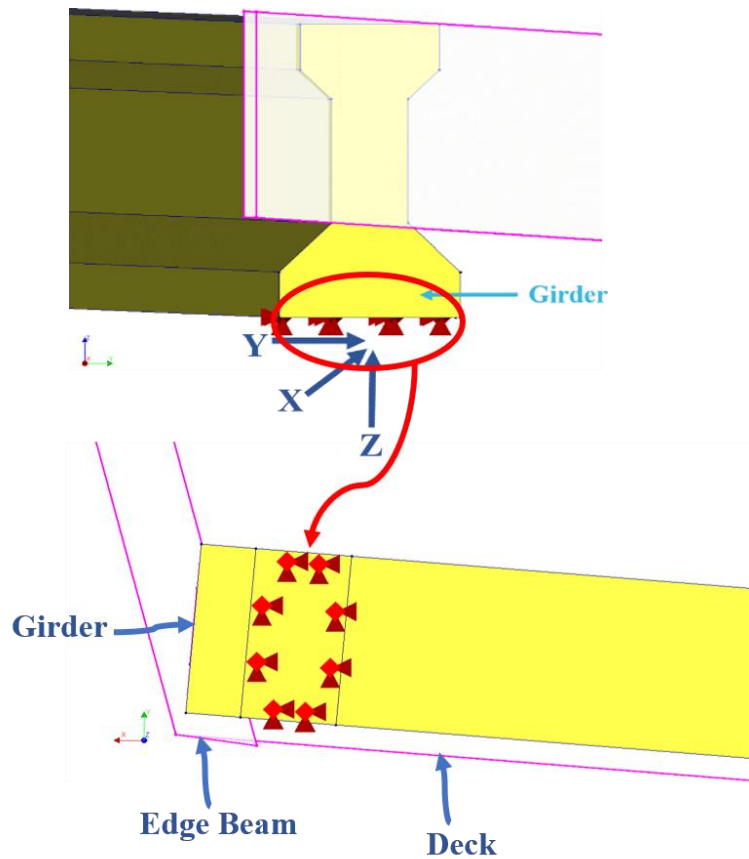


Figure 72 – Structural boundary condition for FR.

4.4.1.2.2 Longitudinally and vertically restrained (LVR) at Intermediate Bent 2

In LVR, the girders are restrained only in the longitudinal and vertical directions, which prohibits longitudinal and vertical movements. This allows the expansion and movement of the bridge in the Y-direction (transversely). This case allows a 0.0625 in. (1.59 mm)

movement in the transverse direction because the 1.125 in. (28.58 mm) holes are specified for the sole plates with 1 in. (25.40 mm) diameter anchor bolts. LVR support condition is illustrated in Figure 73.

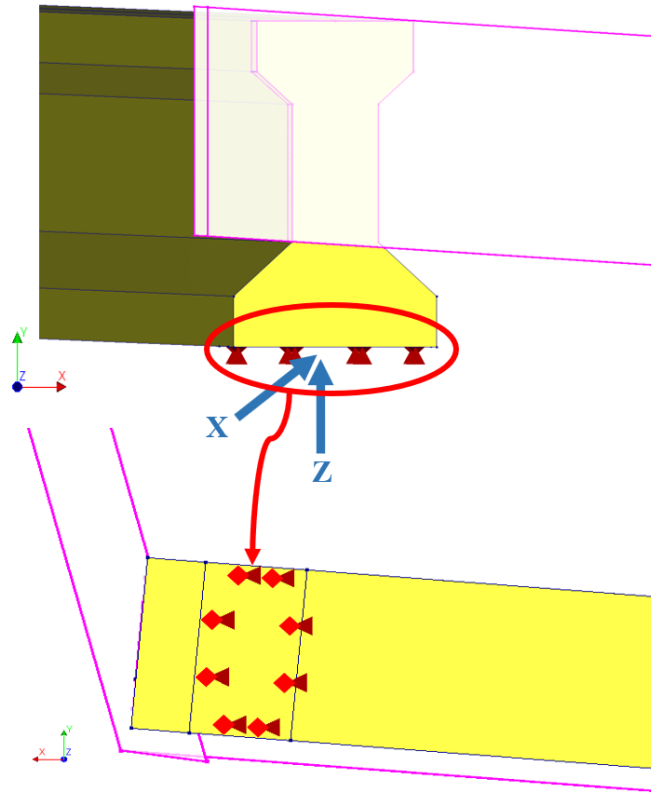


Figure 73 – Structural boundary condition for LVR.

4.4.1.2.3 Vertically restrained (VR) at Intermediate Bent 2

In VR, the girder ends are restrained only in the vertical direction. This condition permits the bridge superstructure to move in longitudinal and transverse directions. Based on the sole plates on the construction drawings, the girder ends are allowed to move longitudinally by 0.75 in. (19.05 mm) and transversely by 0.0165 in. (0.42 mm). Figure 74 illustrates the vertical restraint.

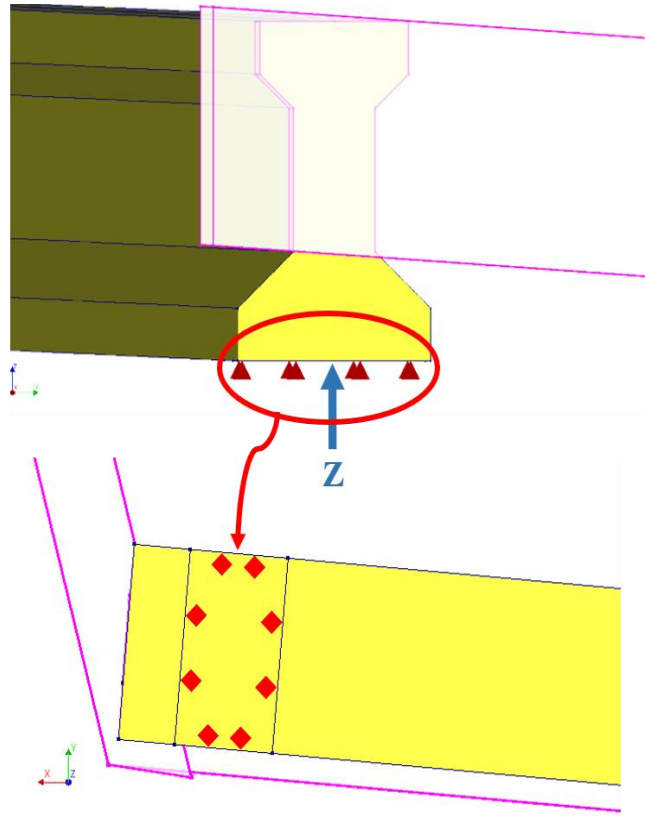


Figure 74 – Structural boundary condition for VR.

4.4.2 Summary

In the FEA model, the following factors are expected to affect thermal movements:

1. Presence of approach slabs and connectivity of girders, endwalls, and deck
2. Restraints resulting from soil pressure against endwalls and wingwalls
3. Bearing plate details
4. Expansion joint details

The boundary conditions described in Section 4.4.1.1 account for items 1 and 2 above, and the three cases created in Section 4.4.1.2 consider the design and as-built conditions of items 3 and 4.

4.5 Element Types

The DIANA software offers a wide range of element types that work with various material models. For complex geometries, three-dimensional solid elements with mid-side nodes are recommended. They are considered the most suitable elements for concrete structures. These solid elements include tetrahedrons, pentahedrons, and hexahedrons. Furthermore, DIANA offers plane interface elements to represent convection surfaces. The steel reinforcement and prestressing strands are modeled as embedded elements within the concrete elements.

The bridge geometry is meshed with hexahedral element 'CHX60.' The CHX60 element, shown in Figure 75 (DIANA, Version 10.2), is a twenty-node isoparametric solid brick element that applies a $3 \times 3 \times 3$ integration scheme. Occasionally, tetrahedral solid elements with 20 nodes compatible with CHX60 are used, particularly when meshing the complex and asymmetric deck geometry.

For thermal analysis, a convection surface is meshed with BQ4HT and BT3HT elements. The BQ4HT is the primary element type, shown in Figure 76 (DIANA, Version 10.2), which is a four-node isoparametric quadrilateral element that describes boundaries in a three-dimensional linear potential flow analysis. Its mathematical solutions are based on linear interpolation and Gauss integration schemes. Three-node isoparametric triangular elements (i.e., BT3HT) compatible with BQ4HT are used, when necessary, to characterize challenging geometries.

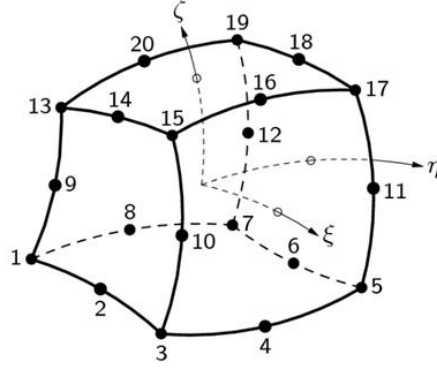


Figure 75 – CHX60 solid brick element (DIANA, Version 10.2).

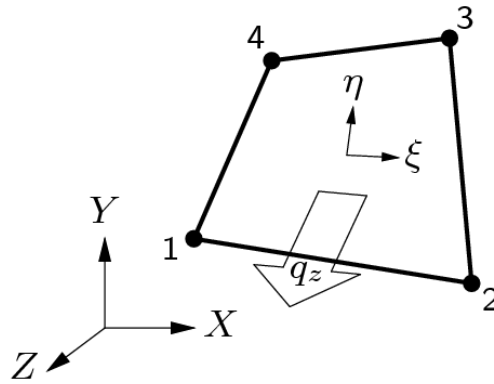


Figure 76 – BQ4HT boundary element (DIANA, Version 10.2).

4.6 Bridge Deck Geometries

The bridge deck geometry is one of the main factors that affect the extent of cracking. Therefore, four bridge deck geometries, including a straight deck, are created to study the effect of inclination, skewness and curvature, and degree of skewness. Furthermore, the four deck models aid in reviewing crack patterns induced by each geometrical feature to isolate the cause of cracking. The geometric parameters of the four deck models are summarized in Table 14.

Table 14 – Bridge deck geometry cases.

Properties	Cases			
	Straight bridge deck	Inclined bridge deck	Skewed and curved bridge deck	Highly skewed bridge deck
Deck shape	Straight	Straight and Inclined	Inclined, curved, and skewed < 20°	Inclined, curved, and skewed > 20°
Side slope	-	7.00% (4.01°)	7.00% (4.01°)	7.00% (4.01°)
Vertical slope	-	0.21% (0.12°)	0.21% (0.12°)	1.07% (0.61°)
Curvature radius	-	-	818.51 ft (249.48 m)	818.51 ft (249.48 m)
Skew angle	-	-	16.15°	23.42° and 30.26°

4.6.1 Straight Bridge Deck

A straight bridge deck model is created by incorporating the SR299 bridge characteristics and dimensions; however, the skewness, curvature, and elevation of the bridge deck are eliminated. Figure 77 shows the corresponding plan view.

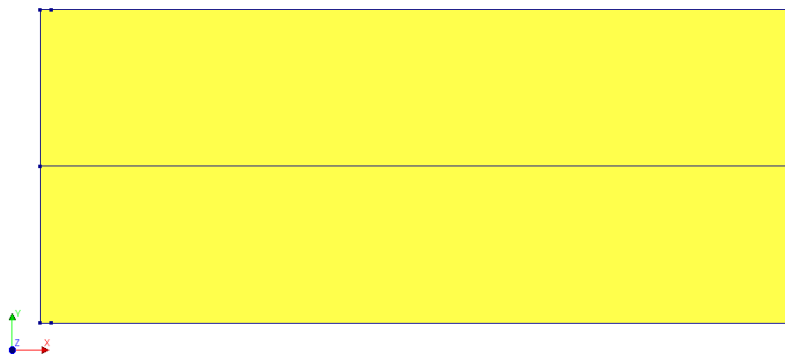


Figure 77 – Plan view of straight bridge deck.

4.6.2 Inclined Bridge Deck

An inclined bridge deck model is created to account for a side slope of 7% and a vertical slope of 0.21% (see Figure 78). The isometric, front, and rear views of the inclined deck are shown in Figure 78, Figure 79, and Figure 80, respectively.

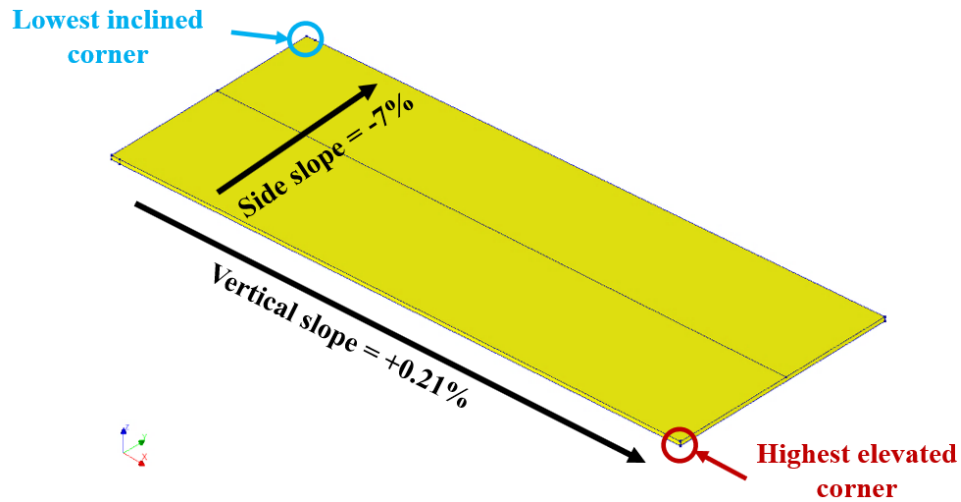


Figure 78 – Isometric view of inclined bridge deck.

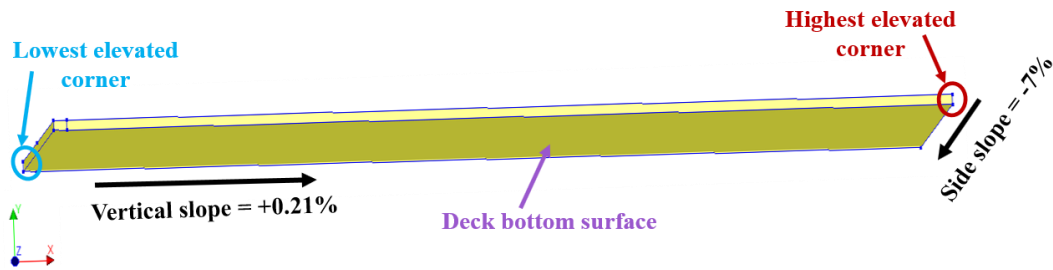


Figure 79 – Front view of inclined bridge deck.

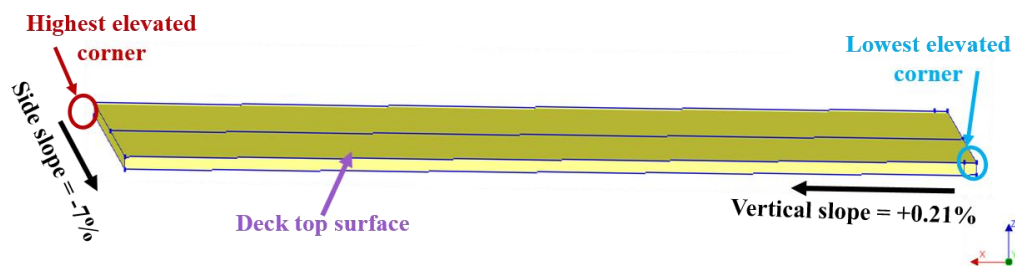


Figure 80 – Rear view of inclined bridge deck.

4.6.3 Skewed and Curved Bridge Deck

Figure 81 illustrates a skewed and curved bridge deck (Span 1 of SR299 bridge) with the inclination described in Section 4.6.2.

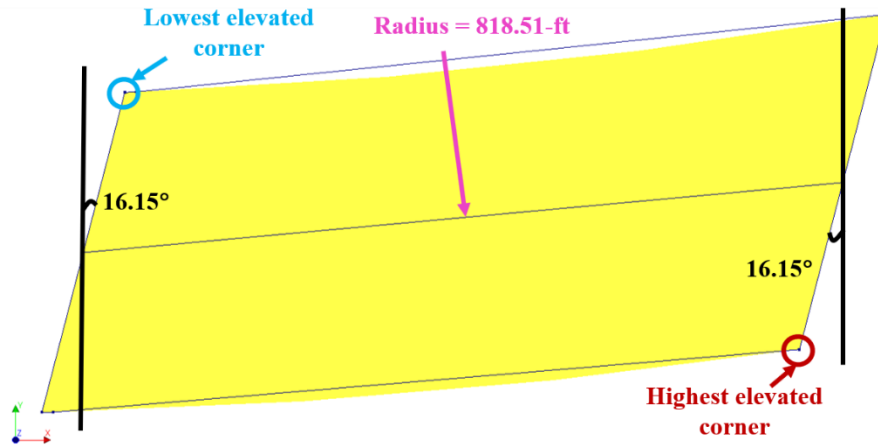


Figure 81 – Plan view of curved and skewed deck (Span 1 of the SR299 bridge).

4.6.4 Highly Skewed Bridge Deck

This case defines the condition of Span 2 of the SR299 bridge. In this case, the bridge deck is inclined with a side slope of 7% and a vertical slope of 1.07%. Additionally, the bridge is curved with a radius of 818.51 ft (249.48 m) and has skewed edges with skew angles of 23.42° and 30.26° (see Figure 82). This case compares Span 1 and Span 2 deck geometries of the SR299 bridge and studies the effect of skew angle on the extent of cracking.

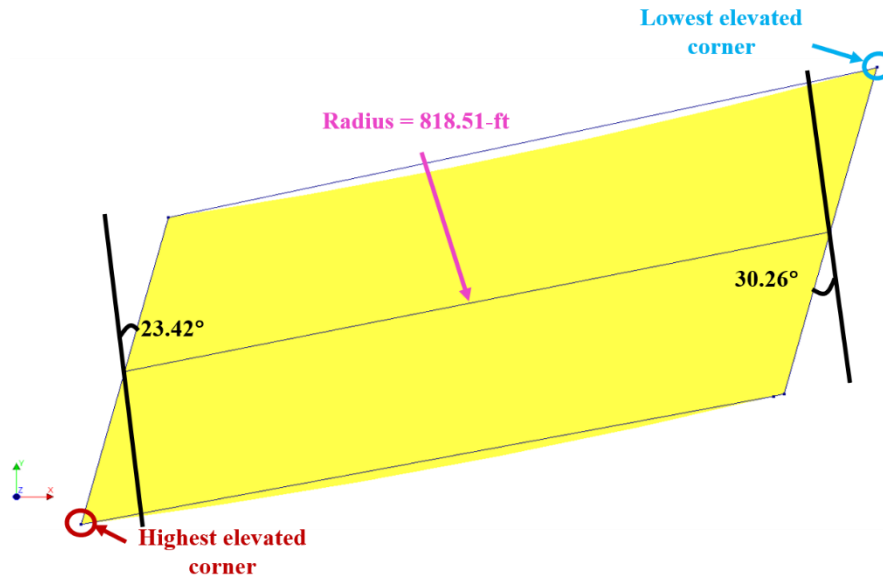


Figure 82 – Plan view of highly skewed deck (Span 2 of the SR299 bridge).

4.7 Thermal Loading

Temperature distribution in a structure is generally governed by three components: heat conduction, convection from the surrounding environment, and solar radiation. Thermal properties of materials (e.g., heat transfer coefficient) account for heat flows (i.e., conduction) between bridge components in direct contact with each other as well as convection. In performing a transient heat transfer analysis, two main factors affect the thermal behavior of the bridge deck models. The first factor is a daily temperature variation in the ambient temperature. In unrestrained structures, this temperature fluctuation results in an overall expansion or contraction but does not cause thermal stress. In symmetrically heated and restrained structures, however, uniform internal thermal-induced stresses develop. As a result, when the bridge deck is placed in a controlled environment and free to expand (i.e., only vertical supports are provided), it is expected to uniformly expand and induce thermal stresses when restrained. The second factor is temperature gradient through the depth of the bridge deck. This temperature differential through the deck thickness

results from prolonged and repeated exposure to the sun (or solar radiation) on the top surface of the bridge deck. The difference in deformation at the top and bottom portions of the deck creates a bending moment, resolving forces in tension and compression, respectively (Imbsen, Vandershaf, Schamber, & Nutt, 1985).

The solar radiation of the bridge deck model is computed in DIANA based on clear sky conditions. The effect of shadows is not considered after reviewing site conditions. The results indicate that a gradient temperature of approximately 20 °F (11.11 °C) exists through the thickness of the bridge deck, which is fairly consistent with a previously reported gradient of 16 °F (8.88 °C) determined from a prior study (Karunaratne, Mampearachchi, & Nanayakkara, 2010). Temperature differentials range between 16 °F (11.11 °C) and 27° F (15 °C) in the literature (Wang, Zou, Li, Xu, & Wang, 2015; Imbsen et al., 1985). However, Imbsen et al. (1985) determined the temperature differential resulting from solar radiation to be 41 °F (22.78 °C), which appears to be conservative because it was based on worst-case conditions. Imbsen et al. (1985) created a map (see Figure 83) dividing the United States into four solar radiation zones with the first zone having the highest temperature differential and the fourth zone having the lowest temperature differential. Accordingly, Imbsen et al. (1985) recommended that the temperature differential through the depth of the bridge superstructure correspond with the profile shown in Figure 84. Table 15 summarizes the associated gradient temperatures.

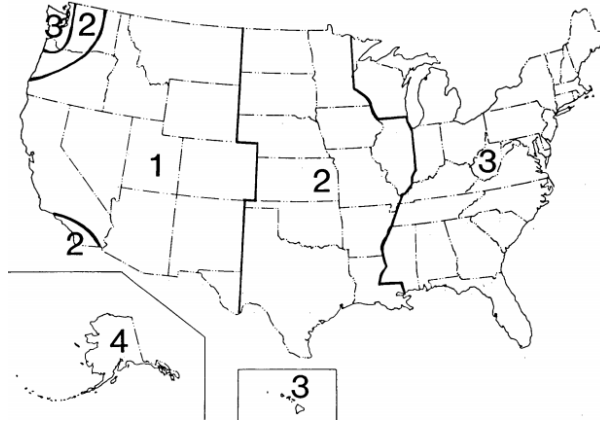


Figure 83 – Maximum solar radiation zones for the United States (Imbsen et al., 1985).

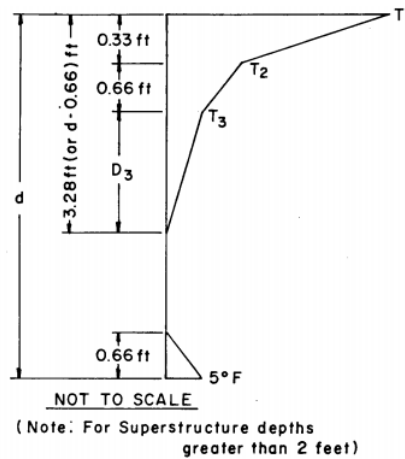


Figure 84 – Temperature gradient within a concrete superstructure (Imbsen et al., 1985).

Table 15 – Temperature differentials within a concrete superstructure (Imbsen et al., 1985).

Zone	T ₁ , °F (°C)	T ₂ , °F (°C)	T ₃ , °F (°C)
1	54 (30)	14 (7.78)	5 (2.78)
2	46 (25.56)	12 (6.67)	4 (2.22)
3	41 (22.78)	11 (6.11)	4 (2.22)
4	38 (21.11)	9 (5)	3 (1.67)

Based on Imbsen et al.'s (1985) map, Georgia resides in the third zone and thus has a maximum temperature differential of 41 °F (22.78 °C) from the top of the bridge deck to

the bottom of the bridge superstructure. Moreover, Imbsen et al.'s (1985) analysis of normal daily maximum temperatures for July indicates an ambient temperature in Georgia of 90 °F (32.22 °C), which creates a maximum effective temperature of 92 °F (33.33 °C) for concrete bridges (Imbsen et al., 1985) since the temperature of concrete is approximately 2 °F (1.11 °C) higher than the ambient temperature.

To perform a transient heat transfer analysis of the SR299 bridge model, the temperature variation for the period of bridge deck construction between April 2017 and August 2017 (when cracks were discovered) was used. The initial temperature of the bridge model is determined to be 53 °F (11.67 °C) based on the estimated placement temperature. This initial temperature is often referred to as a “base” or “reference” temperature, and thus thermal expansion is defined with respect to this temperature. The daily ambient temperature at the closest weather station near the bridge is available online (Chattanooga Metropolitan Airport Weather History, 2019), and the highest ambient temperature during summer 2017 is found to be 96 °F (35.56 °C). Additionally, solar radiation increases the top surface temperature by approximately 20 °F (11.11 °C). Thus, a surface temperature of 116 °F (46.67 °C) is anticipated. Table 16 summarizes the ambient temperatures applied to the bridge deck model during analysis.

Table 16 – Temperatures applied in SR299 bridge deck analysis.

Bridge Element		Ambient Temperature, °F (°C)
Deck	Top	96 plus 20 from solar radiation (35.56 plus 11.11)
	Bottom	96 (35.56)
Girders		96 (35.56)
Diaphragms		96 (35.56)
Endwall/Soil		70 (21.11)
Edge beam		96 (35.56)
Initial/Base temperature		53 (11.67)

4.7.1 Twelve Thermal Analysis Cases

A coupled thermal-structural analysis is performed on the twelve cases summarized in Table 17. Specifically, a transient heat analysis is performed followed by a nonlinear structural analysis on each of the twelve cases reflecting various combinations of thermal boundary conditions and deck geometries. These twelve cases are created to study how variations in support boundary conditions and deck geometries affect the extent of cracking. Figure 85 shows the four deck geometries considered in this study.

In each of the twelve cases, the integrated abutment sides at Bents 1 and 3 are assumed to be fully restrained from thermal movements (see Section 4.4.1.1). The bridge superstructure is exposed to the environmental conditions described in Section 4.7. The straight and inclined deck models are created by removing skewness and curvature from the Span 1 geometry, respectively (see Figure 85 (a) and (b)). The curved/skewed deck model represents the Span 1 geometry (Figure 85 (c)). Finally, the curved/skewed Span 1 model is compared with the Span 2 model (see Figure 85 (d)) to study the effect of skew angle. The Span 2 deck has a skew angle greater than 25° , which is considered highly skewed.

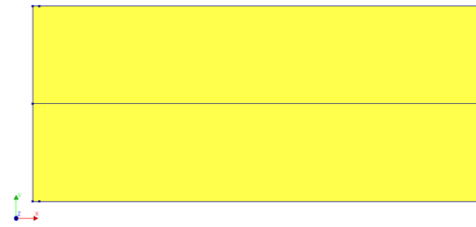
Section 5.2 presents the temperature results from the twelve thermal analysis cases. Subsequently, the results are used as initial conditions (i.e., strain loading) for the structural analysis. In Section 5.3, the results from the twelve thermal-structural analysis cases are compared based on a review of displacements, crack strains, crack widths, and crack orientations.

Table 17 – Twelve analysis cases reflecting thermal boundary conditions and deck geometries.

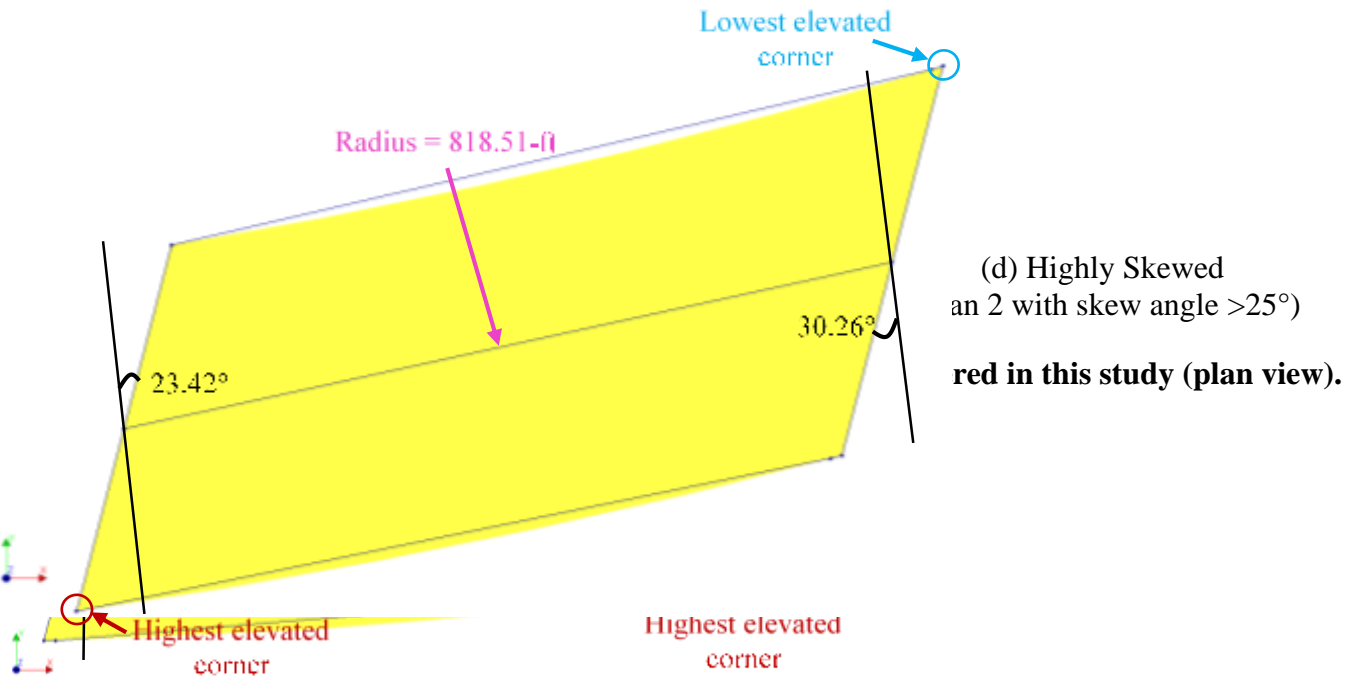
Bridge Deck Geometry	Support Boundary Condition (at Intermediate Bent 2)	Case Designation (deck geometry-boundary conditions at Bent 2)
Straight	Fully restrained	Straight-FR
	Longitudinally and vertically restrained	Straight-LVR
	Vertically restrained	Straight-VR
Inclined	Fully restrained	Inclined-FR
	Longitudinally and vertically restrained	Inclined-LVR
	Vertically restrained	Inclined-VR
Skewed and Curved (Span 1)	Fully restrained	Skewed & Curved-FR
	Longitudinally and vertically restrained	Skewed & Curved -LVR
	Vertically restrained	Skewed & Curved -VR
Highly Skewed (Span 2 w/ skew angle $>25^\circ$)	Fully restrained	Highly Skewed-FR
	Longitudinally and vertically restrained	Highly Skewed-LVR
	Vertically restrained	Highly Skewed-VR



(a) Straight bridge deck



(b) Inclined bridge deck



4.8 Structural Loading

Two truck live load cases are created for the Span 2 model. The two load cases yield the maximum bending moment and shear force in the bridge deck section. Span 2 is selected for analysis because it has larger skew angles (23.42° and 30.26°) than Span 1. The bridge model is designed for three basic live loads for bridges according to Highway Load in the 1993 AASHTO LRFD Bridge Design Specifications (HL-93). Based on the site investigations (see Sections 3.2 and 3.5), the bridge services a significant number of Class 9 trucks, which are 5-axle tractor semitrailers commonly known as the Type 3-S2 trucks shown in Figure 86 (FHWA, 2000). Thus, in the finite element model, the wheel loads of Type 3-S2 trucks are applied as stationary distributed loads over the contact area between truck wheels and deck surface. The contact area is 10×10 in. (254×254 mm) for the front two wheels and 10×20 in. (254×508 mm) for the rest of the tires (AASHTO, 2017). Figure 87 presents the elevation and plan views showing the wheel load distribution and spacing of Type 3-S2 trucks. In addition, the magnitude of each wheel load and applied pressure over the contact area is shown in Figure 87.

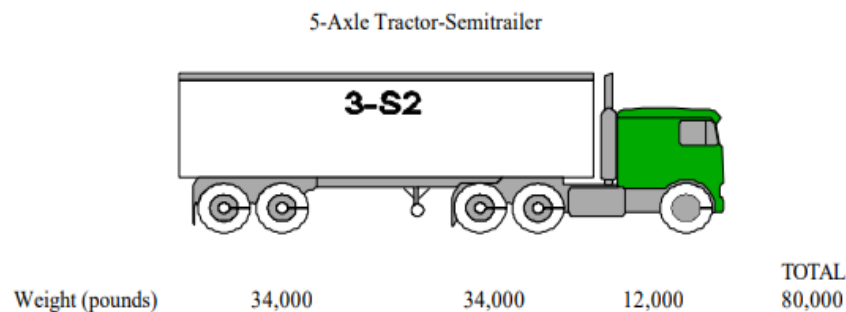


Figure 86 – Applied live load on SR299 bridge (FHWA, 2000).

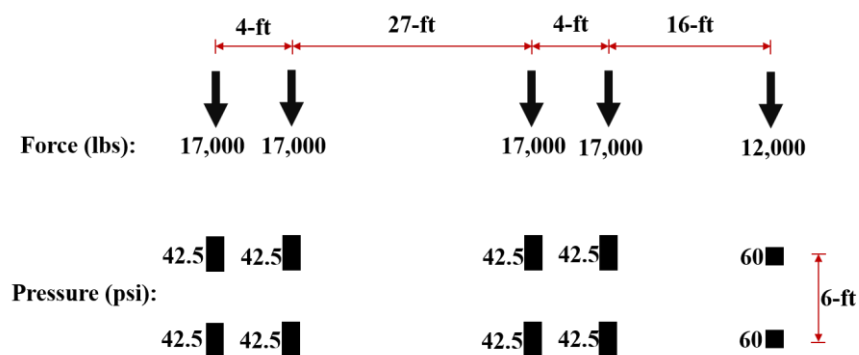


Figure 87 – Type 3-S2 truck load distribution.

4.8.1 Live load Case A

The first case involves the configuration of trucks that yields the maximum bending moment in the bridge deck section. As shown in Figure 88, the bridge is loaded with a total of six trucks, three in each direction. Each lane is loaded with a full-length truck as well as the front two and rear two axles of a truck entering and a truck leaving the span, respectively.

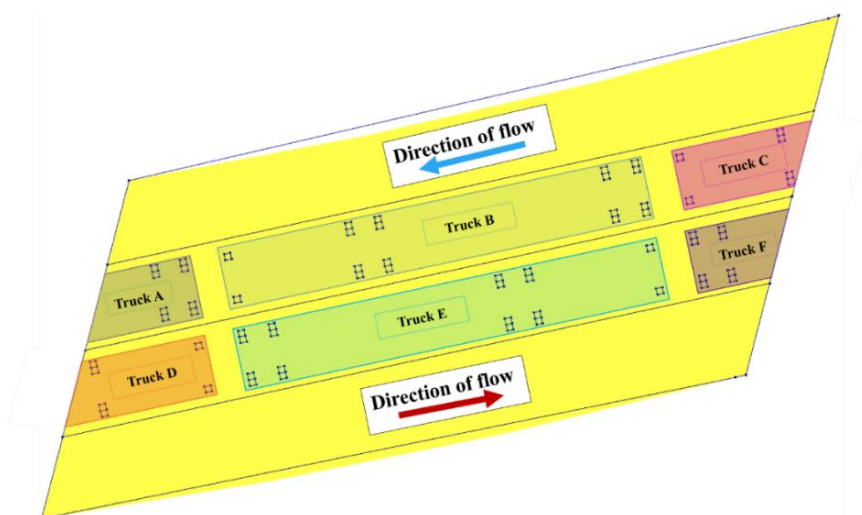


Figure 88 – Truck distribution for maximum bending moment on Span 2.

4.8.2 Live load Case B

Case B represents the configuration of trucks that gives the maximum shear force at the ends of Span 2. Similar to Case A, the bridge deck is loaded with a total of six trucks, three in each direction (see Figure 89). Each lane is loaded with a full-length truck as well as the front three and rear two axles of a truck entering and a truck leaving the span, respectively.

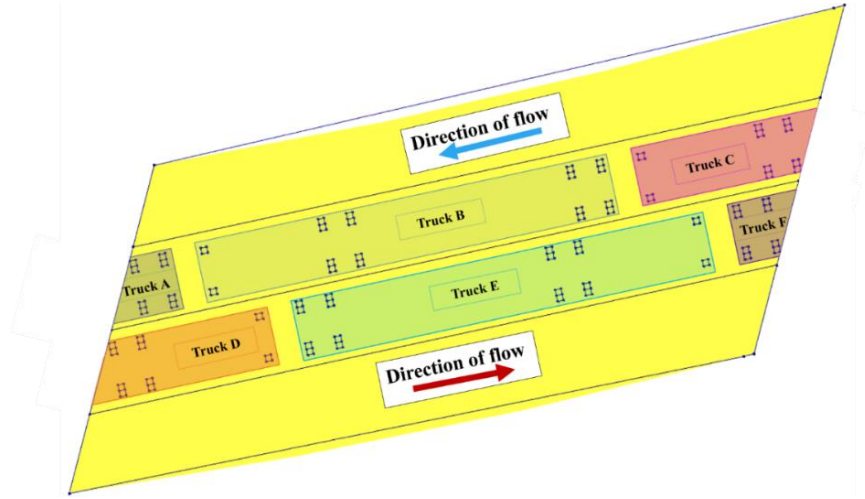


Figure 89 – Truck distribution for maximum shear force on Span 2.

4.9 Vertical Displacement Loading

Since the SR299 bridge was constructed using SPMTs, the bridge superstructure was vertically lifted, removed from temporary supports, moved transversely, and placed on permanent supports. The bridge was lifted from the bottom face of the girders and moved with the two transporters shown in Figure 90 (GDOT, 2016).

Based on the construction drawings (GDOT, 2017), a significant vertical grade existed in the roadway and thus might have affected vertical movements at the bearing locations. Accordingly, vertical movements were continuously monitored while the bridge was moved with the SPMTs and were within the required tolerance of 0.75 in. (19 mm). In

this study, four cases are created to apply the maximum vertical movement allowed during the move.

The bearing locations of Span 2 are shown in Figure 90. In this figure, bearing areas on the girder bases (G1–G7) are indicated as L1–L7 for the first transporter and R1–R7 for the second transporter. Figure 91 shows the bearing locations where the vertical displacements is applied. Table 18 shows the four cases created to encounter the effect of vertical displacements on the bridge superstructure. Maximum vertical displacement of 0.75 in. (19 mm) is applied at the first bearing location of corner for each case.

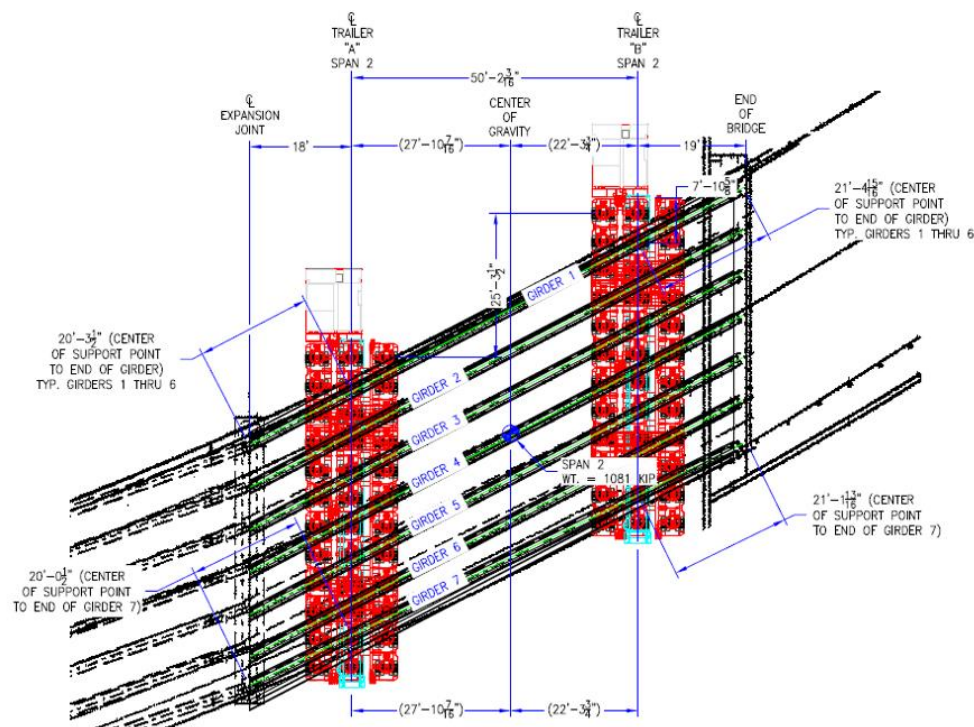


Figure 90 – SPMT location for moving Span 2 (GDOT, 2016).

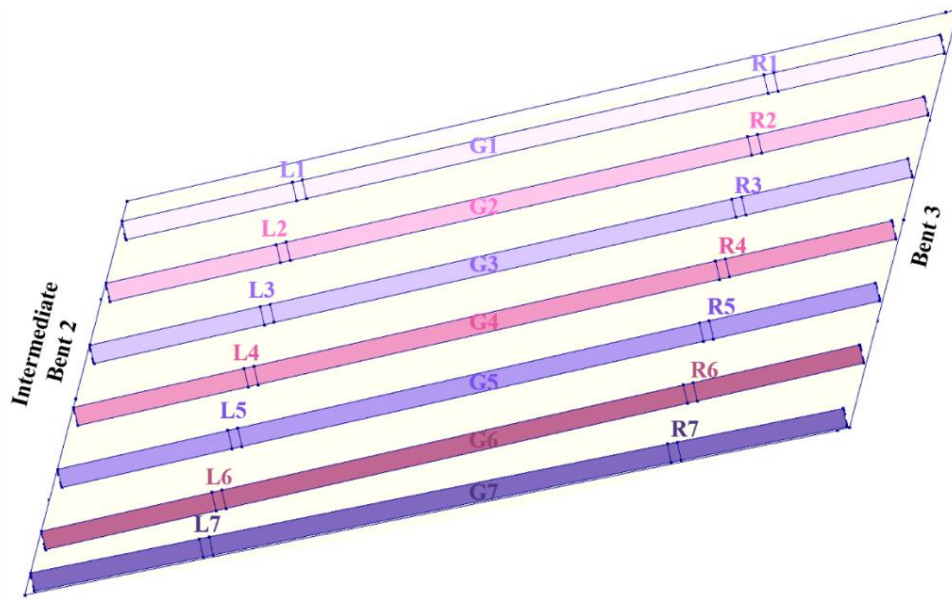


Figure 91 – Bearing locations for moving Span 2 in DIANA.

Table 18 – Induced vertical displacement magnitudes at bearing locations.

Locations	Vertical displacement, in. (mm)			
	Case V1	Case V2	Case V3	Case V4
G1-L1	0.75 (19)	0	0	0
G2-L2	0.64 (16.3)	0.13 (3.3)	0	0
G3-L3	0.51 (13)	0.26 (6.6)	0	0
G4-L4	0.39 (9.9)	0.39 (9.9)	0	0
G5-L5	0.26 (6.6)	0.51 (13)	0	0
G6-L6	0.13 (3.3)	0.64 (16.3)	0	0
G7-L7	0	0.75 (19)	0	0
G1-R1	0	0	0	0.75 (19)
G2-R2	0	0	0.13 (3.3)	0.64 (16.3)
G3-R3	0	0	0.26 (6.6)	0.51 (13)
G4-R4	0	0	0.39 (9.9)	0.39 (9.9)
G5-R5	0	0	0.51 (13)	0.26 (6.6)
G6-R6	0	0	0.64 (16.3)	0.13 (3.3)
G7-R7	0	0	0.75 (19)	0

4.10 Validation and Verification

4.10.1 Validation of the Procedure

The thermal analysis procedure employed in this study has been successfully validated in a previous GDOT project (Chorzepa, Durham, & Hamid, 2019).

4.10.2 Verification of the Bridge Model

4.10.2.1 Verification of mesh size and convergence

Element size (known as mesh density or meshing) affects the convergence of a nonlinear FEA and the accuracy of the results. Previous studies have indicated that large element sizes exaggerate the values of stresses and displacements and have a higher percentage of errors in comparison to smaller element sizes (Dutt, 2015; Shayanfar, Kheyroddin, & Mirza, 1997). Therefore, the analysis results of various mesh sizes should be compared in order to choose the optimum element size for each structure (Sazzad, Islam, Azad, & Rahman, 2017) and, in turn, ensure accurate results.

To obtain an optimum mesh size for accurate results, the mesh size is decreased in 5 in. (12.70 cm) increments from 20 to 5 in. (50.80 to 12.70 cm) with the Span 1 model of the SR299 bridge. Figure 92 shows the deck models with element sizes of 20, 15, 10, and 5 in. (50.80, 38.10, 25.40, and 12.70 cm), respectively. The girders are assigned a constant mesh size of 10 in. (25.40 cm), as shown in Figure 93. The endwall, edge beam, and diaphragms are assigned a constant mesh size of 5 in. (12.70 cm), as shown in Figure 94. The bridge is analyzed for self-weight, and the effect of prestress loading is included in the analysis.

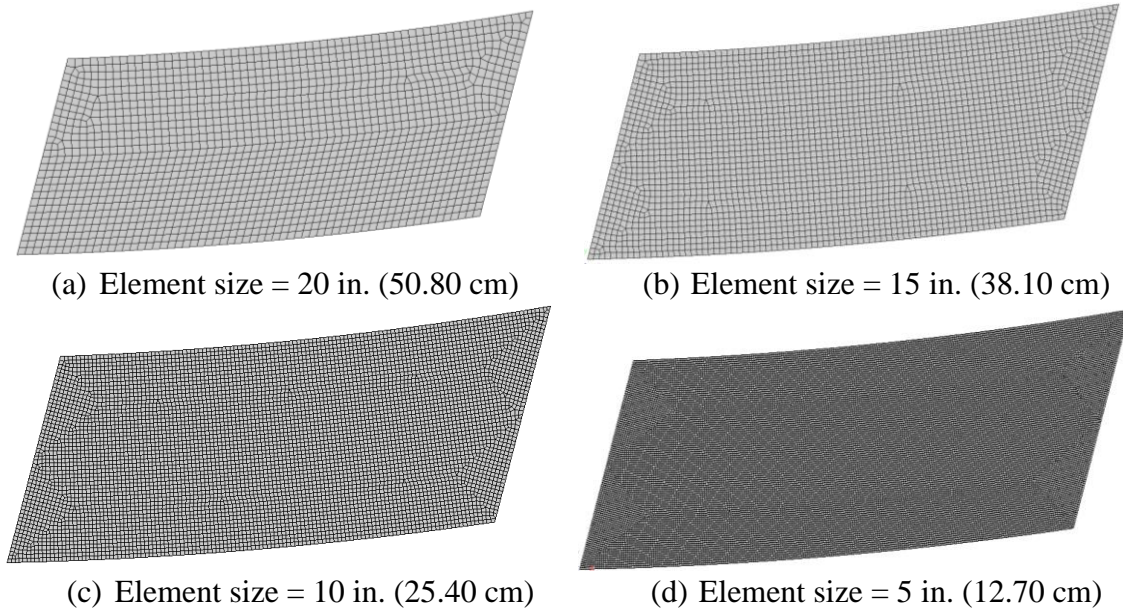


Figure 92 – Top view of deck mesh elements.

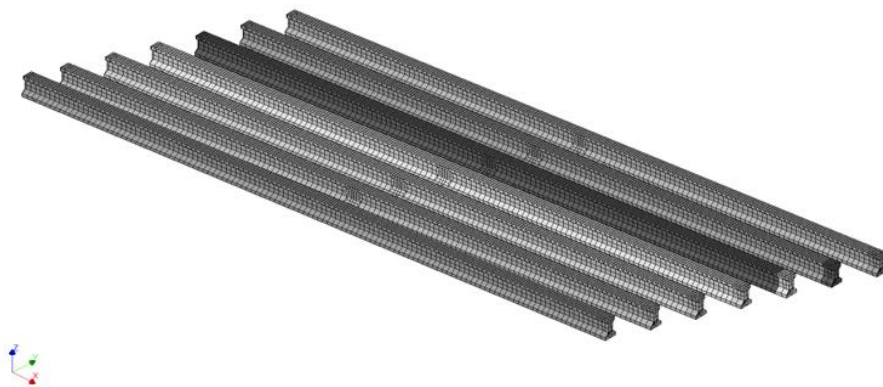


Figure 93 – Isometric view of mesh girder elements.

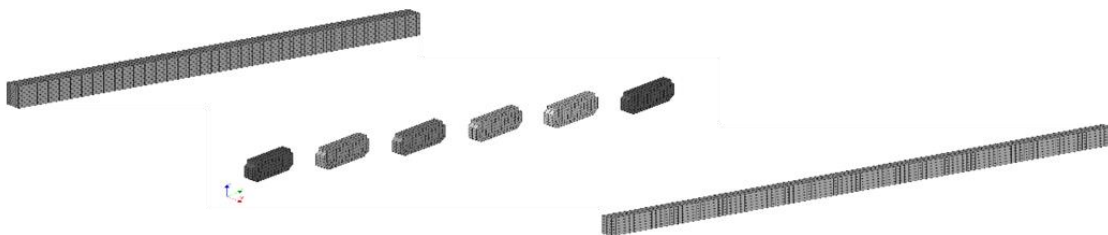


Figure 94 – Isometric view of endwall, diaphragms, and edge beam elements.

Table 19 shows the effects of mesh sensitivity on the analysis results. Vertical and total displacements, principal stress, and principal strain are compared. The total number

of elements and the time consumed for the nonlinear analysis of each mesh size are also presented in the table. Variation in mesh size has no significant effect on displacements. This finding agrees with a previous study that reported the percentage error in deformation is usually lower than the percentage error in strain values (More & Bindu, 2015). Figure 95 shows the relationship between total strain and element size. Based on this figure, the FEA solutions are considered converged with a mesh size of 5 in. (12.70 cm). Thus, the 5-in. (12.70 cm) mesh is selected for the bridge deck model analyses presented in the following sections.

Table 19 – Mesh sensitivity of the Span 1 model.

Analysis Results		20 in. (50.80 cm)	15 in. (38.10 cm)	10 in. (25.40 cm)	5 in. (12.70 cm)
No. of Elements		26,263	28,631	41,863	139,730
<i>u, inch</i> (mm)	<i>TDtZ</i>	0.33 (8.38)	0.33 (8.38)	0.33 (8.38)	0.33 (8.38)
	<i>TDtXYZ</i>	0.40 (10.16)	0.40 (10.16)	0.40 (10.16)	0.41 (10.41)
<i>σ, psi</i> (MPa)		2980 (20.55)	2930 (20.20)	1100 (7.58)	658 (4.54)
<i>ε</i>		6.04×10^{-3}	5.71×10^{-3}	3.08×10^{-3}	2.12×10^{-3}
Duration (hours)		¼	¼	½	5

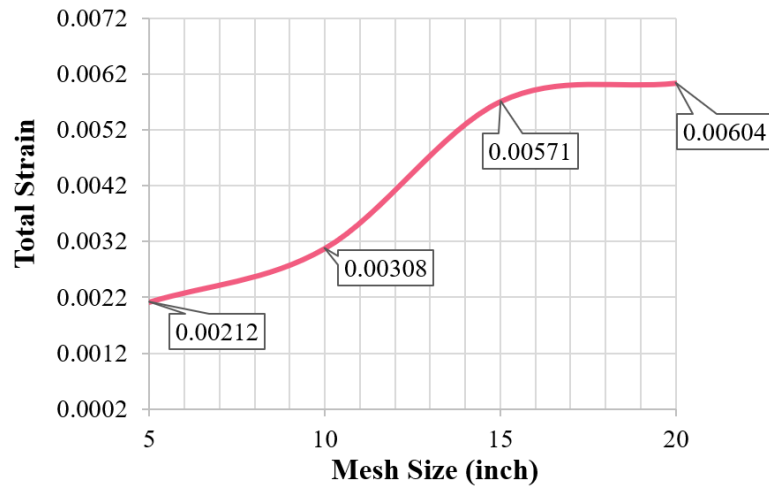


Figure 95 – Strain value vs. element size.

4.10.2.2 Total weight vs. reaction

The total weight of the Span 1 superstructure, obtained from the bridge drawings (GDOT, 2016), is 1131 kips (5031 KN). The reactions at the girder bases are hand-calculated. The Span 1 superstructure model is analyzed for self-weight to determine support reactions. They agree well with reactions obtained from the hand calculations.

5 RESULTS FROM ANALYTICAL INVESTIGATIONS

5.1 Summary of Results

This section presents the results obtained from the analytical investigations described in Section 4. The thermal analysis results indicate that temperature varies through the depth of bridge decks. As a result, bridge decks experience thermal expansion or contraction. The support boundary condition of a bridge superstructure defines the behavior of the bridge deck under thermal expansion. Bridge decks restrained from movement experience cracking due to increased internal stresses. The density of these cracks varies as deck geometries change. In skew decks, bridge decks develop a larger number of cracks, especially in their acute corners.

Service live loads on bridge decks do not initiate cracks on bridge decks. Similarly, hypothetically induced vertical displacements that can potentially result from SPMT moves do not initiate cracking on the bridge deck either, particularly when the maximum tolerance on vertical movements is met.

5.2 Results from Thermal Analysis

Figure 96 shows the temperature-time histories at selected nodes on the top and bottom deck surfaces as well as the exposed outer surface of the girders for Span 1. Span 2 exhibits a similar temperature profile to Span 1, and thus the Span 2 results are not shown here. The maximum temperature of the deck's top surface is about 117 °F (47.22 °C). The maximum temperature at the bottom of the deck surface is about 100 °F (37.78 °C). The maximum temperature at the external surface of the girders is about 97 °F (35.56 °C). The computed temperature distribution throughout the bridge superstructure is shown in Figure 97.

The temperature gradient between the top and bottom surfaces of the bridge deck ranges between 17 °F (9.44 °C) and 25 °F (13.89 °C). A section cut (A-A') is made at mid-span in an elevation view, as presented in Figure 98. Based on this cut, the results indicate that girders are approximately 15°F (8.33 °C) to 20 °F (11.11 °C) cooler than the top surface of the deck. Finally, the temperature distribution through the depth of the bridge deck is shown in Figure 99. The bottom surface of the bridge deck is cooler where it adjoins the girders.

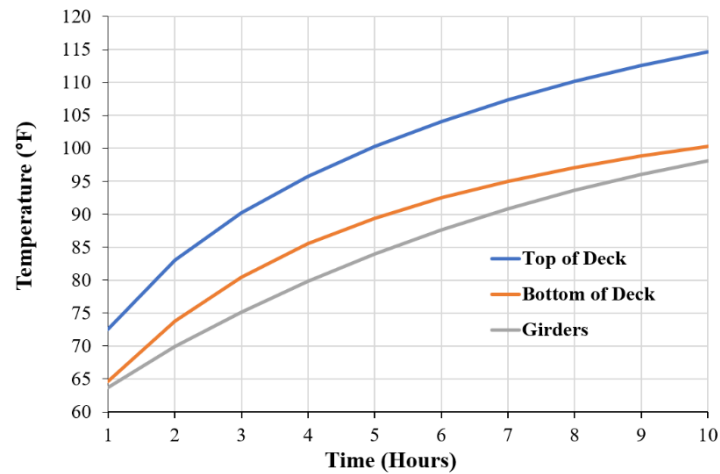
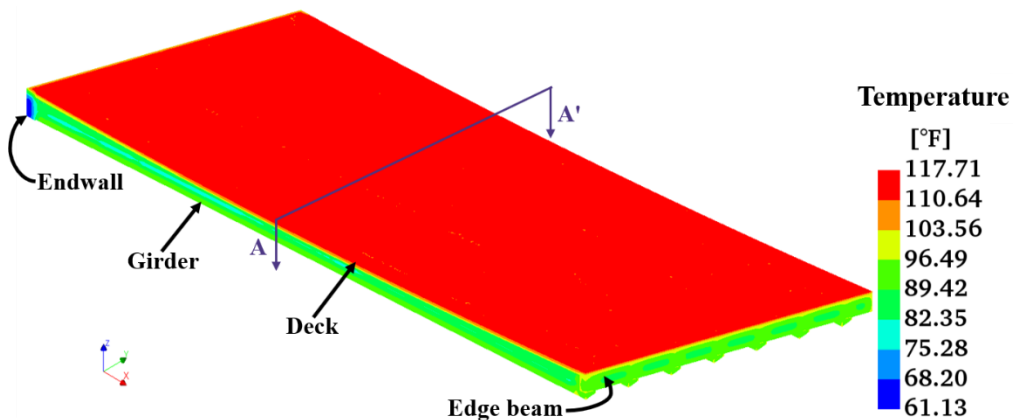


Figure 96 – Temperature rise of SR299 bridge superstructure.



Note: °F = (32°C × 9/5) + 32

Figure 97 – Temperature distribution in the bridge superstructure.

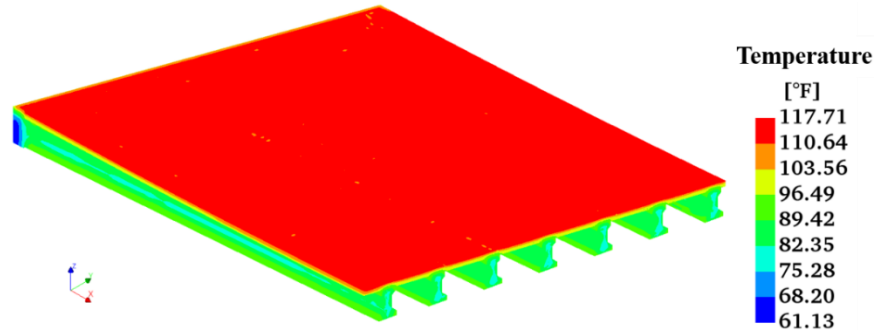


Figure 98 – Temperature distribution through superstructure (Span 1).

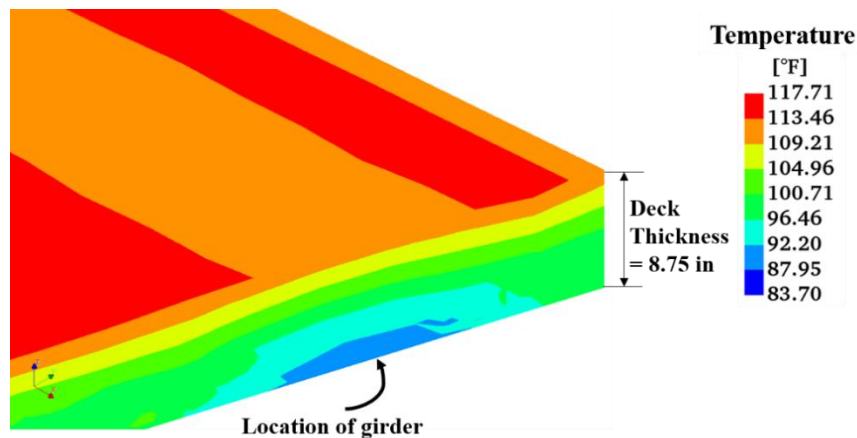


Figure 99 – Temperature distribution through deck depth at mid-span location.

5.3 Results from Coupled Thermal-Structural Analyses

5.3.1 Straight Bridge Deck

The straight deck geometry model is analyzed for three boundary conditions.

5.3.1.1 Case 1: Straight-FR

In this case, the bridge girders are fully restrained (equivalent to pinned) at Bent 2. This condition prohibited the bridge girders from longitudinal (X-direction), transverse (Y-direction), and vertical (Z-direction) thermal movements at the location of the supports (see Section 4.4.1.2.1). Figure 100 shows the total displacement of the bridge superstructure. The maximum displacement indicates that a positive curvature (concave down) develops in the deck. The point of concavity is located close to Bent 2. This is reasonable because

the thermal expansion of the deck is resisted by the soil pressure at the abutment location (i.e., Bent 1), resulting in a restrained condition for analysis.

The longitudinal and transverse displacements of the deck are shown in Figure 101 and Figure 102, respectively. Although the bridge deck has its maximum longitudinal displacement at the Intermediate Bent 2, the girder ends under the deck slab are assumed pinned and thus restrained from thermal movements. As anticipated, the maximum transverse displacement is observed along the free longitudinal edge of the deck. In reviewing the total displacement, it is important to recognize that it includes the effect of cracking.

Figure 103 and Figure 104 show cracked elements on the top and bottom surfaces, respectively. Crack strain ranges between 0 and 10 microstrain ($\mu\epsilon$). Figure 105 shows the crack width plot corresponding to Figure 103. Figure 106 shows the crack orientations magnified by 100. The maximum crack strain calculated for the cracked elements is 3760 microstrain, in turn resulting in a maximum crack width of 1.12×10^{-2} in. (0.28 mm).

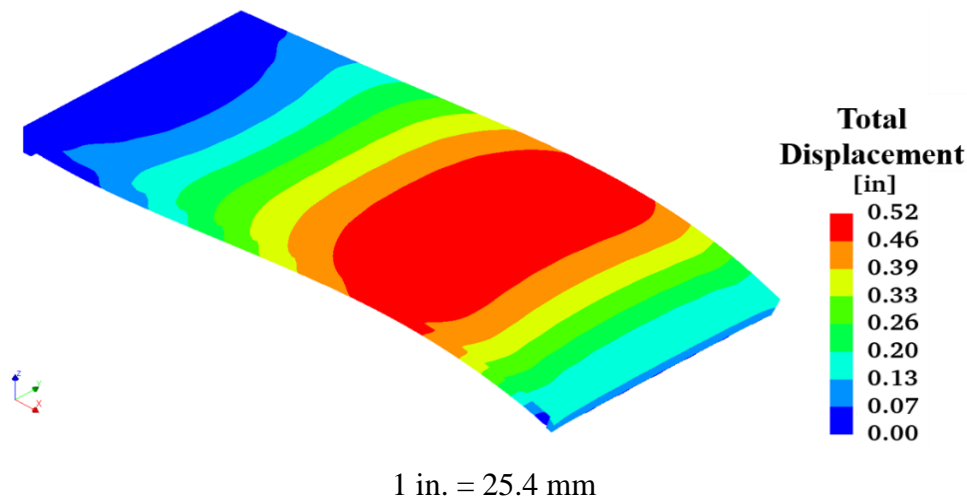


Figure 100 – Total displacement in Straight-FR.

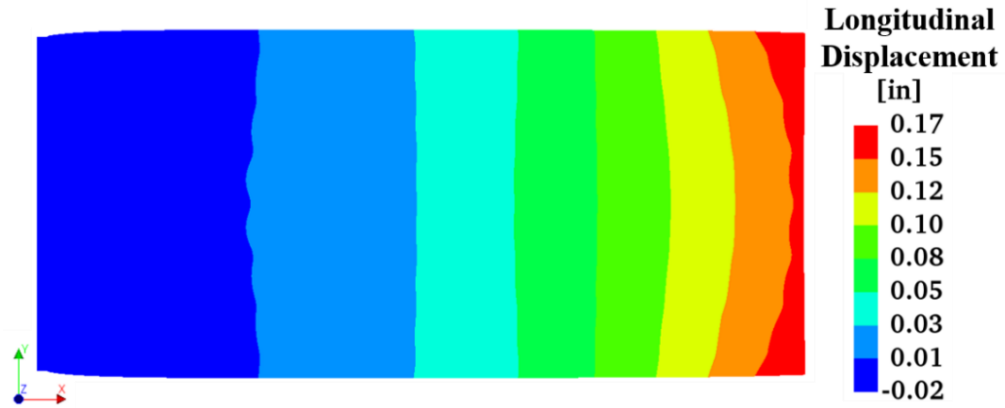


Figure 101 – Longitudinal displacement in Straight-FR.

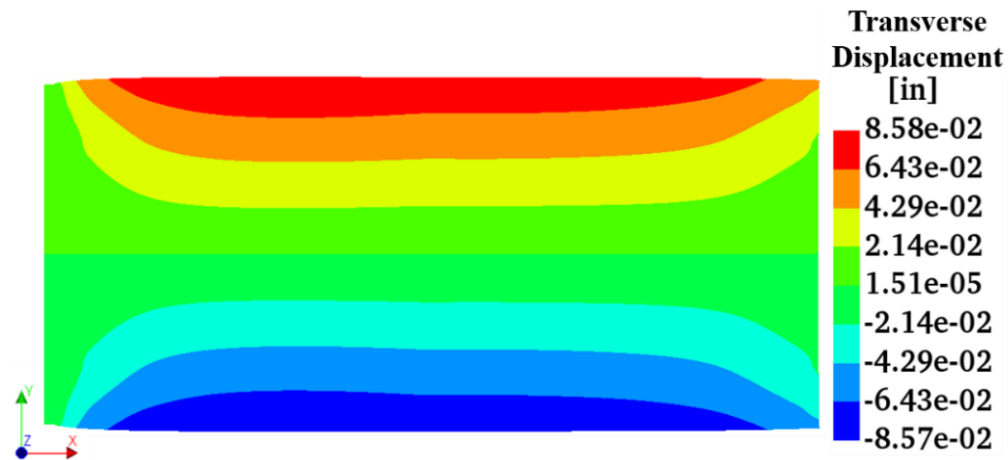
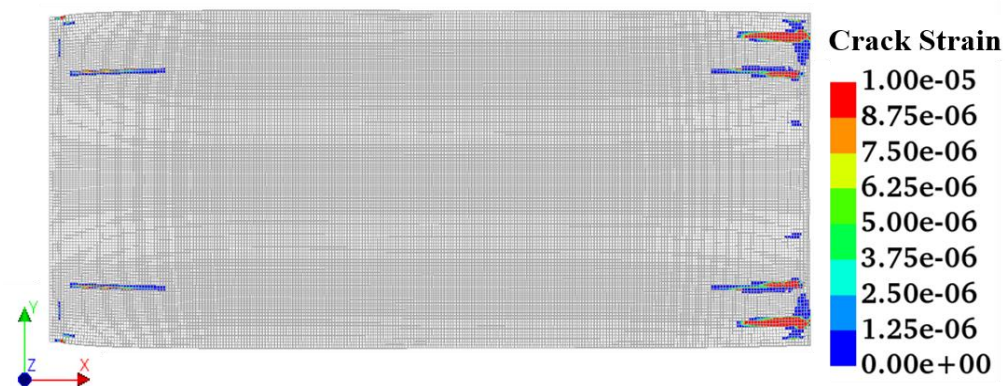


Figure 102 – Transverse displacement in Straight-FR.



Note: Maximum crack strain = 3760 $\mu\epsilon$.

Figure 103 – Top view showing cracked elements in Straight-FR.



Figure 104 – Bottom view showing cracked elements in Straight-FR.



Note: Maximum crack width = 1.12×10^{-2} in. (0.28 mm).

Figure 105 – Top view showing crack widths in Straight-FR.



Note: The crack size is exaggerated for illustration.

Figure 106 – Top view showing crack orientations in Straight-FR.

5.3.1.2 Case 2: Straight-LVR

In this case, the girder ends are restrained in the longitudinal and vertical directions at Intermediate Bent 2 but are free to move in the transverse direction. The total displacement

of the bridge is 0.53 in. (13.46 mm), which is shown in Figure 107. The maximum displacement is located closer to the intermediate bent (i.e., Bent 2). The displacements of the bridge deck in the longitudinal and transverse directions are shown in Figure 108 and Figure 109, respectively.

The top and bottom views of the cracked elements of the deck are shown in Figure 110 and Figure 111, respectively, for a crack strain index of 0 to 10 microstrain. The maximum crack strain for this case is 886 microstrain. Figure 112 shows the crack widths corresponding to the crack strain index shown in Figure 110. The maximum crack width is 4.18×10^{-3} in. (0.11 mm). The crack orientations are shown in Figure 113.

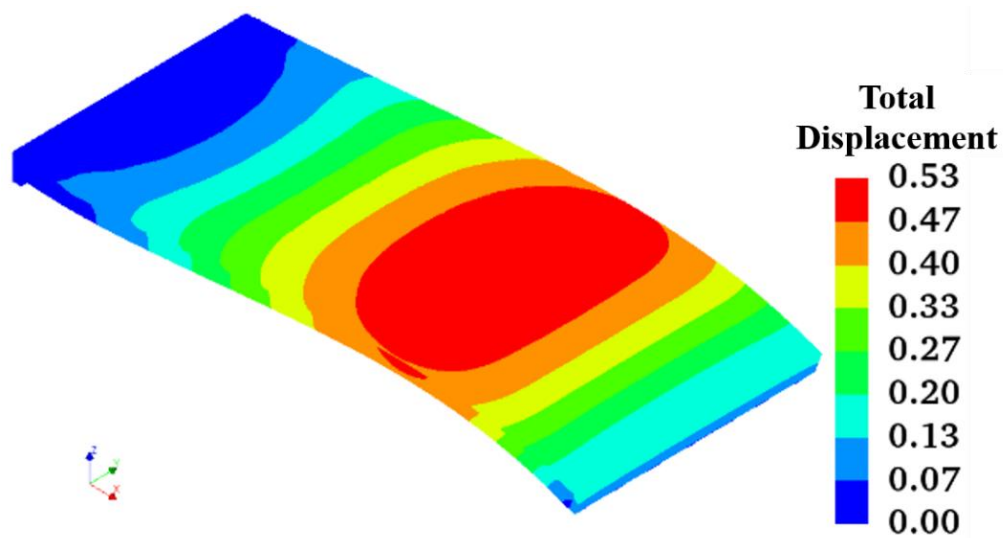


Figure 107 – Total displacement in Straight-LVR.

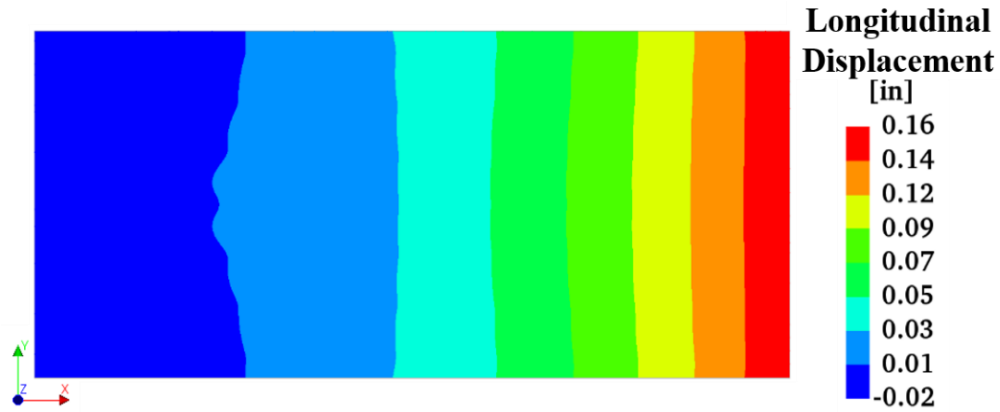


Figure 108 – Longitudinal displacement in Straight-LVR.

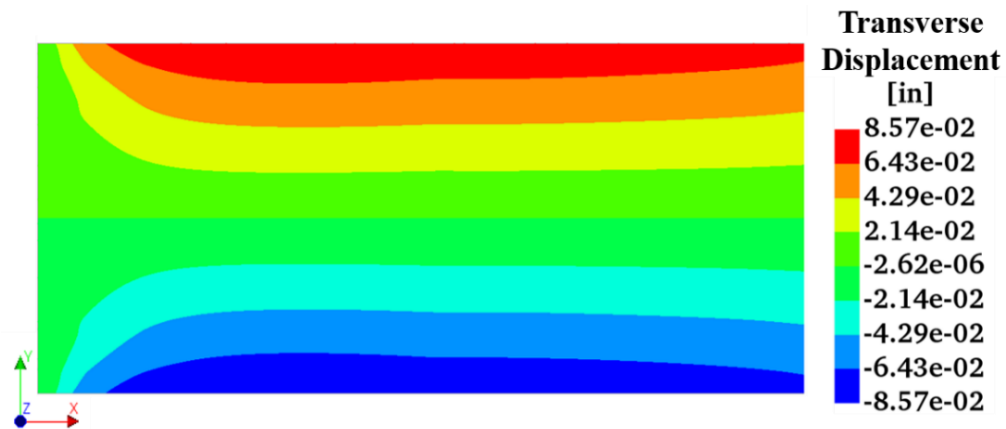
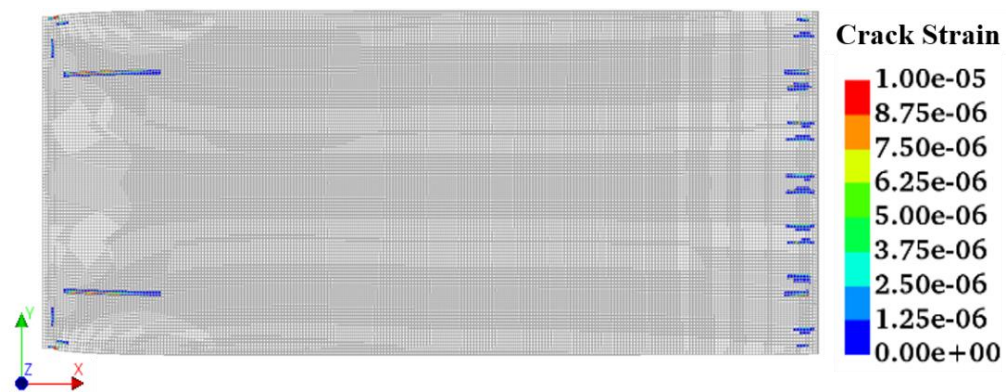


Figure 109 – Transverse displacement in Straight-LVR.



Note: Maximum crack strain = 886 $\mu\epsilon$.

Figure 110 – Top view showing cracked elements in Straight-LVR.

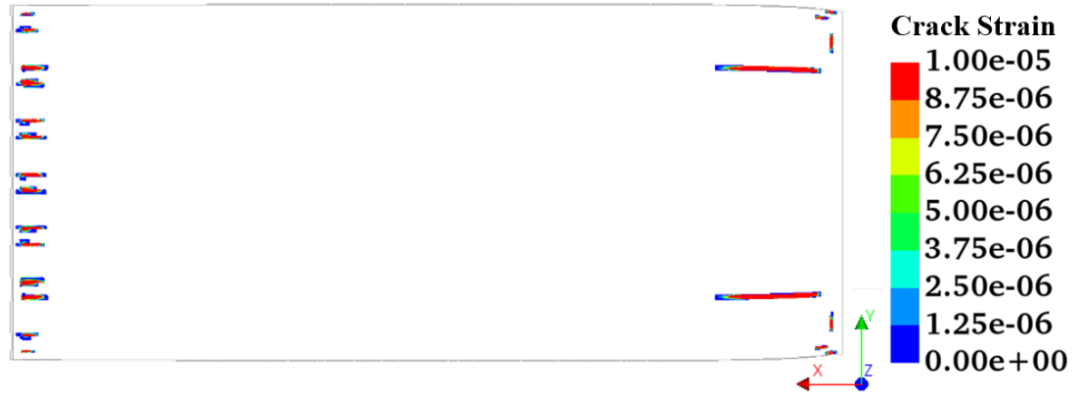
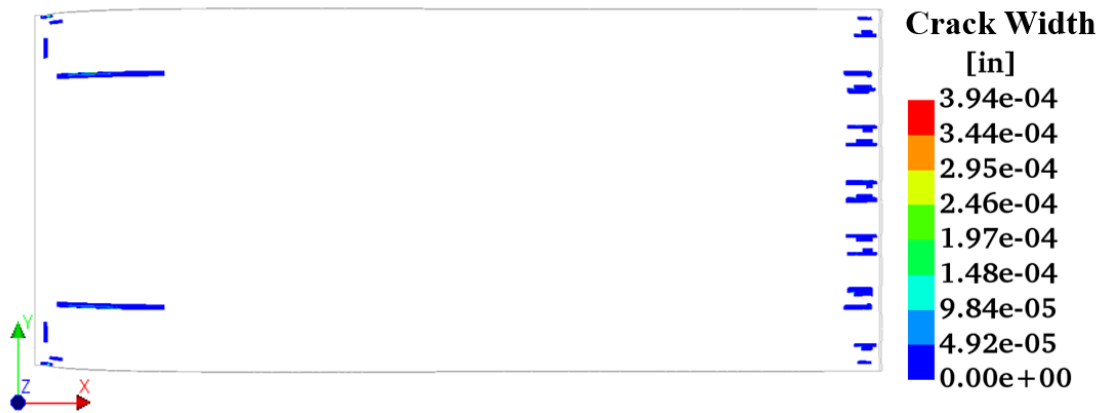


Figure 111 – Bottom view showing cracked elements in Straight-LVR.



Note: Maximum crack width = 4.18×10^{-3} in. (0.11 mm).

Figure 112 – Top view showing crack widths in Straight-LVR.



Note: The crack size is exaggerated for illustration.

Figure 113 – Top view showing crack orientations in Straight-LVR.

5.3.1.3 Case 3: Straight-VR

In this case, the girder ends are restrained in the vertical direction at the intermediate bent and are free to move in the transverse and longitudinal directions. The total displacement of the bridge is shown in Figure 114. The maximum displacement represents the longitudinal movement of the bridge superstructure. Figure 115 and Figure 116 show the longitudinal and transverse displacements of the bridge deck, respectively.

Top and bottom views of the cracked elements with a crack strain index of 0 to 10 microstrain are shown in Figure 117 and Figure 118, respectively. The maximum crack strain is 4530 microstrain, which yields a maximum crack width of 9.29×10^{-3} in. (0.24 mm), as shown in Figure 119. The crack orientations are shown in Figure 120.

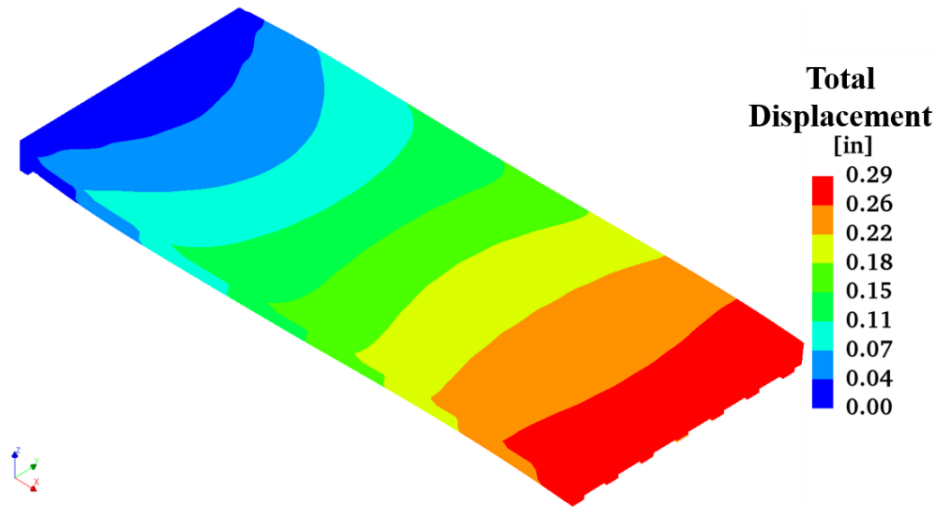


Figure 114 – Total displacement in Straight-VR.

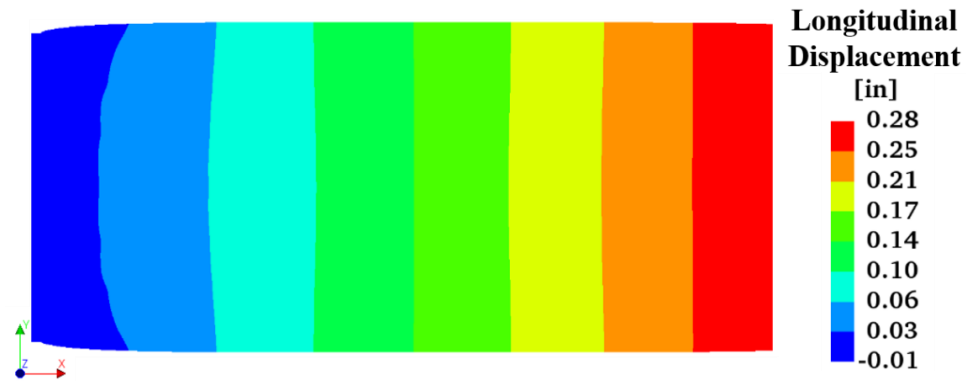


Figure 115 – Longitudinal displacement in Straight-VR.

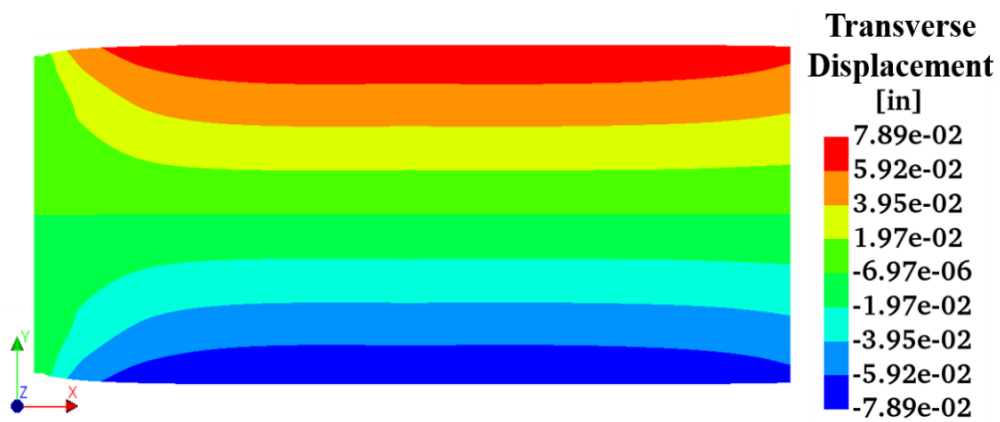
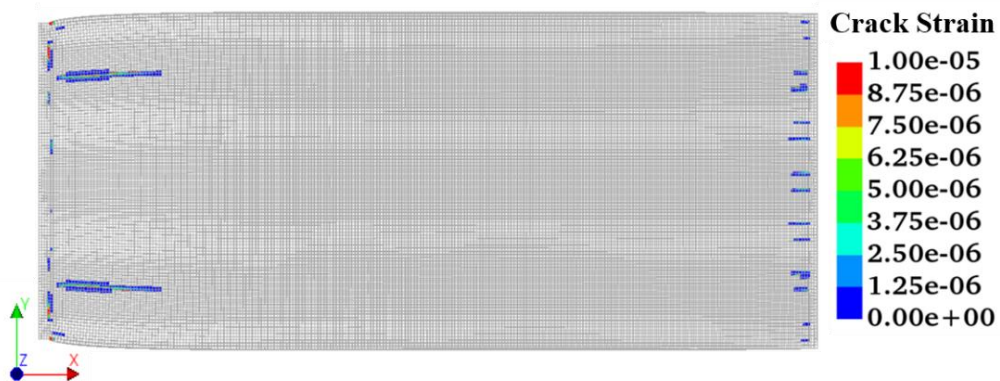


Figure 116 – Transverse displacement in Straight-VR.

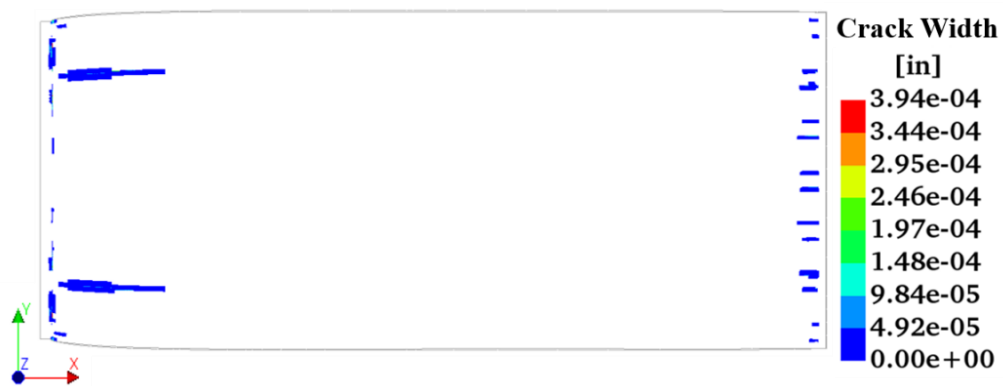


Note: Maximum crack strain = 4530 $\mu\epsilon$.

Figure 117 – Top view showing cracked elements in Straight-VR.



Figure 118 – Bottom view showing cracked elements in Straight-VR.



Note: Maximum crack width = 9.29×10^{-3} in. (0.24 mm).

Figure 119 – Top view showing crack widths in Straight-VR.



Note: The crack size is exaggerated for illustration.

Figure 120 – Top view showing crack orientations in Straight-VR.

5.3.2 Inclined Bridge Deck

Similar to the straight deck cases, the bridge model with an inclined bridge deck geometry is analyzed for three boundary conditions.

5.3.2.1 Case 4: Inclined-FR

The girder ends beneath an inclined deck slab are fully restrained at the intermediate bent and are prohibited from moving in longitudinal, transverse, and vertical directions. The maximum displacement is 0.50 in. (12.70 mm), as shown in Figure 121. The maximum longitudinal displacement is toward the edge of the inclined deck at Bent 2 (see Figure 122). The maximum transverse displacement occurs along the free longitudinal edges of the deck (see Figure 123).

The maximum crack strain in the fully restrained inclined deck is 1500 microstrain, and the maximum crack width is 7.16×10^{-3} in. (0.18 mm). Figure 124 and Figure 125 show the top and bottom views of the crack strains, respectively, with a crack strain index ranging from 0 to 10 microstrain. Figure 126 shows the crack widths corresponding to the crack strain index shown in Figure 124. Figure 127 shows the crack orientations.

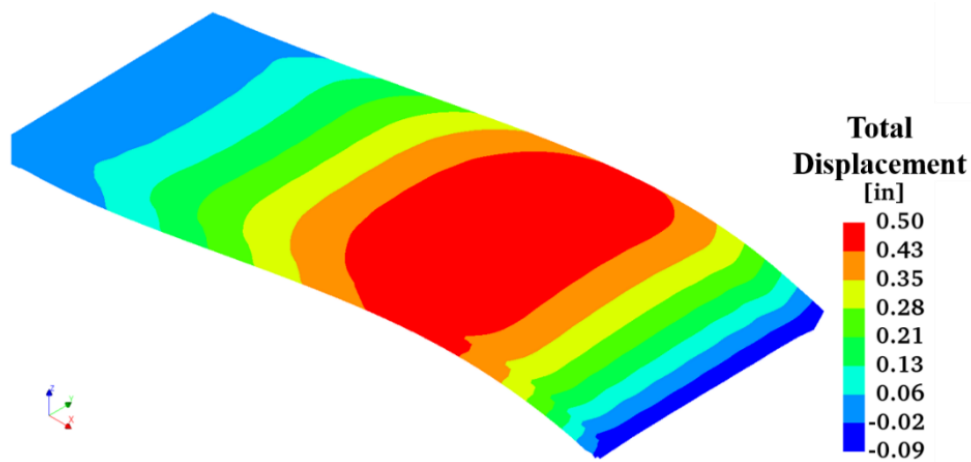


Figure 121 – Total displacement in Inclined-FR.

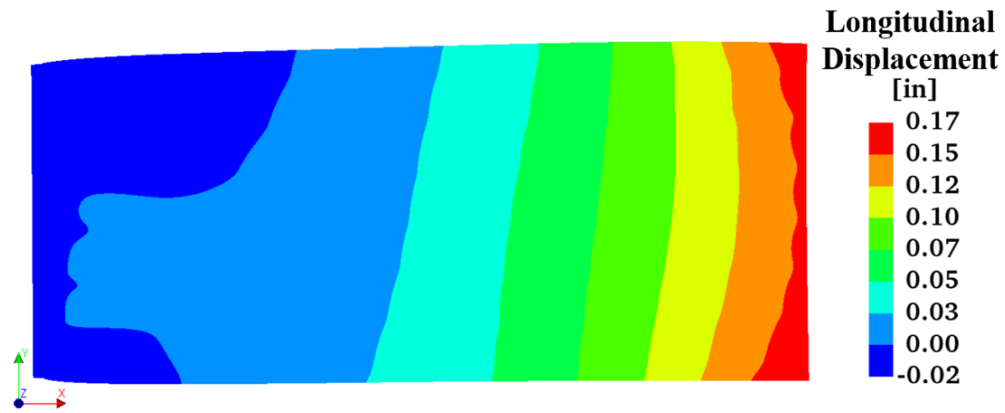


Figure 122 – Longitudinal displacement in Inclined-FR.

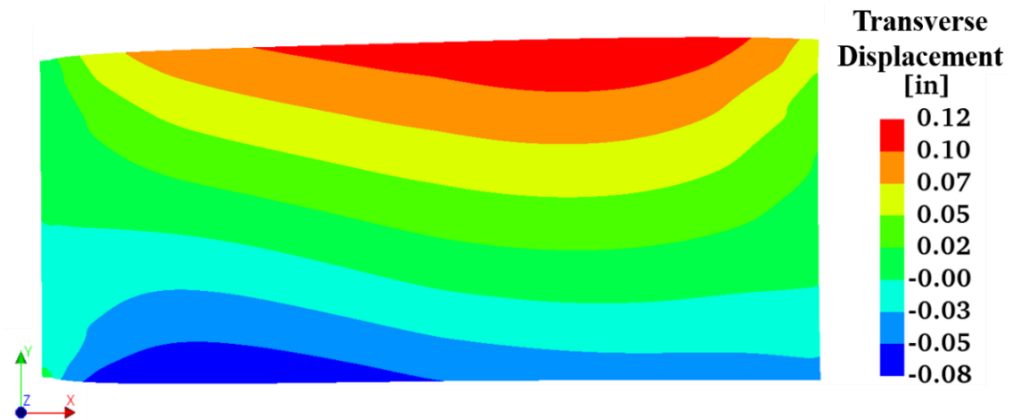
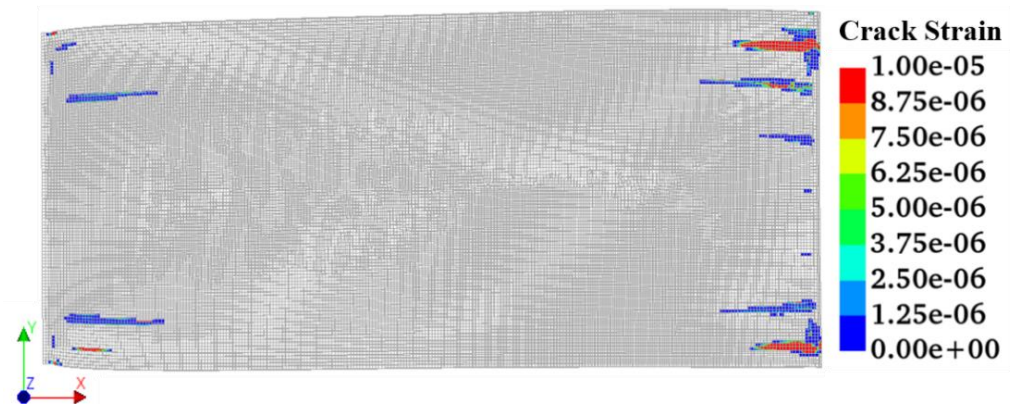


Figure 123 – Transverse displacement in Inclined-FR.

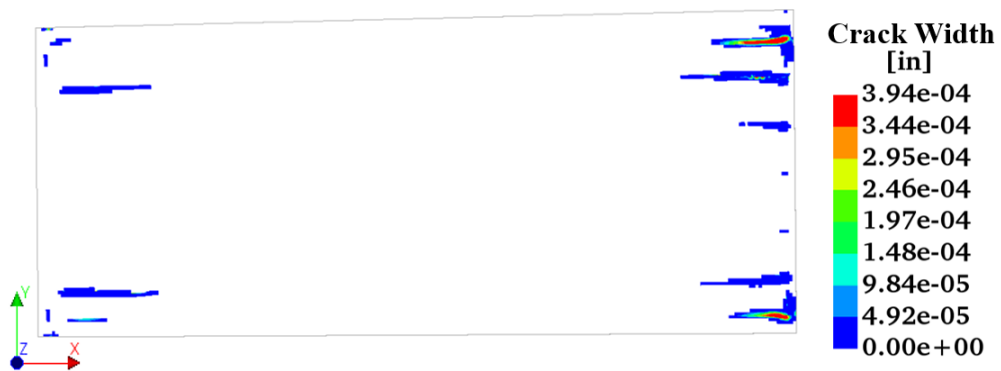


Note: Maximum crack strain = 1500 $\mu\epsilon$.

Figure 124 – Top view showing cracked elements in Inclined-FR.



Figure 125 – Bottom view showing cracked elements in Inclined-FR.



Note: Maximum crack width = 7.16×10^{-3} in. (0.18 mm).

Figure 126 – Top view showing crack widths in Inclined-FR.



Note: The crack size is exaggerated for illustration.

Figure 127 – Top view showing crack orientations in Inclined-FR.

5.3.2.2 Case 5: Inclined-LVR

The girder ends are restrained from longitudinal and vertical movements; the superstructure is allowed to move and expand in the transverse direction. The maximum total displacement of the superstructure is 0.57 in. (14.48 mm), as shown in Figure 128. The maximum longitudinal displacement occurs at the highest point, at the bottom right corner of the deck. Transverse displacement, meanwhile, peaks at the second highest point, at the top right corner of the deck. Figure 129 and Figure 130 show the longitudinal and transverse displacements in inclined-LVR bridge deck.

The maximum crack strain is 1150 microstrain with a maximum crack width of 5.38×10^{-3} in. (0.14 mm). Figure 131 and Figure 132 show the top and bottom views of the cracked elements, respectively, and Figure 133 shows the crack widths for a crack strain index of 0 to 10 microstrain. The crack orientations are shown in Figure 134.

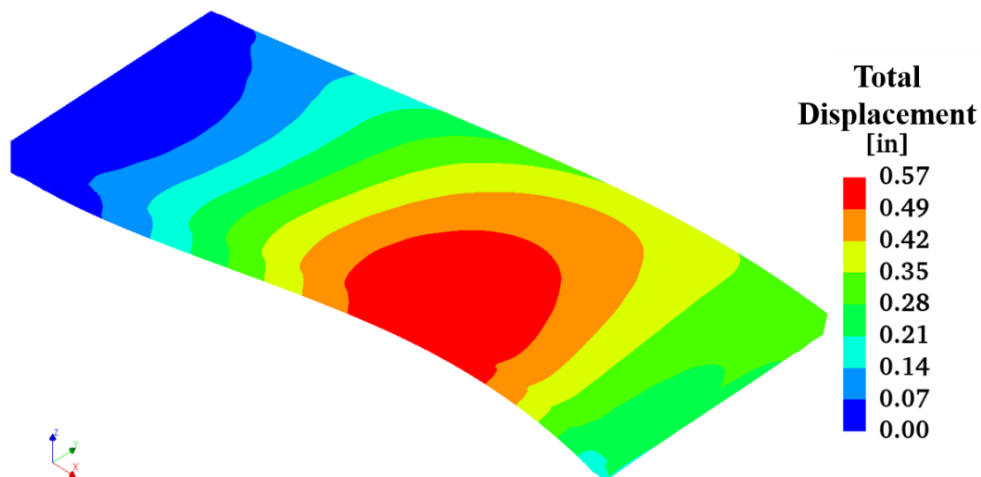


Figure 128 – Total displacement in Inclined-LVR.

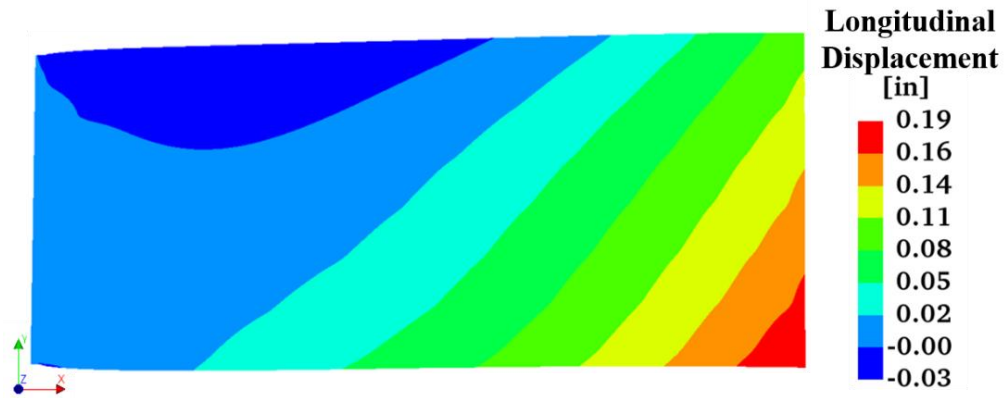


Figure 129 – Longitudinal displacement in Inclined-LVR.

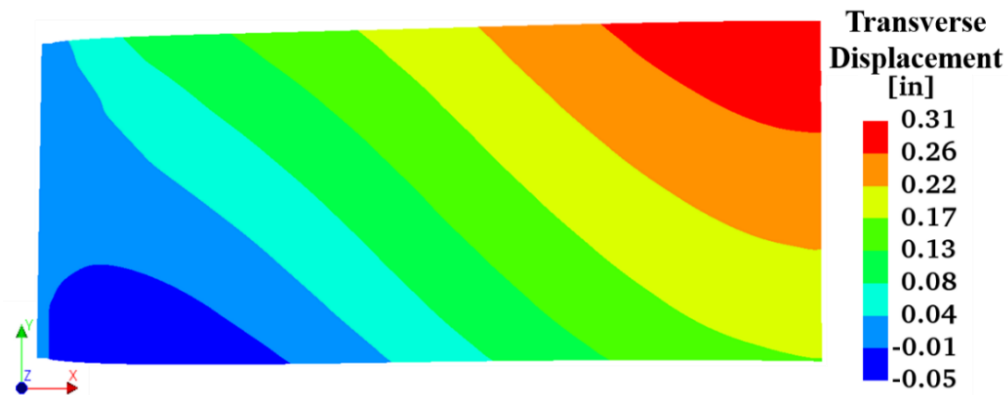
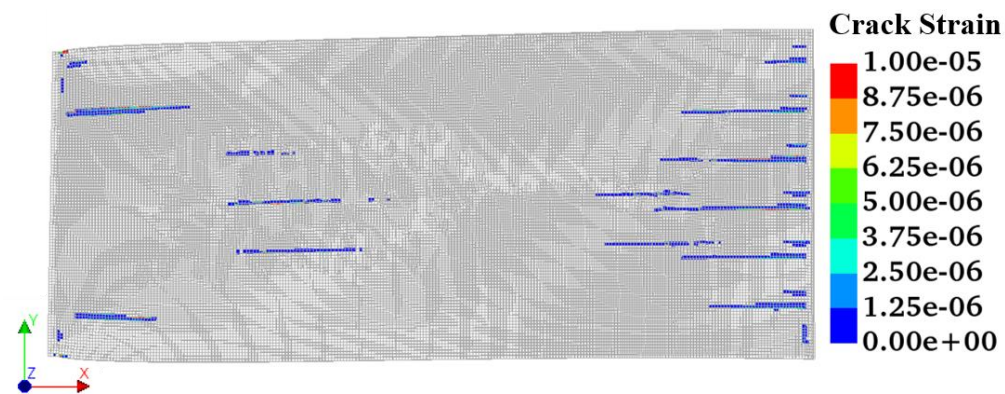


Figure 130 – Transverse displacement in Inclined-LVR.



Note: Maximum crack strain = 1150 $\mu\epsilon$.

Figure 131 – Top view showing cracked elements in Inclined-LVR.

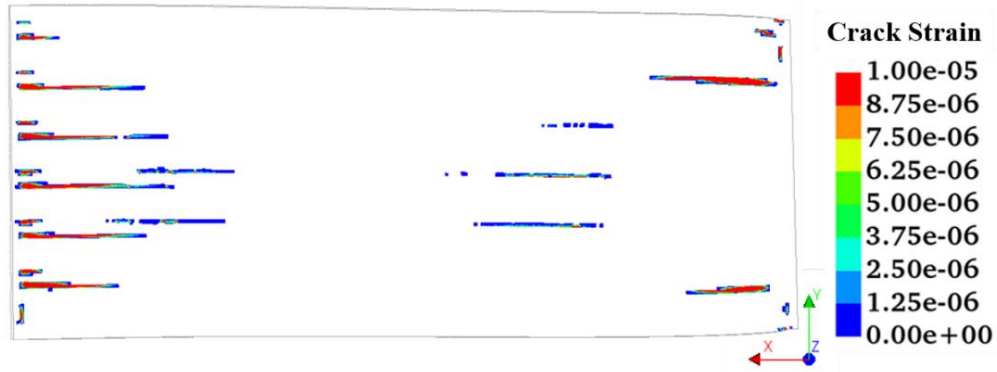
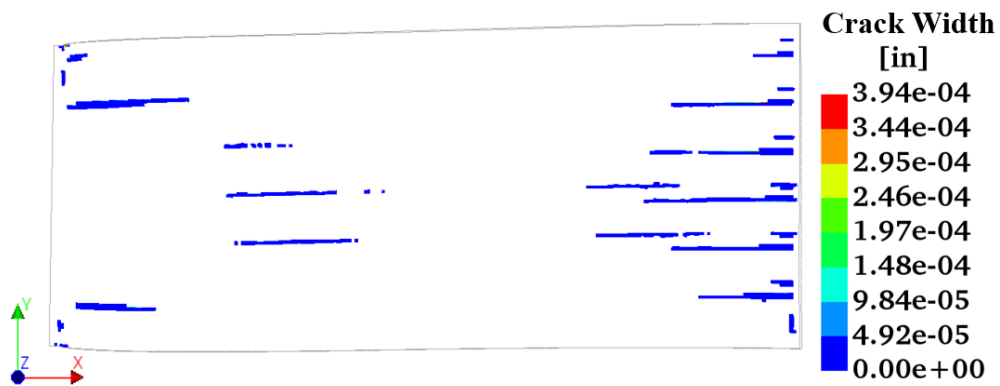
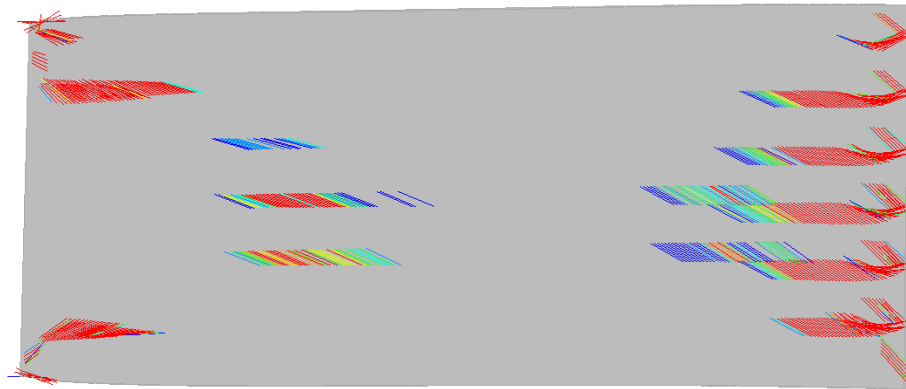


Figure 132 – Bottom view showing cracked elements in Inclined-LVR.



Note: Maximum crack width = 5.38×10^{-3} in. (0.14 mm).

Figure 133 – Top view showing crack widths in Inclined-LVR.



Note: The crack size is exaggerated for illustration.

Figure 134 – Top view showing crack orientations in Inclined-LVR.

5.3.2.3 Case 6: Inclined-VR

The girder ends at Bent 2 are restrained in the vertical direction and are free to displace in the longitudinal and transverse directions. The maximum total displacement is 0.30 in. (7.62 mm), which is shown in Figure 135. The longitudinal and transverse displacements are shown in Figure 136 and Figure 137, respectively.

The maximum crack strain is 668 microstrain and yields a maximum crack width of 3.19×10^{-3} in. (0.08 mm). The cracked elements of the top and bottom deck surfaces are presented in Figure 138 and Figure 139, respectively. Crack widths for a crack strain index of 0 to 10 microstrain are shown in Figure 140. Finally, crack orientations are shown in Figure 141.

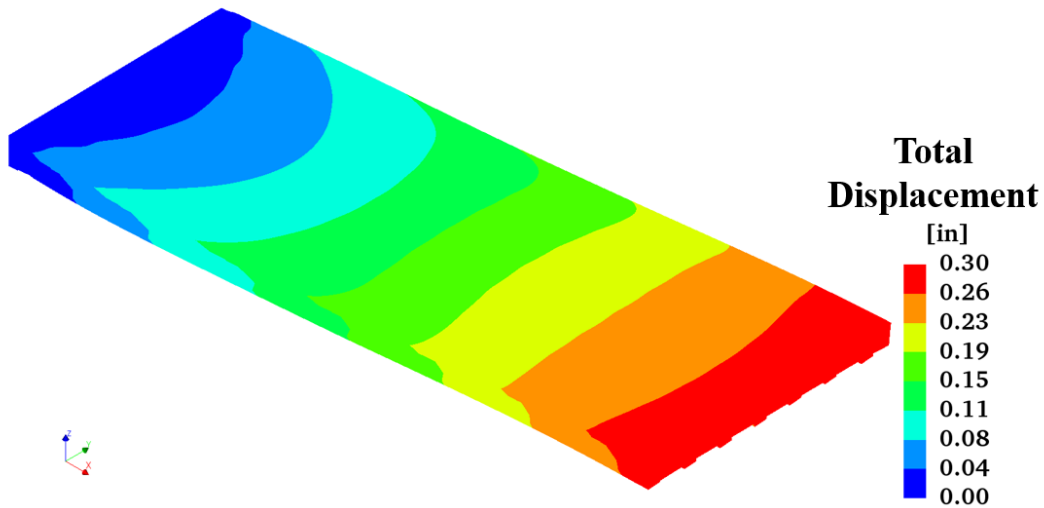


Figure 135 – Total displacement in Inclined-VR.

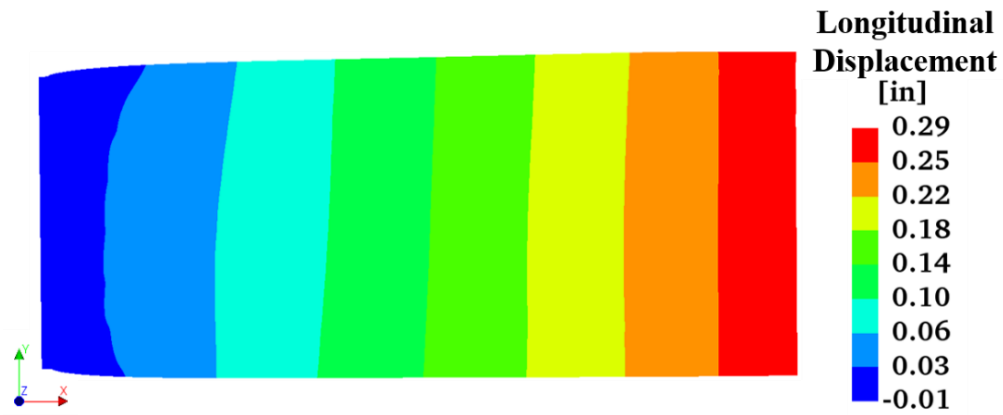


Figure 136 – Longitudinal displacement in Inclined-VR.

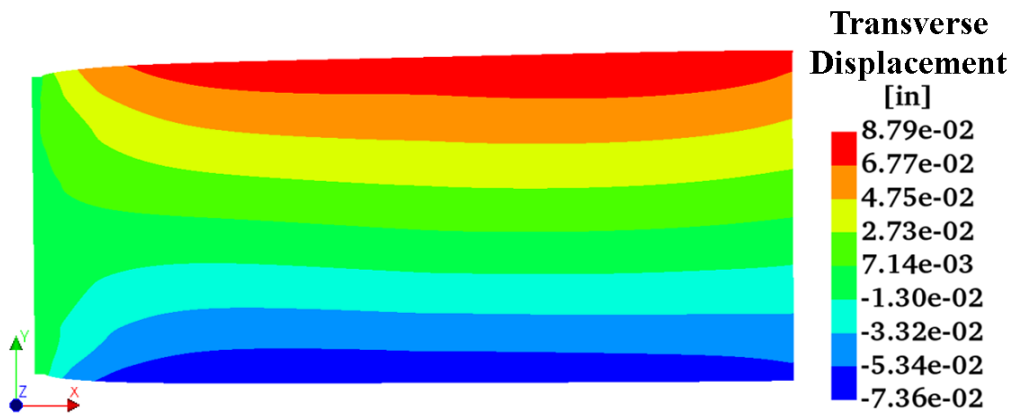
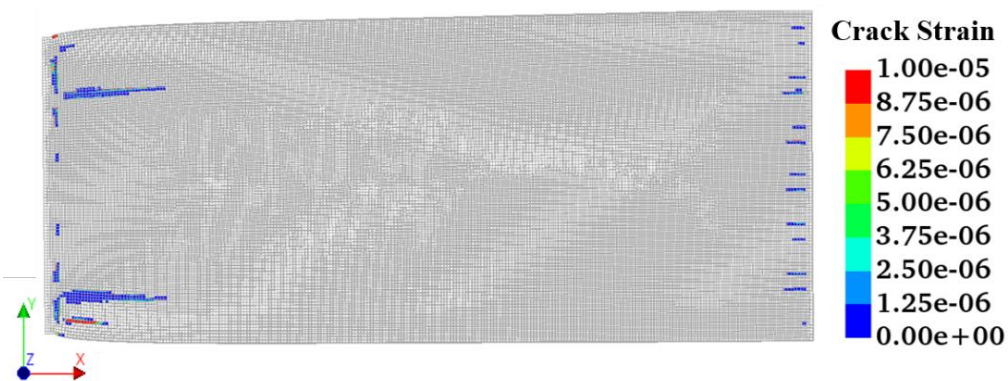


Figure 137 – Transverse displacement in Inclined-VR.



Note: Maximum crack strain = 668 $\mu\epsilon$.

Figure 138 – Top view showing cracked elements in Inclined-VR.

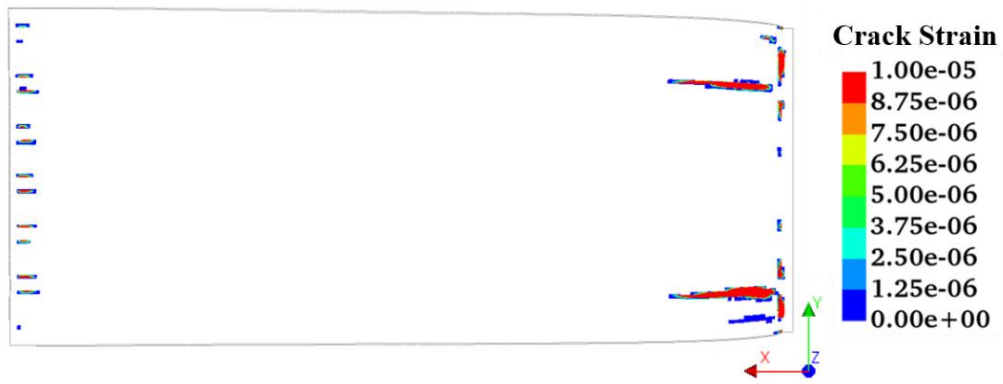


Figure 139 – Bottom view showing cracked elements in Inclined-VR.



Note: Maximum crack width = 3.19×10^{-3} in (0.08 mm).

Figure 140 – Top view showing crack widths in Inclined-VR.



Note: The crack size is exaggerated for illustration.

Figure 141 – Top view showing crack orientations in Inclined-VR.

5.3.3 Skewed and Curved Bridge Deck

The skewed and curved bridge deck model represents the Span 1 geometry of the SR299 bridge and is analyzed for three boundary conditions consistent with Sections 5.3.1 and 5.3.2.

5.3.3.1 Case 7: Skewed & Curved-FR

The girder ends beneath a skewed and curved concrete slab are restrained in the longitudinal, transverse, and vertical directions. The maximum total displacement is 0.50 in. (12.70 mm), as shown in Figure 142. The longitudinal and transverse displacements are shown in Figure 143 and Figure 144, respectively. The maximum longitudinal displacement occurs at the corners of Span 1 at Bent 2 whereas the maximum transverse displacement is observed along the longitudinal edges of the deck. This is anticipated because the concrete slab edges are not restrained from thermal movements. Furthermore, as evident in Figure 144, the transverse displacement along the bottom edge is greater than the displacement along the top edge. This is also reasonable because the radius of the curvature is greater at the bottom edge. Finally, Figure 144 indicates that relatively trivial transverse displacements occur at the acute corners.

Figure 145 and Figure 146 show cracked elements for crack strain indices between 0 and 10 on the top and bottom surfaces, respectively. Corresponding crack widths are shown in Figure 147. The maximum crack strain is 3590 microstrain, and the maximum crack width is 1.14×10^{-2} in. (0.29 mm). Figure 148 shows the crack orientations.

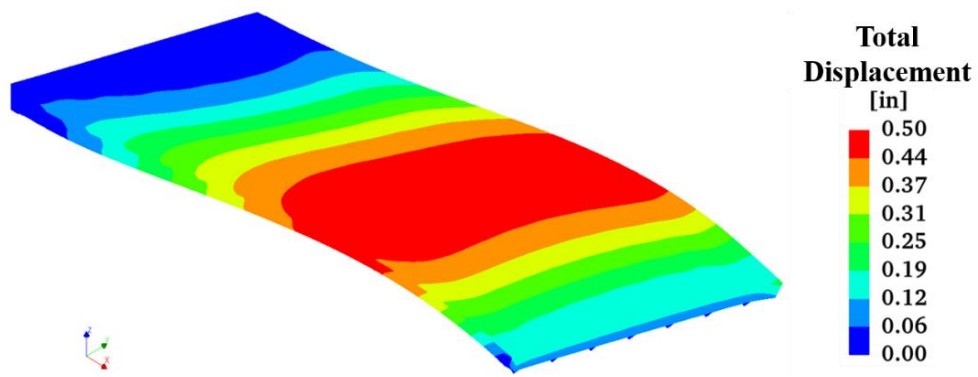


Figure 142 – Total displacement in Skewed & Curved-FR.

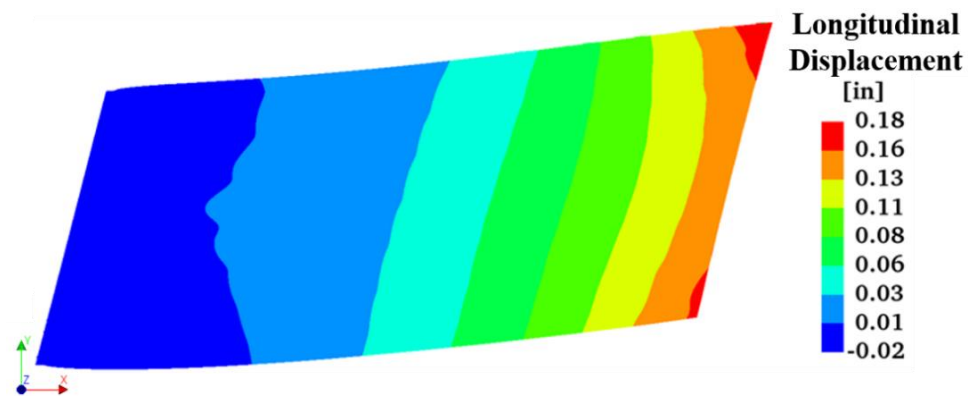


Figure 143 – Longitudinal displacement in Skewed & Curved-FR.

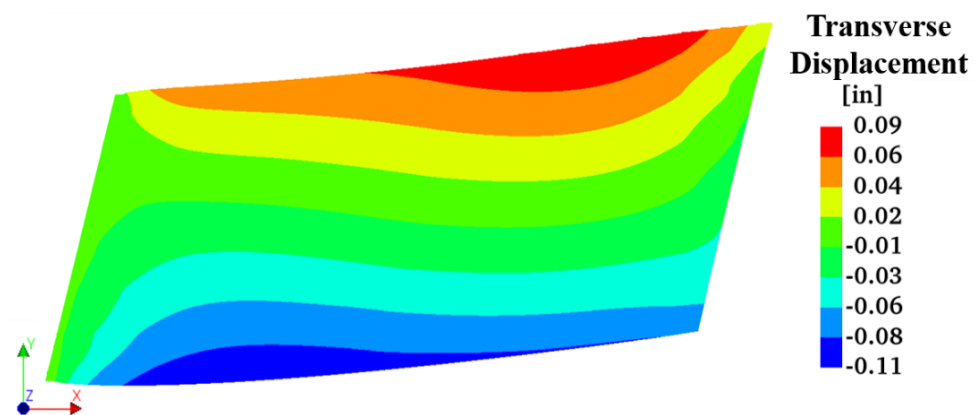
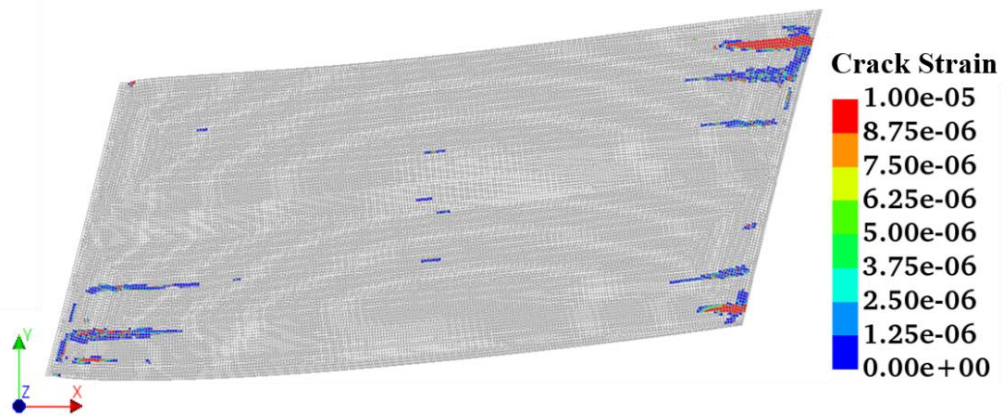


Figure 144 – Transverse displacement in Skewed & Curved-FR.



Note: Maximum crack strain = 3590 $\mu\epsilon$.

Figure 145 – Top view showing cracked elements in Skewed & Curved-FR.

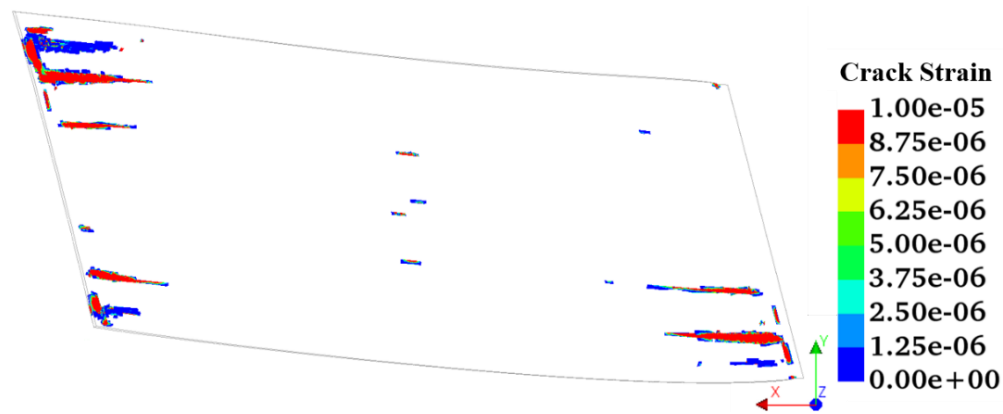
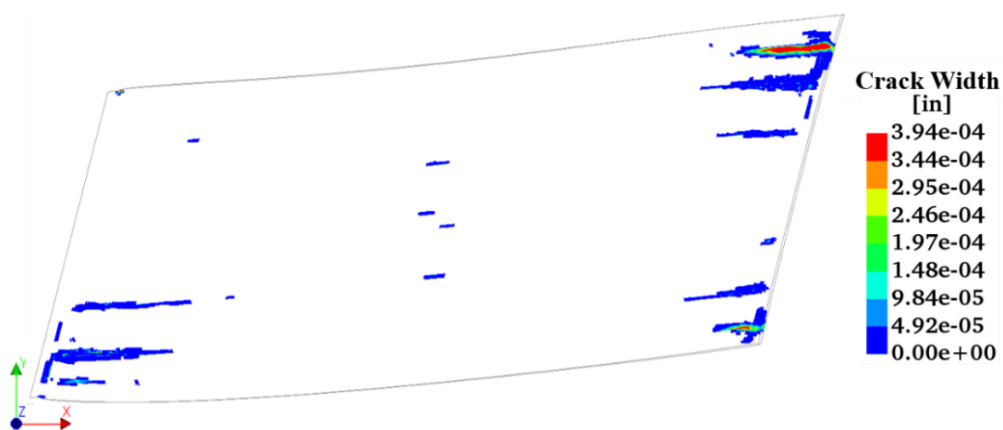
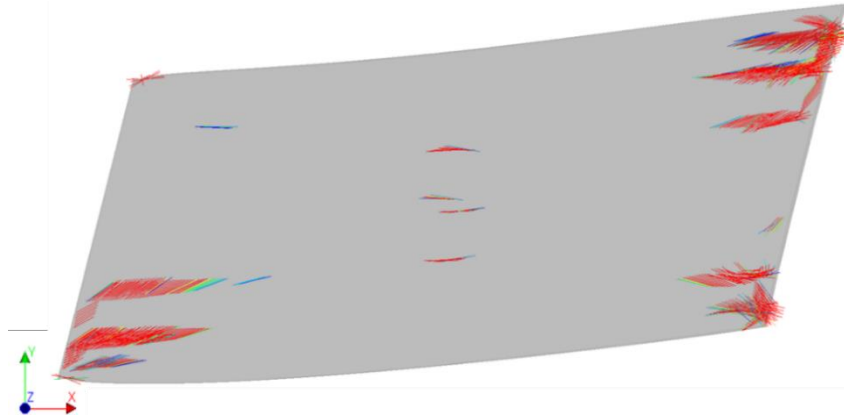


Figure 146 – Bottom view showing cracked elements in Skewed & Curved-FR.



Note: Maximum crack width = 1.14×10^{-2} in. (0.29 mm).

Figure 147 – Top view showing crack widths in Skewed & Curved-FR.



Note: The crack size is exaggerated for illustration.

Figure 148 – Top view showing crack orientations in Skewed & Curved-FR.

5.3.3.2 Case 8: Skewed & Curved-LVR

When girder ends are restrained from longitudinal and vertical movements, a maximum displacement of 0.60 in. (15.24 mm) is predicted, as shown in Figure 149. This includes the effect of cracking. The longitudinal and transverse displacements are greatest at the Bent 2 corners, as shown in Figure 150 and Figure 151, respectively.

The maximum crack strain is 2620 microstrain, and the maximum crack width is 1.30×10^{-2} in. (0.33 mm). Figure 152 and Figure 153 show the cracked elements on the top and bottom surfaces, respectively. Figure 154 shows the crack widths, and Figure 155 illustrates the crack orientations.

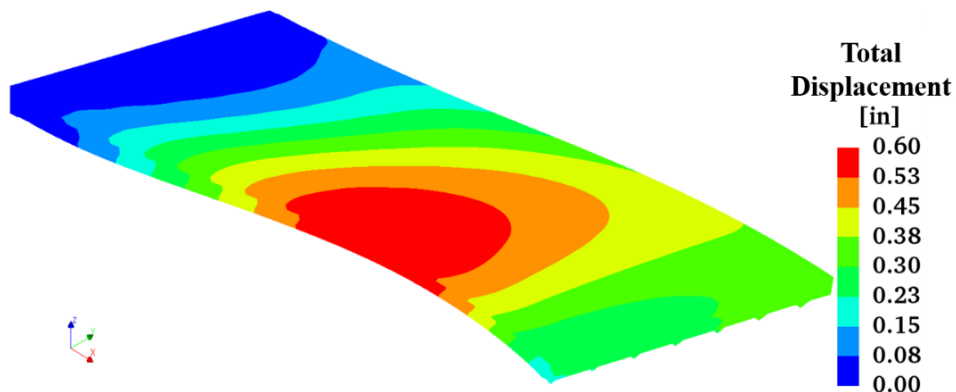


Figure 149 – Total displacement in Skewed & Curved-LVR.

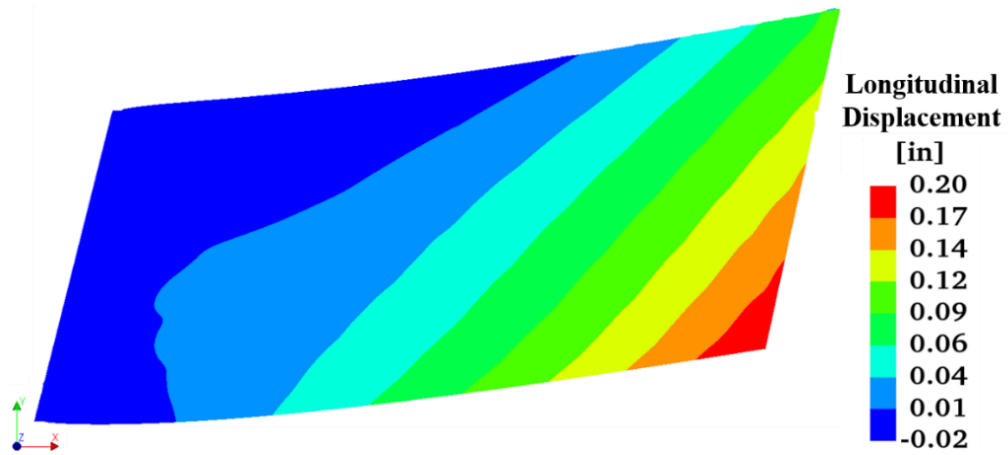


Figure 150 – Longitudinal displacement in Skewed & Curved-LVR.

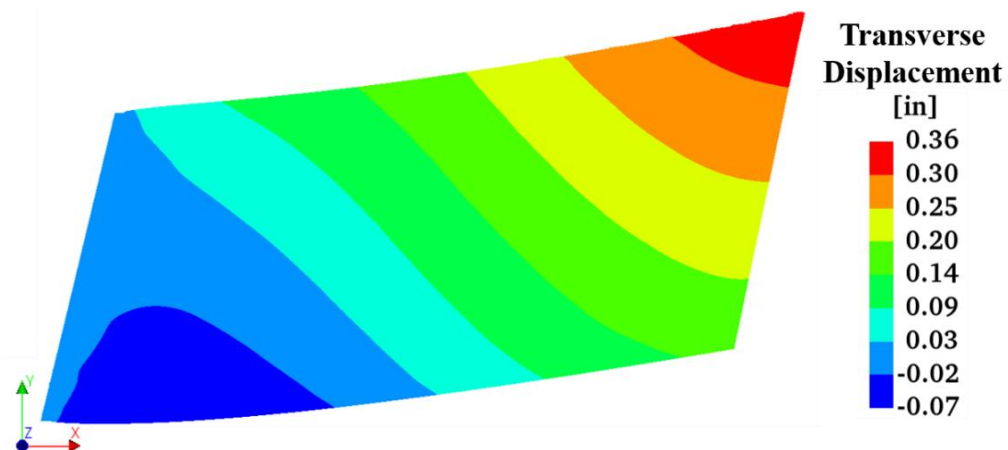
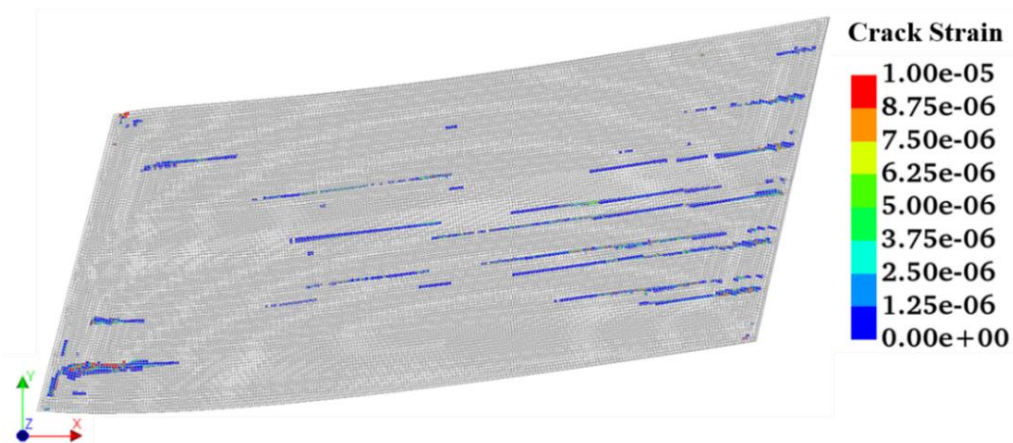


Figure 151 – Transverse displacement in Skewed & Curved-LVR.



Note: Maximum crack strain = 2620 $\mu\epsilon$.

Figure 152 – Top view showing cracked elements in Skewed & Curved-LVR.

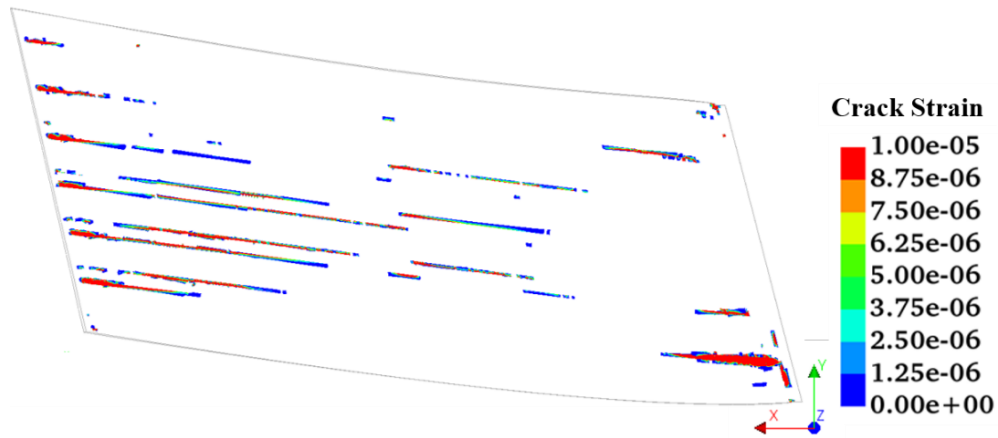
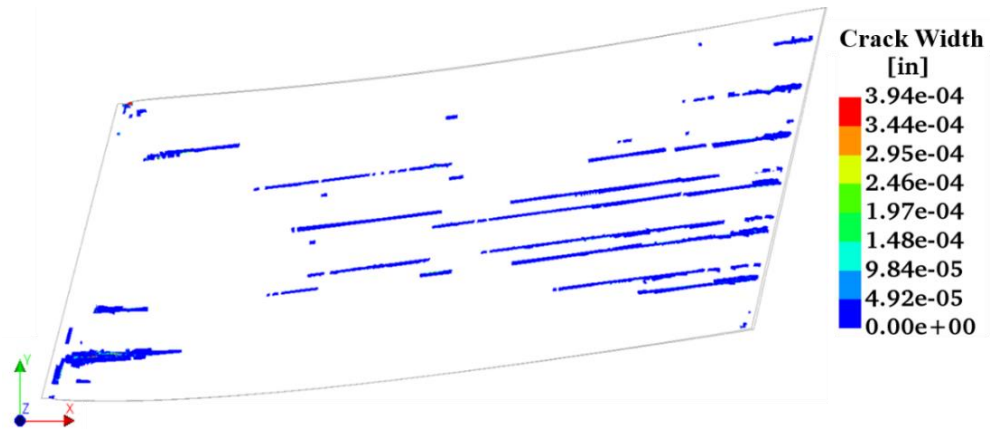
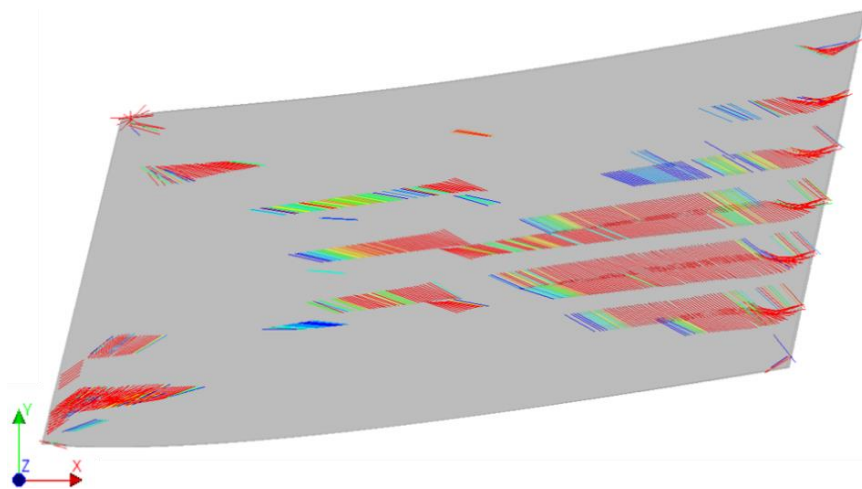


Figure 153 – Bottom view showing cracked elements in Skewed & Curved-LVR.



Note: Maximum crack width = 1.30×10^{-2} in. (0.33 mm).

Figure 154 – Top view showing crack widths in Skewed & Curved-LVR.



Note: The crack size is exaggerated for illustration.

Figure 155 – Top view showing crack orientations in Skewed & Curved-LVR.

5.3.3.3 Case 9: Skewed & Curved-VR

When the girder ends are restrained only in the vertical direction at Bent 2, the maximum total displacement is 0.32 in. (8.13 mm), as shown in Figure 156. The maximum longitudinal displacement occurs at Bent 2 (see Figure 157). Figure 158 shows the maximum transverse displacement, which occurs at the top right corner.

The maximum crack strain and maximum crack width are 3940 microstrain and 9.66×10^{-3} in. (0.25 mm), respectively. The top and bottom views of the cracked elements are shown in Figure 159 and Figure 160, respectively, for crack strain indices of 0 to 10 microstrain. Crack widths are shown in Figure 161. Figure 162 shows the orientation of the cracks.

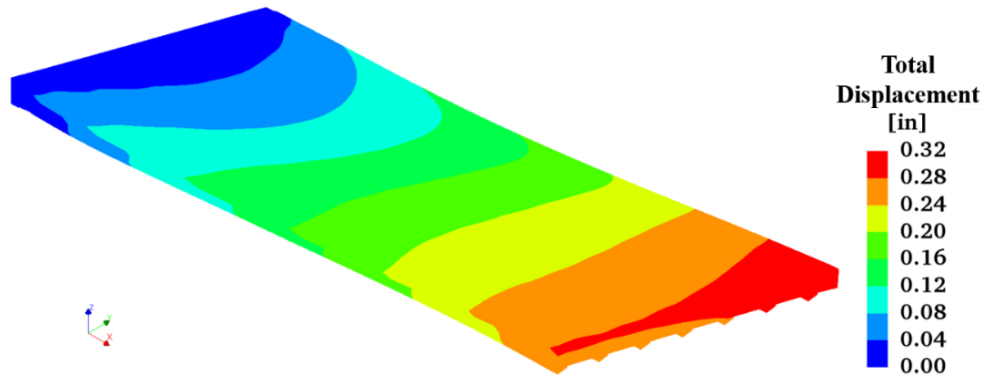


Figure 156 – Total displacement in Skewed & Curved-VR.

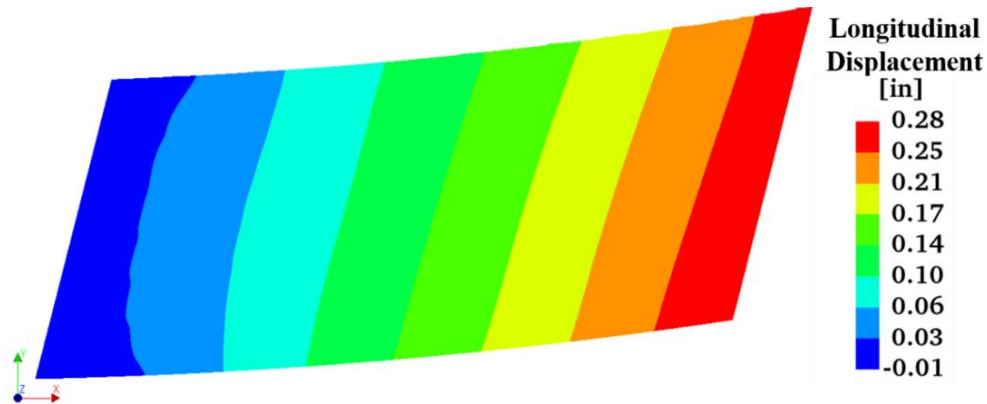


Figure 157 – Longitudinal displacement in Skewed & Curved-VR.

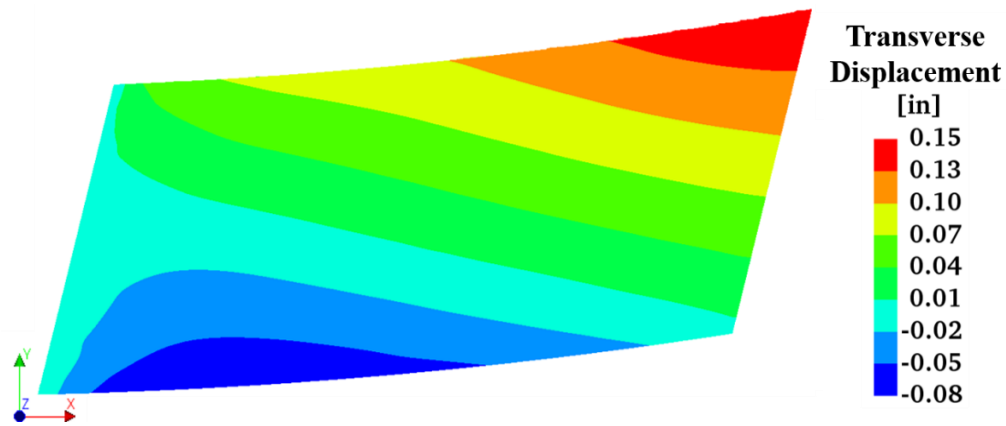
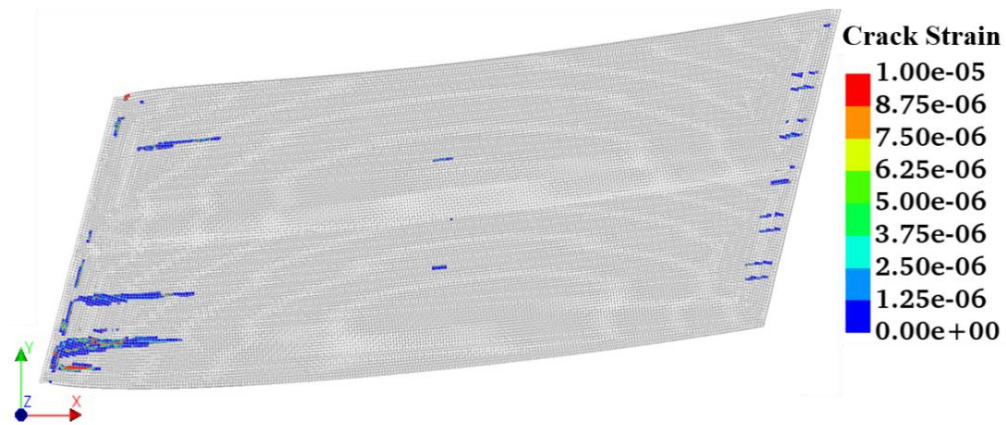


Figure 158 – Transverse displacement in Skewed & Curved-VR.



Note: Maximum crack strain = 3940 $\mu\epsilon$.

Figure 159 – Top view showing cracked elements in Skewed & Curved-VR.

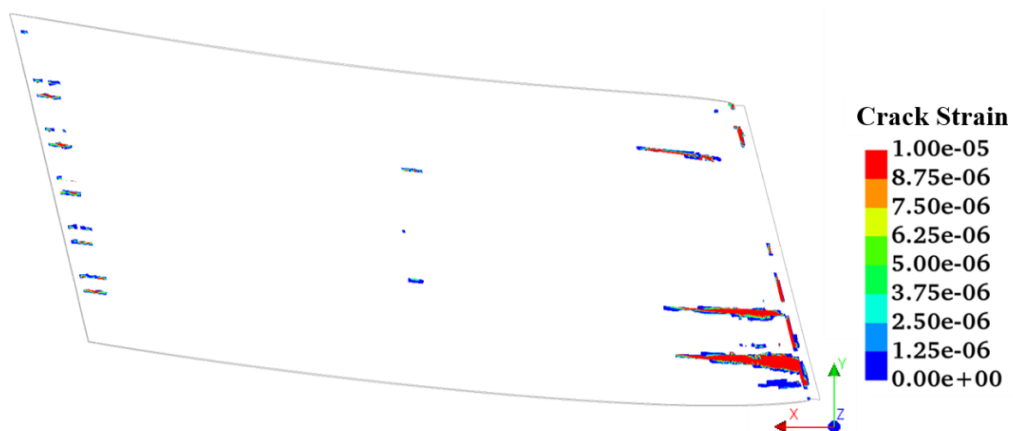
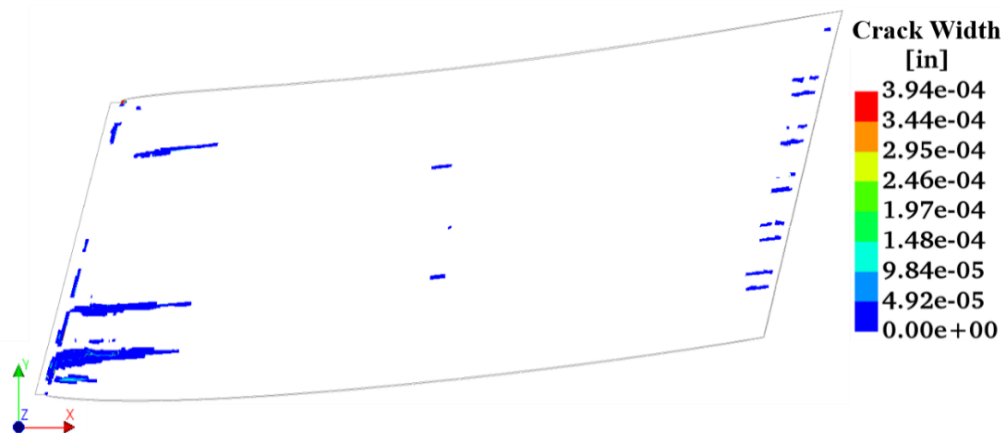
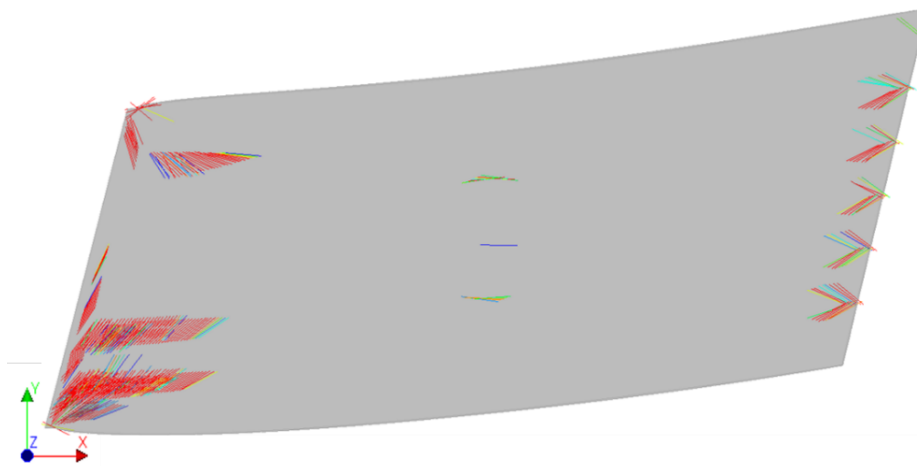


Figure 160 – Bottom view showing cracked elements in Skewed & Curved-VR.



Note: Maximum crack width = 9.66×10^{-3} in. (0.25 mm).

Figure 161 – Top view showing crack widths in Skewed & Curved-VR.



Note: The crack size is exaggerated for illustration.

Figure 162 – Top view showing crack orientations in Skewed & Curved-VR.

5.3.4 Highly Skewed Bridge Deck Geometry

This section includes the results of Span 2 analysis cases for the SR299 bridge. Span 2 is comprised of a highly skewed deck geometry with a skew angle exceeding 25 degrees at the abutment location. Here, the boundary conditions in Span 2 mirror the boundary conditions in Span 1 on opposite ends. That is, the right end is restrained from thermal movement due to the presence of an abutment.

5.3.4.1 Case 10: Highly Skewed-FR

When girders under a highly skewed deck slab are restrained in longitudinal, transverse, and vertical directions at Bent 2, the maximum total displacement in the deck is 0.47 in. (11.94 mm), as shown in Figure 163. Maximum longitudinal displacement of 0.17 in. (4.32 mm) is observed in the corners of the deck at Bent 2 (see Figure 164). Maximum transverse displacement of 0.13 in. (3.30 mm) occurs along the internal curved edge of the bridge deck (see Figure 165).

Figure 166 and Figure 167 show cracked elements for crack strain indices of 0 to 10 microstrain on the top and bottom surfaces, respectively. Corresponding crack widths are shown in Figure 168. The maximum crack strain is 7990 microstrain, and the maximum crack width is 1.07×10^{-2} in. (0.27 mm). Figure 169 shows the crack orientations.

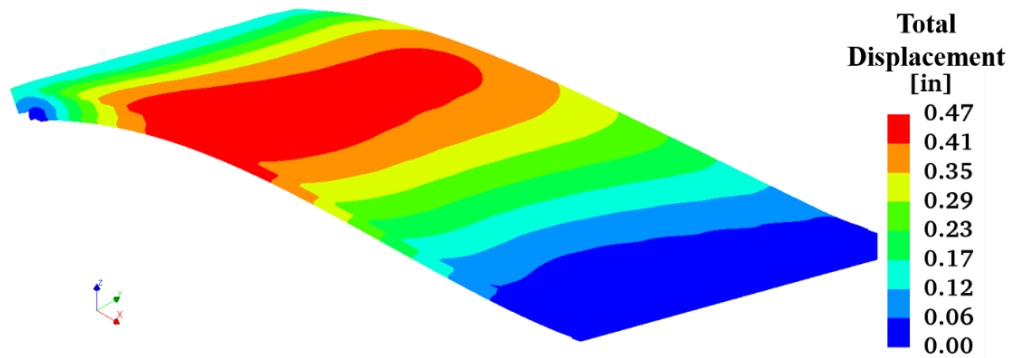


Figure 163 – Total displacement in Highly Skewed-FR.

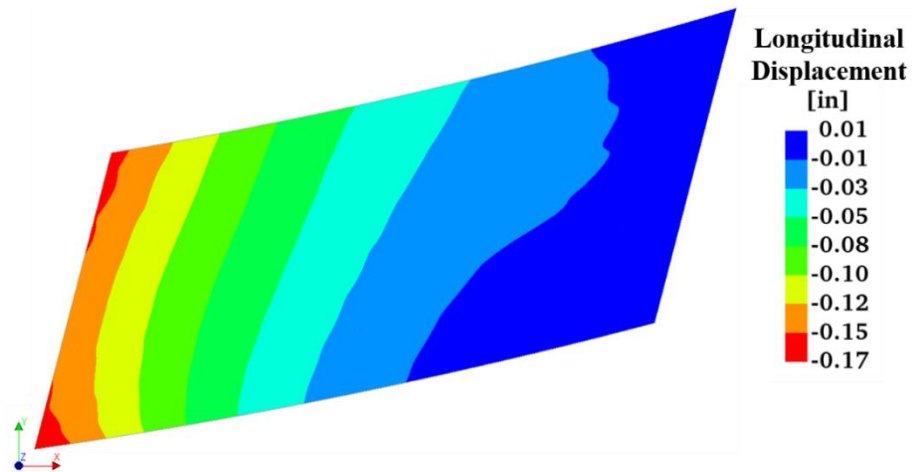


Figure 164 – Longitudinal displacement in Highly Skewed-FR.

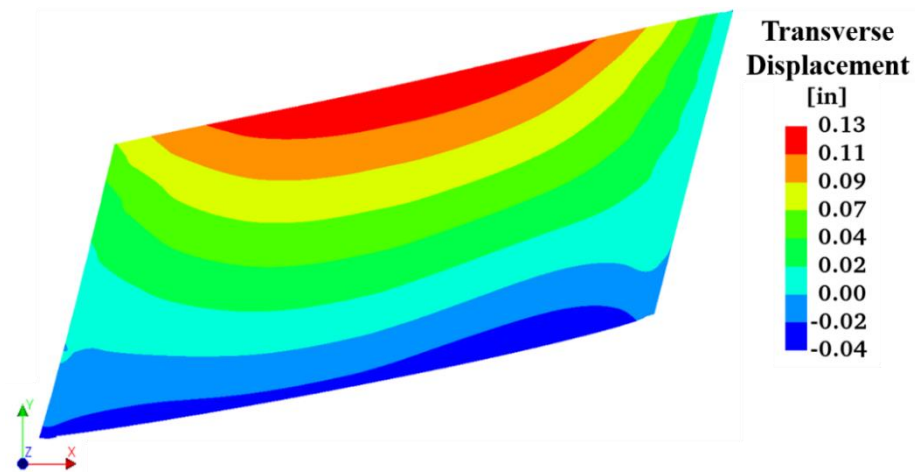
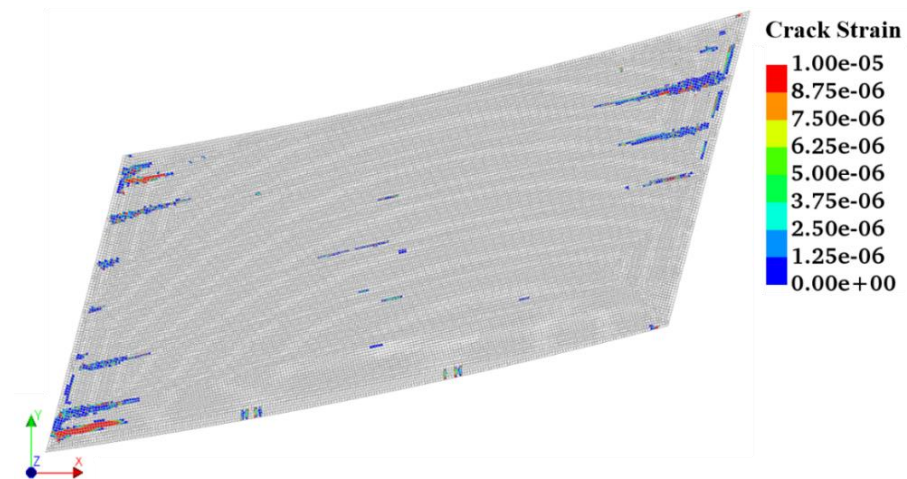


Figure 165 – Transverse displacement in Highly Skewed-FR.



Note: Maximum crack strain = 7990 $\mu\epsilon$.

Figure 166 – Top view showing cracked elements in Highly Skewed-FR.

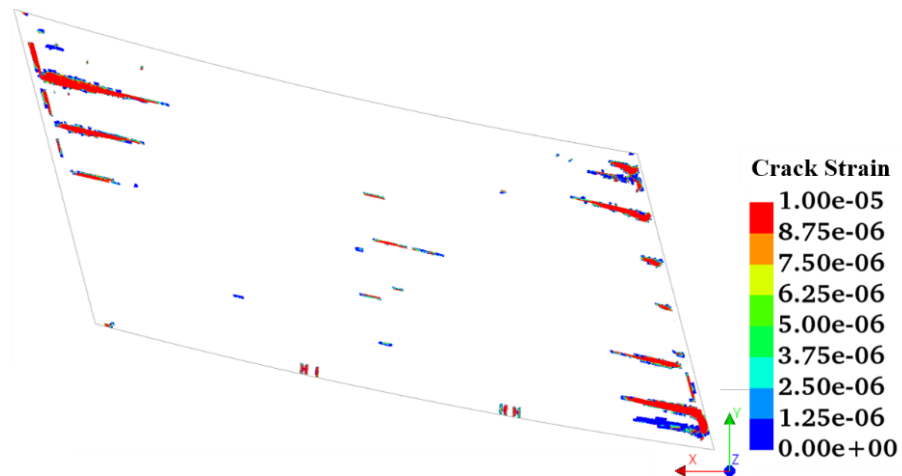
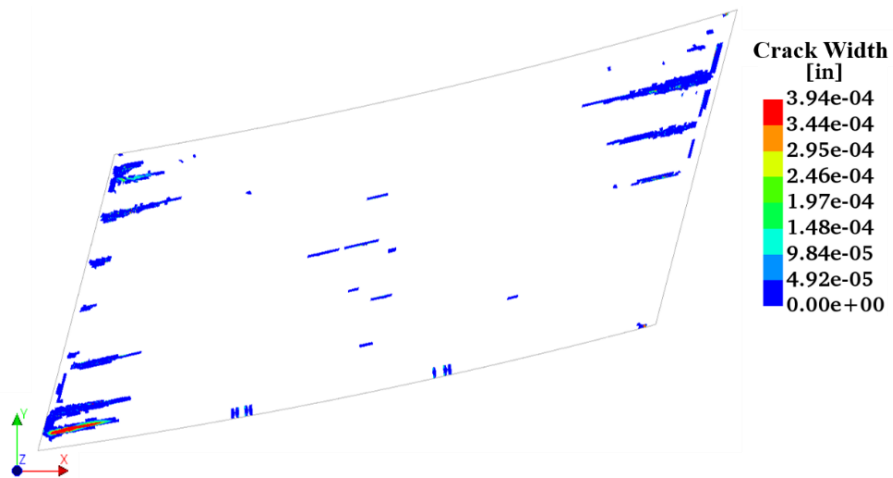
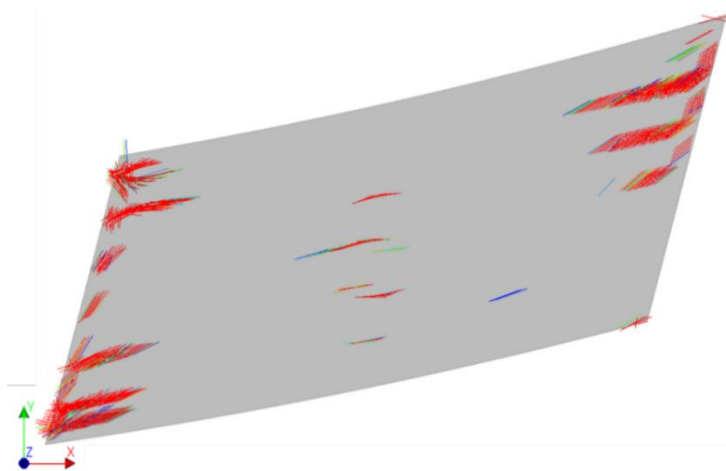


Figure 167 – Bottom view showing cracked elements in Highly Skewed-FR.



Note: Maximum crack width = 1.07×10^{-2} in. (0.27 mm).

Figure 168 – Top view showing crack widths Highly Skewed-FR.



Note: The crack size is exaggerated for illustration.

Figure 169 – Top view showing crack orientations in Highly Skewed-FR.

5.3.4.2 Case 11: Highly Skewed-LVR

By freeing the transverse direction movement at the girder ends, the maximum total displacement slightly increases from 0.47 in. (11.94 mm) to 0.53 in. (13.46 mm), as shown in Figure 170, compared to Case 10. Figure 171 and Figure 172 show the longitudinal and transverse displacements, respectively.

The maximum crack strain is 3530 microstrain, and the maximum crack width is 1.12×10^{-2} in. (0.28 mm). Figure 173 and Figure 174 show the cracked elements on the top and bottom surfaces, respectively. Figure 175 shows the corresponding crack widths, and Figure 176 illustrates the crack orientations.

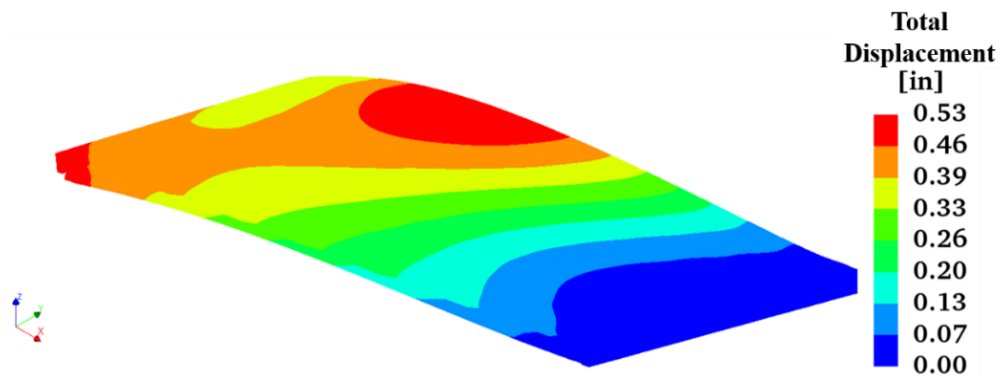


Figure 170 – Total displacement in Highly Skewed-LVR.

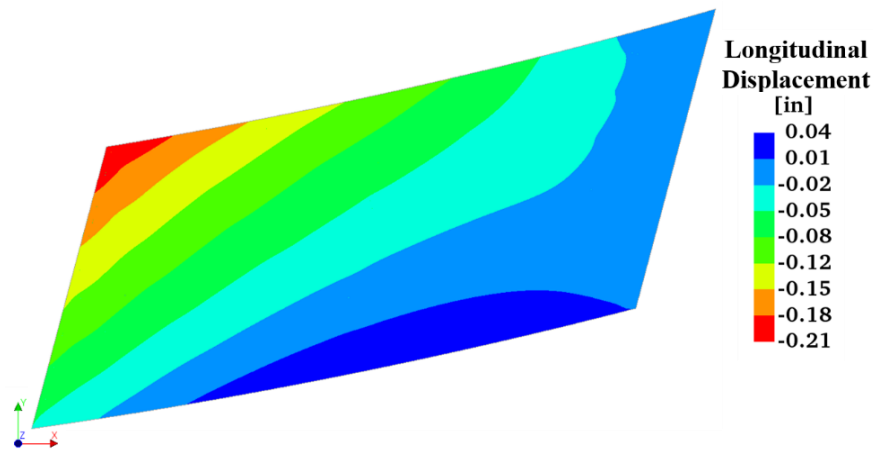


Figure 171 – Longitudinal displacement in Highly Skewed-LVR.

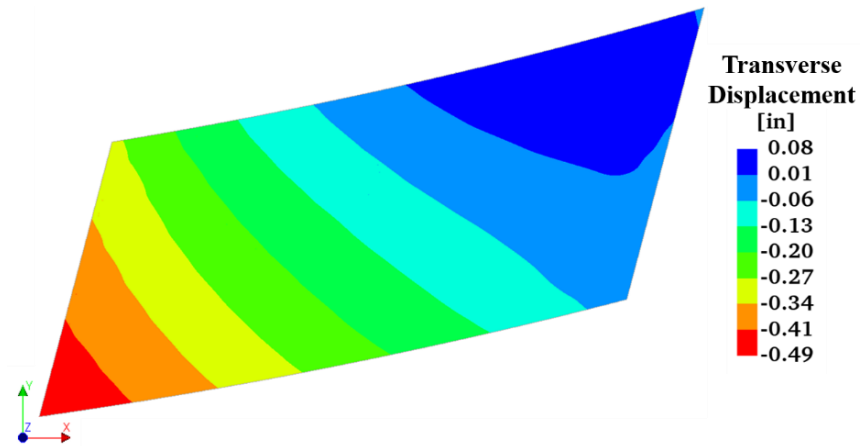
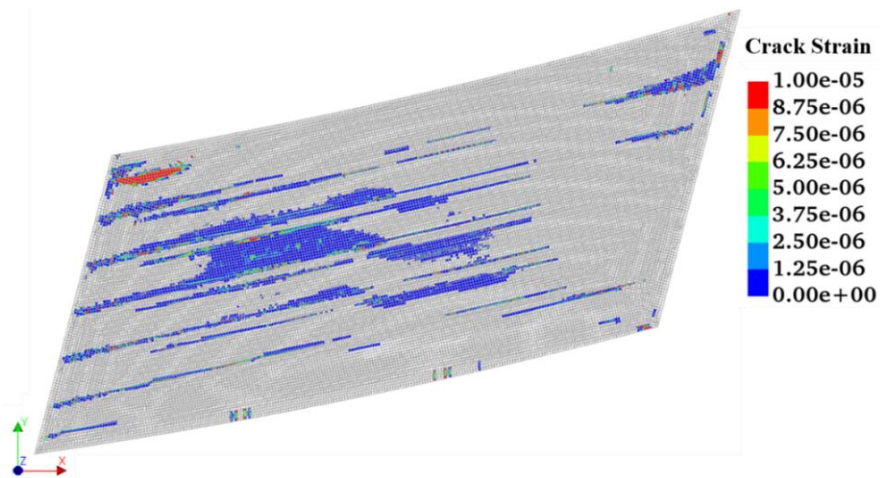


Figure 172 – Transverse displacement in Highly Skewed-LVR.



Note: Maximum crack strain = 3530 $\mu\epsilon$.

Figure 173 – Top view showing cracked elements in Highly Skewed-LVR.

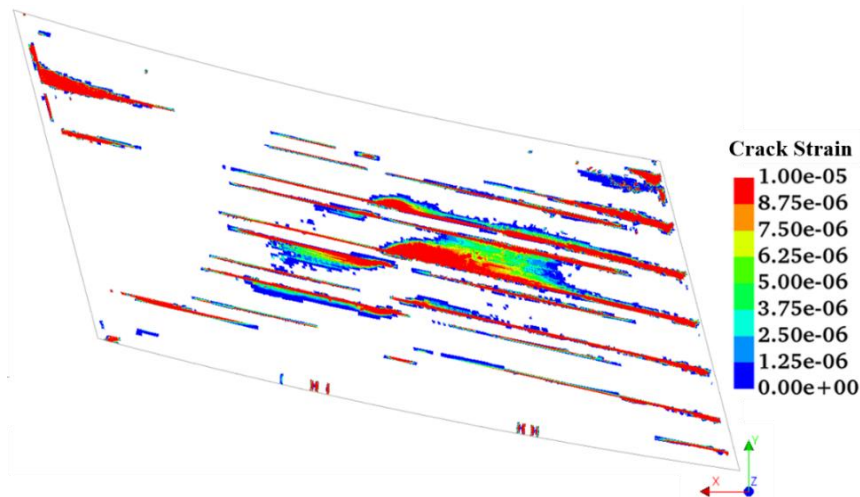
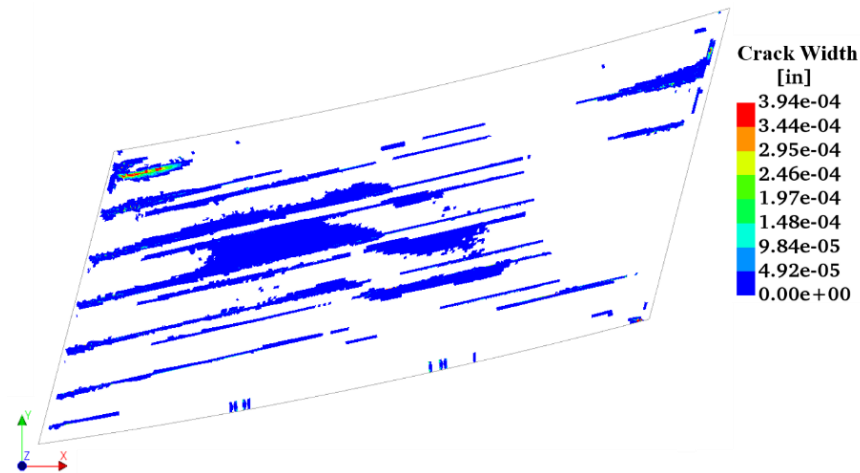
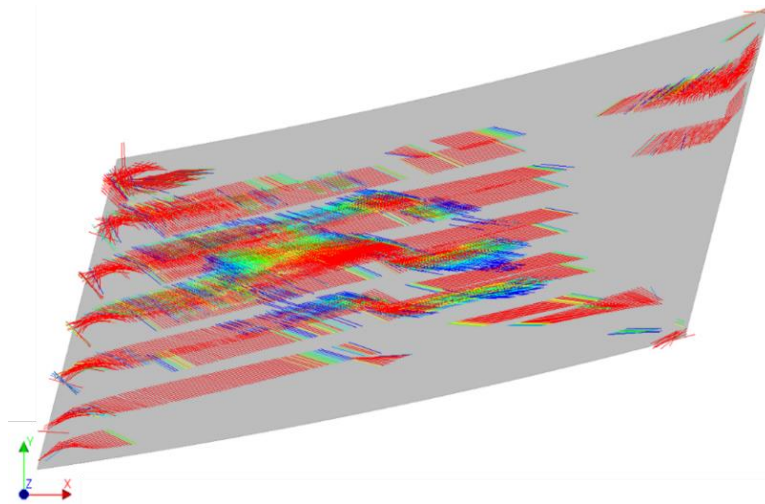


Figure 174 – Bottom view showing cracked elements in Highly Skewed-LVR.



Note: Maximum crack width = 1.12×10^{-2} in. (0.28 mm).

Figure 175 – Top view showing crack widths in Highly Skewed-LVR.



Note: The crack size is exaggerated for illustration.

Figure 176 – Top view showing crack orientations in Highly Skewed-LVR.

5.3.4.3 Case 12: Highly Skewed-VR

When girder ends are not restrained from moving in the longitudinal and transverse directions, the maximum displacement decreases to 0.31 in. (7.87 mm), as shown in Figure 177. Maximum longitudinal displacement of 0.26 in. (6.60 mm) is observed along the transverse edge at Bent 2, and the contour is fairly symmetric (see Figure 178). Maximum

transverse displacement of 0.20 in. (5.08 mm) is observed in the acute corner along the edge at intermediate Bent 2 (see Figure 179).

The maximum crack strain and maximum crack width are 4230 microstrain and 1.12×10^{-3} in. (0.28 mm), respectively. The top and bottom views of the cracked elements are shown in Figure 180 and Figure 181, respectively, and Figure 180 shows the crack strain index of 0 to 10 microstrain. Crack widths are shown in Figure 182. Figure 183 shows the orientation of the cracks.

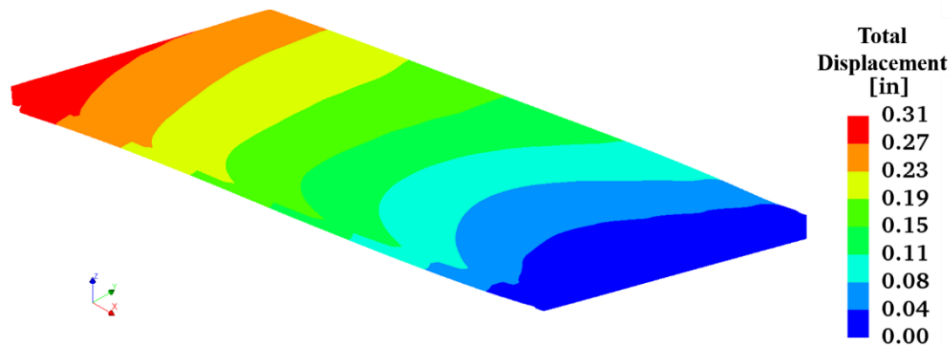


Figure 177 – Total displacement in Highly Skewed-VR.

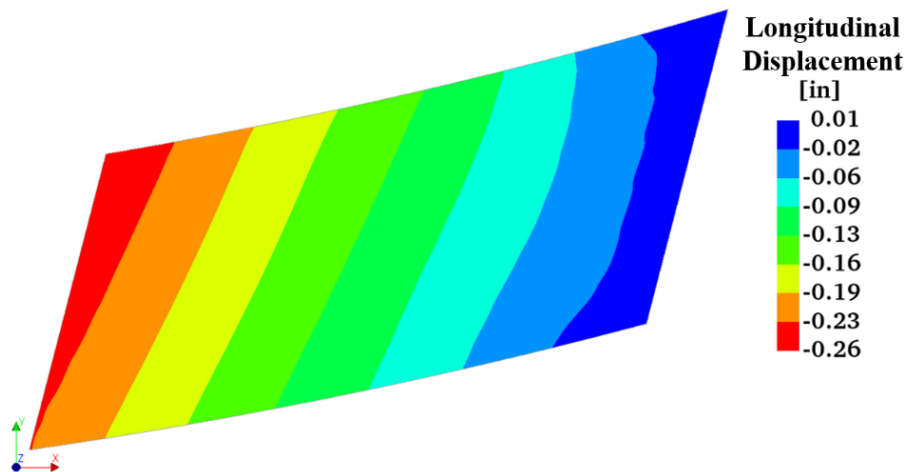


Figure 178 – Longitudinal displacement in Highly Skewed-VR.

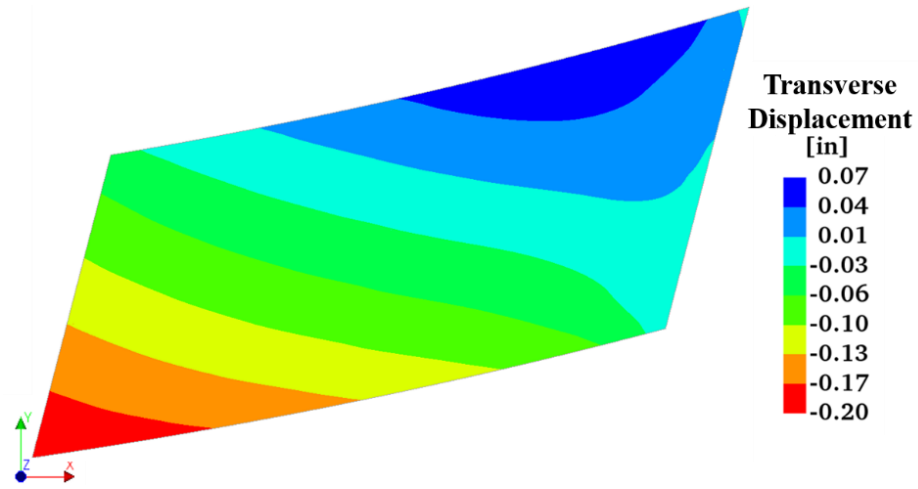
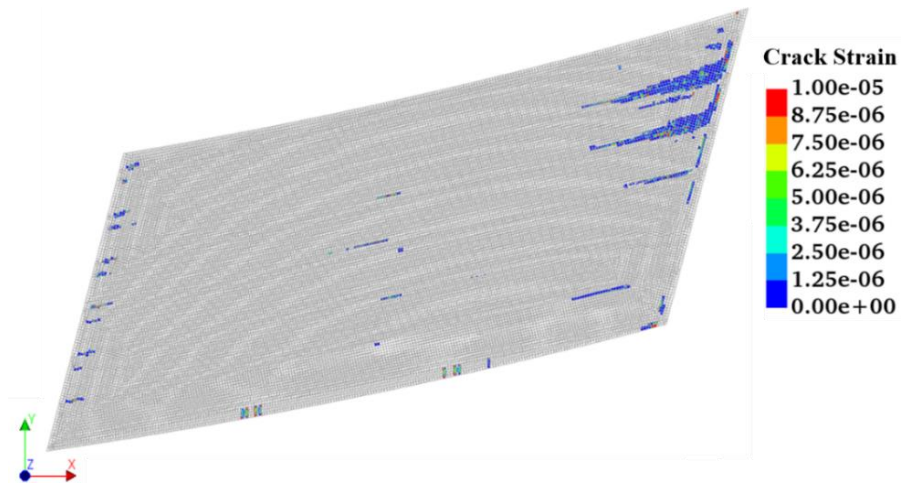


Figure 179 – Transverse displacement in Highly Skewed-VR.



Note: Maximum crack strain = $4230 \mu\epsilon$.

Figure 180 – Top view showing cracked elements in Highly Skewed-VR.

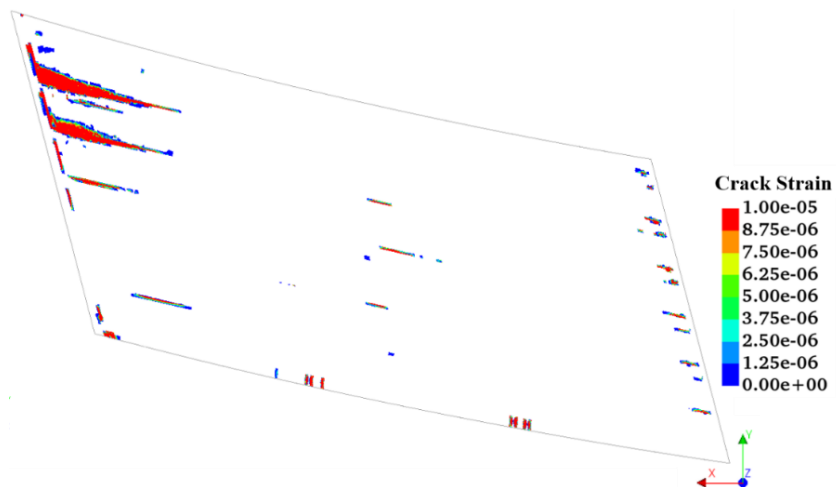
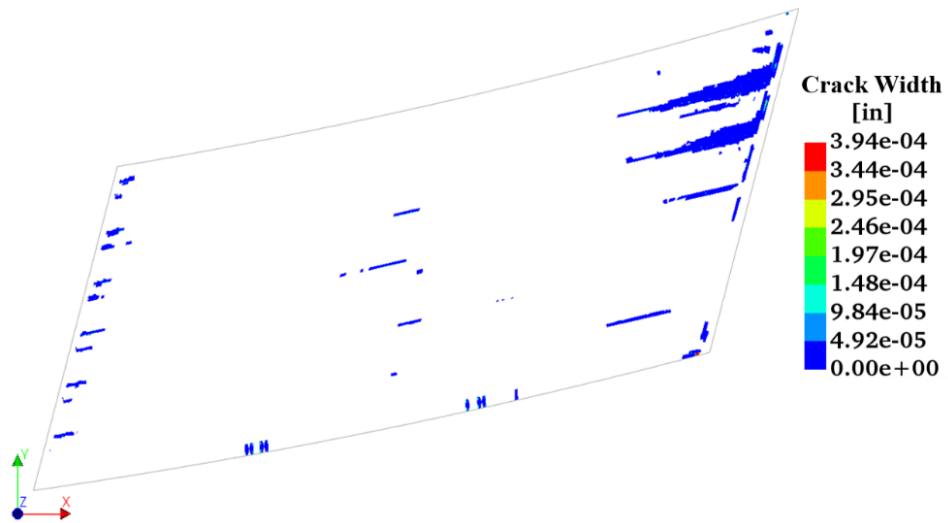
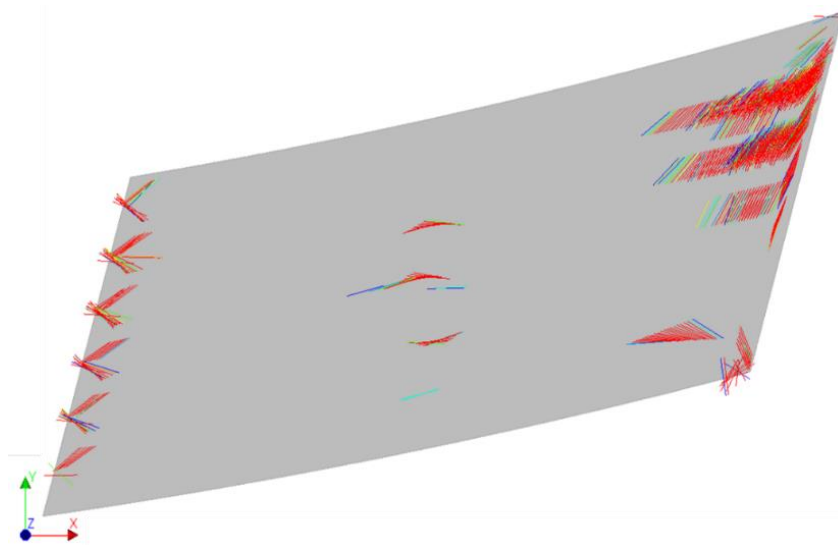


Figure 181 – Bottom view showing cracked elements in Highly Skewed-VR.



Note: Maximum crack width = 1.12×10^{-2} in. (0.28 mm).

Figure 182 – Top view showing crack widths in Highly Skewed-VR.



Note: The crack size is exaggerated for illustration.

Figure 183 – Top view showing crack orientations in Highly Skewed-VR.

5.4 Results from Live Load Analysis

Figure 184 and Figure 185 present a displacement contour for live load Cases A and B (see Section 4.8), respectively. The stress intensity plots are shown in Figure 186 and Figure 187. The maximum displacements from the live load cases occur at the mid-length of the span, and Case 1 yields a slightly larger displacement. The stress plot indicates that the compressive (negative) and tensile (positive) stresses remain small (i.e., elastic response).

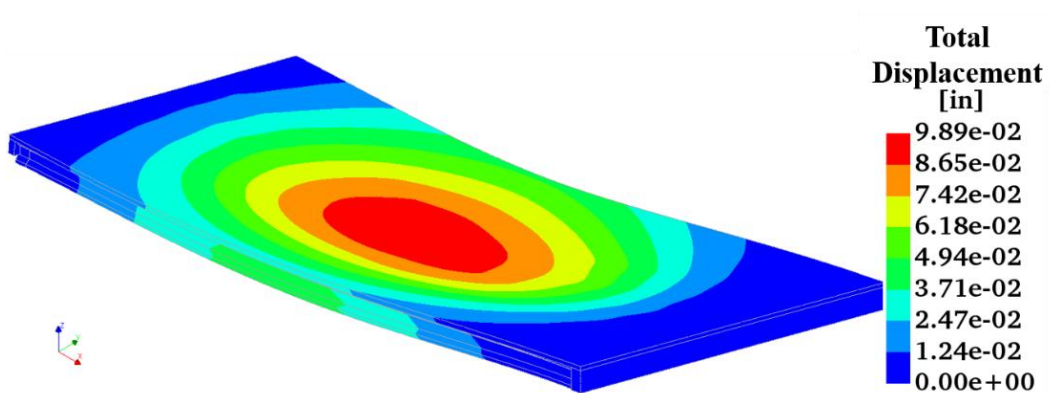


Figure 184 – Total displacement contour for Live Load Case A.

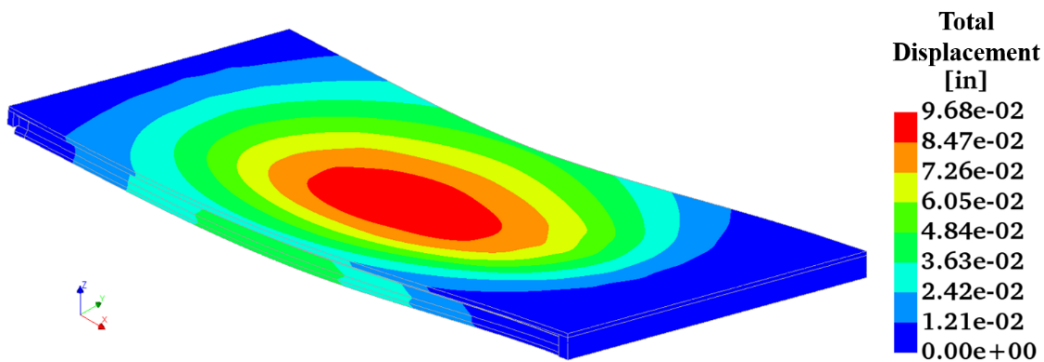


Figure 185 – Total displacement contour for Live Load Case B.

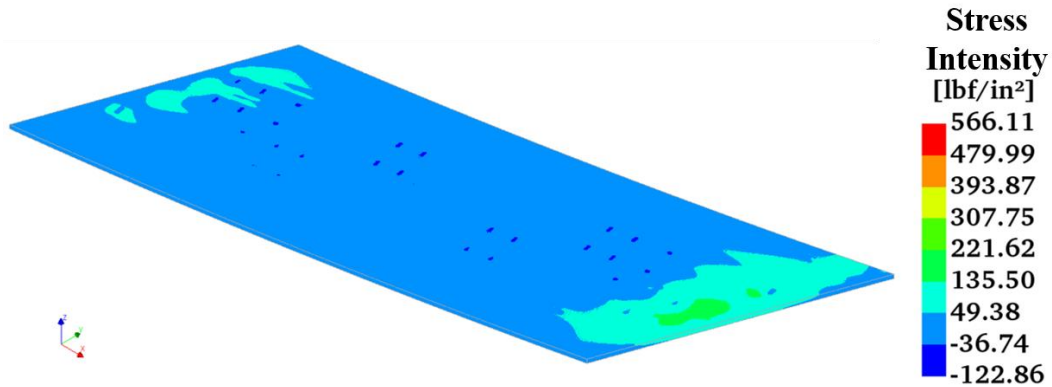


Figure 186 – Stress intensity for Live Load Case A.

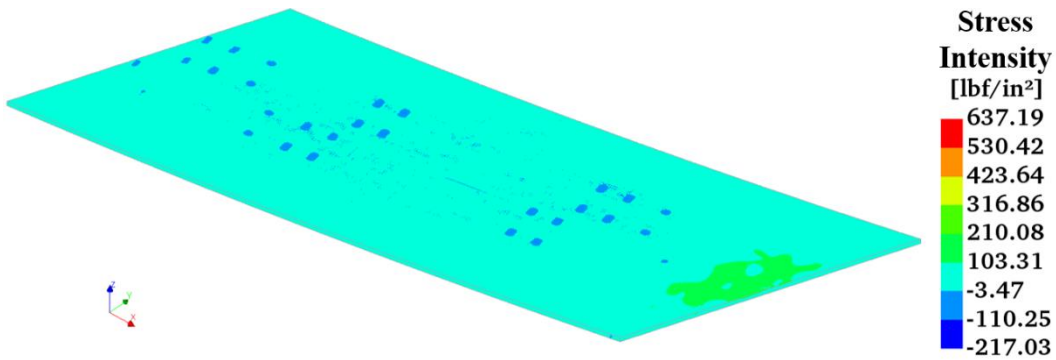


Figure 187 – Stress intensity for Live Load Case B.

5.5 Results from Induced-Displacement Load Analysis

Figure 188 and Figure 189 present a displacement contour and a stress intensity diagram for the worst case, Case V4 (see Section 4.9), respectively. The results from the four displacement cases yield similar outcomes and thus are not presented here. However, when the maximum displacement is induced on the side of the acute corner with the larger skew angle, the largest displacement occurs at the acute corner. Consequently, the tensile stress peaks where the deck adjoins the girders, and its magnitude increases towards the obtuse corner as shown in Figure 189. The peak tensile stress is concentrated at a few localized locations, and thus Case V4 has an overall insignificant effect on deck cracking.

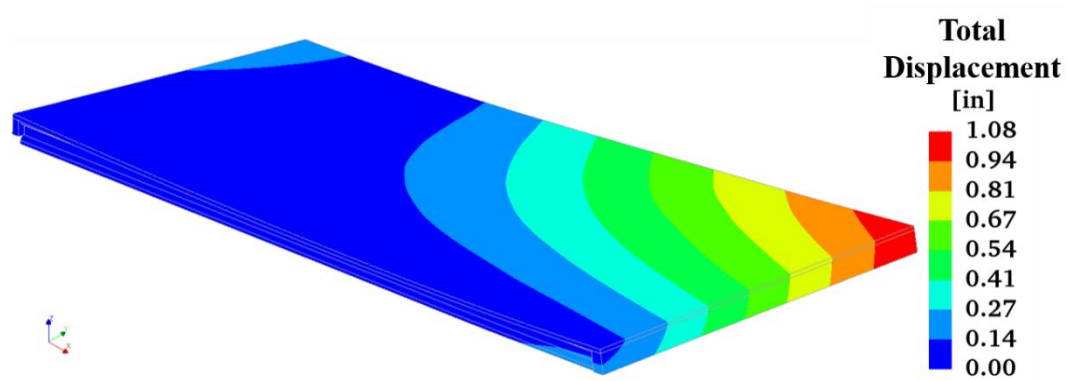


Figure 188 – Total displacement contour for Displacement Case V4.

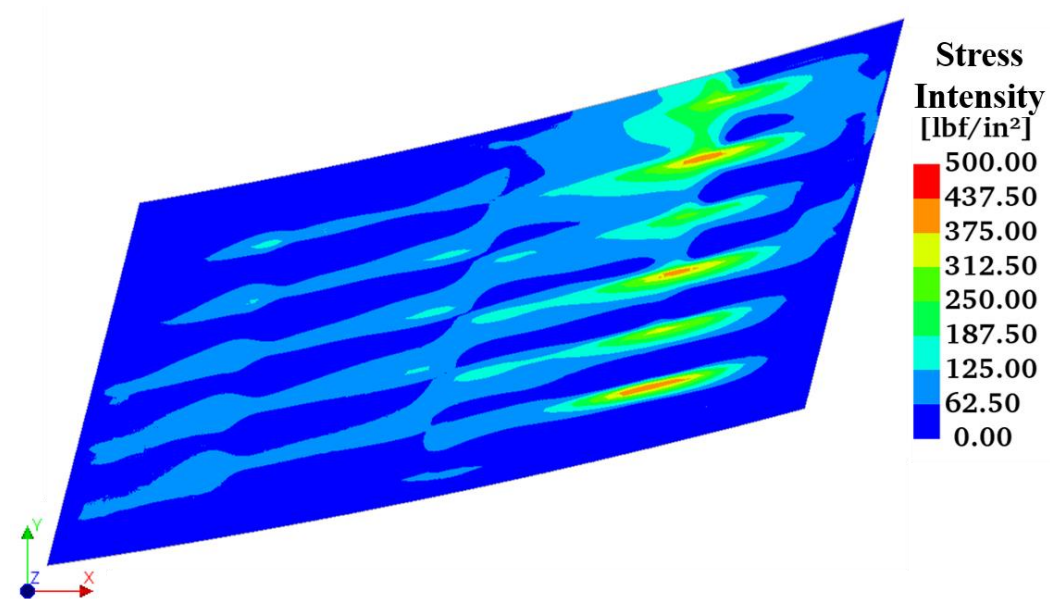


Figure 189 – Tensile stress intensity plot for Displacement Case V4.

6 ANALYSIS AND SYNTHESIS OF THE RESULTS

This section provides an analysis of the FEA results presented in Section 5. Sections 6.1 and 6.2 discuss the results from the twelve thermal analyses. Section 6.3 discusses the findings of a sensitivity analysis conducted with reduced coefficients of thermal expansion. Section 6.4 presents the effect for different reinforcement patterns. Section 6.5 discusses the live load and induced-displacement analysis cases. Section 6.6 presents the potential causes of cracking found on the SR299 bridge by comparing results obtained from field and analytical investigations. Finally, the decision matrix presented in Section 1.4 is completed and presented in Section 6.6.

6.1 Effect of Boundary Conditions for Varying Deck Geometries

Figure 190 through Figure 196 show the effect of boundary conditions (B.C.) on displacements and crack widths for varying deck geometries. The following subsections discuss the main observations from analyzing the results. In summary, the following crack patterns are predominantly observed, regardless of deck geometries:

- Mixed crack patterns (a combination of longitudinal, diagonal, and transverse) with fully restrained conditions
- Longitudinal cracks when restrained in the longitudinal direction
- Diagonal cracks at acute corners when transversely restrained

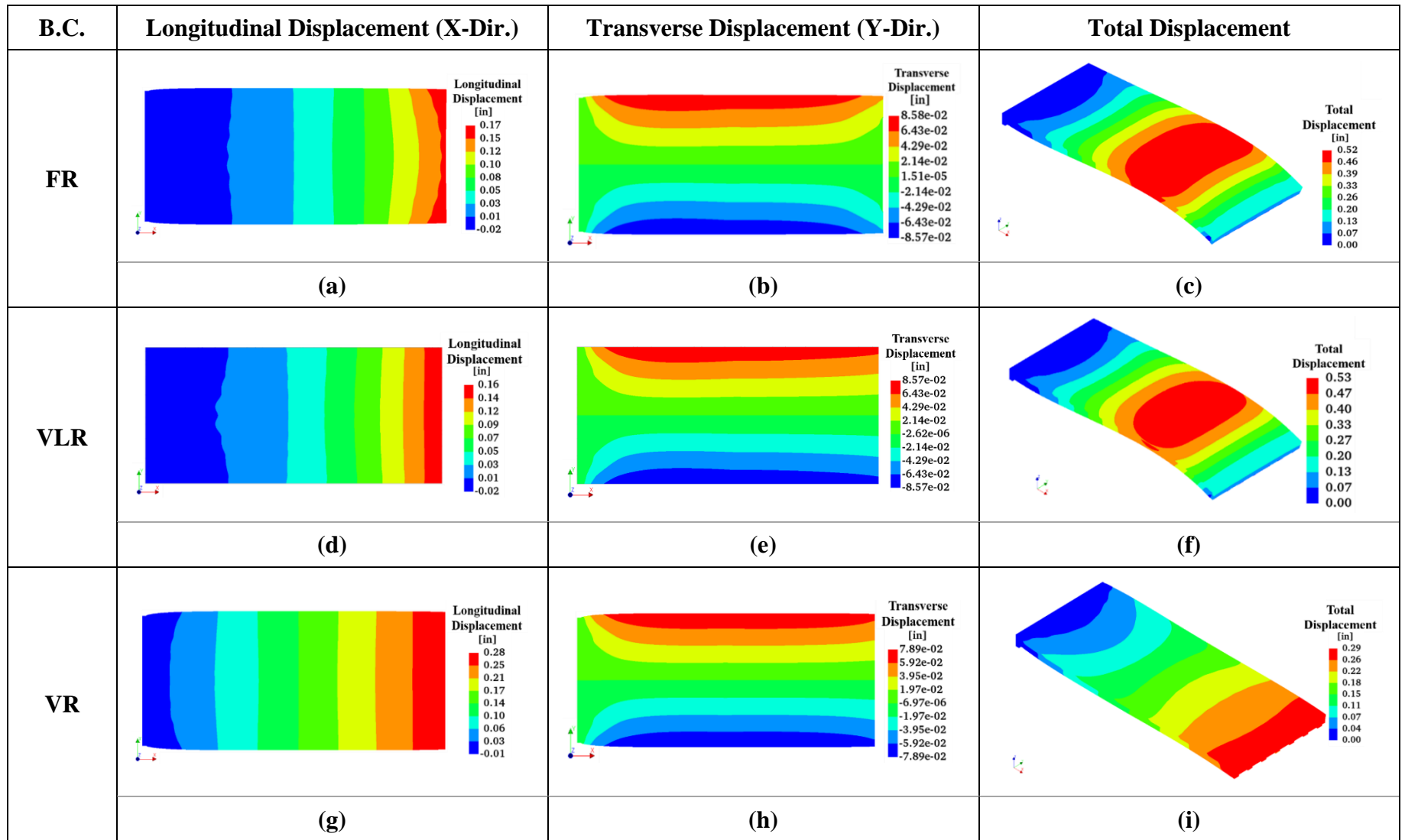


Figure 190 – Effect of restraints on displacements (Straight Deck).

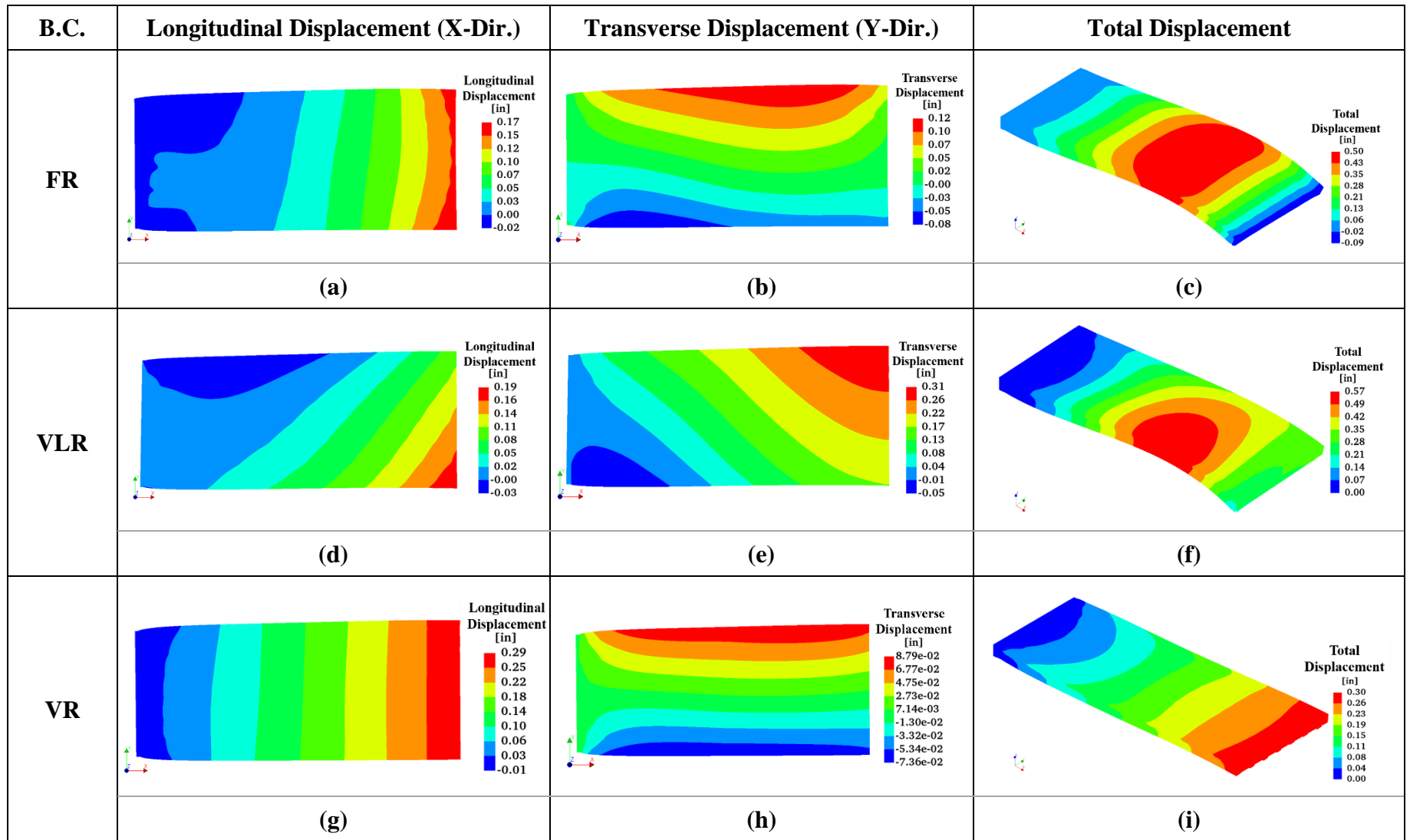


Figure 191 – Effect of restraints on displacements (Inclined Deck).

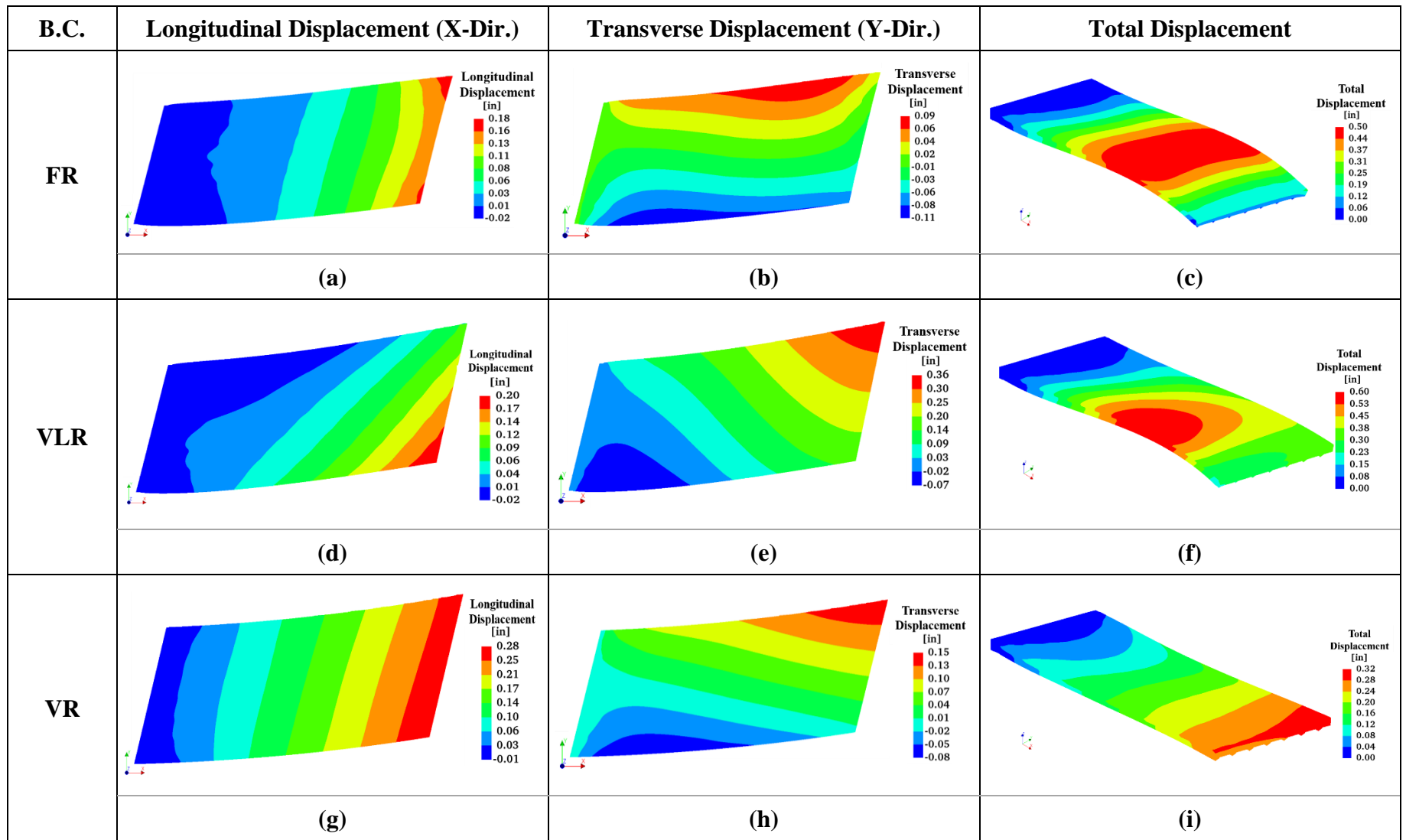


Figure 192 – Effect of restraints on displacements (Skewed & Curved Deck).

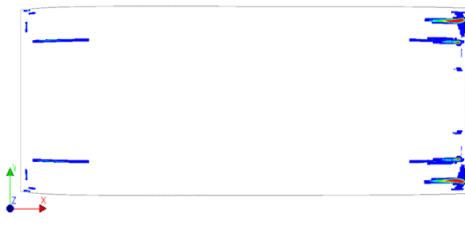
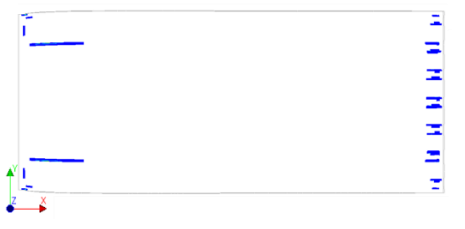
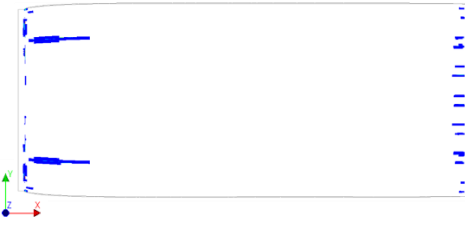
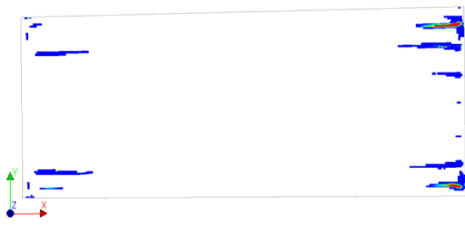


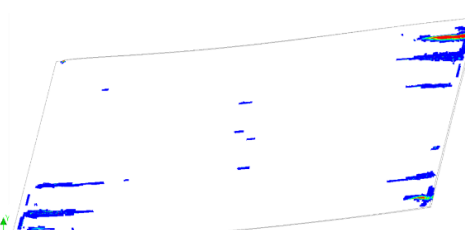
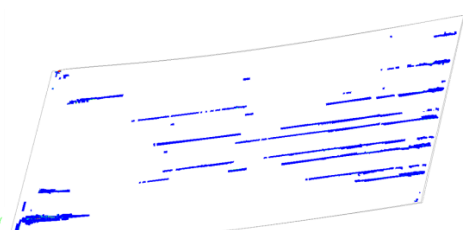
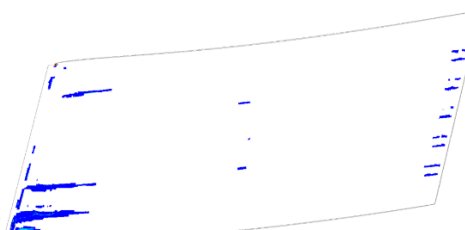
Deck Geometry	FR	LVR	VR
Straight			
	(a) MCW = 1.12×10^{-2} in. (0.28 mm)	(b) MCW = 4.18×10^{-3} in. (0.11 mm)	(c) MCW = 9.29×10^{-3} in. (0.24 mm).
Inclined			
	(d) MCW = 7.16×10^{-3} in. (0.18 mm)	(e) MCW = 5.38×10^{-3} in. (0.14 mm)	(f) MCW = 3.19×10^{-3} in. (0.08 mm)
Skewed & Curved			
	(g) MCW = 1.14×10^{-2} in. (0.29 mm)	(h) MCW = 1.30×10^{-2} in. (0.33 mm)	(i) MCW = 9.66×10^{-3} in. (0.25 mm)

Figure 193 – Effect of restraints and deck geometries on crack width.

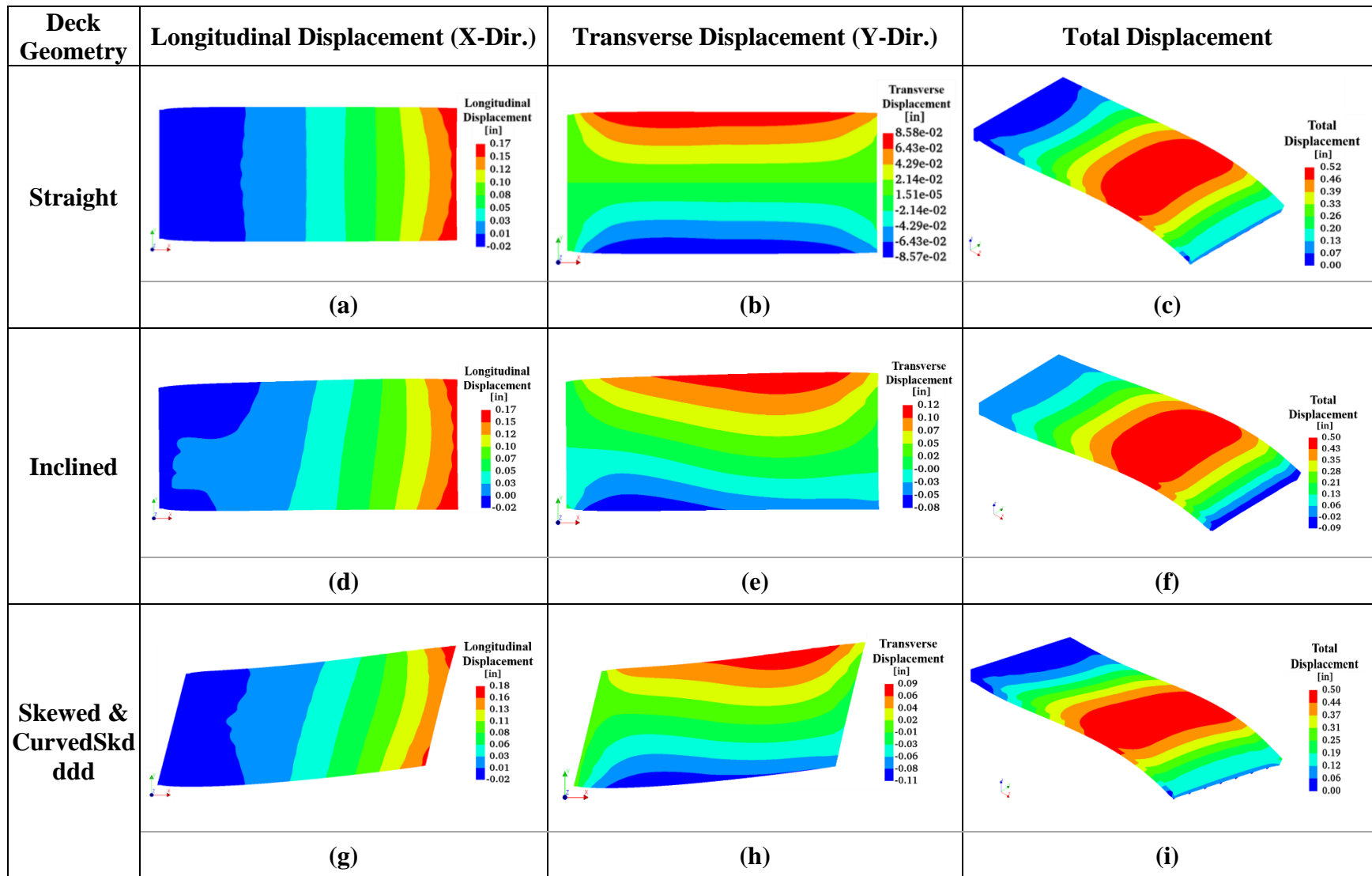


Figure 194 – Effect of deck geometries on displacements (movements fully restrained).

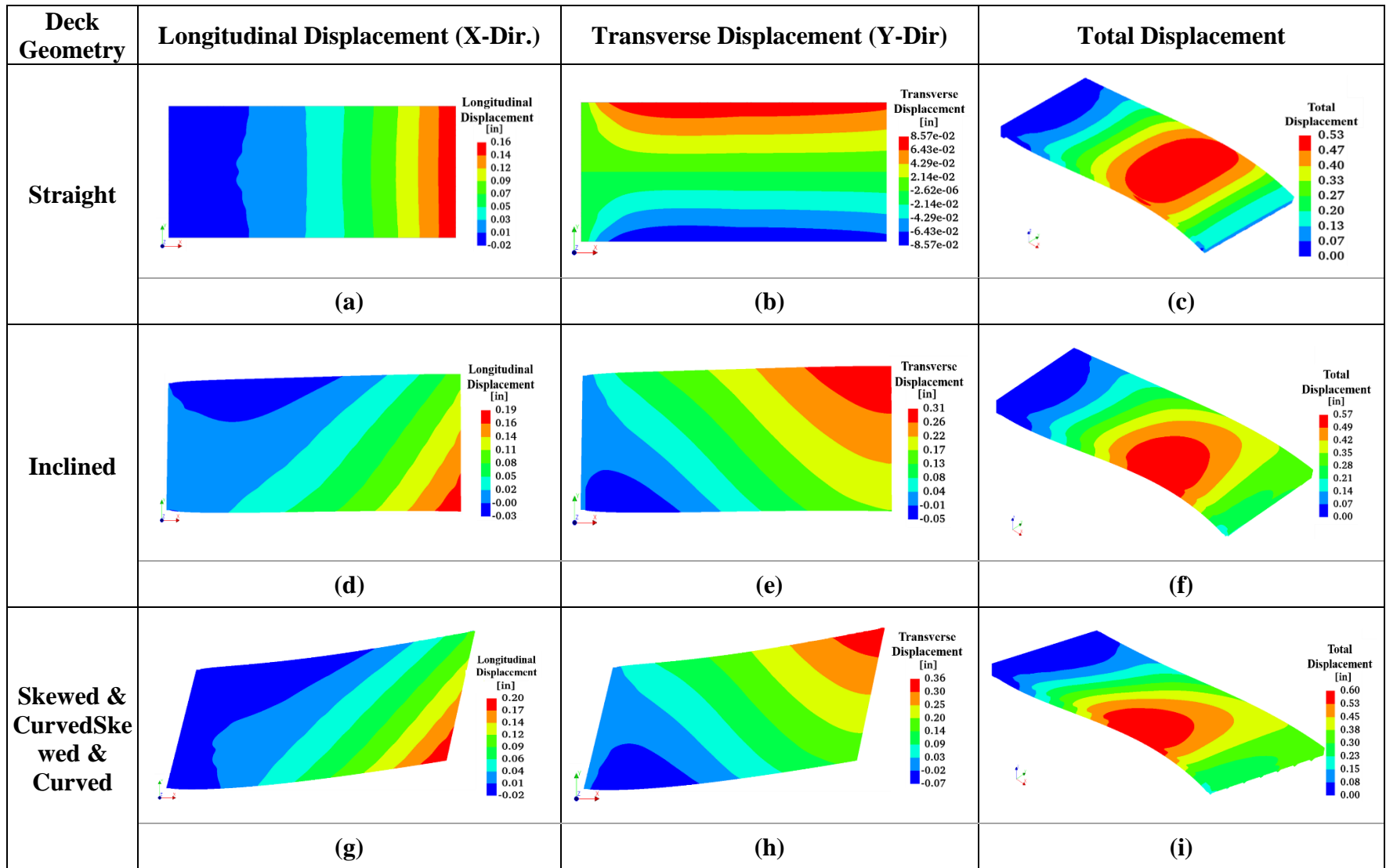


Figure 195 – Effect of deck geometries on displacements (longitudinal and vertical movements restrained).

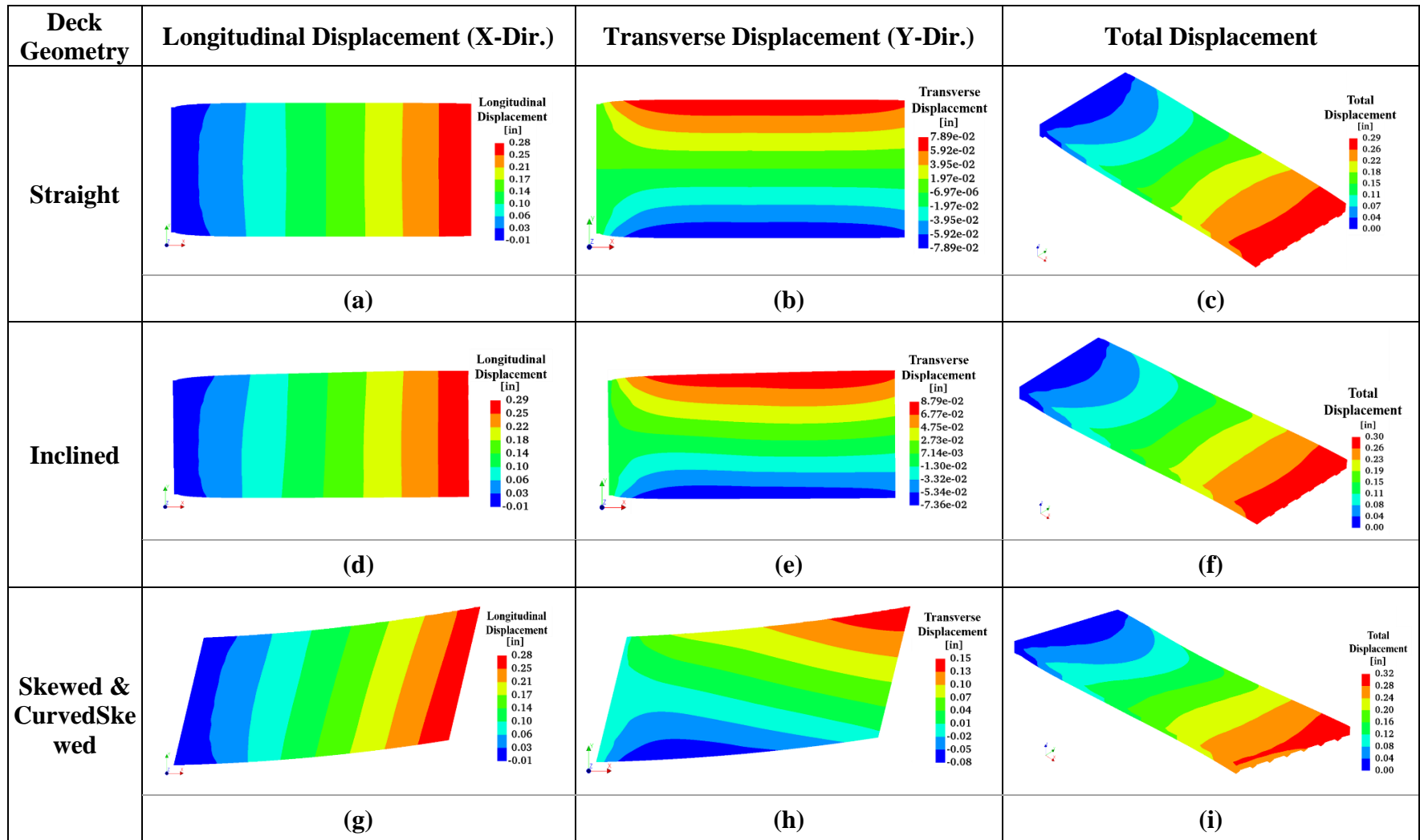


Figure 196 – Effect of deck geometries on displacements (vertical movements restrained).

6.1.1 *Straight Deck*

Figure 190 illustrates the effect of restraints on displacements. Figure 193 shows the crack width predictions for changing boundary conditions (B.C.) and deck geometries.

- As anticipated, when the degree of restraints increases, the extent of cracking and the maximum crack width grow (see Figure 193 (a) through (c)).
- When the deck is restrained from both longitudinal and vertical movements, the total displacement, which includes the effect of cracking, is greatest (see Figure 190).
- Cracks occur at the location of restraints when girder ends at Bent 2 are restrained (see Figure 193 (a)).
- When the girder ends are vertically supported (i.e., no longitudinal and transverse restraints), as detailed in the design drawings, minor cracks (e.g., crack width less than 0.0093 in. or 0.24 mm) form at the integrated abutment ends. This is due to the integrated girder ends, which are inherent in a semi-integral abutment bridge design. These cracks are not expected to be visible to human eyes.

6.1.2 *Inclined Deck*

Figure 191 shows changes in displacements.

- Due to the elevation variation, the deck shows an asymmetric expansion (Figure 191 (d) through (f)) in both transverse and longitudinal directions when asymmetric boundary conditions are provided.
- When the deck is free to longitudinally expand, the largest expansion occurs at the expansion joint location (Figure 191 (g) through (i)).

- When the girder ends are asymmetrically restrained from transverse movements (see Figure 191 (f)), the inflection point, near the highest point in the deck, has the largest total deformation.
- Compared to the straight deck model, decks with an asymmetric elevation profile are more sensitive to asymmetric boundary conditions (see Figure 193 (b) and (e)).

6.1.3 Skewed and Curved Deck

Figure 192 illustrates the effects of asymmetric geometries and associated thermal expansions on the total displacement. Figure 193 shows these effects on crack widths.

- In curved bridges, longitudinal cracks are observed mid-length of the span.
- Diagonal cracks are predicted at the corners of the skewed and curved deck models regardless of the boundary conditions. These cracks are expected to occur at the abutment end on the side that is restrained from movement (see Figure 193 (g) through (i)). Although they are small in width (< 0.013 in. or 0.33 mm), these cracks could widen over the service life.
- Differential thermal expansion occurs in the acute corners at Bent 2 (see Figure 192 (a)). As predicted, the expansion mainly occurs in the longitudinal (longer) direction.
- Similar to the inclined deck, when the girder ends are not allowed to move in the longitudinal direction and are allowed to move in the transverse direction, an asymmetric expansion occurs (see Figure 192 (e)).
- In contrast to the straight deck, an asymmetric displacement contour is primarily observed in the transverse direction (see Figure 192 (b), (e) and (h) versus Figure 190 (b), (e), and (h)) regardless of the symmetry in the boundary conditions at Bent

2. This is also evident from the asymmetric total displacement contours and increased displacements at the acute corners (see Figure 192 (i)).
- With the skewed and curved deck geometry, the displacement in the transverse direction slightly exceeds the allowable 1/8 in. (3.18 mm) hole dimension in the sole plate (see Figure 192 (h)). Therefore, as-built boundary conditions at Bent 2 may approach the FR condition.
 - In reviewing the effect of deck geometry in the FR conditions (see Figure 194) on deck deformation, asymmetric expansions consistent with deck geometry are predicted.
 - When such asymmetric thermal expansions are fully restrained, thermal cracks form in both corners at the Bent 2 location (see Figure 193 (g)).
 - When girder ends are not allowed to expand in the longitudinal direction, cracks form throughout the deck surface, primarily due to the increased asymmetric expansion in the transverse direction (see Figure 195).
 - When girder ends are free to expand (see Figure 196), cracks mainly form (see Figure 193 (i)) at the corner on the abutment side.

6.1.4 Discussion

Ideally, the boundary condition is a fixed condition at the location of End Bents 1 and 3 due to the inherent design feature: the girder ends restrained by an endwall in a semi-integral bridge. At the same time, the girder ends at the intermediate bent are generally detailed to accommodate movement in the longitudinal direction, yet the inspection report indicates otherwise. Therefore, the bearing conditions at the expansion joint location govern the degree of thermal restraints and thus affect the extent of cracking.

Thus, in a semi-integral abutment bridge, acute corners are vulnerable to thermal cracking due to a specific design feature—the integrated girder ends. These cracks may be mitigated by providing additional reinforcement. Meanwhile, the girder ends at the expansion joint location should be detailed to allow for increased thermal expansion from the deliberately restrained conditions at the abutment ends.

6.2 Effect of Skew Angle

In Figure 197 through Figure 201, the results from Span 1 and Span 2 analyses are compared to study the effect of skew angle on thermal expansions and crack widths. In reviewing the results, it is important to recognize the boundary conditions in Span 2 mirror the boundary conditions in Span 1 on opposite ends. Figure 197 shows the crack width results as well as the boundary conditions and skew angles.

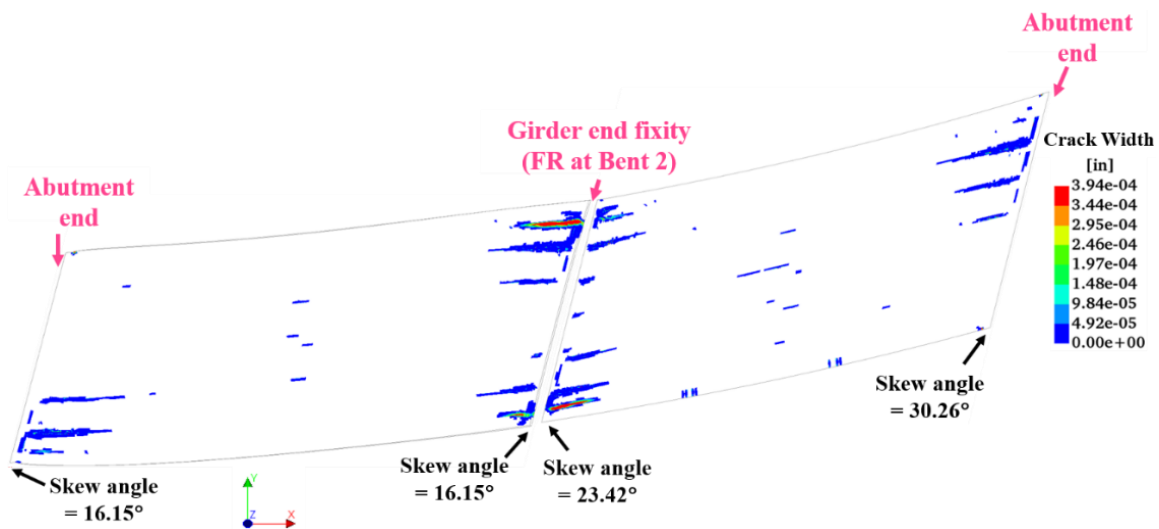


Figure 197 – Predicted cracks in Spans 1 and 2.

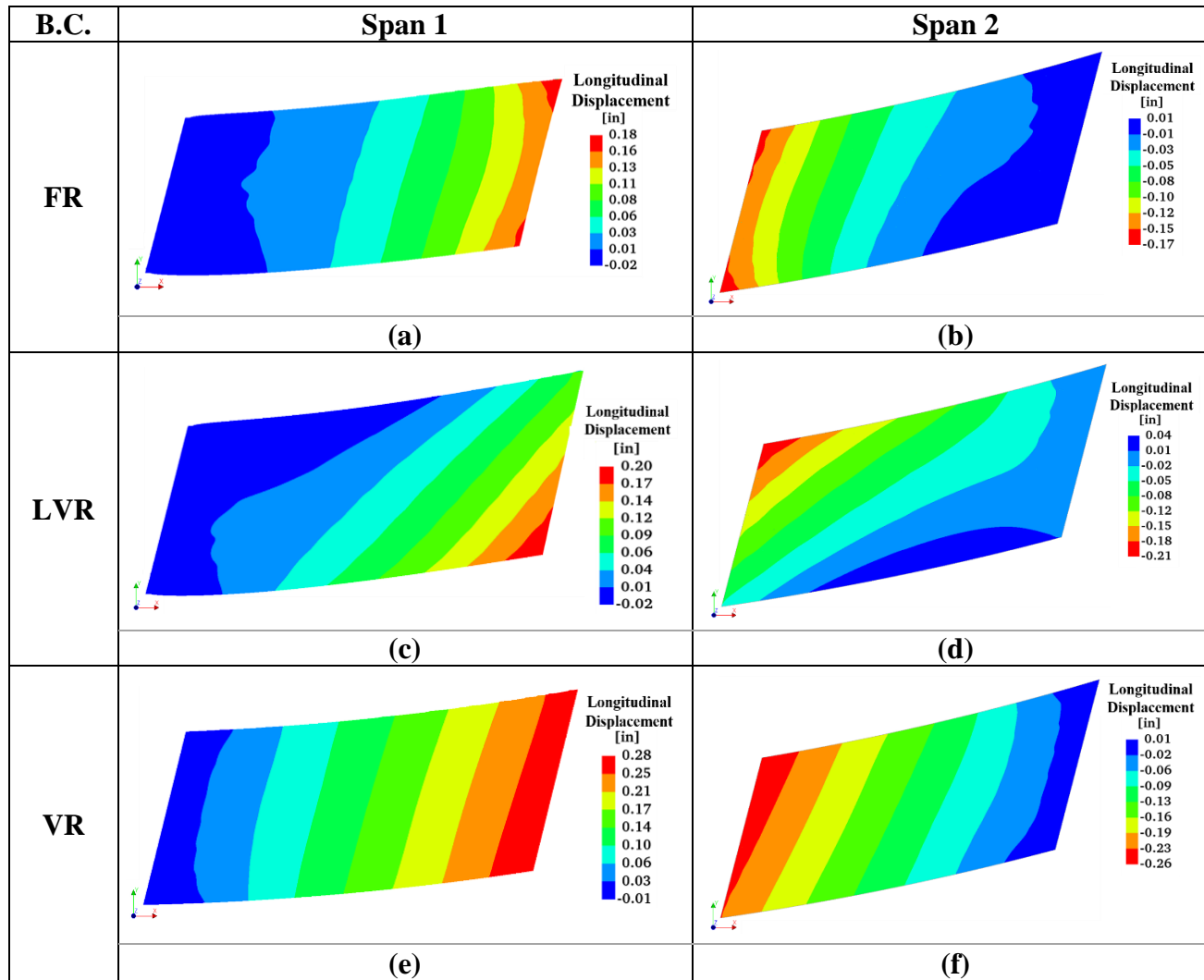


Figure 198 – Comparison of longitudinal displacements between Spans 1 and 2.

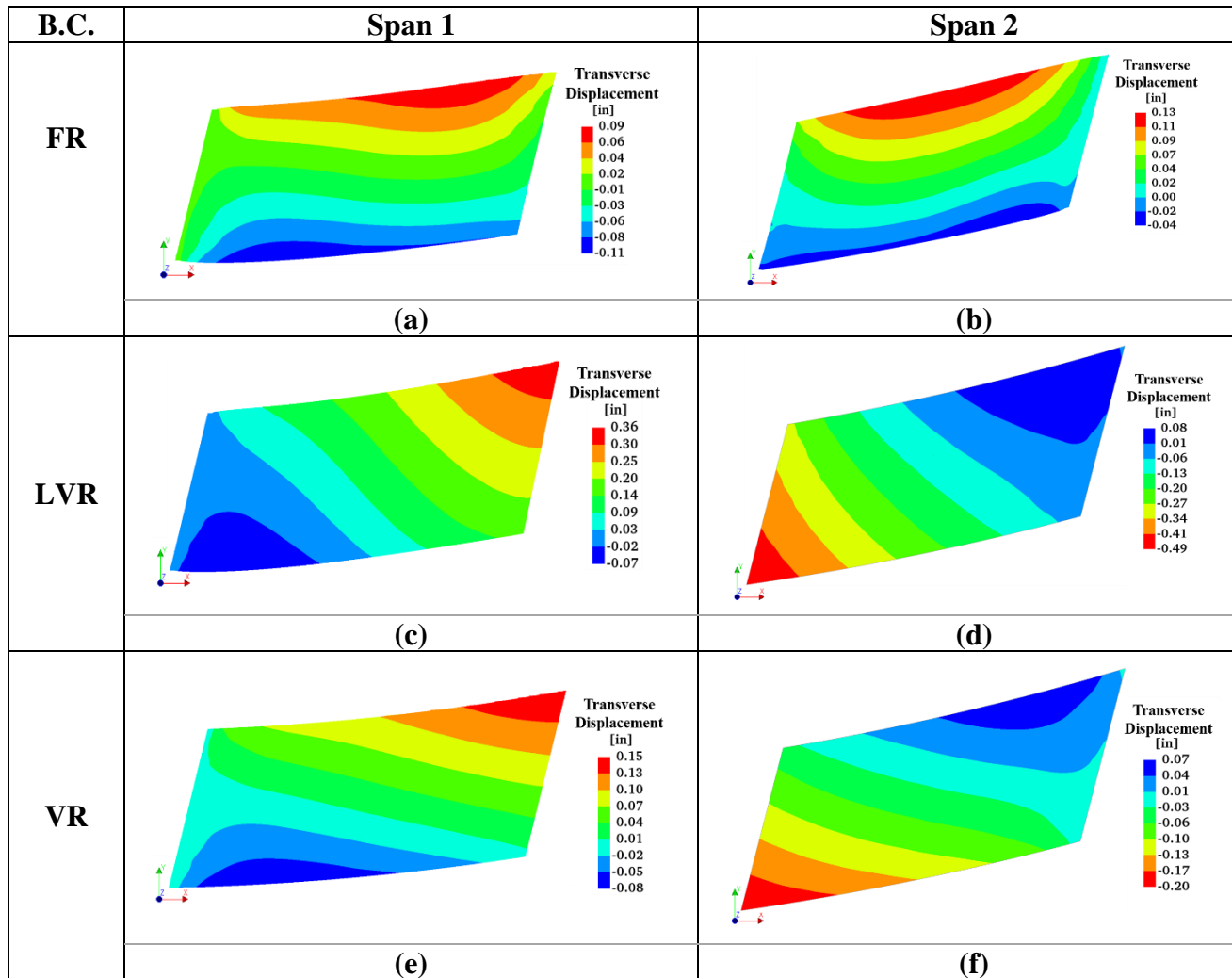


Figure 199 – Comparison of transverse displacements between Spans 1 and 2.

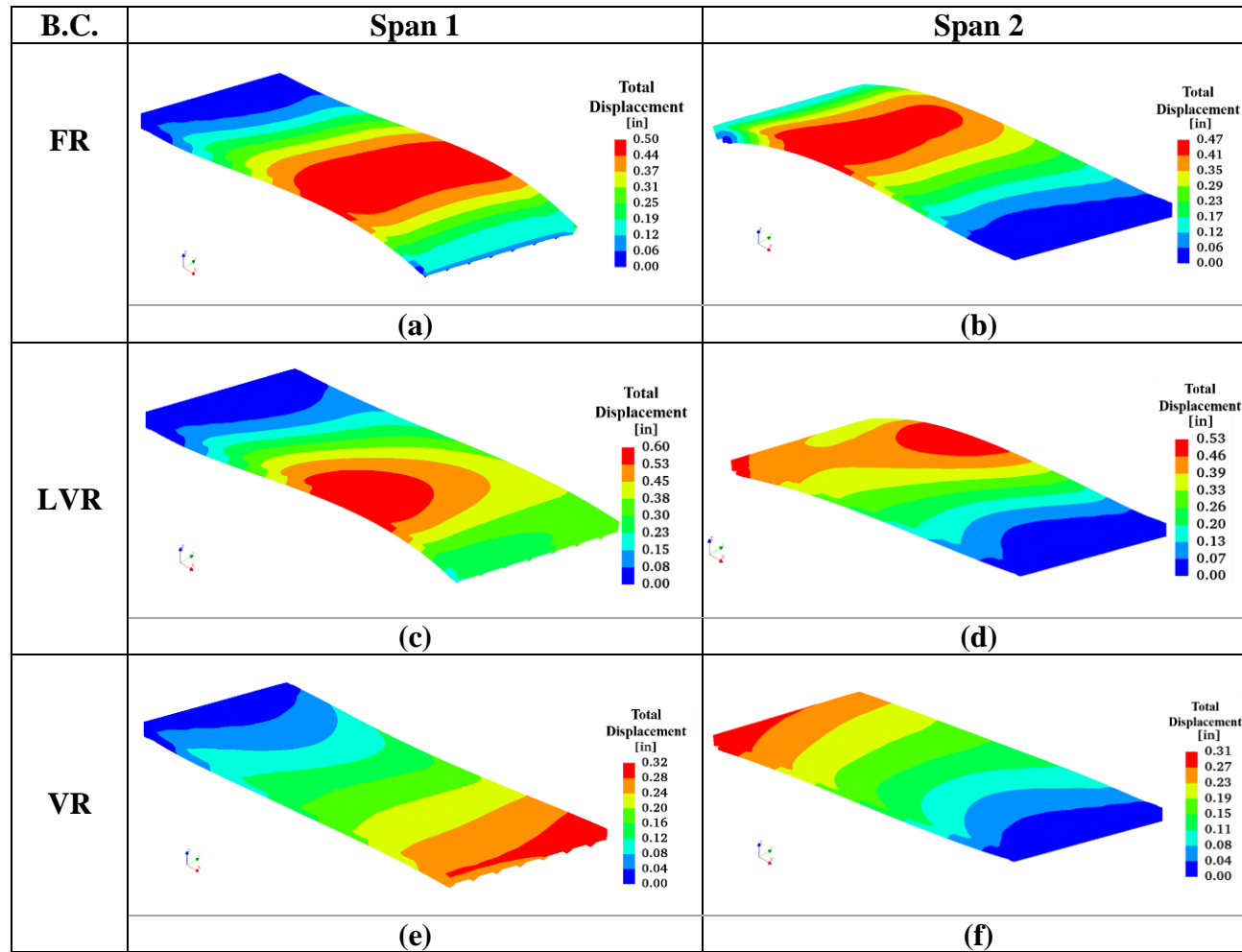


Figure 200 – Comparison of total displacements between Spans 1 and 2.

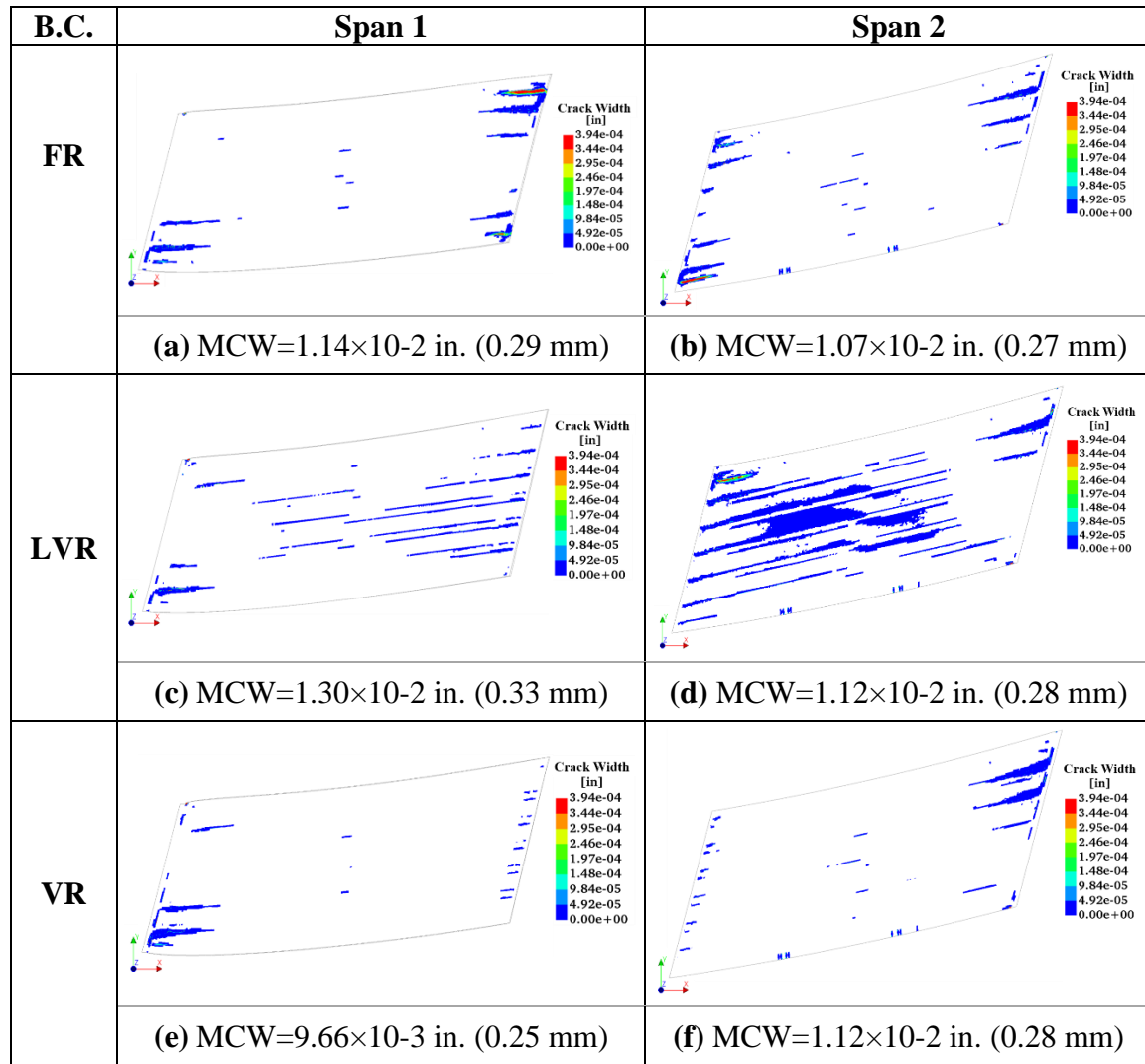


Figure 201 – Comparison of crack widths between Spans 1 and 2.

The following list provides a summary of observations from this comparison:

- The results from Span 2 are consistent with those from Span 1. The cracks primarily occur at the acute corners (see Figure 197).
- With the LVR case, longitudinal expansion is largest in the obtuse corners at Bent 2 (See Figure 198 (c) and (d)).
- Regardless of the boundary conditions at Bent 2, the acute corners on the abutment ends are susceptible to thermal cracking (see Figure 201 (e) and (f)).
- The degree of asymmetric expansion in the longitudinal direction increases at the Bent 2 ends in Span 2 (see Figure 198 (e) and (f)).
- Differential displacements in the transverse direction in FR, LVR, VR cases are 0.20, 0.43, and 0.23 in. (5.08, 10.92, 5.84 mm) for Span 1 and 0.17, 0.57, and 0.27 in. (4.32, 14.48, and 6.86 mm) for Span 2 (see Figure 199), respectively. The increased skew angle in Span 2 overall increases differential expansions between the two corners at Bent 2. This trend is consistent with the total displacements predicted (see Figure 200 (d) and (f)).
- When the girder ends at Bent 2 are free to expand, cracks form on the abutment ends (see Figure 201 (e) and (f)).
- When the girder ends are only allowed to expand in the transverse direction, expansion in the transverse direction increases (Figure 200 (c) and (d)); thus, cracks form throughout the deck area (see Figure 201 (c) and (d)).
- When the girder ends at Bent 2 are restrained from asymmetric expansion, cracks form on all corners.

- The extent of cracking is greater in Span 2 due to the increased skew angle in the deck geometry.

6.3 Effect of Coefficient of Thermal Expansion

In this study, the coefficient of thermal expansion (CTE) value for normal concrete (5.5×10^{-6} in/in/°F or 1.0×10^{-5} cm/cm/°C) is reduced by about 8-10% to account for the limestone aggregate used in the concrete mixture (see Figure 203 (a) for the analysis results). This section considers additional reductions (10% and 20%) in CTE and presents the resulting crack widths. Figure 202 provides a summary of the findings. Figure 203 shows the crack width plots for varying CTE.

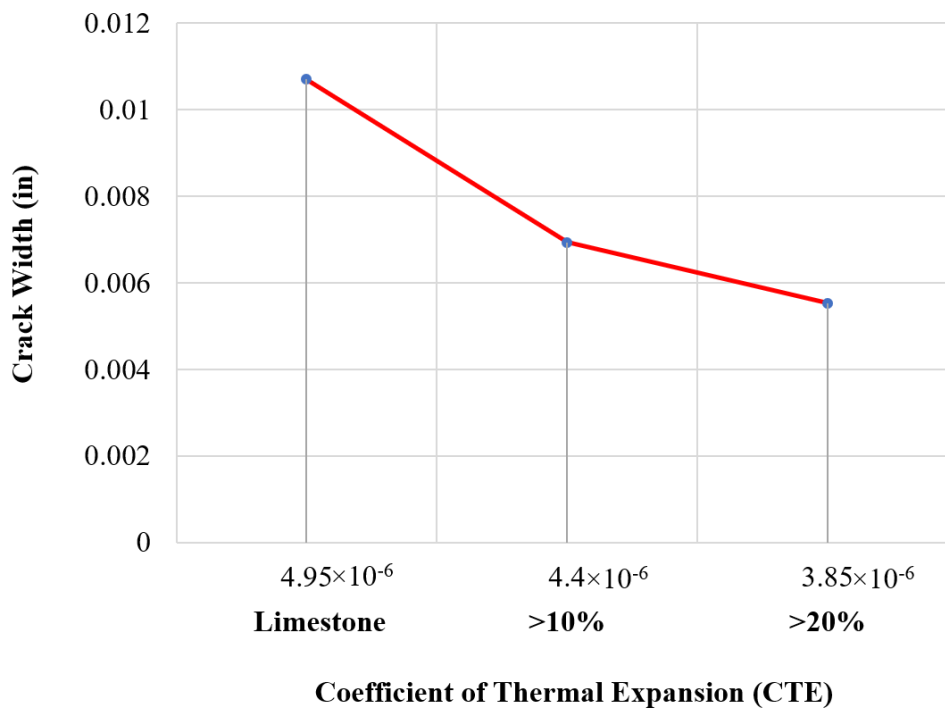
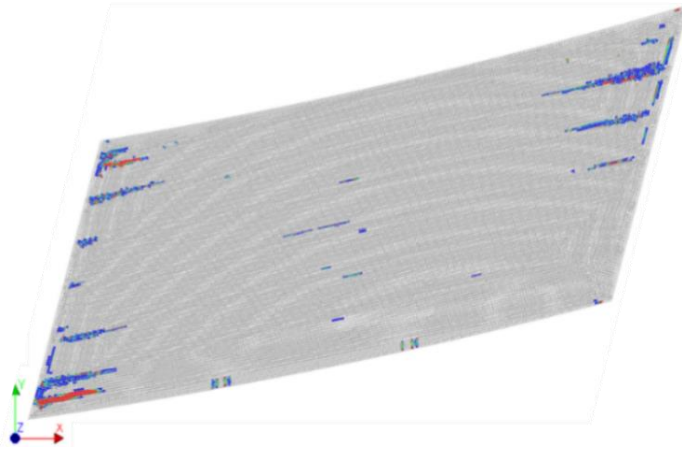
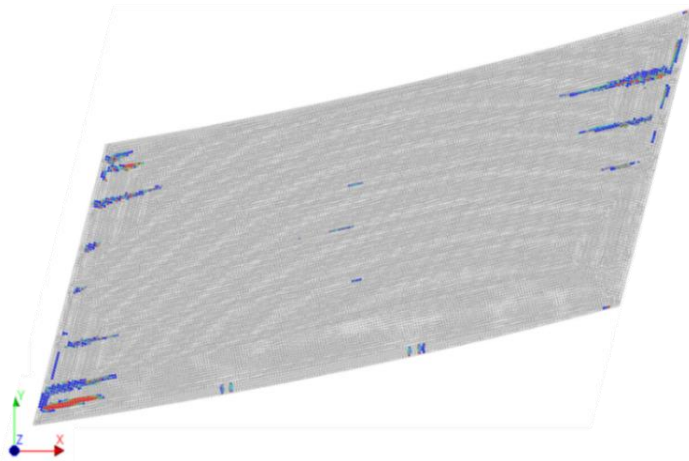


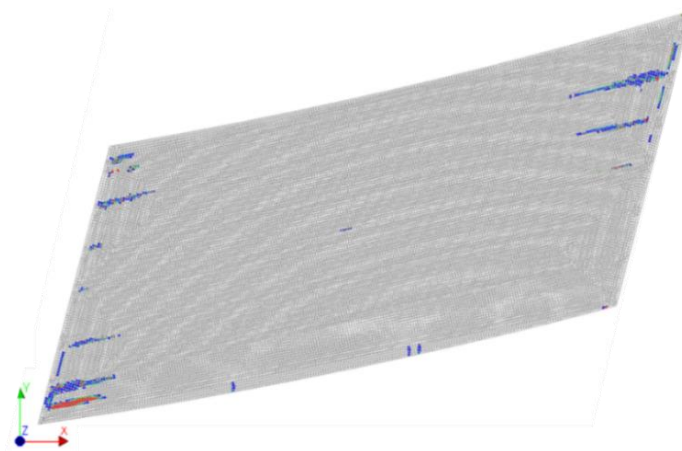
Figure 202 – Sensitivity of Crack width for reduced CTE



(a) CTE used in this study



(b) 10% reduction in CTE

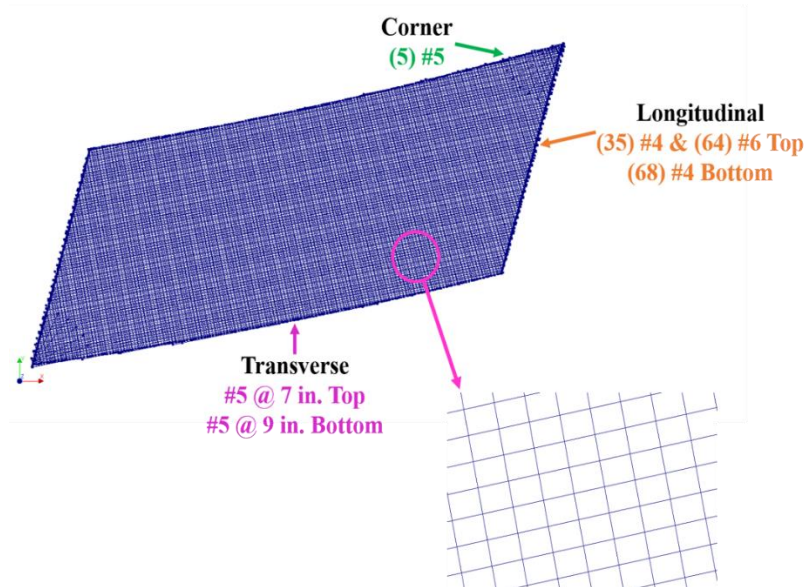


(c) 20% reduction in CTE

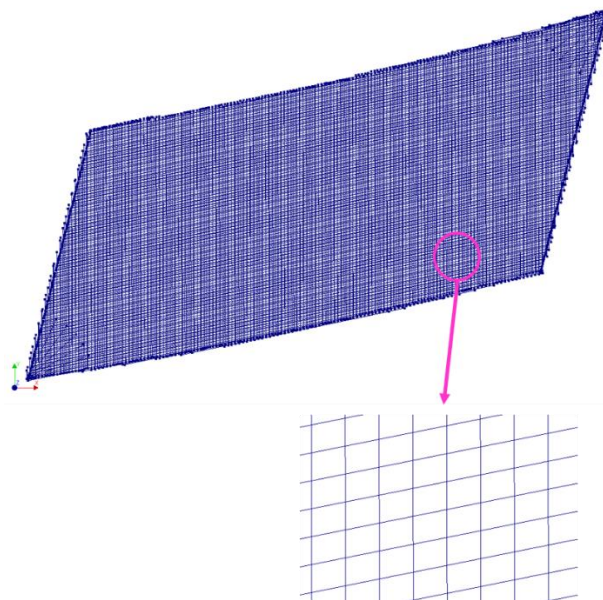
Figure 203 – Crack plots showing the effect of reduced CTE.

6.4 Effect of Reinforcing Steel Pattern in the Deck

Two reinforcement patterns shown in Figure 204 are investigated to study the effect of reinforcement orientations. Figure 205 compares the resulting crack strains and widths.



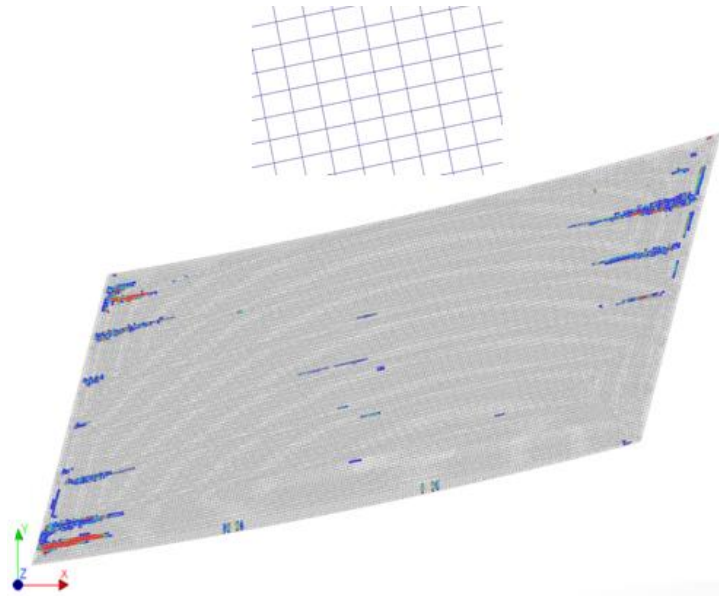
(a) Radial transverse reinforcement (used in this study).



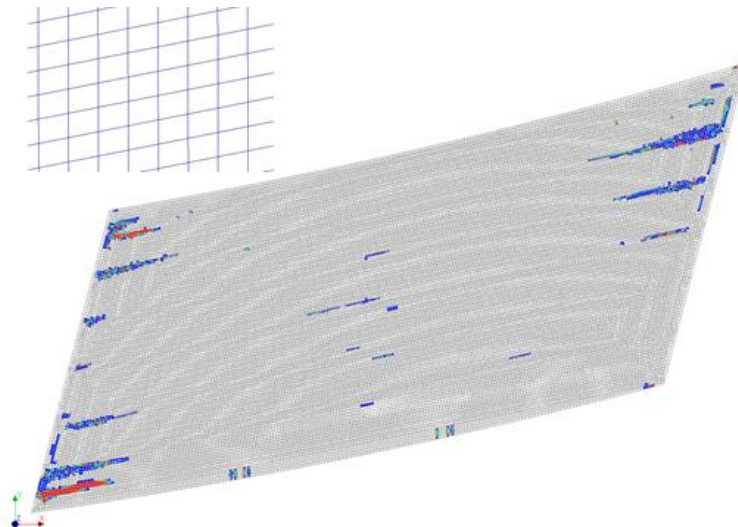
(b) Straight transverse reinforcement.

Figure 204 – Two different reinforcing steel patterns.

In Figure 205, the analysis results indicate there is a slight reduction in the crack width (0.018 in. or 0.46 mm), which is an insignificant change.



(a) Radial Transverse Reinforcement.
maximum crack strain = 7990 $\mu\epsilon$
maximum crack width = 1.07×10^{-2} in. (0.27 mm)



(b) Radial Transverse Reinforcement.
maximum crack strain = 6620 $\mu\epsilon$ (< 17%)
maximum crack width = 1.05×10^{-2} in. (~ 0.27 mm) (< 2%)

Figure 205 – Crack width plots showing the effect of reinforcement pattern.

6.5 Effect of Live Loads and Induced Vertical Displacements

Based on the results (see Sections 5.4 and 5.5) of the live load and hypothetical vertical displacement analysis cases (see Sections 4.8 and 4.9), these loads are not directly related to the cracks developed on the SR299 bridge deck.

6.6 Synthesis of Results and Potential Causes of Cracks

The SR299 bridge is a semi-integral abutment bridge with two span superstructures with rigid foundations (e.g., caisson foundation). The bridge deck is continuous with approach slabs. Thus, only construction joints exist, but expansion joints are not present at the approach ends. The results from the field (see Section 3) and analytical (see Section 5) investigations indicate the potential causes of cracking on the SR299 bridge may include as-built bearing details and environmental conditions. Additionally, the deck geometry is another factor to consider when bridge decks develop cracks in such conditions, particularly in a semi-integral abutment bridge.

Bridge decks are exposed to hot Georgia summer weather and are likely to experience deformation in the form of an expansion. Therefore, at the end of Bents 1 and 3, on the abutment sides, thermal movements are intentionally prevented in a semi-integral bridge. This is evident in the absence of expansion joints at the approach ends. Accordingly, the expansion joint location at the intermediate bent should accommodate thermal movements from both spans. The bridge inspection photos (GDOT BIR, 2017), however, indicate that the bridge girder-to-bearing connection (i.e., bolted to restrain the longitudinal-direction expansion) may be prohibiting the thermal movements of the girders although the deck edges are free to expand at the expansion joint location. Such restraints

create internal stresses in the bridge deck, which are ultimately relieved by developing cracks.

Figure 206 shows a crack map obtained from the field investigations (see Section 3.5.3.2, Figure 28) compared to the Span 1 results from the analytical investigations (see Section 5.3.3.1, Figure 145). Similarly, Figure 207 compares a crack map obtained from the field investigations (see Section 3.5.3.2, Figure 28) with a crack pattern map for Span 2 predicted from the FEA (see Section 5.3.4.1, Figure 166).

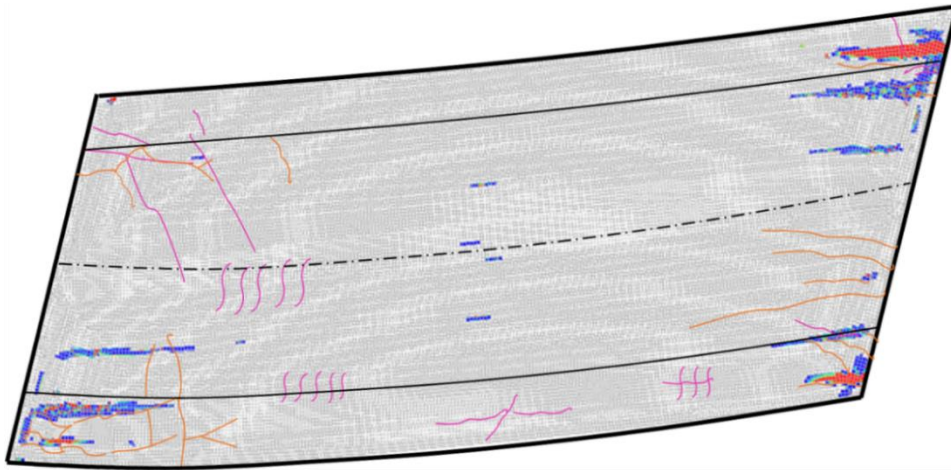


Figure 206 – Observed and computed cracks on SR299 bridge deck (Span 1).

Note: Orange and pink lines indicate cracks observed from the first and second site investigations, respectively, whereas the blue and red color scheme indicates elements identified as cracked from the FEA.

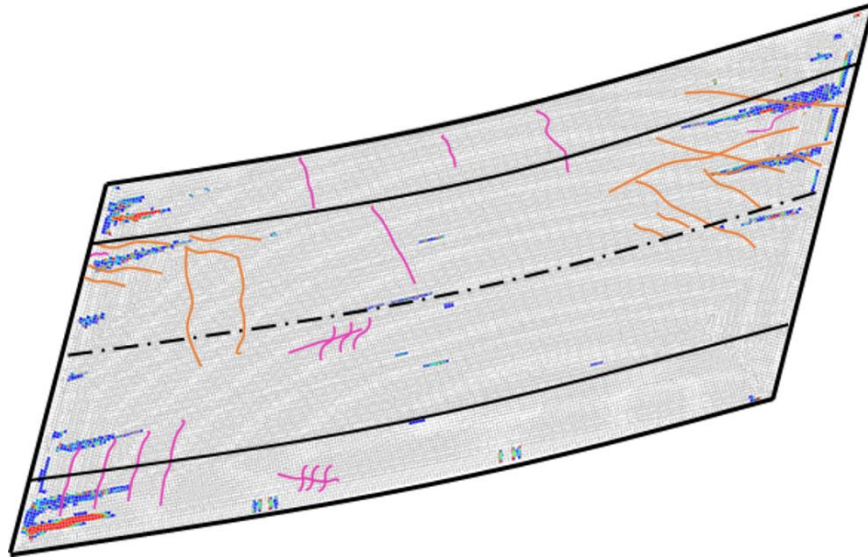


Figure 207 – Observed and computed cracks on SR299 bridge deck (Span 2).

Figure 206 and Figure 207 show that the crack patterns obtained from the analytical investigations are similar in terms of crack location to the crack maps developed from the two field investigations. Cracks are mostly concentrated in the acute corners and are formed as a result of differential thermal expansions and restraints. A few cracks exist along the Span 1 and Span 2 edges at the intermediate bent. In reviewing the computed crack locations, it should be recognized that cracked elements are identified by evaluating stresses at the numerical integration points of each element. The analysis model also assumes homogenous material properties in uncracked solid elements and thus is not able to predict the propagation of cracks. Considering the fact that the analysis model predicts crack initiation, the observed and computed cracks could have propagated into the crack pattern present on the deck in the process of redistributing the thermal stress developed in the deck section.

Skewed decks are known to be vulnerable to cracking due to differential thermal expansions and asymmetric live load distributions in their acute corners. Additionally,

when the girders are restrained from thermal movements at an expansion joint in a semi-integral abutment bridge, they restrain the deck from longitudinal thermal movement. It is concluded that thermal restraints from the girder-to-bearing connection at the expansion joint location might have caused visible cracking in the acute corners and in other areas of the SR299 bridge deck. The skewed deck geometry increases the potential for differential thermal expansion and thus thermal cracking when restrained. However, it is also concluded that, regardless of the deck geometry, the deck would have experienced cracking if girders at the expansion location were not allowed to move.

The decision matrix described in Section 1.4 is completed based on the results obtained from the field and analytical investigations presented herein. Table 20 highlights variables and their corresponding degrees of contribution to deck cracks observed on the SR299 bridge deck. There are two main structural design factors: thermal restraints and skew angles (see the first and third items in Table 20). The thermal restraints define the design and/or as-built bearing and boundary conditions that determine the thermal contraction and expansion behaviors of the bridge deck. The skew angle defines deck geometry and determines the extent of differential thermal expansion and contraction in acute deck corners. Notably, the SR299 bridge was designed to best accommodate such thermal movements, as the design's bearing details show sufficient slot hole dimensions for thermal movement in the structural drawings. Moreover, additional reinforcement was placed at the corners to resist the tension developed in the corners. Despite of the design effort, the integral abutment feature needed for the accelerated construction and the skewed deck geometry necessary for the site appear to yield the cracks observed on the deck. The results from a petrographic examination indicate that the material design used for the

SR299 bridge deck was adequate. Additionally, the bridge was designed to sustain the current live load.

Finally, since the bridge was constructed using the ABC method, potential vertical movements during construction and misalignments of the superstructure are considered. The construction documents indicate that the vertical movements of the bridge deck remained within the tolerance (approx. 0.75 in. or 19.05 mm). While other construction-related factors (see Table 20) also appear adequate, the as-built bearing connections between the girders and substructure appear inadequate. It is critically important to use sole plates with longitudinal slots, as detailed in the design drawings, in order to accommodate thermal movements. In summary, Table 20 reflects the study team's opinions for cracks developed on the SR299 bridge deck.

Table 20 – Decision matrix for screening out factors relevant to cracking.

Category	Factors Causing the Distress	Major	Moderate	Minor
Structural Design	Semi-integral abutment design combined with skewed deck geometries	✓		
	Reinforcement layout			
	Deck thickness			
	Skew angle >25°		✓	
	Deflection during construction			
Material Design	Paste volume			
	Aggregate type			
	Shrinkage/creep			✓
	Water-to-cement ratio			
	Heat of Hydration			
	Supplementary materials			
Construction	Placement method			
	Curing method			
	Weather/time of deck placement			✓
	Elevation corrections during superstructure moves (e.g., SPMT moves/jacking/shimming)			
	Bearing connections	✓		

7 CONCLUSIONS

Many factors contribute to cracking in concrete bridge decks. The factors associated with materials include the aggregate characteristics, modulus of elasticity, creep, the heat of hydration, and concrete shrinkage, to list a few. Factors associated with design include bearing details, integral abutment design, and reinforcement details. Environmental factors affecting concrete deck temperature including solar radiation, wind, and precipitation. Lastly, factors associated with construction are critically important in order to realize the materials and details specified in the design. Based on this study, the following conclusions are made:

- Bridges experience thermal contraction and expansion due to environmental conditions. Integrated endwalls at both ends restrain the bridge superstructure from thermal movements due to the presence of the soil backfill pressure. This is an inherent design feature of a semi-integral bridge. Because of this restriction, it is important to recognize that the bridge superstructure must expand away from the abutments and toward the expansion joint at the intermediate bent.
- Therefore, at expansion joint locations (see Figure 69), bearing details under precast girders significantly affect the thermal movement of the bridge superstructure (see Figure 70). With insufficient room for expansion in sole plates (see Figure 71), bridge girders and deck slabs are restrained from thermal movements and thus are likely to relieve thermal stress by developing cracks.
- When skewed deck geometries exist in a semi-integral bridge, the skewed corners on the abutment sides are vulnerable to developing cracks regardless of the bearing details at expansion joint locations.

- The SR299 bridge was susceptible to thermal cracking due to the skewed deck geometries at the integral bridge ends. The integral abutment bridge design and skewed deck geometry were inevitable design features to enable the ABC technology used in the bridge replacement. Additionally, the inspection report indicates that the sole plate details may not have been adequate to accommodate thermal movements from temperature variations even though the design documents show adequate sole plate details with slots of sufficient size. This potential discrepancy may have exacerbated thermal cracking, particularly in the acute corners and the expansion joint location.

8 RECOMMENDATIONS AND FUTURE WORK

Bridges are normally exposed to the elements of nature, and deck geometry varies due to the topology of roadways. Despite the advantages of semi-integral abutment bridges for addressing environmental and site-related conditions, they pose challenges when they are used with asymmetric bridge decks.

When asymmetric deck geometries (e.g., inclined, curved, and/or skewed decks) exist in a bridge, the following recommendations are made based on this study:

- When designing a skewed bridge, a semi-integral abutment design should be avoided.
- If such asymmetric design is necessary in conjunction with ABC technologies, bearings require greater consideration in order to minimize cracks caused by temperature changes.
- Asymmetric thermal movements should be expected when an asymmetric deck exists. Therefore, bearings and steel reinforcement in the deck must be designed accordingly.
- Finally, a winter placement of the concrete deck is strongly recommended to minimize shrinkage cracks, though few were observed in the SR299 bridge deck.

In addition, based on the literature review in Section 2, the following recommendations and associated future work are proposed:

- When designing a skewed bridge (particularly one with skew angles exceeding 25 degrees), additional reinforcement should be specified to mitigate cracks. For

example, CDOT recommends detailing transverse reinforcement perpendicular to the main supporting members (see Section 2.4.2).

- This reinforcement design is slightly different from the radial reinforcement pattern used in the SR299 bridge, although fan-shaped reinforcement is also provided in the corner areas. Several state DOTs recommend the latter practice.
- In terms of reinforcement orientation and details, there appears to be no strong consensus on how to mitigate cracking in skewed decks. A best practice guide for a wide range of skewed deck geometries is strongly recommended.

REFERENCES

- AASHTO. (2017). *AASHTO LRFD bridge design specifications, Part I: Sections 1-6* (8th ed.). Washington, D.C.: American Association of State Highway and Transportation Officials.
- Alashari, M. (2016). Accelerated bridge construction (ABC): A better approach to bridge construction? *International Journal for Innovation Education and Research*, 4(8), 41-70.
- Albajet, H. (1999). *Behavior of horizontally curved bridges under static load and dynamic load from earthquakes*. Chicago, IL: Illinois Institute of Technology.
- Anusreebai, S., & Krishnachandran, V. (2016). Effect of reinforcement pattern on the behaviour of skew slab. *International Research Journal of Engineering and Technology*, 3(8), 1879-1885.
- Balakumaran, S. S., Weyers, R. E., & Brown, M. C. (2018). *Linear cracking in bridge decks* (Report No. FHWA/VTRA 18-R13). Charlottesville, VA: Virginia Transportation Research Council.
- Barsoum, F., El Safty, A., & Phillip, L. (2012). Using finite element analysis to evaluate the performance of cracked bridge decks. Proceedings from *Structures Congress 2012*. Chicago, IL: American Society of Civil Engineers. 667-674.
- Biggs, R., Barton, F. W., Gomez, J. P., Massarelli, P. J., & McKeel, W. T. (2000). *Finite element modeling and analysis of reinforced-concrete bridge decks* (Report No. VTRC 01-R4). Charlottesville, VA: Virginia Transportation Research Council.
- Caltrans. (2015). *Bridge Design Practice*. Sacramento, CA: California Department of Transportation.
- CDOT. (2018). *CDOT LRFD bridge design manual*. Denver, CO: Colorado Department of Transportation.
- Chattanooga Metropolitan Airport Weather History (2017). *Weather Underground*. Retrieved January 15, 2019, from <https://www.wunderground.com/history/>.
- Chorzepa, M., Durham, S., & Hamid, H. (2019). *Phase II - Evaluation of metakaolin for GDOT concrete specifications (ASTM C618 N Pozzolan) and mass concrete provision* (GDOT Report No. PR 16-30). Atlanta, GA: Georgia Department of Transportation.
- CTDOT. (2003). *Bridge design manual*. Newington, CT: Connecticut Department of Transportation.

Culmo M. (2017). Utah DOT's accelerated bridge program [web training]. *Accelerated Bridge Construction University Transportation Center*. Tallahassee, FL: Florida International University. Retrieved from <https://abc-utc.fiu.edu/>.

Deng, Y., Phares, B. M., Greimann, L., Shryack, G. L., & Hoffman, J. J. (2015). Behavior of curved and skewed bridges with integral abutments. *Journal of Constructional Steel Research*, 109, 115-136.

DeSantiago, E., Mohammadi, J., & Albaijat, H. M. (2005). Analysis of horizontally curved bridges using simple finite-element models. *Practice Periodical on Structural Design and Construction*, 10, 18-21. doi:10.1061/(ASCE)1084-0680(2005)10:1(18)

DIANA. (Version 10.2). Retrieved from <https://dianafea.com/index.php/>.

Dutt, A. (2015). Effect of mesh size on finite element analysis of beam. *SSRG International Journal of Mechanical Engineering*, 2(12), 8-10. doi: 10.14445/23488360/IJME-V2I12P102

ElSafty, A., & Abdel-Mohti, A. (2013, March). Investigation of likelihood of cracking in reinforced concrete bridge decks. *International Journal of Concrete Structures and Materials*, 7(1), 79-93. doi:10.1007/s40069-013-0034-3

Femto Engineering. (2017, May 22). In *FEA, what is linear and nonlinear analysis?* Retrieved from <https://www.femto.eu/>.

FHWA. (2000). Highway infrastructure. *Comprehensive Truck Size and Weight Study* (Publication No. FHWA-PL-00-029 Vol. I). Retrieved from <https://www.fhwa.dot.gov/>.

FHWA. (2011). *Accelerated bridge construction manual* (Publication No. FHWA-HIF-12-013). Washington, DC: U.S. Department of Transportation.

FHWA. (2014). *Slide-in bridge construction* (Publication No. FHWA-HIF-13-056). Washington, DC: U.S. Department of Transportation.

FHWA. (2017, December 31). *Deficient bridges by highway system 2017*. Retrieved from <https://www.fhwa.dot.gov/>.

FHWA. (2018, July 26). *Self propelled modular transporters (SPMT)*. Retrieved from <https://www.fhwa.dot.gov/>.

FHWA. (2018, March 8). *Accelerated Bridge Construction*. Retrieved from <https://www.fhwa.dot.gov/>.

FHWA. (2019). Appendix C: Vehicle types. *Traffic Monitoring Guide*. Retrieved from <https://www.fhwa.dot.gov/>.

FHWA-NHI. (2017, June 27). Design step 7.1 – Integral abutment design. *Comprehensive Design Example for Prestressed Concrete (PSC) Girder Superstructure Bridge with Commentary* (Report No. FHWA-NHI-04-043). Retrieved from <https://www.fhwa.dot.gov/>.

French, C., Eppers, L., Le, Q., & Hajjar, J. F. (1999). Transverse cracking in concrete bridge decks. *Transportation Research Records*, 1688(1), 21-29.

Frosch, R., Blackman, D., & Radabaugh, R. (2003). *Investigation of bridge deck cracking in various bridge superstructure systems*. Indianapolis, IN: Indiana Department of Transportation.

Fu, G., Feng, J., Dimaria, J., & Zhuang, Y. (2007). *Bridge deck corner cracking on skewed structures* (Report No. RC-1490). Wayne State University, MI: Department of Civil and Environmental Engineering.

Fu, G., Zhuang, Y., & Feng, J. (2011). Behavior of reinforced concrete bridge decks on skewed steel superstructure under truck wheel loads. *Journal of Bridge Engineering*, 16(2). doi:10.1061/(ASCE)BE.1943-5592.0000142

GarverUSA. (2013, April 3). *An inside look at designing for Accelerated Bridge Construction (ABC)* [Video file]. Retrieved from <https://www.youtube.com/>.

GDOT. (2016). GDOT-DB working drawings and calculations package for ABC Method. *SR 299 at I-24 Bridge Replacement (Accelerated Bridge Construction) Project*. Atlanta, GA: Georgia Department of Transportation.

GDOT. (2017). Monitoring Data—56 hr move. *SR 299 at I-24 Bridge Replacement (Accelerated Bridge Construction) Project*. Atlanta, GA: Georgia Department of Transportation.

GDOT. (2019). *Bridge and structures design manual*. Retrieved from <http://www.dot.ga.gov/>.

GDOT BIR. (2017). *SR299 bridge inspection report*. Atlanta, GA: Georgia Department of Transportation.

GDOT BuildSmart. (2017). *State route 299 over I-24 bridge replacement*. Retrieved from <http://www.dot.ga.gov/>.

GDOT TADA. (2018). *Road and traffic data*. Retrieved from <https://gdottrafficdata.drakewell.com/publicmultinodemap.asp>.

GDOT-DRW. (2016). *As-built drawings of SR299 at I-24 bridge replacement accelerated bridge construction*. Atlanta, GA: Georgia Department of Transportation.

Goodall, J. (2019). *Replacement of two vehicular bridges at Silver Falls*. Salem, OR: Oregon Department of Transportation. Retrieved from <https://www.oregon.gov/pages/index.aspx>.

Google. (2019). *Maps* [State Route 299, Wildwood, GA]. Retrieved from <https://www.google.com/maps/>.

Hopper, T., Manafpour, A., Radlińska, A., Warn, G., Rajabipour, F., Morian, D., & Jahangirnejad, S. (2015). *Bridge deck cracking: Effects on in-service performance, prevention, and remediation*. Harrisburg, PA: Pennsylvania Department of Transportation.

Imbsen, R., Vandershaf, D., Schamber, R., & Nutt, R. (1985). *Thermal effects in concrete bridge superstructures*. (NCHRP Report No. 276). Washington, DC: Transportation Research Board.

IOWADOT. (2014). *Bridge maintenance manual*. Ames, IA: Iowa Department of Transportation.

Itani, A. M., & Reno, M. L. (1999). Horizontally curved bridges. In: W. Chen, & L. Duan (Eds.), *Bridge Engineering Handbook*. Boca Raton, FL: CRC Press LLC.

Karunaratne, A., Mampearachchi, W., & Nanayakkara, A. (2010). *Modelling of thermal effects due to solar radiation on concrete pavements*. Sri Lanka: University of Moratuwa.

Krauss, P., & Rogalla, E. (1996). *Transverse cracking in newly constructed bridge decks*. (NCHRP Report No. 380). Washington, DC: Transportation Research Board.

Leonhardt, F. (1988). Cracks and crack control in concrete structures. *PCI Journal*, 124-145.

Ma, F., & Kwan, A. (2017). Finite element analysis of concrete shrinkage cracks. *Advances in Structural Engineering*, 21(10). 1454-1468. doi:10.1177/1369433217746346

Marx, H. J., Khachaturian, N., & Gamble, W. L. (1991). Design criteria for right and skew slab-and-girder bridges. *Transportation Research Record*, (1319), 72-85.

Menassa, C., Mabsout, M., Tarhini, K., & Frederick, G. (2007). Influence of skew angle on reinforced concrete slab bridges. *Journal of Bridge Engineering*, 12(2), 205-214.

MnDOT. (2011). Bridge deck cracking. *Transportation Research Synthesis* (Report No. TRS1105). St. Paul, MN: Minnesota Department of Transportation. Retrieved from <https://lrrb.org/>.

More, S. T., & Bindu, R. (2015). Effect of mesh size on finite element analysis of plate structure. *International Journal of Engineering Science and Innovative Technology*, 4(3), 181-185.

NYDOT. (2007). *Integral abutment bridges: Comparison of current practice between European countries and the United States of America*. Albany, NY: New York Department of Transportation. Retrieved from <https://www.dot.ny.gov/index>.

Ofil, M. (2015). *State of the Accelerated Bridge Construction (ABC) in the United States*. (University Honors Program Thesis). Georgia Southern University, Statesboro, GA. Retrieved from <https://digitalcommons.georgiasouthern.edu/>.

Pantelides, C. P., & Weber, E. D. (2011). *Evaluation of bridge deck seal treatment for Accelerated Bridge Construction (ABC) bridge decks using precast panels* (Report No. UT-11.17). Taylorsville, UT: Utah Department of Transportation. doi: UT-11.17

Purvis, R., Babaei, K., Udani, N., Qanbari, A., & Williams, W. (1995). Premature cracking of concrete bridge decks: Causes and methods of prevention. Proceedings from *Fourth International Bridge Engineering Conference*. San Francisco, CA: Transportation Research Board. 163-175.

Rajagopalan, N. (2006). *Bridge superstructure*. Chennai, India: Alpha Science International Ltd.

Ramey, G. E., & Wright, R. (1994). *Assessing and enhancing the durability/longevity performances of highway bridges* (Report No. HRC 2-13506). Auburn University, AL: Highway Research Center.

Rettner, D. L., Melanie, F. S., Synder, M. B., & MacDonald, K. A. (2014). *Analysis of bridge deck cracking data*. (Report No. MN/RC 2014-09). St. Paul, MN: Minnesota Department of Transportation. Retrieved from <https://www.dot.state.mn.us/>.

Russell, H. (2017). *Control of concrete cracking in bridges*. (NCHRP Synthesis No. 20-05/Topic 47-01). Washington, DC: Transportation Research Board. doi:10.17226/24689

Sazzad, M., Islam, T., Azad, S., & Rahman, F. I. (2017). Effect of mesh size on floor slab against lateral loads while using Etbas Program. *International Journal of Advanced Structures and Geotechnical Engineering*, 6(1), 40-44.

Schindler, A. K., Hughes, M. L., Barnes, R. W., & Byard, B. E. (2010). *Evaluation of cracking of the US 331 bridge deck* (Report No. FHWA/ALDOT 930-645). Auburn University, AL: Highway Research Center. Retrieved from <https://rosap.ntl.bts.gov/>.

Schmitt, T. R., & Darwin, D. (1995). *Cracking in concrete bridge decks* (SM Report No. 39). Lawrence, KS: University of Kansas Center for Research.

Shayanfar, M., Kheyroddin, A., & Mirza, M. (1997). Element size effects in nonlinear analysis of reinforced concrete members. *Computers & Structures*, 62(2), 339-352.

Sindhu, B., Ashwin, K., Dattatreya, J., & S.V, D. (2013). Effect of skew angle on static behavior of reinforced concrete slab bridge decks. *International Journal of Research in Engineering and Technology*, 50-58.

Steinkamp, N. (1971). Bridge deck deterioration. Proceedings from *Purdue Road School 1971*. West Lafayette, IN: Purdue University. Retrieved from <https://docs.lib.purdue.edu/>.

TxDOT. (2018). *Bridge design manual-LRFD*. Austin, TX: Texas Department of Transportation.

Vargas, V. V. (2012). *Bridge deck cracking investigation and repair* (UNF Master's Thesis). University of North Florida, Jacksonville, FL. Retrieved from <https://digitalcommons.unf.edu/>.

Wan, B. (2010). *What's causing cracking in new bridge decks?* (Report No. 0092-09-06). Madison, WI: Wisconsin Department of Transportation. Retrieved from <https://wisconsindot.gov/Pages/home.aspx>.

Wan, B., Foley, C., & Komp, J. (2010). *Concrete cracking in new bridge decks and overlays* (Report No. WHRP 10-05). Milwaukee, WI: Marquette University. Retrieved from <https://wisconsindot.gov/Pages/home.aspx>.

Wang, Y., Zou, Y., Li, C., Xu, L., & Wang, S. (2015, January). Analytical methods for temperature field and temperature stress of column pier under solar radiation. *Mathematical Problems in Engineering*, 2015, 8. doi: <https://doi.org/10.1155/2015/278072>

WSDOT. (2008). *Bridge design manual*. Olympia, WA: Washington State Department of Transportation.

Zhuang, Y., Fu, G., Ji, T., & Chen, B. (2011). FEA of deck corner cracking on skewed bridge structures. *Advanced Materials Research*, 255-260, 1240-1243. doi: <https://doi.org/10.4028/www.scientific.net/AMR.255-260.1240>

APPENDIX A

Infrared and High-Definition Bridge Deck Scan

by

NEXCO-West USA, Inc.



Table of Contents

1. Introduction	2
2. Technology and Software	3
3. Field data collection and weather conditions	10
4. Summary of findings	14
4.1 Findings from the high-speed scan	14
4.2 Deficiency maps	17
4.3 Conclusion	20

1. Introduction

This demonstration was undertaken to introduce NEXCO-West USA's bridge deck and roadway pavement scanning technology to the University of Georgia's Engineering Department and officials from Georgia's Department of Transportation. The technology was applied to a bridge deck on State Route 299 crossing over Interstate 24 in Wildwood, GA (Figure 1). The demonstration's scope included the high-speed field scanning of a single bridge deck, and a sample evaluation of the deck's condition. This evaluation report features the scaled notation of deficient features (cracking, spalling, patchwork, delamination) on a scaled plan-view diagram (shown in section 4 of this document).

The DTSS system was developed to locate, classify, and quantify deficiencies in roadway structures at posted speed limits up to 70mph, so its methodology rules out the necessity of lane closures by maintaining traffic flow. As a result, very large amounts of surface area can be taken in a short amount of time. The application of this technology could potentially range from individual bridge deck assessments to the rapid scanning of bituminous roadways on county or state-wide levels. The recording of both infrared and RGB imagery into solid-state drives (SSD) or hard drives (HDD) brings on-site analysis back to the safety of the office, where data can be reviewed by whomever, whenever, and wherever. Recordings result in a more permanent and objective record of roadway conditions and can even be used to comparatively track the progression of damaged areas over time. The above benefits will assist structural owners in tracking over-arching tendencies in their structures and allocate future budgets accordingly.



Figure 1: SR 299 Bridge in Wildwood, GA

2. Technology and Software

NEXCO provides concrete, asphalt, and façade condition assessment services using its various imaging technologies. The Deck Top Scanning System (DTSS) is a mobile platform which can be loaded/mounted onto a vehicle (Figure 2a). It consists of an infrared thermography (IR) camera, two line-scanning cameras, a GPS unit, and a speedometer unit that, combined, locate surface and sub-surface defects in bridge decks or roadways. Post analysis software called IrBAS (infrared) and JeEditor (visual) is used to combine the data from each of these instruments (Figure 2b and 2c). The infrared camera is mounted facing the opposite direction of traffic, and captures around a 15ft range. The two line-cameras are mounted in a similar fashion on either end of the back frame and individually capture a 13ft range, but overlap to capture a 18ft range. The photographic range is dependent on the angle and height at which the cameras are mounted, so these ranges can be altered as needed. The DTSS can operate at 10 to 70 mph, ruling out the need for lane closures.



Figure 2a: The Deck Top Scanning System (DTSS)

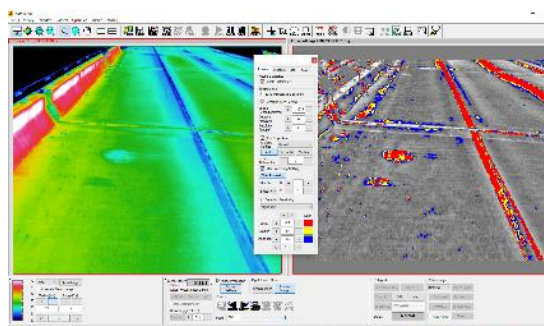


Figure 2b: IR image analysis software Ir-BAS (left) and A6701sc IR camera (right)

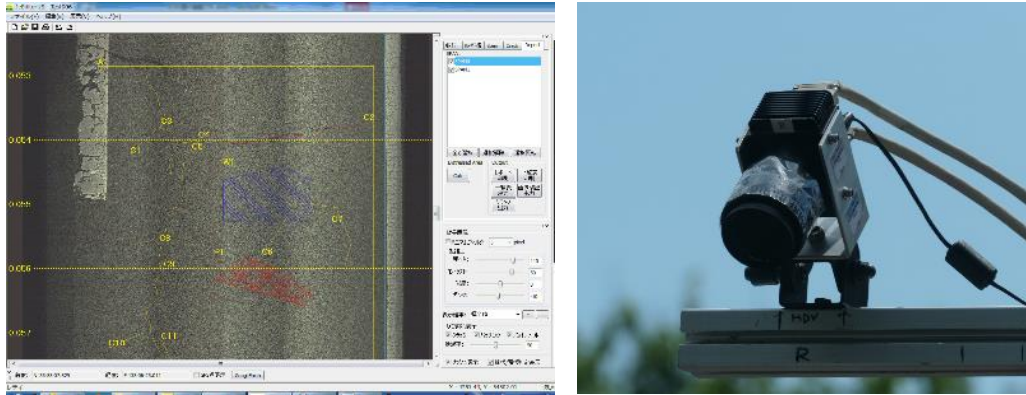


Figure 2c: RGB image analysis software JeEditor (left) and Basler LSC camera (right)

Infrared imaging is used to capture the temperature of a target surface. Defects, or unsound areas, on the surface and subsurface tend to exhibit a different temperature in comparison to normal, or sound, areas during periods of ambient temperature change. In general, the thermal change in structures is caused by changes in air temperature, exposure to radiation during the day, and radiative cooling at night. Figures 3 and 4 below illustrate the behavior of temperature in both sound and unsound portions of concrete over the course of a day. Unsound areas will exhibit slightly high temperatures after an increase in ambient temperature, and slightly lower temperatures after a decrease in ambient temperature.

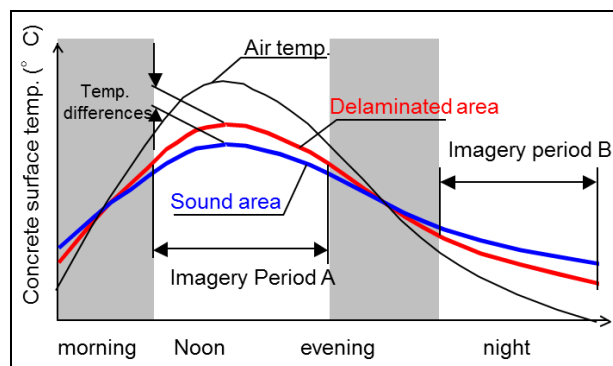


Figure 3: Ambient and concrete temperature variation a day

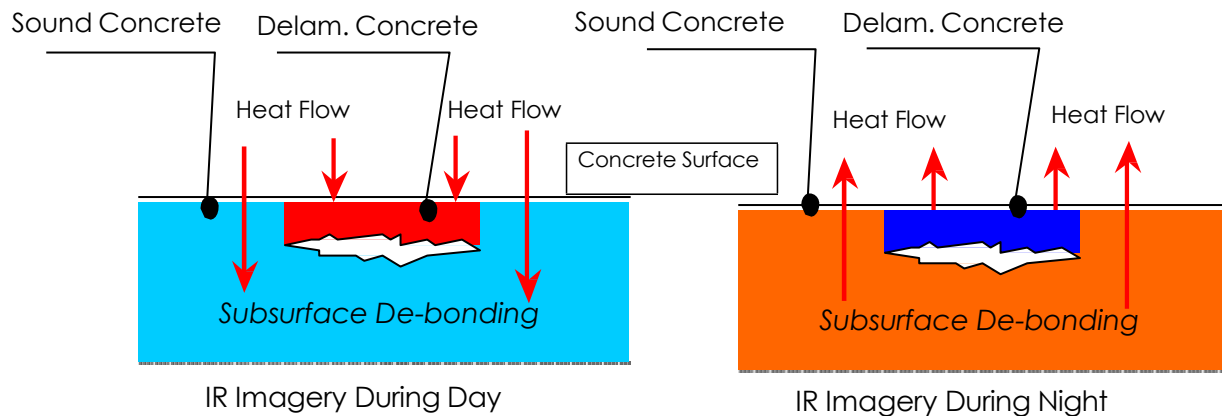





Figure 4: Thermal flow in concrete structures during day and night

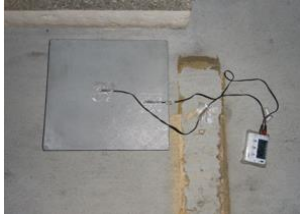
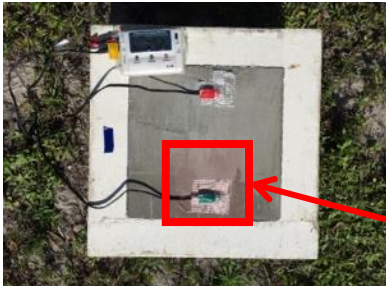
A high integration and exposure time (an IR camera's "shutter speed") allows the FLIR A6701sc camera (Figure 2b) to record at highway speeds and still maintain an excellent level of accuracy during daytime or nighttime. The camera's cooled detector, an InSb model, also helps to achieve low margin of error by stabilizing the machine's internal temperature: it achieves a 0.18 °F margin of error without blurring individual frames.

IR imagery is recorded and analyzed for temperature differentials automatically by IrBAS (Figure 2b) during the scan, and later proofed by a trained IR specialist during post-analysis. Based on an advanced thermal gradient and pattern analysis function, the software is able to pinpoint locations of probable delamination. It is very challenging and time-consuming to analyze raw thermographs, so the software helps to interpret them by displaying potential delaminations on a separate image, which NEXCO calls a "processed image." This function utilizes a database of a vast amount of past infrared inspections conducted over a ten-year period. It allows a margin for false positives due to temperature anomalies caused by other reasons. The color of objects especially has a very influential effect on heat absorption and retention of materials, and while it is not realistic to use the same criteria for each and every area of a bridge, areas with irregular coloration may show up as detections. Nonetheless, the processed imagery is a powerful tool when compared alongside both raw thermographs and visual images.

To determine the precise location of defects, a GPS and a speedometer are used to assign coordinates to every frame of the recording during IR and visual scanning respectively. The GPS data is linked to the IR frames and allows selected frames to be opened in Google Maps or Earth, where the location of that frame and a picture copy of it are displayed. Potential findings are quantified, then classified according to adjustable conditions. Condition ratings can be formatted to meet AASHTO condition state standards for inspection of highway structures. The output of the scanning system is flexible and can be linked or changed to various formats for presentation. Specifications for all IR-related components are outlined in Table 1 below.

Table 1: Infrared Component Specifications

■ Infrared (IRT) Scanning System																	
High End IRT Camera	Camera Specifications																
	<table><tr><td>Model</td><td>FLIR A6701sc </td></tr><tr><td>Detector</td><td>Indium Antimonide (InSb), cooling detector¹⁾</td></tr><tr><td>Spectral Range</td><td>3.0 μm to 5.0 μm</td></tr><tr><td>Resolution</td><td>640 x 512</td></tr><tr><td>Thermal Sensitivity: NETD@25°C</td><td>< 25mK</td></tr><tr><td>Integration Time</td><td>500 ns ²⁾</td></tr><tr><td>Full Frame Rate</td><td>Programmable 0.0015 Hz to 125 Hz</td></tr><tr><td>Lens Type</td><td>13mm</td></tr></table>	Model	FLIR A6701sc 	Detector	Indium Antimonide (InSb), cooling detector ¹⁾	Spectral Range	3.0 μm to 5.0 μm	Resolution	640 x 512	Thermal Sensitivity: NETD@25°C	< 25mK	Integration Time	500 ns ²⁾	Full Frame Rate	Programmable 0.0015 Hz to 125 Hz	Lens Type	13mm
	Model	FLIR A6701sc 															
	Detector	Indium Antimonide (InSb), cooling detector ¹⁾															
	Spectral Range	3.0 μm to 5.0 μm															
	Resolution	640 x 512															
	Thermal Sensitivity: NETD@25°C	< 25mK															
	Integration Time	500 ns ²⁾															
Full Frame Rate	Programmable 0.0015 Hz to 125 Hz																
Lens Type	13mm																
1), 2) A very short integration time is required when driving at high speed (45 mph). The uncooled detector used in conventional IRT cameras detects changes in resistance, voltage or current when heated by infrared radiation, thus requiring longer exposure time to take the IRT image.																	
Proprietary Software, Ir-BAS	1) Filtering Function The thermal gradient--often caused by differing thermal conditions (e.g. exposure to sunshine or shade, different																

	<p>thickness of a structural member, etc.) and tends to hide a thermal anomaly caused by a real delamination--is filtered out by the software.</p> <p>2) Filtering Function The thermal gradient--often caused by differing thermal conditions (e.g. exposure to sunshine or shade, different thickness of a structural member, etc.) and tends to hide a thermal anomaly caused by a real delamination--is filtered out by the software.</p> <p>3) Damage rating function (Fig. 2b) Temperature distribution is interpreted into ratings by the software based on a comprehensive database developed by NEXCO over ten years that relates temperature distribution patterns to the severity and type of defects.</p> <p>4) Skew correction function Skewed IRT images are reformed to normal viewing by software to accurately locate defects on deck surface. Each delamination is identified and plotted on plan view drawings of the deck.</p> <p>5) Location on Google Map A GPS system is used during data collection to support accurate geo-location of defects.</p>
Concrete Test Pieces	<p>Effective application of infrared technology is highly dependent on environmental conditions. In order to determine the optimum temperature conditions for data collection, a concrete test piece developed by NEXCO with an artificial delamination in the middle is used to monitor the temperature of both sound and unsound concrete during the scanning period. It acts as a kind of quality control mechanism for IR evaluation.</p> 
Thermo-Recorder (for environmental monitoring)	<p>"Thermo-Recorder" TR-71Ui To record temperature variation during the time of scanning, multiple thermo-recorders are placed in strategic locations near the site, and temperature readings of concrete and ambient air are taken in 30sec-1minute intervals.</p>  <p>Artificial Delamination</p>

The two line-scanning cameras are used to capture high-definition visual imagery. These cameras were originally developed to detect small-scale deformities in factory-printed materials (like textiles), but they also excel at generating scaled diagrams of roadway surfaces. The visual imagery can be used to identify and measure cracking, spalling, and any other visually identifiable characteristic. Additionally, it provides a visual proof for the IR data. Frequently, things such as discoloration, oil spills, or other markings can result in false detections when reviewing the IRT thermographs, so it is necessary to compare both visual and IRT data side-by-side (or by overlaying one on top of the other). Cracks down to a 0.3mm width can be recognized on the line scan, and generally these detections are measured and drawn manually onto the images by a trained engineer.

Each individual camera scans at a 13ft width (around 18ft in total, with 8ft overlapping), in a constant stream. The camera requires motion, ideally a steady speed, to operate, but the frequency and spacing of recorded lines are adjusted in real-time by a high-performance speedometer. See more details about the LSCs in Table 2 below.

The line data is processed and analyzed with an image manipulation and crack editing software called JeEditor. Based on intervals determined by speedometer and GPS, the software arranges the visual line data (rows of 1 x 4010 mm² pictures) and provides an interface which the user can overlay scaled gridlines and deficiencies. The deficiencies can be classified based on type, area, width, etc. Various light-correction functions allow the user to enhance the image and make hairline cracks easier to detect. Areas/lengths drawn in the interface are quantified, and can be output to excel for report composition. One reason behind taking both a visual and an infrared scan is the necessity of visual proofing of the IR data, or checking for false positives. While interpreting IR scanning results, it is important to differentiate and subsequently exclude false positives on the deck surface caused by things such as spilled paint, roadway striping, or other unusual objects. Without making this comparison, it is possible to misinterpret a discoloration as a delamination, because they tend to exhibit similar temperature differentials.

An LSC system is the recommended alternative to high resolution area-scanning photography or video, because it avoids the distortion caused by the rounded lenses on most other cameras. In our experience, the DTSS using LSC and IR in combination has provided higher resolution image results (resolution: 1mm²/pixel) in assessing and documenting defects, and does not result in blurring commonly observed in area-scanning cameras.

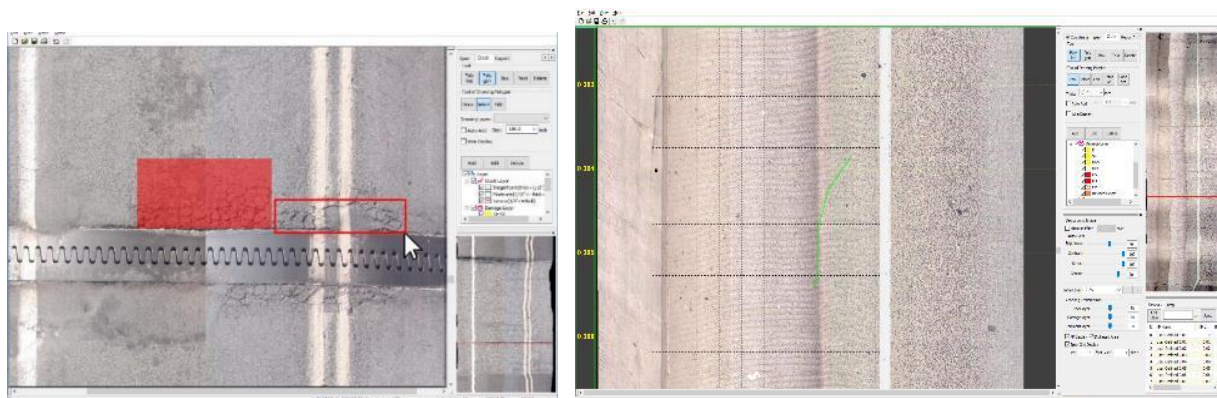
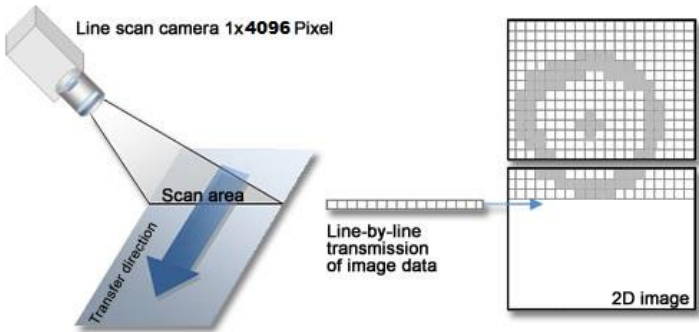



Figure 5: JeEditor interface

Table 2: Line Scanning Camera System

Line Scanning Cameras	
Line Scan Camera	<p>Area scan cameras deliver a sequence of images of a moving object. An unbroken image of continuous materials is achieved by capturing overlapping images. Software then painstakingly crops the individual, overlapping images, eliminates distortion, and finally assembles the images in the correct sequence. Line scan cameras, on the other hand, have a single row of light-sensitive pixels, which continuously scan moving objects at a high line frequency. Digital images collected by the line scan camera present a vertical view, perpendicular to the deck surface.</p> 

	Camera Specification	
	Model	Basler
	Type	Color
	Line rate	38.6 kHz
	Number of pixels	4,096 pixels/line x 2 cameras Detectable crack width = 0.3 mm
High Accuracy Speedometer	A spatial filter speed measuring apparatus is used as a speedometer.	
	Performance specification	
	Speed range	0.3 – 250 km/h
	Distance resolution	1.5 mm
	Measurement accuracy	< $\pm 0.2\%$ FSO
	Measurement frequency	250 Hz
		

3. Field data collection and Weather conditions

The field data collection for IR and digital imagery was taken twice: at night on October 25th between 10:15 pm and 10:20 pm and on the following day between 1:00 pm to 1:05 pm.

In order to ensure a successful scan with IR technology, it is critical to select the best time window for the field data collection, in respect to temperature conditions. The best and most stable time window generally occurs from the start of an intensive thermal flow from the concrete to the air at sunset, and lasts until the temperature differential between the concrete and air stabilize. Differentials and thermal anomalies can be detected at this time using an infrared camera with a high thermal sensitivity and fast exposure time. In general, this thermal flow is created by both ambient temperature

and radiative cooling at night. Figures 5 and 6 below illustrate the behavior of temperature and radiation within concrete structures over the course of a day.

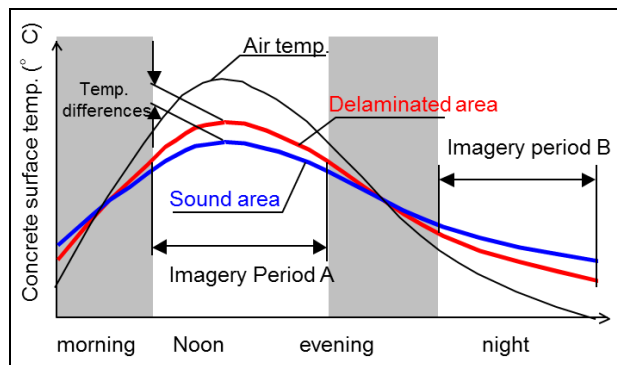


Figure 5: Ambient and concrete temperature variation a day

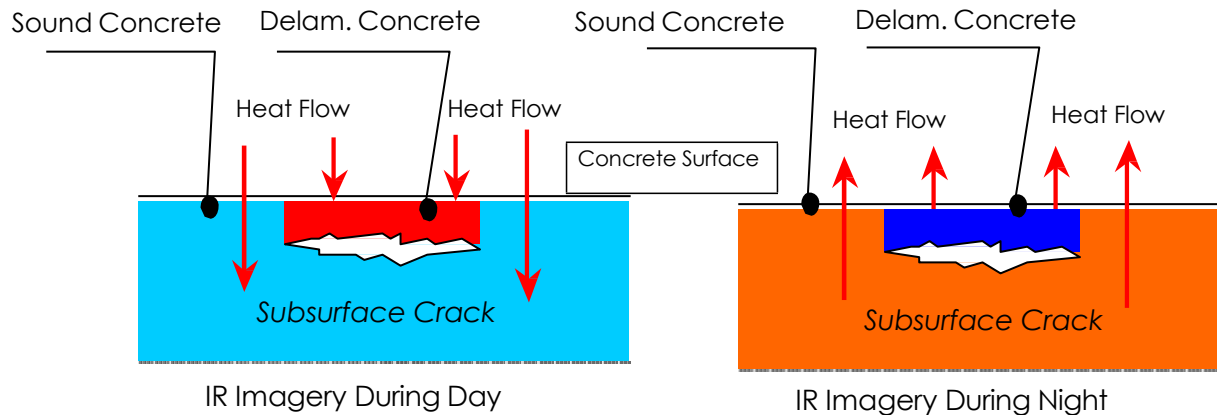


Figure 6: Thermal flow in concrete structures during day and night

After investigating weather and temperature conditions on-site during the inspection period, it was determined that the conditions were satisfactory. Ideally a temperature record should be taken near the site, but during this demonstration, the inspection team un able to find a suitable location to install a test piece. The temperature of ambient air (light blue) and a sample test piece concrete (red and green for unsound and sound concrete, respectively) are recorded at an area nearby the inspection site. See figure 7 for an example record from another site.

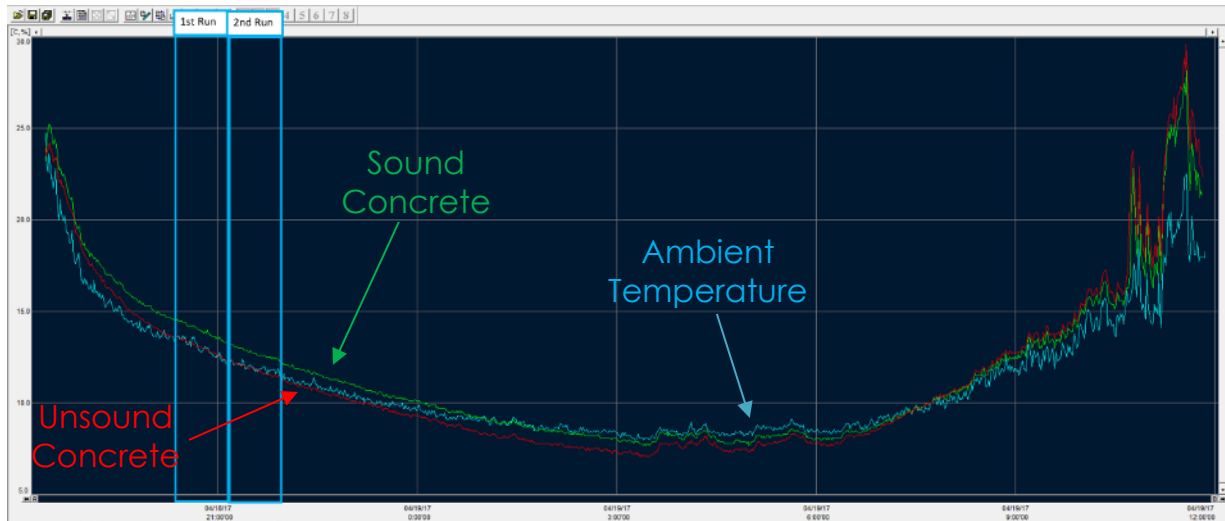


Figure 7a: Daily temperature record of concrete test piece

Instead of a test piece temperature record, we pulled records for 10/25 and 1026 from Weather Underground (wunnderground.com):

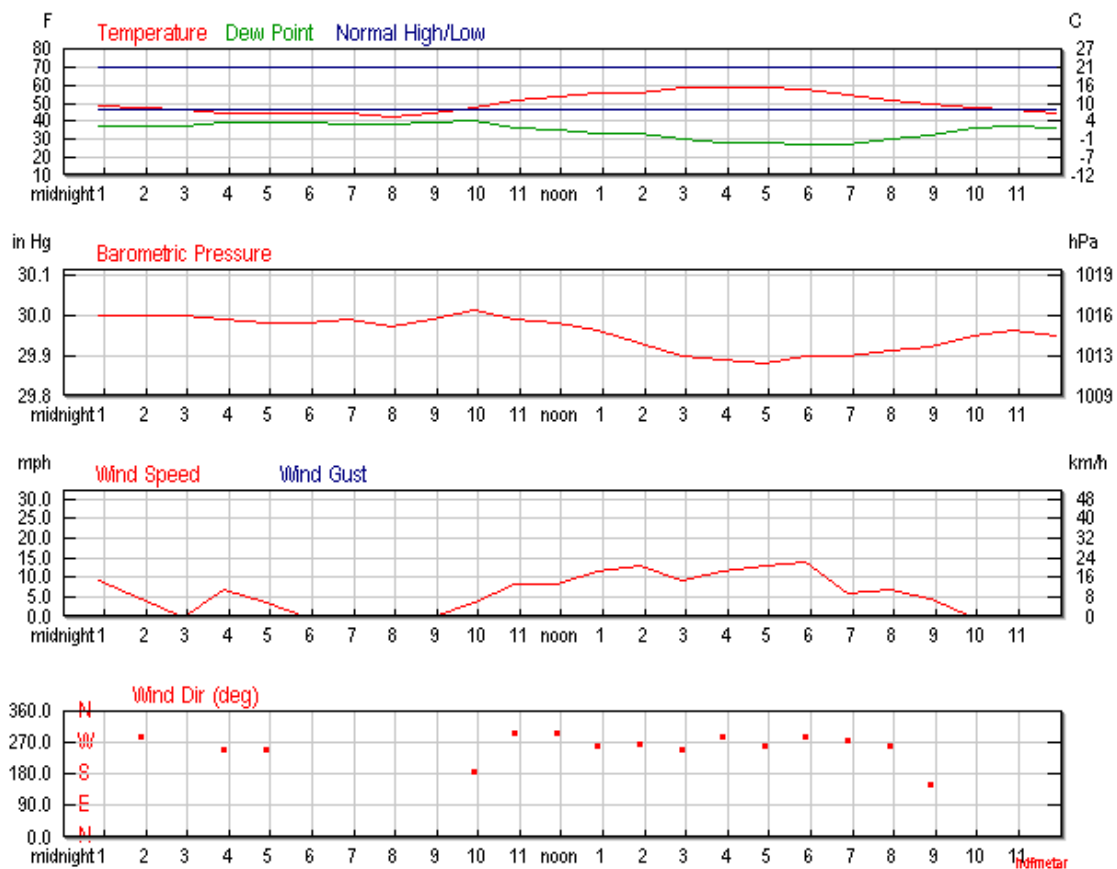


Figure 7b: 10/25/2017 daily temperature record

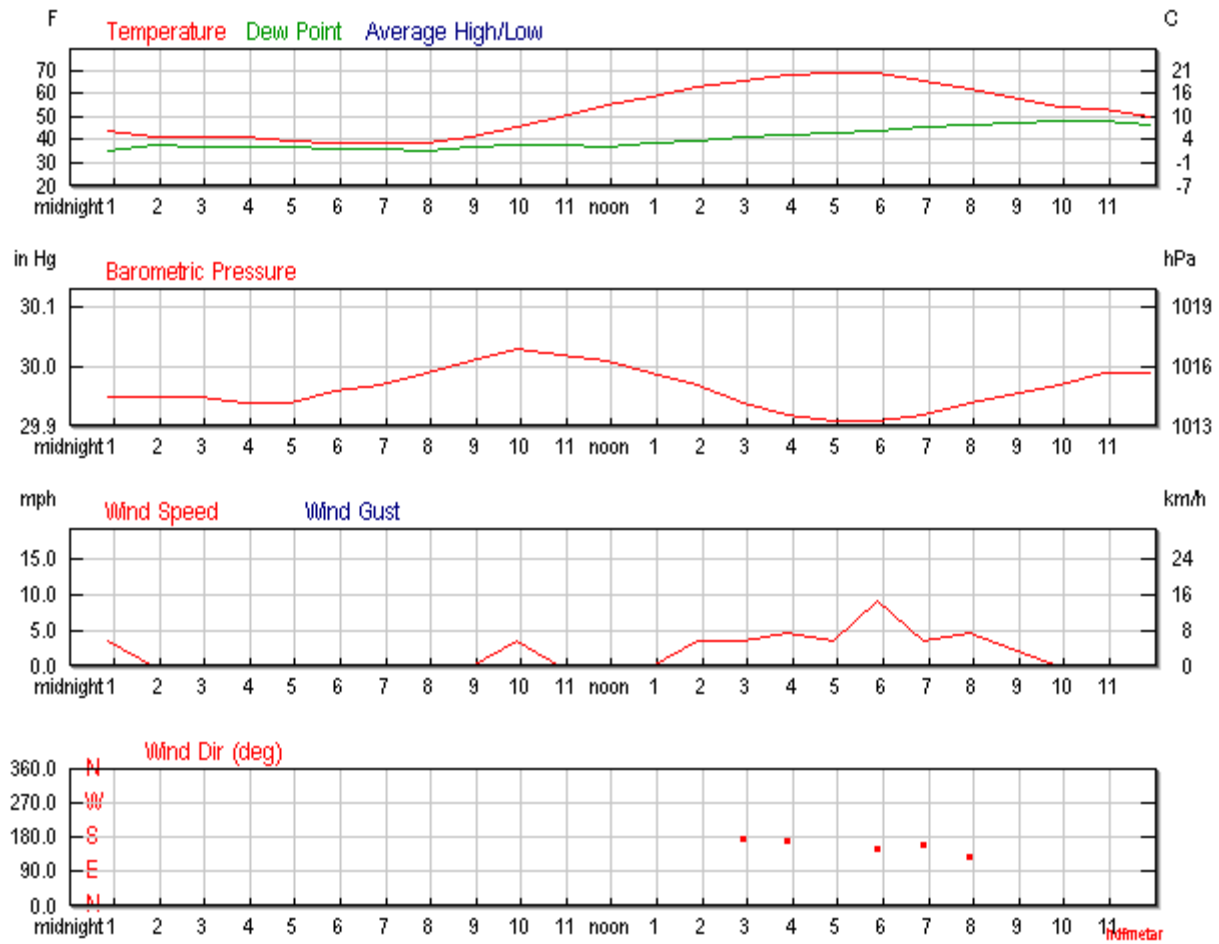


Figure 7c: 10/26/2017 temperature record

4. Summary of findings

4.1 Findings from the high-speed scan

Favorable weather conditions and a smooth scan resulted in a successful analysis of the bridge. All data collected—raw infrared, processed infrared, and visual—were compared closely side-by-side to eliminate false positives. The AASHTO Manual for Bridge Element Inspection, First Edition (AASHTO, 2013) provides a guideline for condition state definition of bridge elements based on the severity of delamination, spalling, exposed rebar, and cracking conditions. The distribution and location of the AASHTO-categorized deficiencies for each bridge was also prepared in the form of a plan-view map, where the deficiencies were highlighted and super-imposed onto an image of the bridge deck. Percentage of deck areas for each condition state was also summarized for each span of the bridge and graphically displayed as shown in Figure 8. This information can be used by bridge owners as a general assessment, and can help to prioritize future repair/rehabilitation programs by identifying deficient areas in their early stages.

Direction	SPAN	Repaired Crack	Insignificant	Moderate	Severe
Bridge information		CRACK(ft)			
EB	2	122	21.05	3.27	0
EB	1	0	1.89	5.8	0
EB	Total	0	22.94	9.07	0
Bridge information		CRACK(ft)			
WB	1	123	1.26	0	0
WB	2	34	9.29	0	0
WB	Total	157	10.55	0	0



DELAM	SOUND PATCH	MINOR SPALL	MODERATE PATTERN CRACKING	CS2 Total	Percentage of CS2 Area
CS2(ft2)					(%)
58	0	0	0	58.4	2.718%
37	0	0	0	37.44	1.710%

96	0	0	0	95.84	2.209%
CS2(ft2)					(%)
105	0	0	0	104.5	4.992%
113	0	0	0	112.55	5.208%
217	0	0	0	217.05	5.102%



UN SOUND PATCH	MAJOR SPALL	HEAVY PATTERN CRACKING	CS3 Total	Percentage of CS3 Area	Surface Area(ft2)
CS3(ft2)				(%)	
0	0	0	0	0.000%	2148.63
0	0	0	0	0.000%	2189.11
0	0	0	0	0.000%	4337.74
CS3(ft2)				(%)	
0	0	0	0	0.000%	2093.45
0	0	0	0	0.000%	2161.05
0	0	0	0	0.000%	4254.5

Figure 8a: Quantifications by span

Condition state summary for SR299 bridge (Eastbound)

Span Number	Element Description	Unit of Measure	Total Quantity	Condition State 1	Condition State 2	Condition State 3	Condition State 4
2	Reinforced Concrete Deck	ft ² (%)	4,338 (100%)	4,242 (97.791%)	95.84 (2.209%)	0 (0.000%)	0 (0%)

Condition state summary for SR299 bridge (Westbound)

Span Number	Element Description	Unit of Measure	Total Quantity	Condition State 1	Condition State 2	Condition State 3	Condition State 4
2	Reinforced Concrete Deck	ft ² (%)	4,255 (100%)	4,037 (94.898%)	217.05 (5.102%)	0 (0.000%)	0 (0%)

Figure 8b: Quantifications by East/Westbound halves

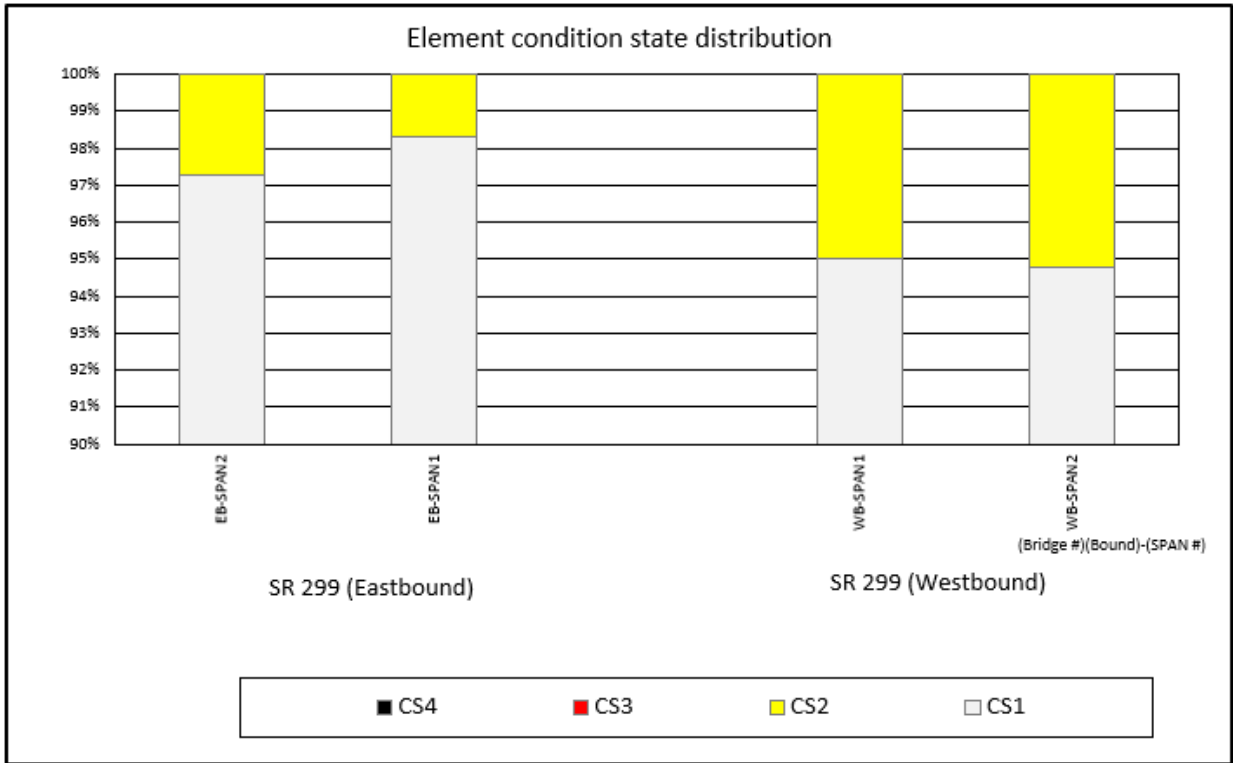


Figure 8c: Condition state distribution for each span

4.2 Deficiency maps

The result from the high-speed scanning was displayed on the following plan-view diagrams, or “deficiency maps” (see Figures 9 and 10 for examples). The tables in the deficiency map show the percentage of deck areas which fall into each AASHTO condition state. The base of the diagram consists of the LSC image with a grid overlay. The overlay is boxed into square feet and shows intervals of 10ft running along the side of each image. These numbers may be a bit difficult to see in the pasted images below, but show clearly in high-resolution outputs and in the software interface itself.

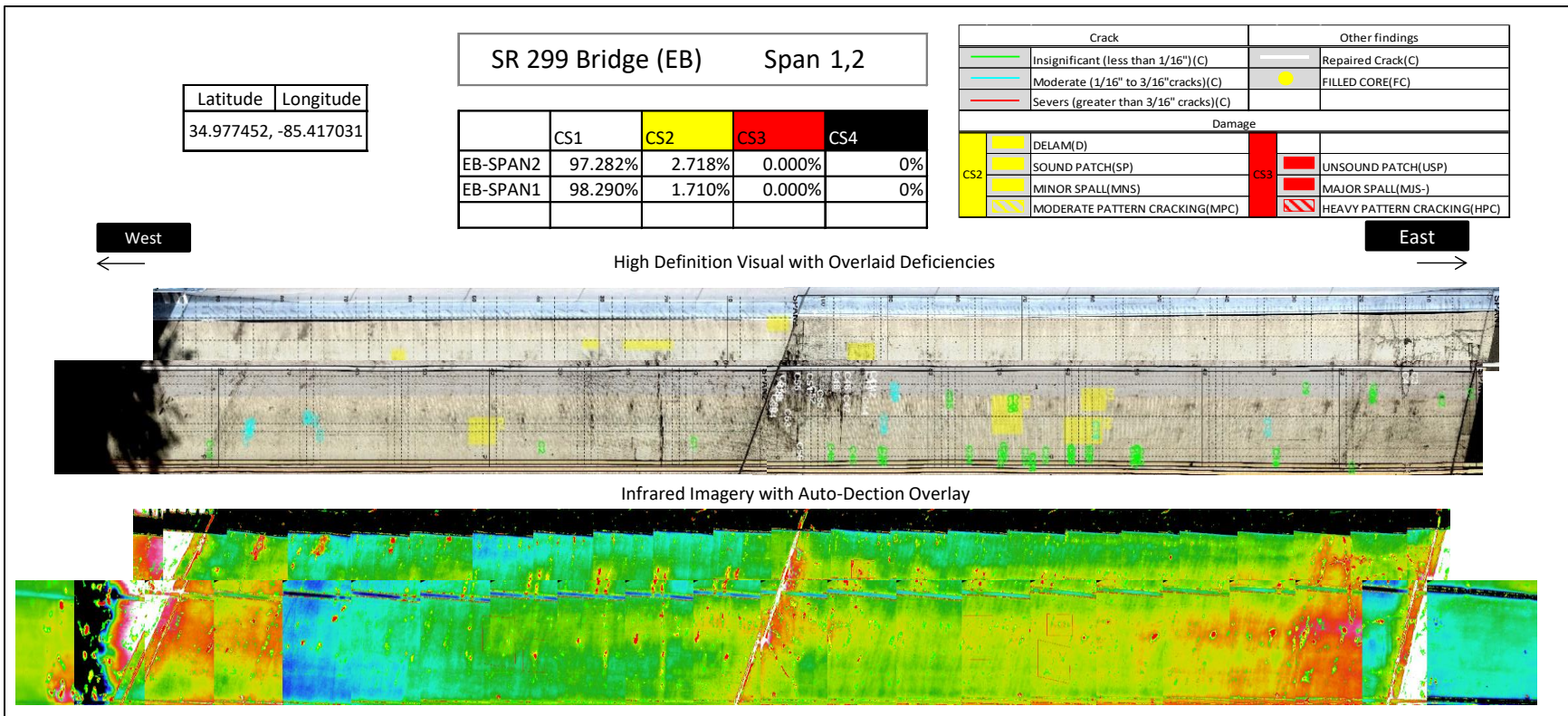


Figure 9: Deficiency map for the Eastbound Side

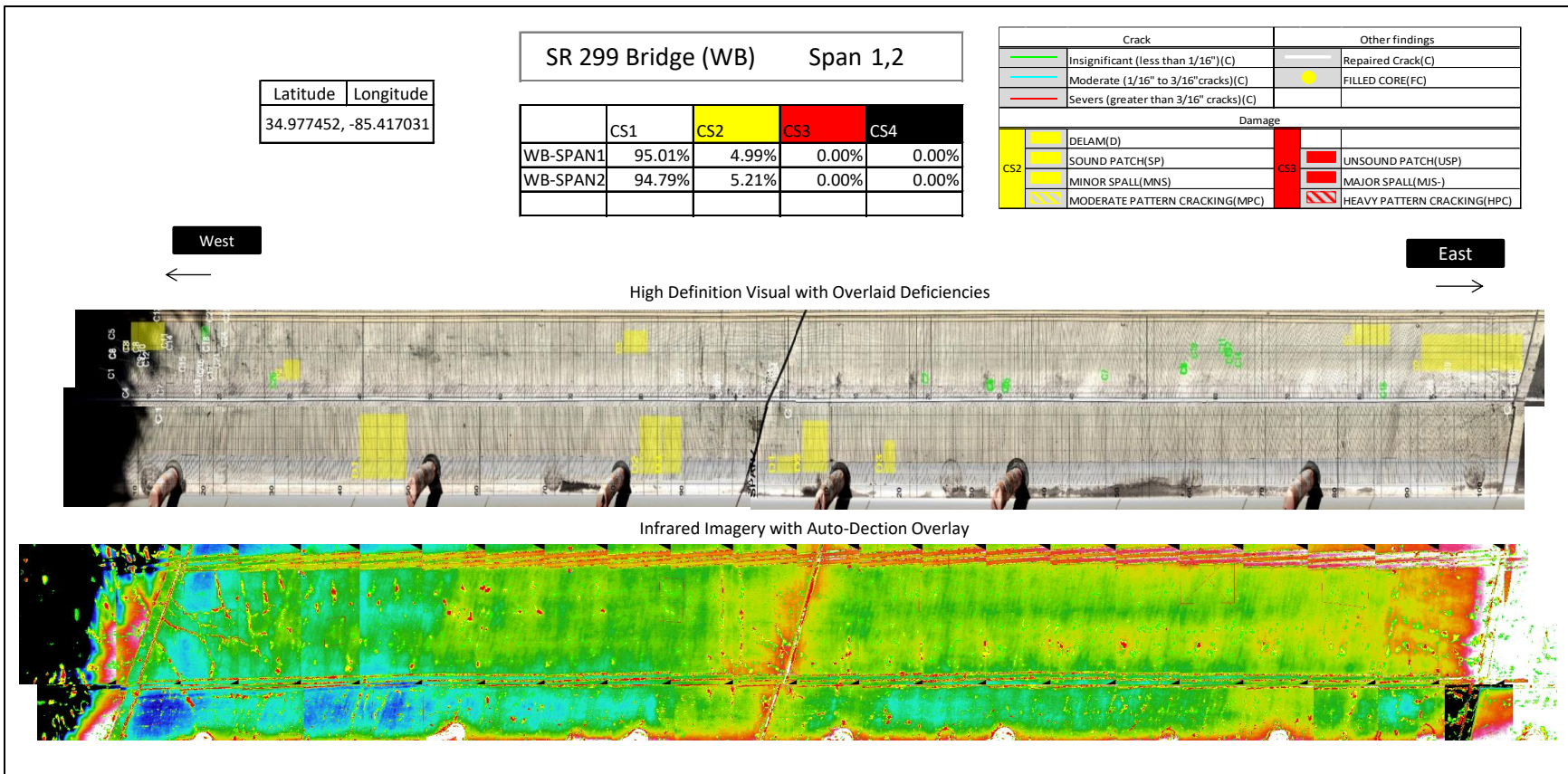


Figure 10: Deficiency map for the Westbound Side

4.3 Conclusion

It was observed that the bridge had some light cracks and a large amount of repaired cracking on both east and west-bound sides. Probable delamination was mainly found on the westbound side, and occurred sporadically in both the shoulders and lanes.

Output and formatting of this data is flexible, and can be altered upon request. Please contact us regarding any preferred representations of either the IR or visual data. To-scale, high definition data is also available, but is quite heavy must be transferred by file transfer programs (NEXCO utilizes Sharefile or Google Drive to transfer large files).

Thank you for allowing us to demonstrate NEXCO's inspection capabilities, and opportunity to learn more about UGA's upcoming projects.

References

1. AASHTO (The American Association of State Highway and Transportation Officials) (2013): Manual for Bridge Element Inspection, First Edition

END OF REPORT

APPENDIX B

Design, Construction, and Inspection Recommendations for Bridges with Skewed Deck Geometries and Integral Abutments

1. Introduction to Scope and Limitations

Skewed and/or integrated bridge designs employing Accelerated Bridge Construction (ABC) must be reviewed and assessed on a case-by-case basis, possibly utilizing a nonlinear and coupled thermal-structural analysis program. With this in mind, the following recommendations are made solely based on this study and the literature review conducted for this study. Therefore, the recommendations may be highly biased by the attributes of the SR299 bridge considered herein. The interpretation and use of assessment measures, assessment results, and concluding statements presented in this report should not be applied to other cases and bridges. Consequently, the following recommendations should be viewed as lessons learned from this study and should not be construed as confirmatory advice or a recommendation on any skewed and/or integral abutment bridges employing ABC.

2. Design Recommendations

When designing a skewed bridge employing ABC, thermal boundary conditions, including the use of a semi- or fully-integral abutment design and locations of expansion joints, should be carefully reviewed.

- Bearings and steel reinforcement patterns should be reviewed in order to adequately accommodate asymmetric thermal movements, if any, resulting from skewed deck geometries.
- When designing a skewed bridge deck (particularly one with skew angles exceeding 25 degrees), an elevated level of caution should be exercised to mitigate cracks, specifically in the acute corners of the bridge deck.

- The literature suggests that a bridge deck thickness should be greater than 6.5 in. (165 mm) (French et al., 1999; Krauss & Rogalla, 1996; ElSafty & Abdel-Mohti, 2013). Reducing rebar size or increasing rebar spacing should be considered to reduce transverse cracking (French et al., 1999). The existing literature offers widely different recommendations on reinforcing amounts and reinforcement patterns.

3. Construction Recommendations

- During construction, structural elements that establish thermal boundary conditions (such as bearing/sole plates and expansion joints) should be carefully constructed or installed in compliance with design drawings. If any changes are deemed necessary with such elements, the construction team should consult with the design engineer(s) before making any alteration.
- During construction, it is strongly recommended that both as-built elevations of temporary and permanent support structures be documented and/or carefully reviewed before temporarily or permanently placing a bridge deck. This will help identifying vertical alignment issues that may exist in a deck placement.
- The literature recommends that a construction team should avoid a concrete placement when the variation in daily ambient temperature reaches 50 °F (10 °C) (French et al., 1999) and recommends casting concrete in ambient air temperature between 40 °F (4.44 °C) and 90 °F (32.22 °C) (French et al., 1999). In high or low humidity conditions, casting concrete members at night (Russell, 2017), curing for at least seven days, and applying a curing compound (Russell, 2017) is recommended. Finally, immediately applying water, covering, or providing thermal

insulations after concrete placement is generally recommended to prevent the rapid evaporation of water during curing (Leonhardt, 1988). Although these recommendations do not directly apply to the SR299 bridge, they are important components of a concrete bridge deck placement.

4. Inspection Recommendations

It is strongly recommended that the Georgia Department of Transportation carefully inspect thermal boundary conditions including bearing and expansion joint installations.

Specific inspection items include, but are not limited to:

- Fixity conditions and associated bearing/sole plate details. In case of the SR299 bridge, the (side) elevation view shows FIX-EXP and EXP-FIX conditions.

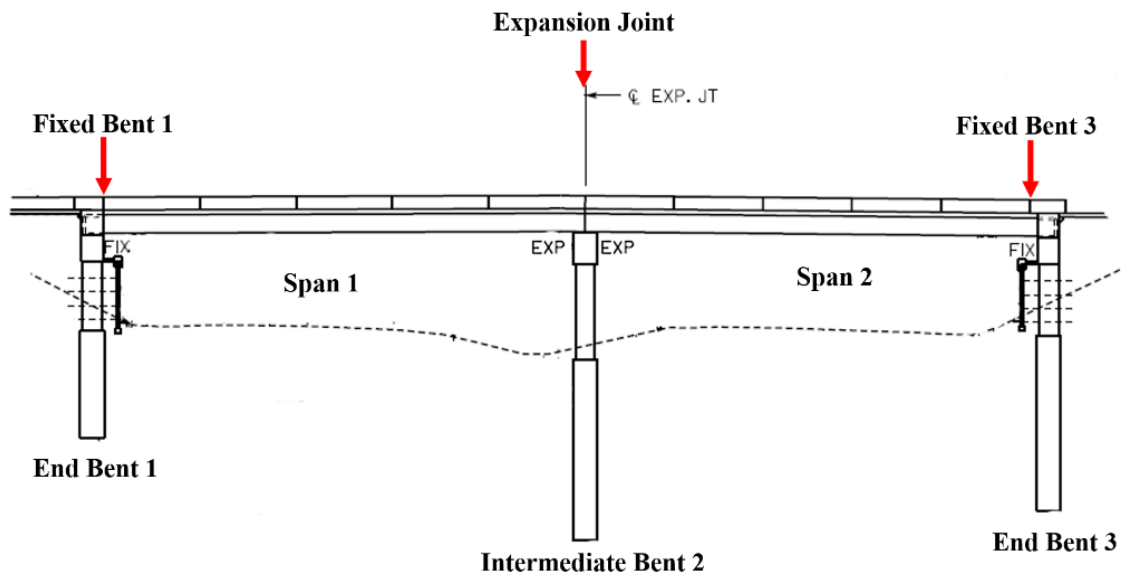


Figure B-1: Elevation view of the SR299 bridge showing the fixity conditions.

- At the fixed girder bearing end (or Bents 1 and 3 locations), the sole plates are designed for the fixed condition and thus should be detailed as shown in Figure B-2, unless otherwise approved by the design engineer(s).

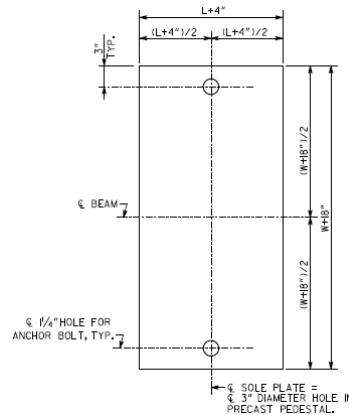


Figure B-2: Girder bearing details showing a sole plate at the “FIX” end (Bents 1 and 3).

- At the expansion girder bearing end (or Bents 1 and 3 locations), the sole plates are designed for the expansion condition and thus should be detailed as shown in Figure B-3, unless otherwise approved by the design engineer(s). During inspection, it is recommended to document the slotted hole dimensions. Non-compliance with the design (e.g., missing slotted holes) should be documented and/or reported immediately after discovery.

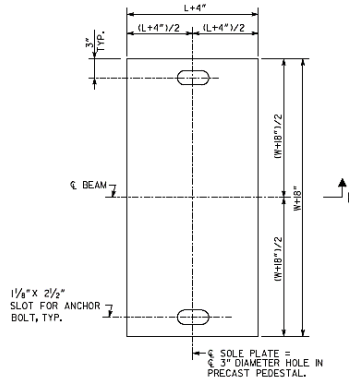


Figure B-3: Girder bearing details showing a sole plate at the “EXP” end (Bent 2).

- Inspect for the compliance of a gap (e.g., dimension = 2½ inches) that must exist in the expansion joint (see Figure B-4).

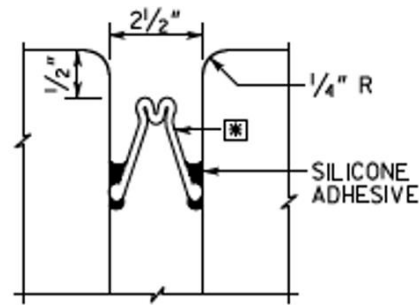


Figure B-4: Expansion joint at Intermediate Bent 2.

5. Concluding Remarks

The major direction of corner cracking in the existing literature considerably varies - “perpendicular to the radial”, “radial”, “transverse”, “longitudinal”, and/or “random.” Restraint conditions are presented as one of the most important factors for potentially mitigating deck cracking herein, particularly for the SR299 bridge including skewed deck geometries and semi-integral abutment designs. Nonetheless, it is strongly recommended that GDOT should review and assess each bridge project on a case-by-case basis.